Characterization of the Quasi-Static and Fatigue Behavior of Forged AZ31B Magnesium Alloy

by

Dwayne Toscano

A thesis
presented to the University of Waterloo
in fulfillment of the
thesis requirement for the degree of
Master of Applied Science
in
Mechanical and Mechatronics Engineering

Waterloo, Ontario, Canada, 2018

Author's Declaration

I hereby declare that I am the sole author of this thesis. This is a true copy of the thesis, including any required final revisions, as accepted by my examiners.

I understand that my thesis may be made electronically available to the public.

Abstract

Light-weighting is being aggressively targeted by automotive manufacturers as a method to reduce emissions. Magnesium (Mg) alloys due to their low density and high specific strength have therefore gained significant interest for automotive applications. As cyclic loading is a major concern for load-bearing automotive components, this thesis aims to characterize the fatigue response of AZ31B Mg alloy that may be forged to its final component geometry.

Initially, the effect of open die forging on cast AZ31B alloy was investigated. A partially refined microstructure with strong basal texture was developed in forged material. Tensile yield and ultimate strengths increased by a remarkable 143 percent and 23 percent respectively whereas the compressive yield strength was unchanged owing to the activation of extension twins for both conditions. Nevertheless, the ultimate compressive strength for the forged material increased by 22 percent compared to the as-cast material. The influence of open-die forging on the low cycle fatigue (LCF) behavior of cast AZ31B was also investigated. The forged material was generally found to exhibit longer fatigue life and also achieved significantly higher stresses at the same level of total strain amplitude compared to cast AZ31B. The Smith-Watson-Topper (SWT) model and Jahed-Varvani (JV) energy model were employed and both models accurately predicted the experimentally obtained fatigue life of both cast and forged alloy conditions.

Next, the effect of processing temperature and pre-form condition on the quasi-static response, and stress-controlled fatigue behavior of closed-die forged AZ31B Mg alloy was investigated. The forging process was conducted on billets of cast as well as extruded AZ31B at temperatures of 250°C and 375°C and a forging rate of 20mm/s. The obtained mechanical test results showed a strong influence of processing temperature and initial material condition on the mechanical response of the forged product. For a given starting condition (either cast or extruded) a lower forging temperature resulted in superior quasi-static and cyclic properties whereas for a given processing temperature, the extruded starting billet displayed better mechanical properties compared to its cast counterpart post-forging. Extruded AZ31B forged at 250°C was observed to yield the best overall mechanical properties.

Finally, quasi-static tension and shear tests in addition to cyclic axial and cyclic shear tests were also performed to characterize the uniaxial cyclic response of the previously determined optimal forgings. The cyclic axial behavior of the forging was superior to the starting extruded material while the cyclic shear behavior was comparable to low cycle behavior of extruded AZ31B in literature. Multi-axial fatigue tests revealed an increase in cyclic hardening as a result of non-proportionality however, overall fatigue life showed only a weak sensitivity of phase difference. A modified SWT model and Jahed-Varvani (JV) model were developed using the uniaxial cyclic test results. The modified SWT model was found to provide good life prediction for all the tested multi-axial load cases. The multi-axial formulation of the JV model yields good life predictions for in-phase and 45° out-of-phase multi-axial scenarios but slightly over-predicts fatigue life for certain 90° out-of-phase loading cases.

Acknowledgements

I would like to express my sincerest gratitude to my supervisor, Prof. Hamid Jahed for the opportunity to work on this project and for this invaluable support and guidance at every step of my research.

I would also like to thank Dr. Behzad Behravesh and Dr. Sugrib Shaha for sharing their exceptional research experience as well as their technical expertise in terms of performing experimental work and microscopy/fractography sample preparation.

Lastly and most importantly, I express my deepest gratitude to my amazing parents who have instilled in me an incredible sense of curiosity and responsibility. This work would not have been possible without their unfailing support.

Table of Contents

List of Figures

List of Tables

Chapter 1: Introduction

Human assisted climate change has revealed itself to be a global pandemic threatening our way of life. Sixteen of the 17 warmest years on record have occurred within the last 100 years along with arctic summer sea ice being at the lowest recorded levels in history as of 2012 [1]. A major contributor to overall climate change is the emission of greenhouse gases (CO_2, CH_4, N_2O etc.) resulting from human activity (Fig 1).

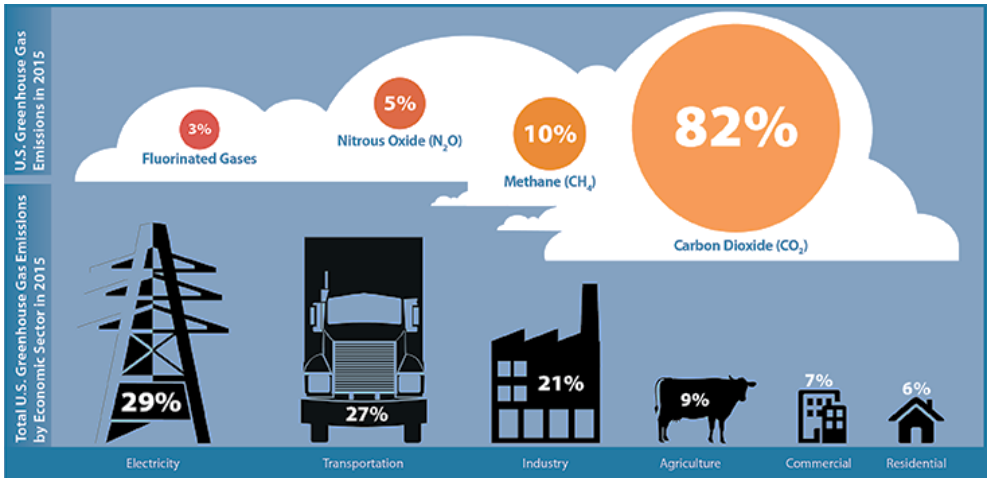

Fig 1: *Break down of greenhouse gas emissions by sector* [2].

With the transportation sector accounting for nearly a third of total greenhouse gas emissions, governments have passed regulation requiring manufacturers to meet fleet-wide CO_2 emission targets. This has led to automotive manufacturers investing heavily in active (e.g. hybridization, electrification etc.) as well as passive (e.g. lightweighting) technologies in order to meet these targets. The concept of lightweighting involves the use of new materials such as composites and alternative metals in place of more traditional steel or aluminum alloys to reduce the curb weight of a vehicle. The benefits of lightweighting can be observed by considering the equation for acceleration:

$$\vec{a} = \frac{P.t}{m.|\vec{d}|}\hat{u} \qquad (1)$$

Where, $\vec{a}$ is vehicle acceleration, $\vec{d}$ is the distance over which the acceleration occurs, and P, t and m represent the power required for the acceleration, the time over which the acceleration occurs and the mass (m) of the vehicle respectively. Note that $\hat{u}$ is a unit vector in the direction of the vehicles displacement. From Eq. 1 it is clear that a lighter vehicle will require less power to achieve

a given acceleration. Considering that engine power is a function of total cylinder displacement (i.e. engine swept volume), Eq. 1 dictates that a lighter vehicle can equipped with a smaller engine thereby reducing overall full consumption and emissions. In fact, at lower driving speeds, vehicle mass is the largest factor affecting fuel consumption [3], [4] with a 5% – 10% decrease in vehicle mass translating to approximately 1.3% – 3.6% reduction in fuel consumption [5]–[7]. To this end, the automotive industry has developed significant interest in the use of lightweight materials for future vehicle construction with one such material being *magnesium* (Mg) alloys. The attractiveness of Mg alloys lies in their low density (approximately two-thirds as dense as aluminum), high specific strength, excellent machinability and good recyclability [8], [9].

Magnesium components have been used in automotive construction since the year 2000 typically in the form of die castings for powertrain and sub-assembly closures. More recently, high-end exotic vehicles such as the Porsche 911 GT2 RS makes use of Mg alloy sheet for roof panels for the purpose of lowering the vehicle's center of mass. However, the current use of Mg alloys has been largely limited to either non-structural components or to components in very low production vehicles. This has been largely due to the challenges related to factors such as their limited formability and poor corrosion resistance.

In order for Mg alloys to be widely adopted by the automotive industry, these challenges need to be overcome. With this is mind, a project was initiated to investigate the potential of using an Mg alloy to replace a current aluminum *Front Lower Control Arm* (FLCA) on a mass market passenger vehicle. This project was conducted by researchers at the University of Waterloo in collaboration with CanmetMATERIALS, and oversight from Multimatic Technical Corporation and Ford Motor Company. Funding for the project was provided by the *Natural Sciences and Engineering Research Council of Canada* (NSERC) and the *Automotive Partnership Canada* (APC). The proposed FLCA would be manufactured using an industrial hot forging process commonly used to manufacture load-bearing vehicle components. For this project three commercial Mg alloys – AZ31B, AZ80 and ZK60 were considered with both cast and extruded pre-form conditions investigated. Due to limited experience pertaining to forming of magnesium alloys and a similar lack of literature regarding the same, this project was initiated through small scale forging tests and subsequently expanded upon up to full-scale component fabrication.

1.1. Objectives

The overall goal of this project is to develop a feasible Mg alloy FLCA for use on a mass market production vehicle. The project is divided into several tasks including forging, design, fatigue, corrosion and residual stress. The goal of this thesis is to characterize the fatigue behavior of one of the selected alloys (AZ31B) post-forging by investigating the underlying mechanisms responsible for any changes observed. A thorough investigation of the fatigue response of the selected AZ31B alloy is required as fatigue is the leading cause of pre-mature failure in engineering applications. The objectives of this thesis are outlined and described below.

- *Quasi-static and cyclic behavior of open-die forged AZ31B*

  Quasi-static tension and compression tests are used to compare the behavior of cast versus forged AZ31B. Microstructure and texture measurements will be made on the pre- and post-forged material. Fatigue behavior will be investigated using fully reversed strain-controlled tests on both the cast and forged material conditions. Differences in behavior will then be linked to any evolution in microstructure and texture that occurs as a result of the forging process.

- *Influence of forging temperature on mechanical properties*

  Closed-die forging of both cast and extruded AZ31B pre-forms are to be performed at several temperatures. At each temperature, the mechanical properties of the forgings will be evaluated. An optimization function based on the intended engineering application is to be developed to objectively evaluate the forgings. An optimal forging temperature will then be selected based on the obtained results.

- *Investigation of axial, torsional and multi-axial fatigue response of optimally forged AZ31B*

  Closed-die forged AZ31B, forged at the optimally selected temperature will be evaluated under fully reversed strain-controlled uniaxial tension-compression and shear. Bi-axial loading cases including in-phase and out-of-phase scenarios will also be considered. The effect of axial/shear strain components and phase angle on cyclic hardening and fatigue life is to be investigated. Fatigue properties will be extracted from the uniaxial tests and incorporated into available fatigue models to evaluate their predictive ability under multi-axial loading scenarios.

1.2. Thesis Overview

This thesis consists of three major parts: literature review, open-die material characterization, and closed-die material characterization.

Chapter 2 contains a literature review including a brief description of the general properties of magnesium and of the selected alloy (AZ31B). The effect of wrought processing on the static and uniaxial cyclic response of Mg alloys as presented in current literature is included. This chapter also introduces the general stages of fatigue failure in metals. Lastly, the results of available multi-axial tests are presented. Note that an introduction of any employed fatigue models and their associated fatigue parameters will be discussed in their respective chapters.

Chapter 3 presents the effect of open-die forging on the quasi-static tension and compression properties of cast AZ31B. Changes in the microstructure and texture of the cast alloy due to forging are presented. The chapter includes a detailed discussion on the underlying mechanisms responsible for the changes observed in the mechanical response.

Chapter 4 discusses the influence of the open-die forging presented in chapter 3 on the *Low Cycle Fatigue* (LCF) properties of the alloy. Fully reversed ($R_\varepsilon = -1$) strain-controlled cyclic tests were conducted on both the cast and forged material conditions. Post-failure metallography and fractography is used to support the changes in fatigue behavior between the two alloy conditions. A strain-based and energy-based fatigue model was employed for both conditions to evaluate the predictive capabilities of these models for the current alloy conditions.

Chapter 5 looks at the effect of forging temperature on the mechanical properties of closed-die forged AZ31B. Two forging temperatures (250°C and 375°C) were used to forge pre-forms of cast as well as extruded material. The evolution of microstructure and texture due to forging is presented for each case. Quasi-static and stress-controlled ($R_\sigma = -1$) cyclic tests at select stress amplitudes (120MPa – 160MPa) are also included. Results from these mechanical tests are combined with an optimization function to determine the optimal pre-form condition (i.e. cast vs extruded) and forging temperature.

Chapter 6 examines a full low cycle fatigue characterization of optimally forged AZ31B. The sample extraction of flat dog-bone and thin-walled tubular specimens is presented. Fully reversed

strain-controlled axial ($R_\varepsilon = -1$) and torsion ($R_\gamma = -1$) fatigue tests are performed. Fatigue parameters introduced in chapter 2 are derived for the optimal forged condition. Fatigue models discussed in chapter 4 are calibrated for the current material condition. Multi-axial (axial & shear) tests are performed with the two waveforms being in-phase, 45° out-of-phase and 90° out-of-phase. The effect of axial and shear strain components and phase angle on the deformation behavior, cyclic hardening and fatigue life is presented. The calibrated model from uniaxial tests is used to predict the multi-axial fatigue response.

Lastly, chapter 7 summarizes the conclusions of the work presented in chapters 3–6. This chapter also goes on to provide recommendations for future work.

Chapter 2: Literature Review

AZ31B is a commercially available magnesium alloy that is commonly available in the form of castings, sheet, and extrusions. The primary alloying elements of the alloy are aluminum (Al), zinc (Zn) and manganese (Mn), with Al and Zn serving to improve room temperature strength while Mn facilitates grain refinement and improves corrosion resistance by sequestering iron [10]. The proportions of these elements are included in Table 1.

Table 1: *Composition of Mg alloy AZ31B.*

Element	Al	Zn	Mn	Mg
Content (%)	2.5-3.5%	0.7-1.3%	0.2-1.0%	Balance

Unlike conventional steel and aluminum alloys, the *hexagonal close-pack* (HCP) crystal structure of Mg and its alloys lack the five independent slip systems required for arbitrary strain accommodations at temperatures below about 200°C [11]–[13]. This makes forming complex Mg components challenging. Specifically, at room temperature basal $\langle a \rangle$ slip is the only available slip mode as the *Critical Resolved Shear Stress* (CRSS) for prismatic $\langle a \rangle$ and pyramidal $\langle a \rangle$ and $\langle c + a \rangle$ slip is generally much higher [14], [15]. However, basal slip alone does not permit extension or contraction along the c-axis of the HCP unit cell and therefore at room temperature, magnesium alloys also demonstrate twinning behaviour primarily though $\{10\bar{1}1\}\langle 10\bar{1}\bar{2}\rangle$ compression twins and $\{10\bar{1}2\}\langle 10\bar{1}1\rangle$ extension twins [16], [17]. A summary of the slip and twin systems recognized for Mg and its alloys is illustrated in Fig 2.

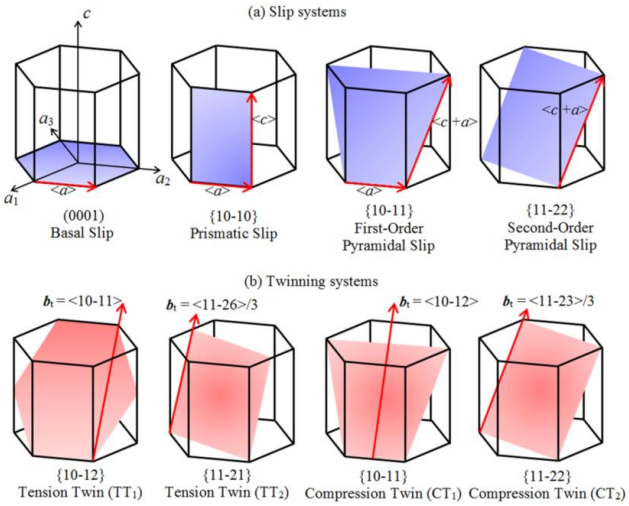

Fig 2: *Schematic illustration of the slip and twinning systems of Magnesium and its alloys* [18].

The poor formability of Mg alloys has limited their use in engineering applications to primarily die-cast applications. It should be noted that the CRSS required for activation of non-basal slip diminishes with temperature and consequently formability of magnesium alloys at elevated temperatures increases (Fig 3) [19]. Such thermo-mechanical (wrought) forming results in material with superior properties to its cast counterpart [20] and opens up the possibility of fabricating load bearing components from Mg alloys.

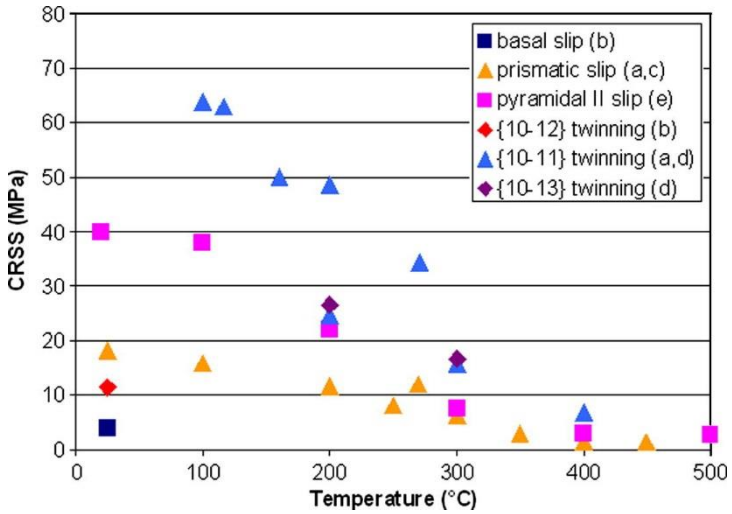

Fig 3: *Temperature dependency of various slip/twin systems in Mg alloys* [15].

Such wrought processes are expected to alter the internal structure of the alloy which in turn would affect the macro-scale properties of the material. One such expectation is the occurrence of grain refinement by *Dynamic Recrystallization* (DRX) occurring due to deformation at elevated temperatures [21]–[23]. DRX is a mechanism by which new grains are nucleated and grow in a material in order to relieve internal stresses during deformation at elevated temperatures (Fig 4).

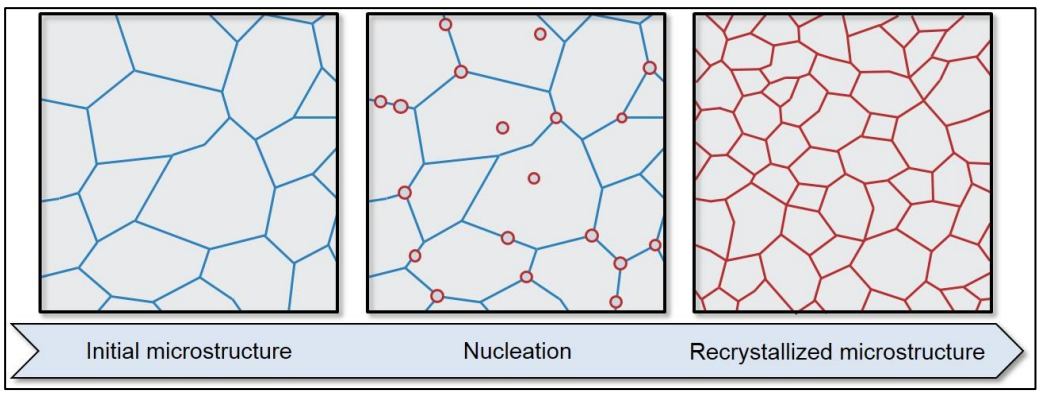

Fig 4: *Schematic illustration of the DRX process* [24].

In addition to the development of a recrystallized grain structure, thermo-mechanical processes result in a preferred HCP unit cell orientation or "*texture*" in the processed alloy, with the c-axis typically aligned with the deformation direction [25]. For example, extruded magnesium alloy displays a wire texture such that the basal planes are aligned parallel to the extrusion direction [9] whereas, rolled magnesium alloy displays a strong basal texture with the basal plane virtually parallel to the rolling direction [26]. Notably, it is such a texture development and corresponding twinning behaviour that is responsible for the well-known tension-compression asymmetry of magnesium alloys [27], [28], which is different from the similar asymmetry due to hydrostatic stresses in high strength steel known as the strength differential effect [29]. To be more specific, $\{10\bar{1}2\}\langle 10\bar{1}1\rangle$ extension twinning (the most common twinning mode) is activated when loading is applied parallel to the c-axis in tension or perpendicular to the loading direction in compression [30]. The occurrence of extension twins result in an 86.3° rotation of the c-axis towards the loading direction and this is the primary mode of texture evolution in magnesium alloys during room temperature to warm deformation [11], [31], [32]. However, at higher temperatures (i.e. hot deformation), twinning is not the primary reorientation mechanism. Instead, at such elevated temperatures non-basal slip (prismatic $\langle a\rangle$, pyramidal $\langle a\rangle$ and pyramidal $\langle c+a\rangle$ slip) becomes active resulting in a change in the unit cell orientation from a hard slip direction to a softer more stable slip direction and it is this slip behaviour that is thought to be responsible for the texture development at these higher temperatures [33], [34]. It should be noted that the intensity of texture developed by non-basal slip tends to be lower than that resulting from twinning [35].

Hot forging is a wrought process that uses severe plastic deformation to fabricate a component. During such a process, a pre-form of the material is placed between dies of a forging press which imparts large-scale plastic deformation into the pre-form until it take the desired shape. The forgability of several AZ-family Mg alloys (including AZ31) was investigated by Graf et al. [36], [37] who deemed Mg alloys as suitable candidates for forging operations. Hot forging as a method to refine cast Mg-Zn-Y alloy was investigated by Garcés et al. [38]. In their study the authors employed cast billets which were forged at 400°C along the billet axis to a height reduction of 92%. Following the forging process, it was reported that the cast microstructure was indeed refined as expected, and a sharp basal texture was developed. The authors also noted an improvement in material strength which they attributed to the texture intensity and the refinement in microstructure. Similar microstructural changes were observed for extruded AZ80 [39] and ZK60 [40] alloys

following semi-closed die forging at 400°C and 450°C respectively. The effect of processing temperature on the anisotropy of rolled AZ31 was examined by Ma et al. [41] through compression of cylindrical specimens at temperatures between 623K to 823K. At all temperatures, DRX grains were observed with a positive correlation between average grain size and processing temperature (Fig 5a); these results were in good agreement with those reported in [36], [37]. The authors also noted a rotation of the as-received texture towards the compression direction with the magnitude of texture modification being more substantial during lower temperature deformation. Ma et al. [41] further performed room temperature tensile tests on the compressed samples and reported a directional and temperature dependency of the yield and tensile strengths as well as the elongation of the alloy (Fig 5 b-c).

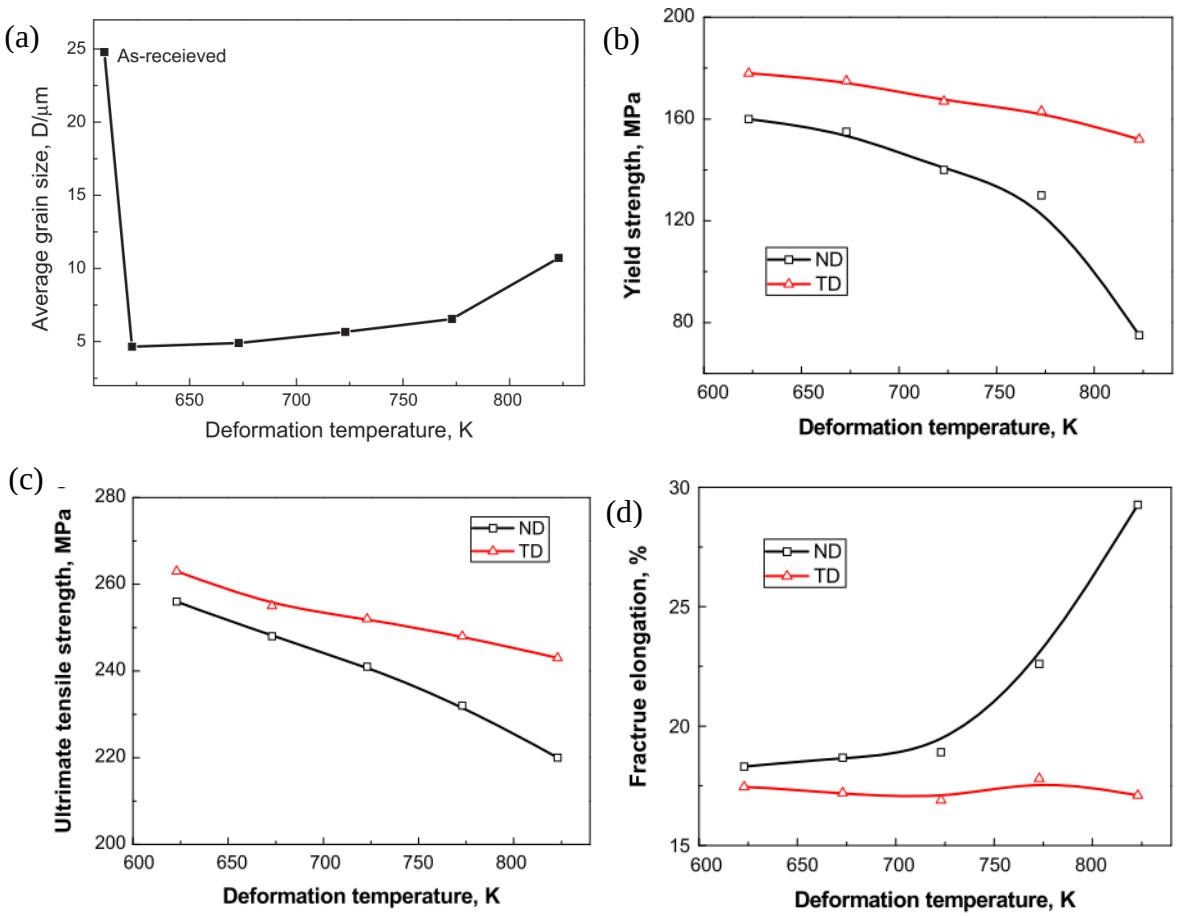

Fig 5: *Effect of compression temperature on (a) average grain size, (b) yield strength, (c) ultimate strength, and (d) fracture elongation of rolled AZ31 as reported in* [41].

The temperature dependency of cast AZ31 during cyclic-die forging was investigated by Guo et al. [42] for temperatures between 350°C and 450°C. The fraction of recrystallized grains was found to increase with increasing number of passes and the average grain size was observed to decrease with temperature, and these modifications were concluded to be responsible for the improved strength and ductility of the alloy (Fig 6).

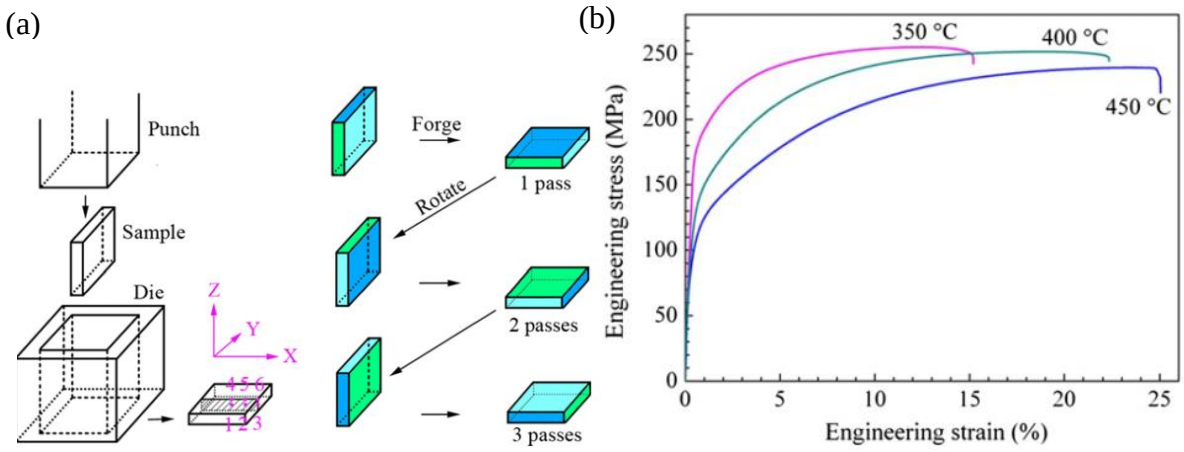

Fig 6: *Figures extracted from* [42] *illustrating (a) the cyclic forging process employed in the study and (b) the room temperature tensile behavior of the AZ31 alloy processed at temperatures ranging from 350-450°C*

Wrought processing is not limited to changes in just quasi-static material behavior but has also been found to alter the cyclic behavior of Mg alloys. Currently, the author is aware of only three studies that investigate the effect of hot forging operations on the fatigue response of Mg alloys with only two cyclic studies related to AZ31B. One of these studies was performed by Kang et al. [43] for cast alloy and the other by Gryguc et al. [44] for extruded AZ31B. Kang et al. [43] did not provide sufficient details about the employed forging process and the study was limited to an evaluation of microstructure and fatigue strength following load-controlled cyclic tests with no comparative study being presented. However, Gryguc et al. [44] did report a 30MPa increase in fatigue strength at 10^7 cycles under load-controlled conditions. Finally, Gryguc et al. [45] also investigated the strain-controlled fatigue behavior of radially upset (i.e. forged) cast AZ80 alloy at 400°C. The authors' noted that the forged condition exhibited asymmetric hysteresis behavior and superior fatigue properties compared to the cast condition over the entire range of tested strain amplitudes (Fig 7). The asymmetry in cyclic behavior of the forged alloy was attributed to the intensification of basal texture compared to the cast condition.

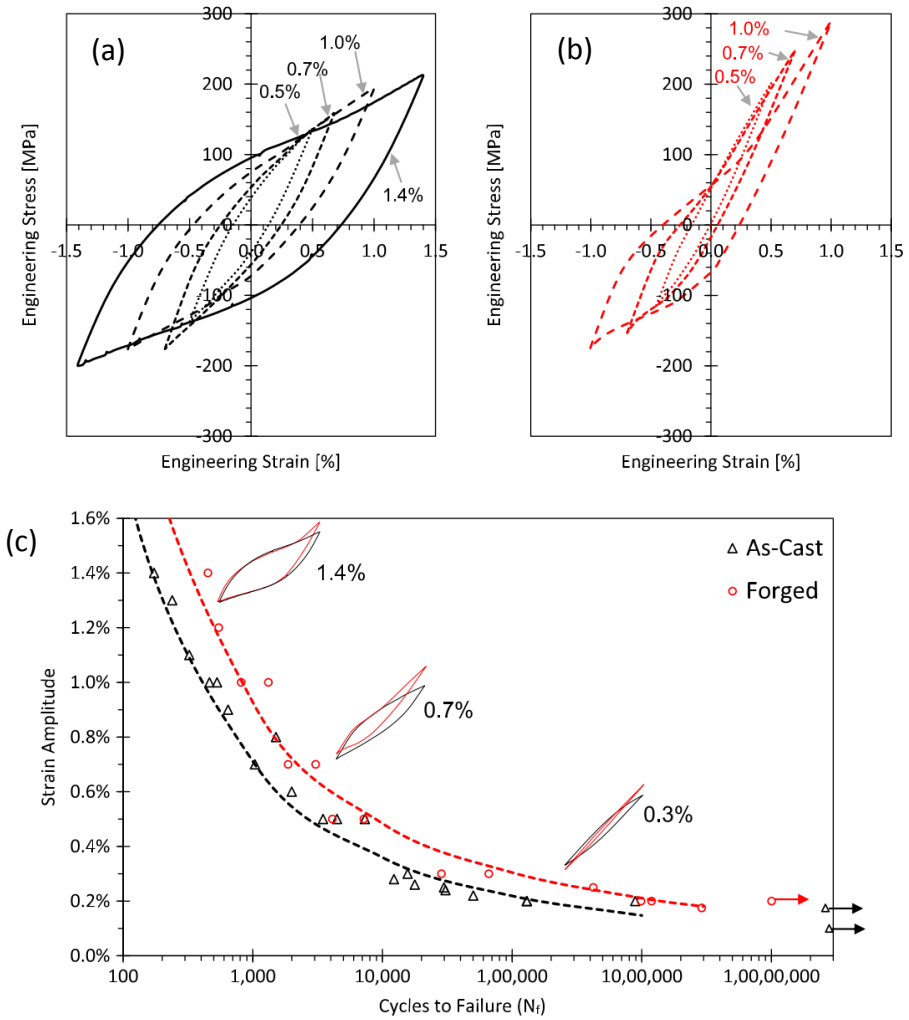

Fig 7: *Figures extracted from* [45] *illustrating the stabilized hysteresis loops for (a) cast and (b) forged AZ80, and (c) strain amplitude vs. cycles to failure for cast and forged AZ80 alloy under fully reversed strain controlled cyclic tests.*

Despite the general lack in forging related fatigue studies, the results of other thermo-mechanical processes such as rolling and/or extrusion should provide some insight on the expected cyclic changes resulting from wrought processing. Huppmann et al. [46] performed stress- and strain-controlled uniaxial cyclic tests on extruded AZ31 with varying final microstructures (obtained by varying the extrusion parameters). They noted a superior fatigue resistance for the finer grained extrusion condition which they attributed to the suppression of twin activation and lower plastic strain during cyclic loading. A similar result was observed by Kamakura et al. [47] who investigated various extrusion temperatures on the stress-controlled fatigue life of AZ31 and AZ61 Mg alloys. An improvement in fatigue life and an increase in fatigue limit (at 10^7 cycles) was reported by both alloys (and particularly for AZ31) for extrusion conditions that resulted in a decreased grain size (Fig 8).

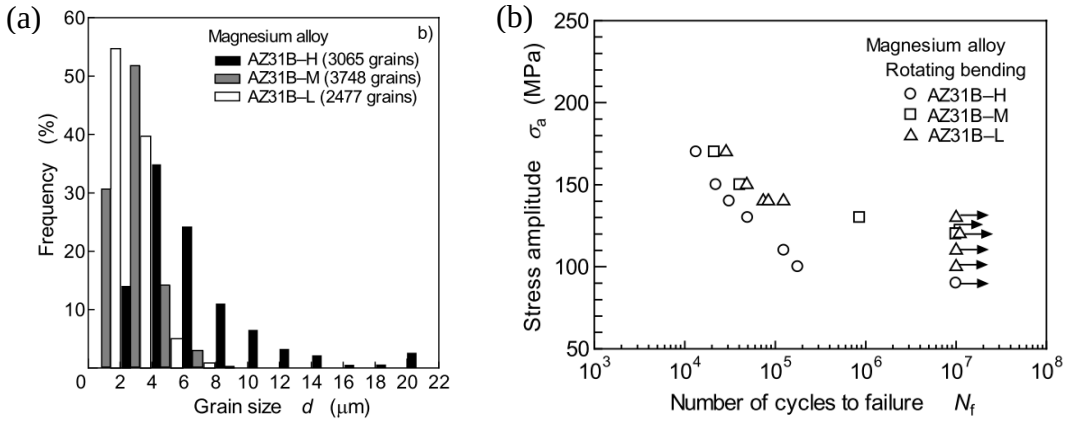

Fig 8: *Results presented by Kamakura et al.* [47] *showing (a) grain size distribution for the studied AZ31B conditions and (b) the associated stress-life plot.*

Low cyclic stress- and strain-controlled tests of rolled AZ31 was investigated by Park et al. [48] who noted that the strong basal texture of the rolled alloy resulted in pronounced asymmetric deformation behavior during cyclic loading (Fig 9a). As a result, a mean tensile stress was developed during strain-controlled tests (Fig 9b). Formation of residual twins with continued cycling was also reported and was found to alter the cyclic hardening behavior of the alloy.

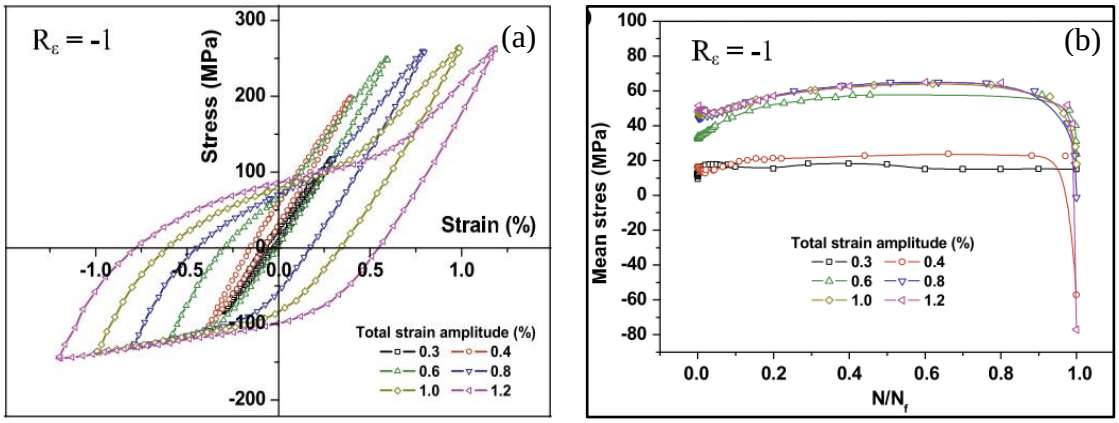

Fig 9: *Figures provided in* [48] *for rolled AZ31 showing (a) stabilized hysteresis loops for fully-reversed strain controlled tests and (b) related mean stress evolution for the tests.*

The results reported by Park et al. were supported by those observed by Wu et al. [49] during LCF testing of rolled AZ31. In their study, it was reported that the rolled AZ31 alloy displayed similar fatigue behavior in the rolling and transverse directions due to in-plane texture symmetry. A significant contribution of twinning/de-twinning behavior on the fatigue life of the alloy was also highlighted in [50], [51] for rolled AZ31B.

However, while the uniaxial behavior of Mg and its alloys have relatively well documented, investigation in to the shear and multi-axial response of Mg alloys is considerably less ample. The scarcity of such data is particularly troubling as engineered components are rarely subject to uniaxial loading conditions. Considering the low volume of work available on the multi-axial behavior of Mg alloys, and given that the majority of component failures in engineering applications result from a fatigue mechanism, it is imperative that the multi-axial fatigue behavior of the current alloy be investigated thoroughly to identify any additional affects that may arise due to multi-axiality or non-proportionality.

Albinmousa et al. [52], [53] investigated the low cycle multi-axial response of an extruded AZ31B alloy. The authors tested thin-walled specimens under several combinations of axial and shear strain amplitudes and for three phase differences between the axial and shear loading (in-phase, 45° out-of-phase and 90° out-of-phase). The pure axial and shear hysteresis loops were also presented (Fig 10) with axial loading showing the well-documented asymmetry whereas the cyclic shear loading displayed symmetric hysteresis loops at all the presented shear strain amplitudes.

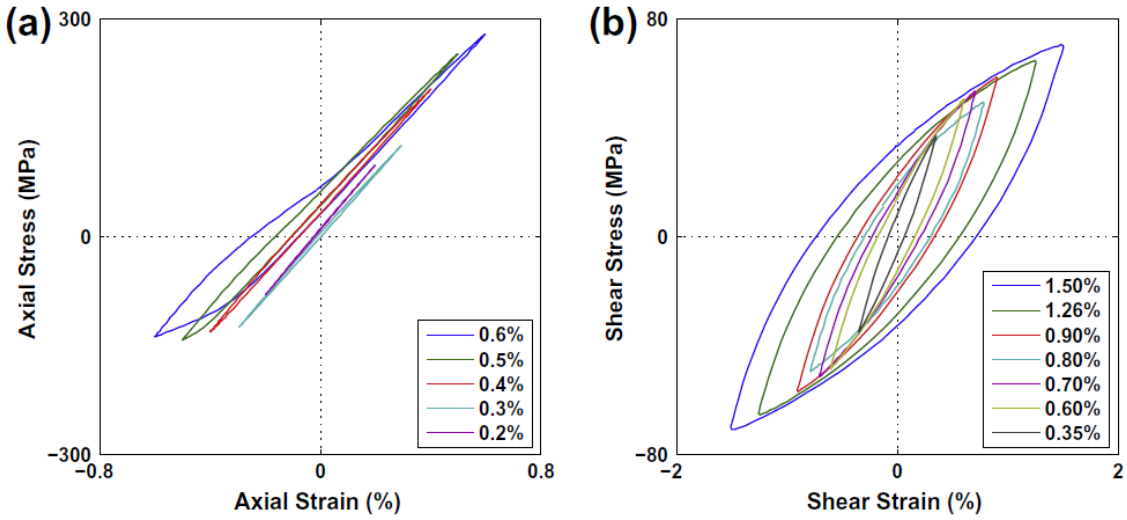

Fig 10: *Stabilized hysteresis loops presented in* [52] *for extruded AZ31B obtained during (a) cyclic axial and (b) cyclic shear.*

Contrary to observations in other materials such as steel which have pronounced additional hardening due to non-proportional loading [54], [55], differences in phase angle was found to have little effect on the fatigue life of the AZ31B alloy (Fig 11). However the extent of cyclic hardening was found to increase with increased phase difference. Finally, the authors employed several models

included the critical plane based Smith-Watson-Topper (SWT) model and energy based Jahed-Varvani (JV) model and found that both models provided satisfactory predictions. The predictive power of these models for bi-axial loading scenarios was also found to be satisfactory for extruded AM30 Mg alloy [56].

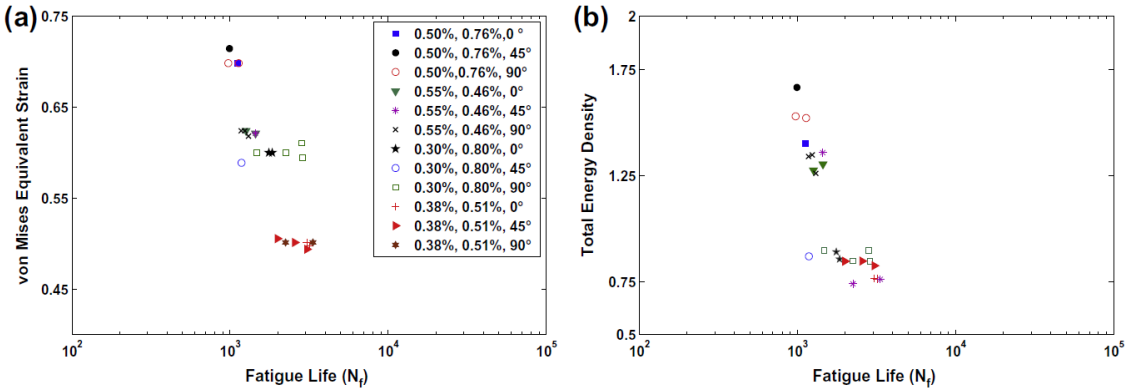

Fig 11: *Plots of (a) Von-Mises equivalent strain vs. cycles to failure and (b) total energy density vs. cycles to failure as presented in* [52] *for extruded AZ31B. Note that the legend is in the format: axial strain amplitude, shear strain amplitude, phase difference.*

A similar study to those by Albinmousa et al. was performed by Xiong et al. [57] for extruded AZ31B. However in this study the authors concluded that phase angle did affect the fatigue life with non-proportional loading conditions resulting in lower lives than proportional loading, for identical equivalent strain amplitudes (Fig 12b).

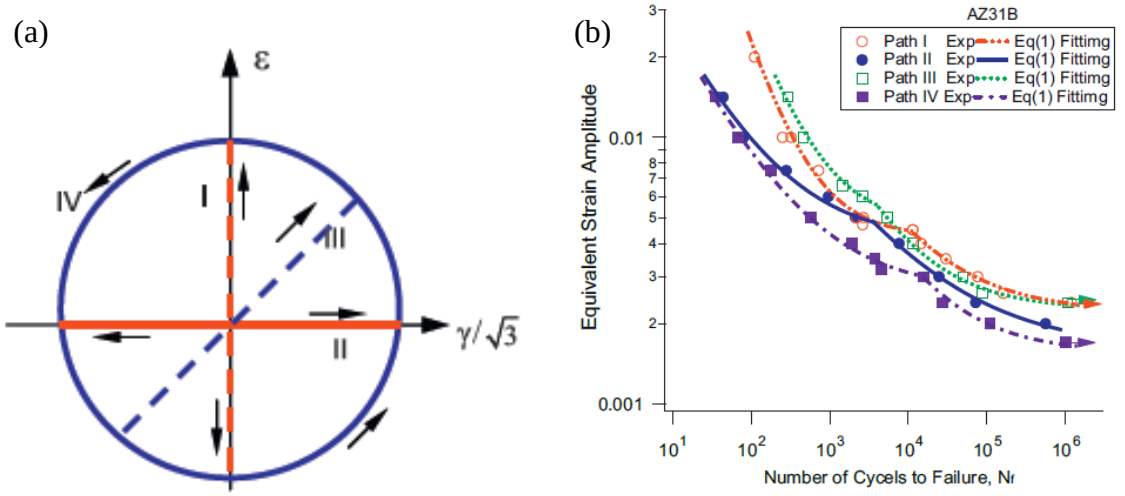

Fig 12: *Images extracted from* [57] *illustrating (a) the various cyclic strain paths employed in testing and (b) plot of equivalent strain amplitude versus cycles to failure for the different strain paths.*

This study also employed a modified SWT model, and the Jiang critical-plane multi-axial fatigue criterion and found that both models yielded satisfactory life estimates for the extruded alloy under multi-axial loading.

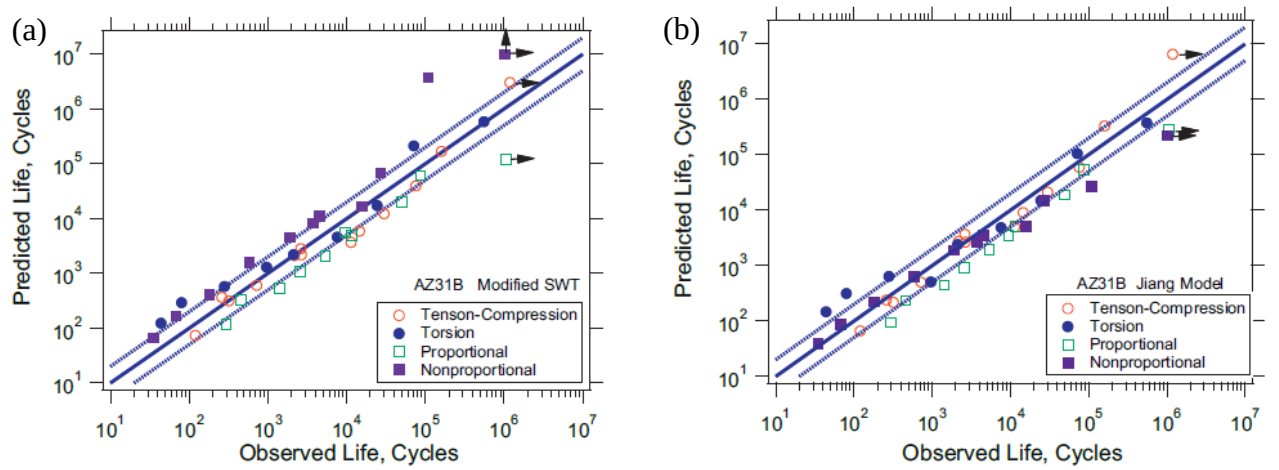

Fig 13: *Images extracted from* [57] *illustrating the predictive power of (a) the modified SWT model and (b) the Jiang critical-plane fatigue criterion for extruded AZ31B under several cyclic strain paths.*

Yu et al. [58] reported a similar effect of phase angle on fatigue life for extruded AZ61A alloy. In their paper the authors also noted the significant effect of axial mean stress on the fatigue life of fully reversed strain-controlled torsion with a static tensile load reducing fatigue life and a static compressive load significantly enhancing the number of cycles to failure. Finally, Zhang et al. [59] also investigated the multi-axial deformation behavior of extruded AZ61A and reported results similar to those by Yu et al., with the cyclic deformation behavior of the alloy being heavily dependent on the strain path.

Chapter 3: Influence of open-die forging on the microstructure, texture and uniaxial properties of cast AZ31B Alloy

The effect of open die forging on cast AZ31B alloy was investigated in terms of the evolution of microstructure, texture, and quasi-static mechanical properties. A partially refined microstructure with strong basal texture was developed in forged material. Tensile yield and ultimate strengths increased by a remarkable 143 percent and 23 percent respectively. During room temperature compression the forged alloy displayed significant in-plane asymmetry and unchanged yield strength compared to the cast alloy owing to the activation of $\{10\bar{1}2\}\langle 10\bar{1}1\rangle$ extension twins in both the cast and forged conditions. Nevertheless, the ultimate compressive strength for the forged material increased by 22 percent compared to the as-cast material. Microstructure and texture analysis of the post-fracture samples confirmed that the deformation in the forged samples was dominated by slip during tension and twinning during compression. In comparison, both slip and twins were observed in the cast samples for similar testing conditions. The increased strength of the forged material was attributed to the refinement of grains and the formation of a strong basal texture which activated slip on the prismatic and pyramidal slip systems instead of extension twins.

3.1. Experimental Details

3.1.1. Forging process

The material investigated in this study is AZ31B in as-cast condition. The cast AZ31B material used in the study was procured from Magnesium-Elektron in the form of cylindrical billets with 300 mm diameter and a height of 100 mm (as seen in Fig 14a). Smaller cylindrical billets, 65 mm in length and with a diameter of 63.5 mm were extracted from the original billet (Fig 14a). The extracted billets were heated for 3 hours in a furnace to a temperature of 450°C prior to being placed in a hydraulic press. The flat dies on the forging press were heated to match the billet temperature. A 450°C forging temperature was selected due to the availability of flow curve and material property data in literature that could be used for verification of forging simulations (not in the scope of this thesis). The heated billet was forged in a single step such that the forging direction was parallel to the radial direction of the billet, and graphite was used to lubricate the dies. The iso-thermal forging was conducted at a constant rate of 39 mm/min until the billet experienced a ~80% reduction in diameter.

The forging operation resulted in flattened coupons with approximate dimensions of 135 mm × 130 mm × 13 mm (Fig 14b). The finished forgings were air-cooled back down to room temperature.

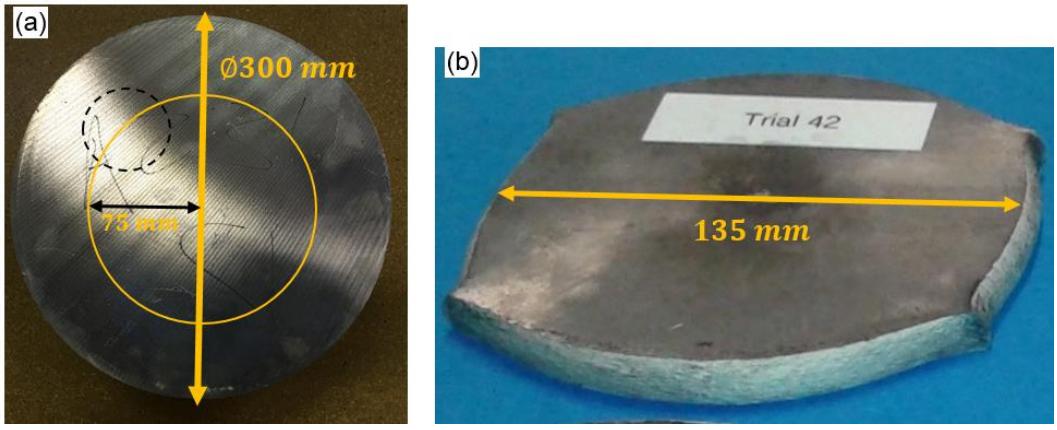

Fig 14: *Photographs of (a) as- cast AZ31B billet and (b) the AZ31B coupon forged at a temperature of 450 °C and ram speed of 39 mm/min. Note the dashed black circle in Fig. 14a illustrating the extraction location of the forging billet.*

3.1.2. Microstructure and texture analysis

Microstructure and texture analysis was performed for both as-cast and forged conditions. For the cast alloy (Fig 15a), a cubic sample of 10 mm edge length was extracted from a radial distance of 75 mm from the center of the original billet. Due to the non-uniform strain distribution expected during the above discussed forging process, three microstructure/texture samples were extracted from different locations of the final forging to investigate spatial variations: the edge, one-quarter and one-half of the width of the forging (Fig 15b).

All microstructure specimens were prepared by first grinding with 600, 800 and 1200 grit silicon carbide paper followed by polishing with 6, 3, 1 and 0.1-µ diamond paste with an oil based lubricant on imperial cloth. A final polishing step with 0.05 µ colloidal silica on a black CHEM pad was performed followed by etching with acetic-picral as mentioned in [60]. Microstructure was analyzed using an Olympus metallurgical microscope and grain size was calculated using the line-intercept method. A Scanning Electron Microscope (SEM) equipped with Quanta Field Emission Gun (FEG)-and an Energy Dispersive X-Ray Spectrometer (EDS) was used to analyze microstructure and intermetallics.

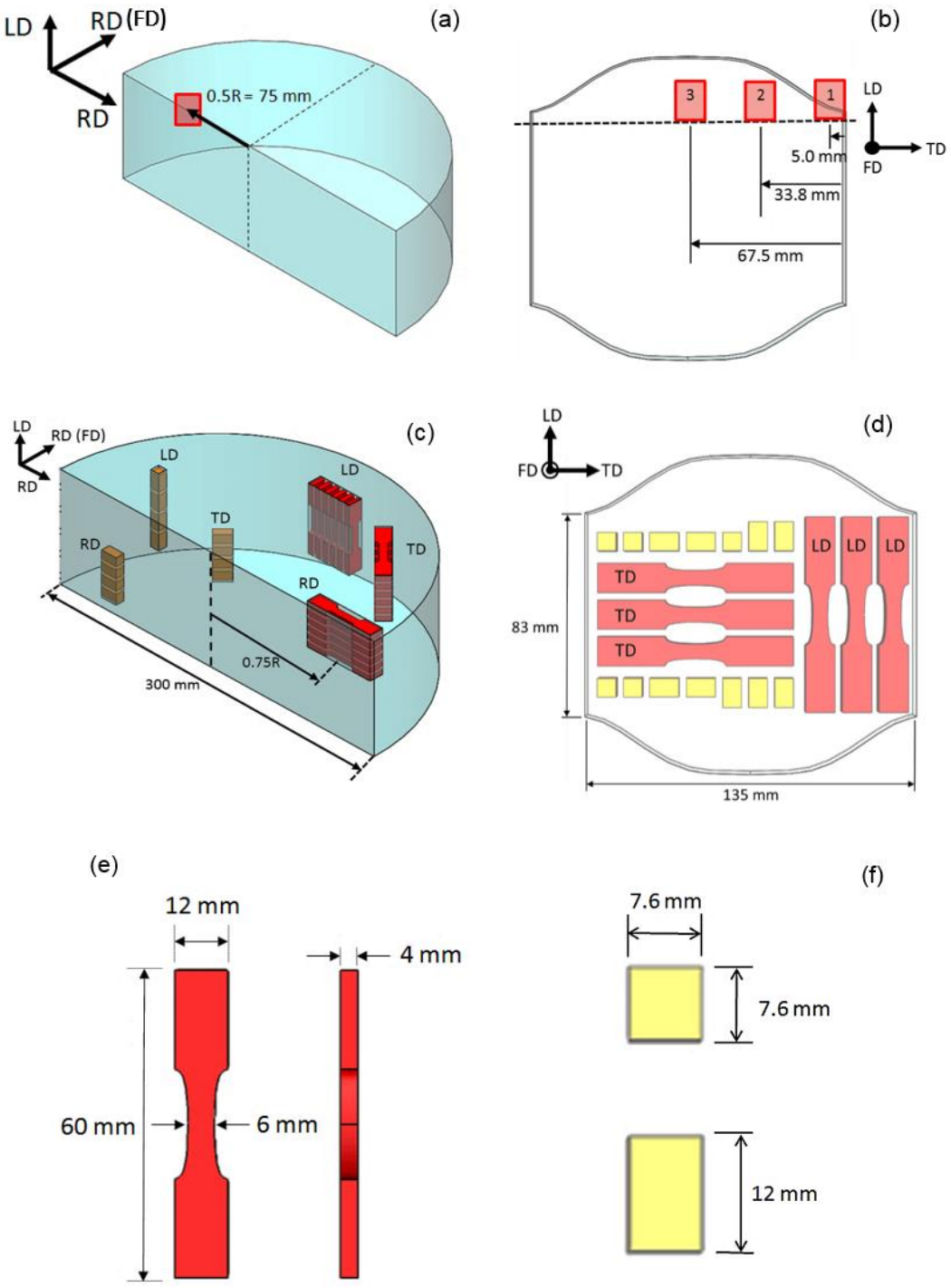

Fig 15: *Illustration of the sample extraction locations for (a, b) microstructure and texture and, (c, d) quasi-static tension and compression testing of (a, c) as cast and (b, d) forged AZ31B. The figure also shows the (e) tensile specimen geometry and (f) compression specimen geometry. Note: LD – Longitudinal Direction, TD – Transverse Direction, RD – Radial Direction and FD – Forging Direction.*

Texture analysis was performed on the polished and etched samples using a Bruker D8-Discover equipped with a VÅNTEC-500 area detector and using Cu-Kα radiation at 40kV and 40 mA. The incident x-ray beam and the detector were placed at a fixed 2θ angle of 40° for texture measurement. The samples were tilted between 0° and 75° with a step of 15°, considered as the Ψ-scan while the sample rotation known as Φ-scan was between 0° and 360° with a step size of 5°. The sample was scanned for 20s at each orientation. The Debye–Scherrer diffraction rings were collected using the area detector in a two-dimensional diffraction image. Then, the incomplete pole figures for the $\{0001\}$, $\{10\bar{1}0\}$, $\{10\bar{1}1\}$ and $\{1\bar{1}02\}$ planes were extracted from the diffraction rings. The complete pole figures were then calculated using the DIFFRAC.Suite:Texture software.

3.1.3. Quasi-static testing

Tension dog-bone and cuboid compression samples were extracted from the as-cast billet using a Computer Numerically Controlled (CNC) mill according to the illustration in Fig 15c. To avoid the effects of non-homogenous microstructure distribution across the billet, samples were extracted such that the gauge section of all samples lay on a radius equivalent to 75 percent of the billet radius (Fig 15c). Samples were extracted from the radial, transverse, and longitudinal directions (RD, TD, and LD, respectively) to investigate anisotropy (or lack thereof) in material properties. Tension samples were extracted along the LD and TD of the forged material as depicted in Fig 15d while compression samples were extracted along the LD, TD and forging direction (FD). Monotonic tension and compression testing were performed on an MTS 810 uniaxial load frame with a capacity of 50kN and strain was measured using an ARAMIS 3D Digital Image Correlation (DIC) system. All monotonic tests were performed in accordance with ASTM E8 and E9 standards at a constant displacement rate of 1 mm/min. A minimum of 2 samples and up to 6 samples were tested for each direction. The details about the sample geometry are illustrated in Fig 15 e/f, and the test procedure has also been described in [60].

3.2. Results

3.2.1. Microstructure and texture post-forging

Optical micrographs of AZ31B Mg-alloy in the as-cast and forged conditions are shown in Fig 16. The as-cast alloy exhibits equiaxed grains with an average grain size of ~278 μm ±30 and a dendritic microstructure consisting of α–Mg and a network-like eutectic phase containing β-$Mg_{17}Al_{12}$ particles (Fig 16a-d). These intermetallics were formed in the inter-dendritic region during

solidification of the alloy and similar intermetallics were reported in literature for other AZ type Mg-alloys [44], [61]. The microstructure of the forged AZ31B modified by the forging process is shown in Fig 16e/f. No significant differences were observed between the microstructure at the three examination locations in the forging. It is clear that the forged material displays a strong bimodal grain morphology with large deformed grains surrounded by a fine DRX grain structure; the average size of these DRX grains is ~14 μm ±5. The dendritic structure observed in the cast material disappeared and the concentration of intermetallics decreased significantly following the forging process. This can be attributed to homogenization of the forging billet by pre-heating to 450 °C for three hours prior to forging and also to partial/incomplete DRX occurring during forging.

Fig 17a shows the (0002) and $(10\bar{1}0)$ pole figures for as-cast AZ31B alloy with a maximum intensity of 4.57 and 4.62 MRD (*multiples of random distribution*), respectively. The cast material showed no preferred crystallographic orientation suggesting a fairly random unit cell orientation as schematically illustrated in Fig 17a. In comparison to the as-cast sample, the forged condition showed a sharp texture with a high intensity value of 11.82 and 3.14 MRD for the same poles as the cast condition. According to Fig 17b and the schematic diagram, the c-axis of the magnesium unit cells in the forged material are largely parallel with the FD. In other words, the basal (0002) planes are perpendicular to the FD. As a result, a set of basal textures, i.e., $\{0001\}\langle 2\bar{1}\bar{1}0\rangle$ are identified for the current forged AZ31B Mg-alloy. The change from random texture in the cast material to a sharp texture in the forged material is related to Rotational Dynamic Recrystallization (RDRX) as discussed in [62].

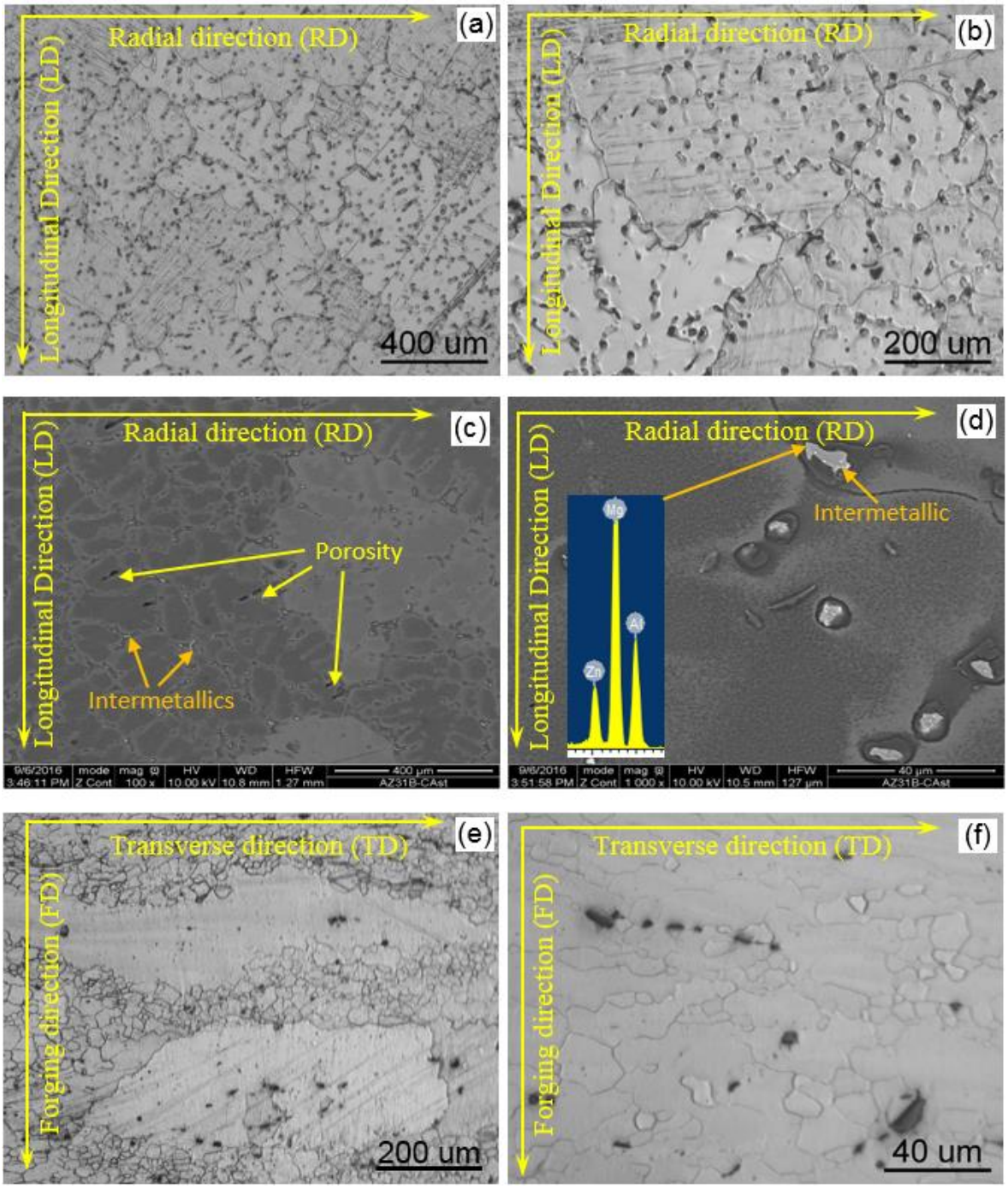

Fig 16: *Optical and SEM micrographs of the AZ31B alloy considered in this study: (a, b) optical micrographs of the cast material, (c) backscatter electron image of the as-cast material, (d) EDX analysis of intermetallics observed in the cast material and (e, f) optical micrographs of the forged alloy.*

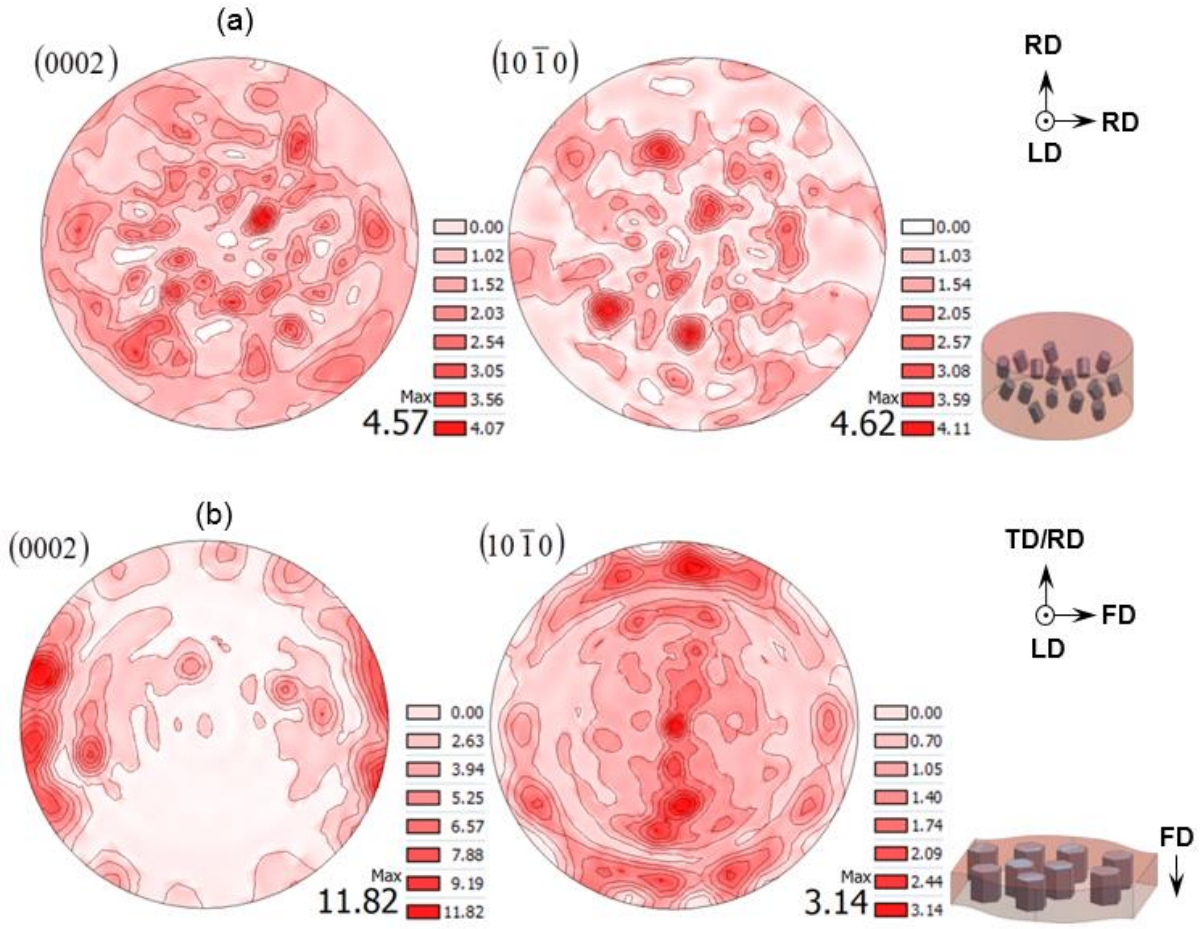

Fig 17: (0002) *and* (10$\bar{1}$0) *pole figures for the AZ31B alloy samples in (a) as-received cast and (b) forged conditions.*

3.2.2. Quasi-static tension properties

The true tension stress-strain curves for the as-cast and forged material conditions are shown in Fig 18. No material anisotropy was observed between LD and RD/TD direction of the as-cast or forged samples. The as-cast material displayed a slight sigmoidal behavior between true strains of 2 to 8 percent indicative of the occurrence of extension twins under loading. In contrast, the forged specimens did not exhibit a sigmoidal shape indicating slip dominated deformation. Fig 19 summarizes the *tensile yield strength* (TYS), *ultimate tensile strength* (UTS), and *tensile failure strain* (TFS) of the as-cast and forged AZ31B tested under tension. The TYS and UTS of the tested AZ31B increased by ~143% and 23% respectively compared to the as-cast condition as a result of the employed forging process. A similar improvement in strength was observed by Gryguc et al. [44] following uniaxial upsetting of extruded AZ31B. Surprisingly, failure elongation decreased by 21% as a result of forging and a possible explanation for this decrease is discussed later.

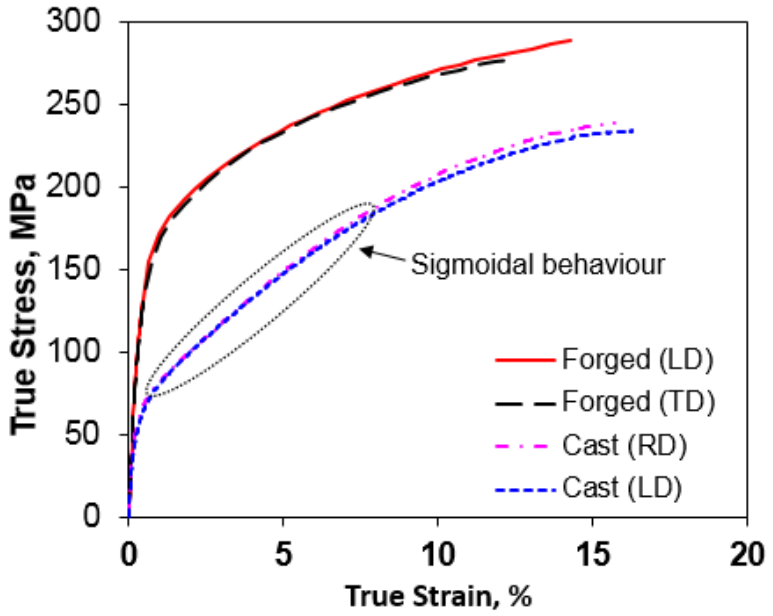

Fig 18: *True stress vs true strain tension curves for cast and forged AZ31B considered in this study.*

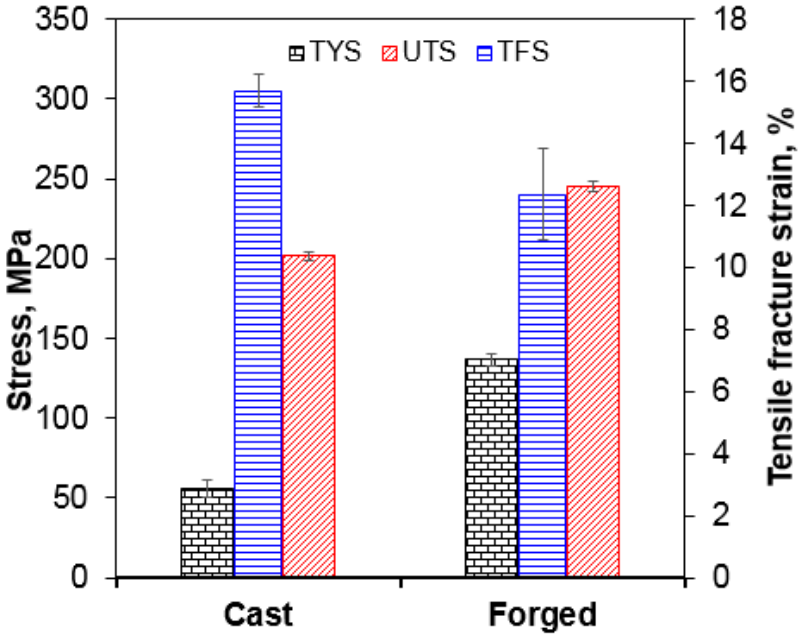

Fig 19: *Summary of tension properties for the cast and forged AZ31B considered in this study.*

The *hardening capacity* (*HC*) of a material may be defined as the ratio of *ultimate strength* (*US*) to *yield strength* (*YS*) [63]:

$$\boldsymbol{HC_{\frac{T}{C}} = \frac{US\ [MPa]}{YS\ [MPa]}} \qquad (2)$$

The *HC* was evaluated for the current AZ31B alloy in both as-cast and forged conditions and is summarized in Table 2. Note that the *HC* under tension decreased from 3.58 to 1.80 as a result of forging.

The plastic deformation of a material can also be characterized by the strain hardening exponent, n, and strength coefficient, K, determined from the true stress-strain curves illustrated in Fig 18. The values of *n* and *K* were calculated by plotting Ludwik's equation,

$$\sigma = \sigma_y + K\varepsilon_p^n \qquad (3)$$

where σ is the true stress and ε_p is the corresponding true plastic strain beyond the yield point (σ_y). The calculated values of n and K are summarized in Table 2 and it was observed that the as-cast condition demonstrated a higher tensile strain hardening exponent and strength coefficient compared to the forged condition. This might be a result of the nucleation and growth of twin boundaries in the as-cast material (suggested by the slight sigmoidal behavior in Fig 18) which serve to further hinder dislocation movement resulting in higher overall strain hardening compared to the forged material [64], [65].

Table 2: *Hardening capacity and Ludwik hardening parameters for the as-cast and forged AZ31B obtained for the current study.*

		Tension			Compression		
		HC_T	n	K, MPa	HC_C	n	K, MPa
Cast	LD	3.58	0.69	711	3.64	0.76	700
	RD	3.58	0.71	765	3.64	0.73	659
Forged	LD	1.80	0.48	402	4.01	-	-
	TD	1.80	0.48	423	4.06	-	-
	FD	-	-	-	2.40	0.58	702

3.2.3. Quasi-static compression properties

The true stress–strain curves for the as-cast and forged AZ31B under uniaxial compression are shown in Fig 20 with the compressive properties summarized in Fig 21. The *compressive yield strength* (*CYS)*, *ultimate compression strength* (*UCS*) and *compression failure strain* (*CFS*) in addition to the strain hardening exponent, *n*, and strength coefficient, *K* for the appropriate compression tests are summarized in Table 2. For the as-cast condition, the shape of the compressive curves are very similar to those of the as-cast tensile curves (Fig 18). The forged samples compressed along the LD and TD showed strong sigmoidal hardening behavior, indicative of the activation of

extension twinning, whereas the sample compressed along the FD displayed monotonic hardening behavior. The as-cast AZ31B exhibited very similar behavior in different material directions (isotropic), however a mild tension-compression asymmetry was observed for the as-cast material.

In comparison, the forged condition displayed significant asymmetry and anisotropy during compression as is evident from Fig 20. The presence of a strong basal texture in the forged material with the c-axes of most grains aligned with the FD direction (Fig 17b), suggests that the specimens compressed along the LD and TD were subjected to compressive loading perpendicular to the c-axes resulting in the activation of $\{10\bar{1}2\}\langle 10\bar{1}1\rangle$ extension twinning. Thus, the room temperature flow curves for LD and TD exhibited a low CYS and a similar sigmoidal nature (Fig 20), characteristic of twinning-dominated deformation.

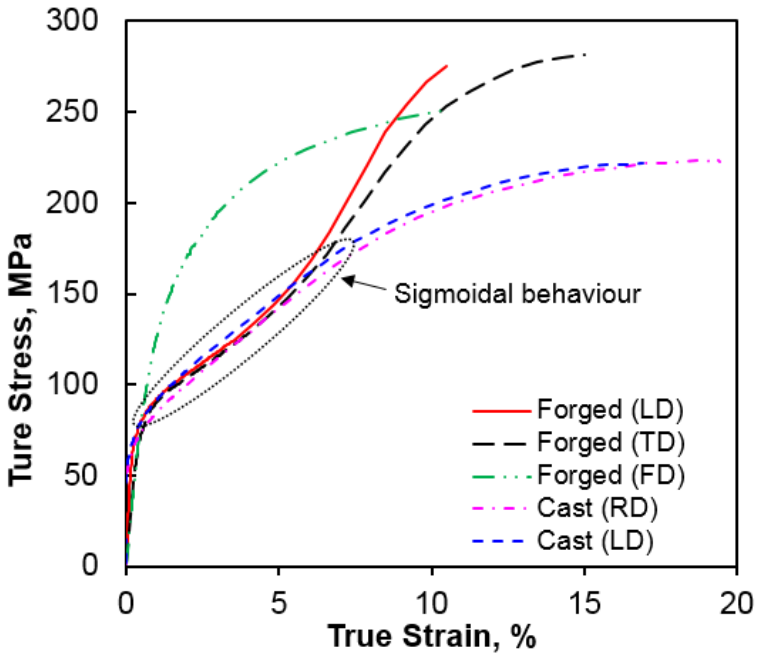

Fig 20: *True stress versus true strain compression curves for the cast and forged AZ31B.*

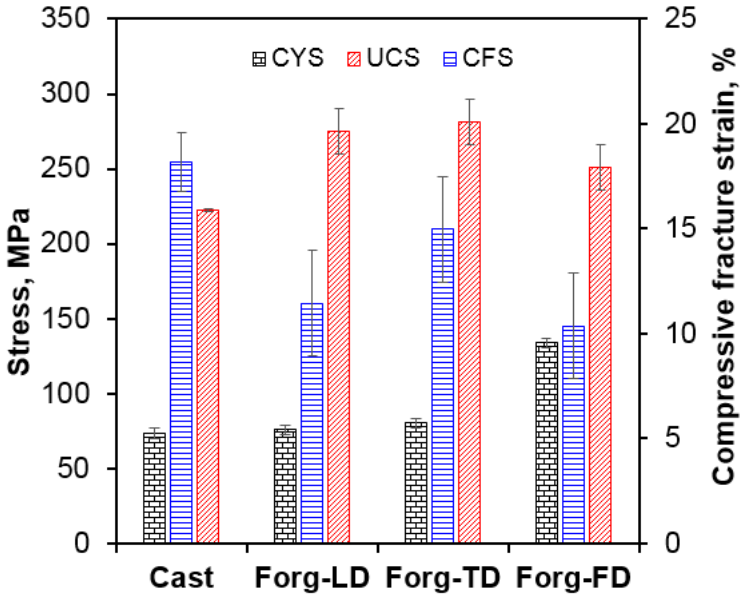

Fig 21: *Summary of the compressive properties for the cast and forged AZ31B.*
Note: LD – loading direction, TD – transverse direction and FD – forging direction.

3.2.4. Fracture analysis

Fracture surfaces of the cast and forged samples obtained post-tension testing along LD is shown in Fig 22. It is observed that the facture surface of as-cast samples (Fig 22a-d) exhibits ductile features such as dimples, as well as brittle fracture features such as cleavage (Fig 22c) and secondary cracks (Fig 22d). The as-cast fracture surface (Fig 22b) also displays numerous voids, dimples and microscopic secondary cracks (indicated by orange arrow). The forged surface (Fig 22e-g) displays a shear fracture surface indicative of ductile fracture. However, several instances of voids are observed on the fracture surfaces of the forged sample which is unexpected and might explain the lower failure elongation for forged material observed in Fig 18. The lower failure elongation of forged compared to as-cast AZ31B will addressed in the discussion section.

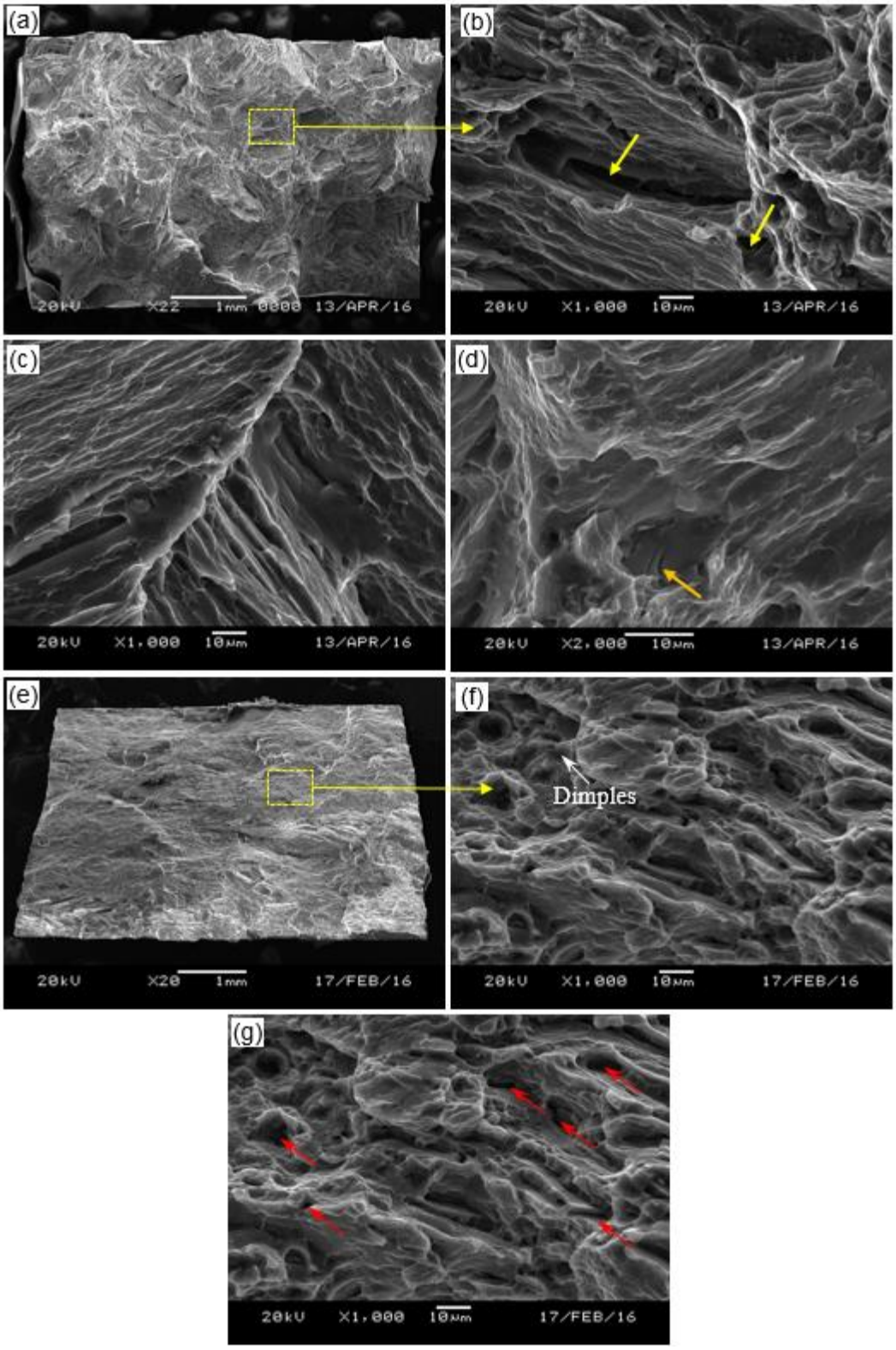

Fig 22: *SEM images showing an overall and magnified view of the tensile fracture surface of AZ31B in (a-d) cast and (e-g) forged conditions. The yellow arrows indicate voids observed in the cast material while the red arrow indicate voids in the forged material. The orange arrow points to secondary cracks in the cast material.*

3.2.5. Microstructure and texture after deformation

Samples obtained adjacent to the tension fracture surface of as-cast and forged AZ31B specimens were prepared for microstructural and texture analysis and the results are presented in Fig 23 and Fig 24, respectively. The as-cast sample suggested that deformation occurred through a combination of slip and twinning (Fig 23a). However, in some cases the growth of twins was inhibited by the presence of intermetallics (Fig 23b) as was also reported by Gharghouri et al. [66]. In comparison, there was virtually no extension twinning observed in the post-failure specimen of the forged AZ31B (Fig 23c, d). Texture results on the post-tension fracture samples also support the above microstructural results. As indicated by Fig 24a, the basal (0002) poles of the as-cast sample displayed some reorientation along the loading direction due to extension twins which decreased the maximum intensity to 4.31 MRD compared to the random texture in the as-received material (Fig 17a). In contrast, the forged sample did not show any significant change in texture as the tensile deformation was dominated by slip (Fig 24b). The observed post-tension microstructure corresponds well with slightly sigmoidal shape exhibited by the as-cast material while the forged sample showed typical monotonic tensile stress-strain behavior (Fig 18).

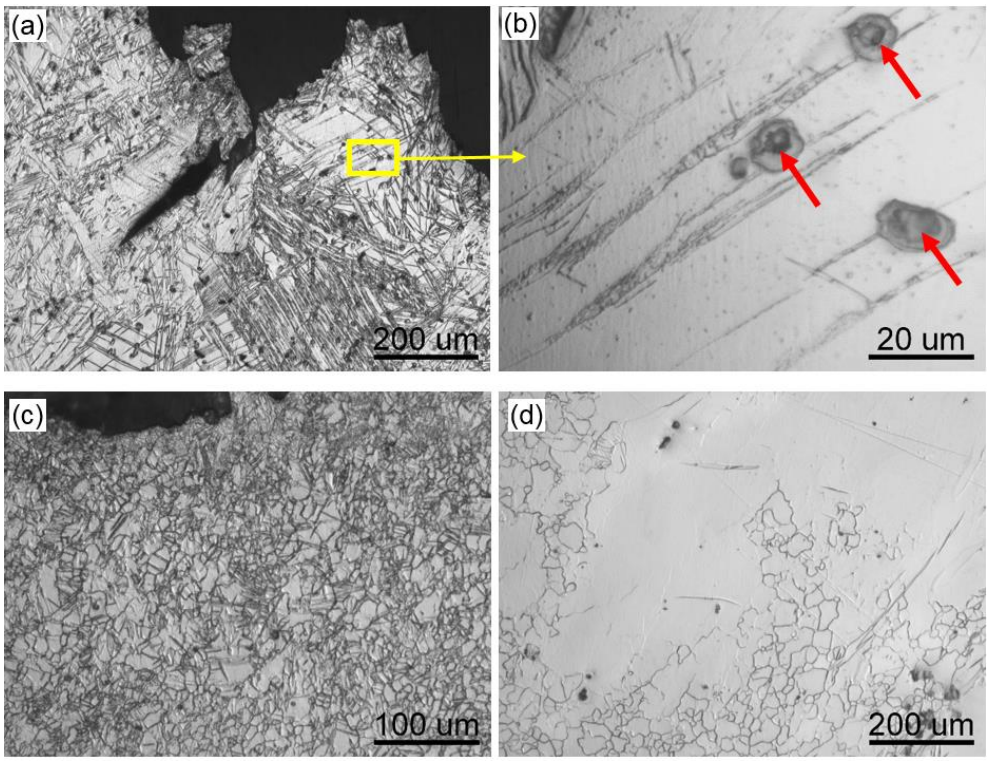

Fig 23: *Optical micrographs of tension specimens post-fracture for (a, b) cast AZ31B and (c, d) forged AZ31B. Note the micrograph in Fig 23d is taken just below the micrograph in Fig 23c to indicate the lack of twins in large grains. Extension twins being intersected by intermetallic particles are indicated by red arrows.*

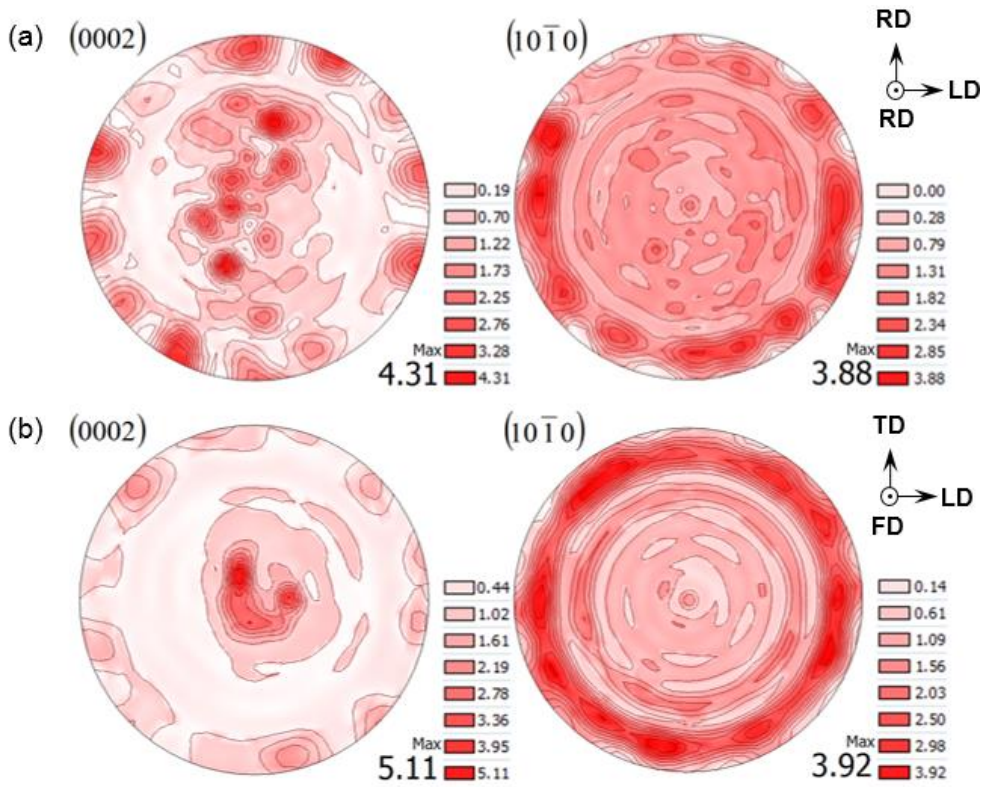

Fig 24: (0002) *and* (10$\bar{1}$0) *pole figures for the current AZ31B alloy post-tension testing for the (a) cast condition tested along the RD and (b) forged condition tested along LD.*

In a similar manner to the tension specimens, the change of texture during compression for the as-cast and forged samples is shown in Fig 25. As seen in Fig 25a, the (0002) pole of cast alloy presented an intensity of 12.32 MRD toward the compression direction which indicates a c-axes rotation towards the compression direction. In the forged sample compressed along the FD direction (Fig 25b), the basal pole position remains unchanged indicating no texture change due to the compressive loading. However, the intensity increased to 14.45 MRD compared to the starting forged alloy (Fig 17b). For the forged sample compressed along the LD, the c-axes were rotated towards the LD with an intensity of 10.68 MRD. The microstructure near the fracture surface (Fig 26a), of the as-cast material tested in compression was different from the initial microstructure displayed in Fig 16a; extensive $\{10\bar{1}2\}\langle10\bar{1}1\rangle$ twins with a lenticular shape were observed in several grains. The same type of twins were also reported in other studies [67], [68]. As a lower CRSS is required for the formation of $\{10\bar{1}2\}\langle10\bar{1}1\rangle$ extension twins compared to other twinning modes, the microstructure exhibits extension twins compared to $\{10\bar{1}1\}\langle10\bar{1}\bar{2}\rangle$ contraction twins. It is also observed that forged AZ31B compressed along LD (Fig 26c, d) exhibits twinning in all grains while

the sample tested in the FD direction (Fig 26e, f) was twin free. This is due to the fact that the random texture of the as-cast alloy results in twins only in certain favorably oriented grains whereas twinning is far more extensive in the strongly textured forged alloy. It was reported that, in compression, $\{10\bar{1}2\}\langle 10\bar{1}1\rangle$ extension twins starts to nucleate at strain values as low as ~2%. As the compression strain increases the twins grows and coalesce, causing a progressive decrease in twin boundaries [67], [68]. Since the microstructure of the samples were obtained after fracture, twin saturation occurred which can consume whole grains resulting in a disappearance of twin boundaries. Sarker et al. [68] studied the twin growth of extruded AM30 Mg alloy during compression at room temperatures. They reported that after a certain amount of strain (~8%), severe twin growth occurred which fully consumed grains. Gharghouri et al. [66] reported that the deformation twins interact with secondary phases and (i) the twin consumes the precipitates, (ii) the precipitate hinders the movement of twin boundary and (iii) the twinning dislocations tends to bypass the precipitate by bowing around. Consequently, the existence of precipitates in the as-cast alloy act as a barrier for the migration of twin boundaries and hindered the rate of twin propagation; such behaviour was observed in Fig 23b. When the forged alloy was compressed along the FD direction, the c-axis is parallel to the loading direction resulting a slip dominated deformation. In contrast, when the sample is compressed along the TD/LD, the c-axis is perpendicular to the loading axis, and the c-axis of the unit cell rotates about 86.3° towards the LD/TD by forming $\{10\bar{1}2\}\langle 10\bar{1}1\rangle$ extension twins as seen in Fig 25c. Similar types of extension twinning were also reported for room temperature deformation of AM30 Mg-alloy [67].

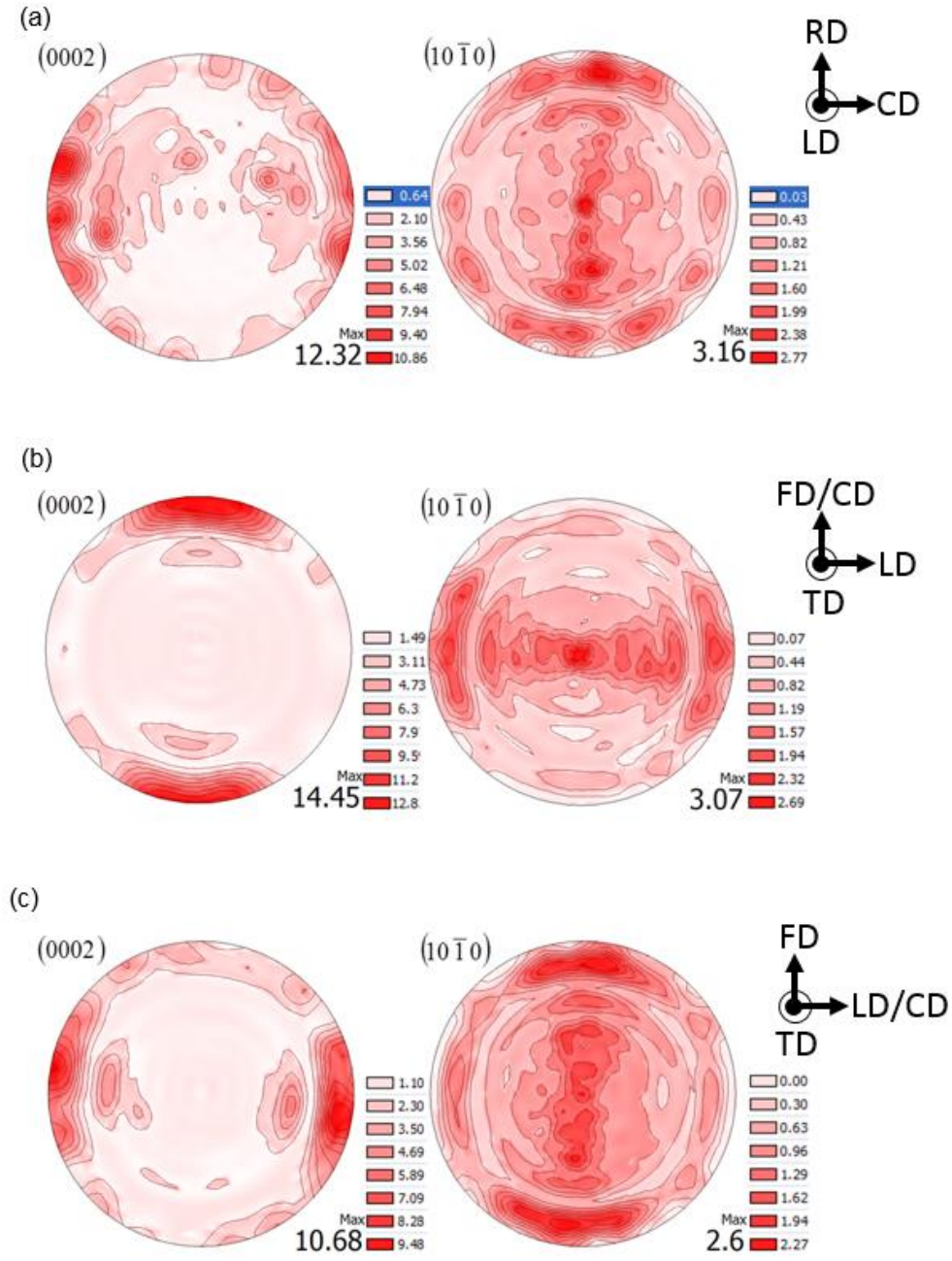

Fig 25: (0002) *and* (10$\bar{1}$0) *pole figures for the current AZ31B alloy post-compression testing for (a) cast condition compressed along the RD and (b) forged condition compressed along FD and (c) forged condition compressed along LD. Note: RD – radial direction, LD – longitudinal direction, FD – forging direction, TD – transverse direction and CD – compression direction.*

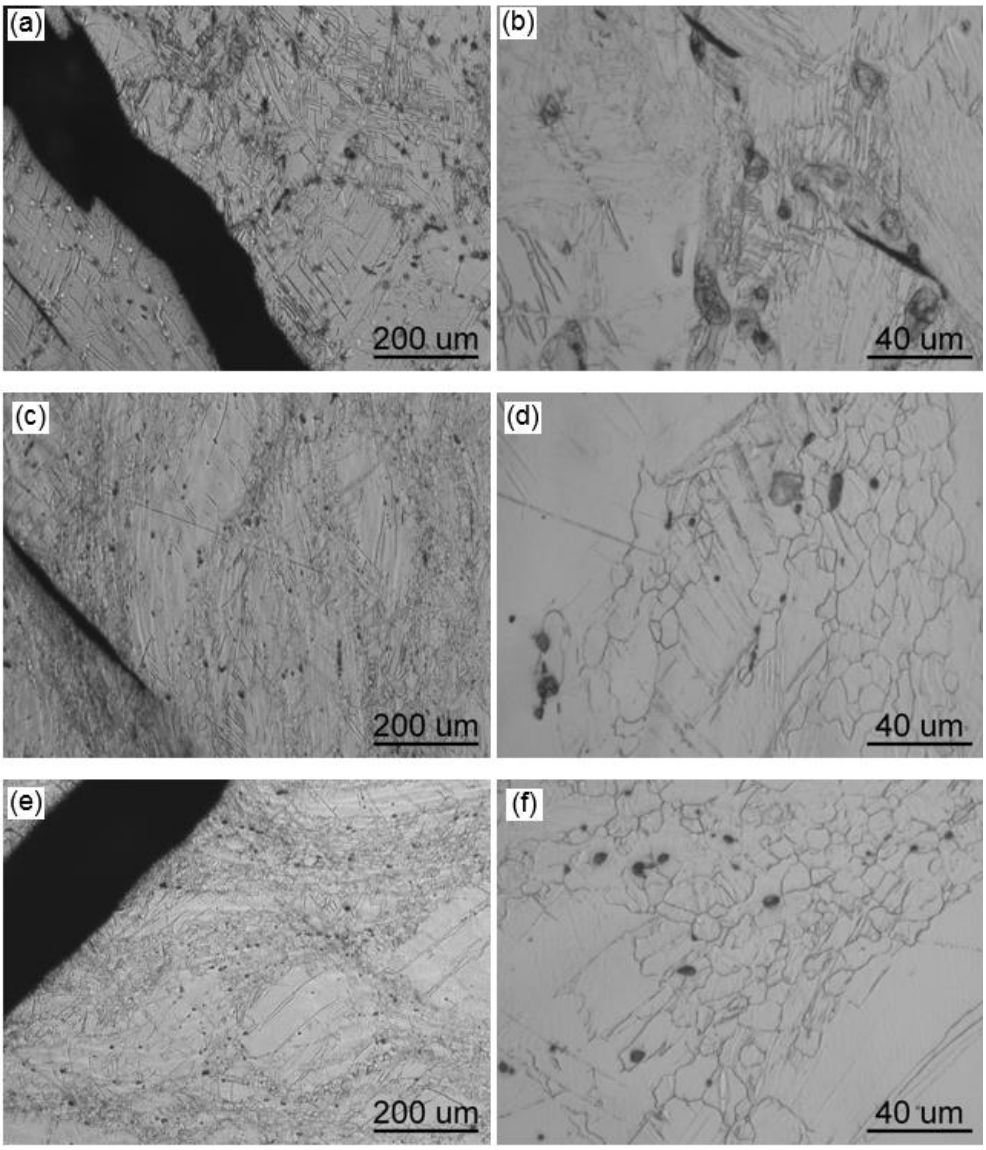

Fig 26: *Optical micrographs of the post-fracture compression specimens for (a, b) cast, (c, d) forged and compressed along FD and (e, f) forged and compressed along LD.*

3.3. Discussion

As suspected based on a review of existing literature, hot forging cast AZ31B resulted in a substantial degree of grain refinement as a result of DRX initiating at the original grain boundaries of the un-deformed cast material [69]. The grain refinement in the forged alloy was heterogeneous, displaying a bimodal grain distribution as a result of incomplete or partial recrystallization [70]. The forging process also resulted in the development of a clear basal texture compared to the random texture in the cast material. As discussed in the previous section, compression at room temperature resulted in twinning, causing a c-axis rotation nearly parallel to the loading direction [67]. This was

observed experimentally by measuring the texture of the post-fracture compression specimens (for both as-cast and forged conditions) and noting an 86.3° shift in the unit cell orientation, to lie parallel to the compression axis (Fig 25). However, at elevated temperatures (i.e. hot deformation), non-basal slip rather than twinning becomes active, resulting in a change in the unit cell orientation from a hard slip to stable slip direction [33], [71], [72]. It is noteworthy that the intensity of texture developed by non-basal slip tends to be lower than that resulting from twinning [35] which is confirmed by the relatively mild texture intensity displayed in Fig 17b.

Due to a reduction of grain size and development of a basal texture in the forged material, the forged AZ31B displayed significantly improved tensile yield and ultimate strengths compared to the as-cast material. Specifically, the measured TYS increased by about 143 percent as a result of the employed forging process. Considering the developed texture in the forged material and the orientation of tension specimens extracted from the forging (Fig 15d), the direction of loading (in tension) would be virtually perpendicular to the c-axis thereby inhibiting the activation of $\{10\bar{1}2\}\langle 10\bar{1}1\rangle$ extension twins and instead requiring yielding through the activation of non-basal slip and/or $\{10\bar{1}1\}\langle 10\bar{1}2\rangle$ compression twins [65]. At room temperature $\{0001\}\langle 11\bar{2}0\rangle$ basal slip is the easiest activated slip system in HCP crystals (lowest CRSS). However, the near perpendicular orientation between the c-axis of the forged specimens and the tensile loading direction would result in a negligible shear component parallel to the basal planes [11], [38], [42]. Therefore, the yield stress increases until the shear stresses in the material are sufficiently high to activate non-basal systems such as $\{10\bar{1}1\}\langle 11\bar{2}0\rangle$ prismatic slip [19], [73]. The accommodation of plastic strain by the activation of non-basal slip is thought to be primarily responsible for the increased yield strength of the forged alloy when compared to the as-cast material [42], [74].

In conventional BCC and FCC metals, yield stress follows the Hall-Petch relation of being inversely proportional to the square root of the average grain size [75]. A similar trend has also been reported for Mg alloys with an increase in the yield and ultimate strengths resulting from a decrease in average grain size [41], [42]. In the context of the current study, the reduction in the average grain size (from 278 μm to 14 μm) of the forged material occurred as a result of partial recrystallization due to hot deformation. This recrystallization resulted in the formation of the observed DRX grain structure (Fig 16e, f) which along with the developed basal texture serves to increase the yield strength of the forged material.

Wrought Mg alloys are well known for exhibiting tension-compression asymmetry due to material texture. Such asymmetry was observed to varying degrees in both the cast and forged material conditions. The yield strength of the cast alloy showed a mild tension-compression asymmetry with the ratio of compression to tension yield strength being approximately 1.31. This asymmetry is attributed to easier $\{10\bar{1}2\}\langle 10\bar{1}1\rangle$ twin activation during tension compared to compression, and similar behavior was also observed in other studies [76], [77]. It should also be noted that while the forging process considerably increased the ultimate compressive strength of AZ31B (Fig 21), the in-plane yield strength (i.e. LD and TD) did not demonstrate a meaningful change due to the activation of the same yielding mechanism (viz. extension twinning) in the forged material due to the sharp basal texture. Twinning behavior in the in-plane directions was confirmed by texture analysis of the compression specimens post-deformation, which indicated a rotation of the c-axis to lie virtually parallel to the loading direction (Fig 25). Compression tests in the FD displayed a 57 percent increase in yield strength compared to the cast material thought to be due to inhibition of twinning and basal slip in favor of non-basal slip systems to accommodate the imposed strains.

An interesting observation of the current study is the effect of forging on the failure elongation of AZ31B. Cast alloys are generally expected to exhibit poorer elongation compared to their wrought counterparts due to (i) a brittle dendritic morphology, (ii) coarse grain structure, and (iii) casting defects such as inclusions and voids that act as stress concentrators. In the present investigation however, the reverse appears to be true with the as-cast AZ31B displaying higher elongation compared to the forged condition (15.7% vs. 12.4%). It is believed that this behavior is due to the occurrence of a combination of twin and slip deformation during tension loading of the as-cast alloy. This was confirmed by post-failure microstructure (Fig 23) and texture (Fig 24) behavior. The activation of twin activity in the as-cast material may serve to increase overall elongation: (i) directly through strain accommodation by twinning and (ii) indirectly as a reorientation mechanism for unfavorable grains to be more conducive to slip. Barnett [78] and Byeong-Chan et al. [79] observed a similar effect of extension twins in extruded AZ31 were twinning resulted in an increase in the uniform elongation and formability compared to the same material in which twinning was inhibited. It is noteworthy that several voids were observed on the fracture surfaces of the forged material (Fig 22g). Similar voids in wrought Mg alloys were observed by Barnett [31] and Shi et al. [80] and were attributed to embrittlement of the material due to the formation of $\{10\bar{1}1\} - \{10\bar{1}2\}$ double twins

during deformation which resulted in premature failure. While a more in-depth study on the underlying mechanism responsible for these voids is required, the mechanism described in [31], [80] is consistent with the lack of detection of such voids prior to deformation in the forged material.

3.4. Chapter Conclusions

This study investigated the effect of hot forging on the microstructure, texture and mechanical properties of cast AZ31B Mg alloy and the following conclusions are be drawn:

- Forging as-cast AZ31B at 450 °C at a speed of 39 mm/min resulted in a partially recrystallized grain structure with a bimodal grain size distribution.
- Forging resulted in an increase in the tensile-compression asymmetry of the alloy. However, a substantial increase in tensile yield strength of 143 percent and ultimate strength of 23 percent was measured while the maximum yield strength and ultimate strength in compression increased by 75 percent (in the FD) and 22 percent, respectively.
- Microstructure and texture analysis of the forged specimens compressed at room temperature showed that $\{10\bar{1}2\}\langle 10\bar{1}1\rangle$ extension twins controlled the deformation along the LD/TD accompanied by a c-axis rotation of about 86.3° to be aligned with the compression direction. Extension twinning also occurred in the as-cast samples although to a lesser degree.
- The occurrence of extension twinning in the as-cast material during tension loading appeared to increase the overall elongation of the specimens prior to failure resulting in the as-cast material displaying higher failure elongation compared to the forged material.

Chapter 4: Influence of open-die forging on the low cycle fatigue (LCF) behavior of cast AZ31B alloy

The influence of open-die forging on the low cycle fatigue (LCF) behavior of cast AZ31B was investigated. Fully reversed (R_ε=-1) strain-controlled cyclic tests were performed on as-cast and forged materials under total strain amplitudes ranging from 0.1% to 1.2%. The forged material was generally found to exhibit longer fatigue life, especially at the lower tested strain amplitudes. This improvement was attributed to the grain refinement and the developed basal texture that changed the deformation behavior of the alloy. The forged material also achieved significantly higher stresses at the same level of total strain amplitude compared to cast AZ31B. Substantial cyclic hardening occurred during cyclic loading of both alloy conditions with considerable tension-compression asymmetry observed in the forged AZ31B during LCF testing. The Smith-Watson-Topper (SWT) model and Jahed-Varvani (JV) energy model were employed and both models accurately predicted the experimentally obtained fatigue life of both cast and forged alloy conditions. The JV model accurately predicted fatigue life within a factor of 1.5, especially the asymmetric behavior of forged AZ31B.

4.1. Experimental Details

4.1.1. Sample Preparation

The forging process employed in this study was identical to that described in chapter 3. Dog-bone shape specimens with the same gauge profile used for quasi-static testing but with increased overall length were extracted for cyclic tests following ASTM E8 (Fig 27a). The as-cast specimens were extracted from locations as described in chapter 3. Forged specimens were extracted such that the testing direction was aligned with LD of the forging (Fig 27b). All specimen surfaces were ground with #2000 SiC paper to remove machining marks prior to testing. Sample preparation for microstructure and texture studies were identical to that described in section 3.1.2.

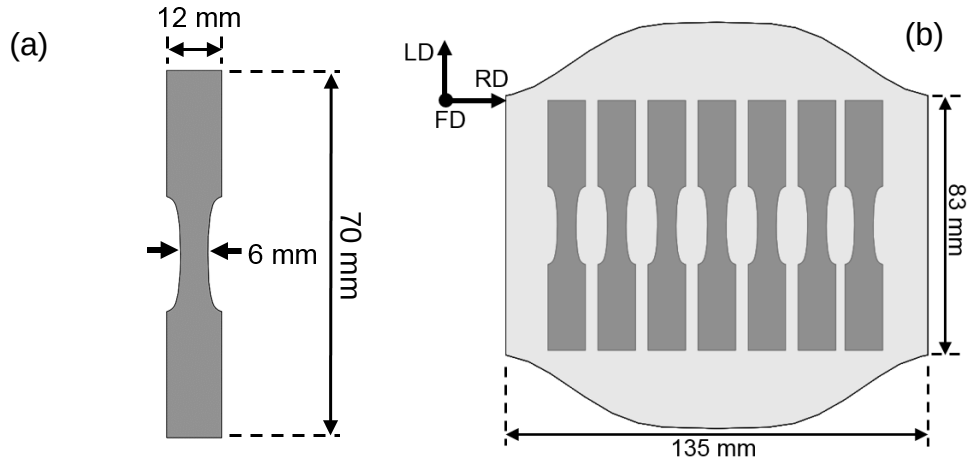

Fig 27: *Illustration of (a) the geometry of the dog-bone shaped specimens and (b) dog-bone shape specimen extraction locations from the finished forging.*

4.1.2. Strain-controlled testing

A MTS 810 servo hydraulic load frame equipped with a 25kN actuator was used for the fully reversed ($R_\varepsilon = -1$) strain-controlled fatigue testing of both as-cast and forged materials in accordance with ASTM E606. Strain was monitored using a MTS extensometer with a gauge of 7.6 mm which was mounted to the specimens using steel springs, and secured with Loctite 380 instant adhesive and Loctite 7452 accelerant. Testing was performed at total strain amplitudes ranging from 0.1% to 1.2% at increments of 0.1%. The test frequency was varied between 0.2 Hz and 2.5 Hz depending on the tested strain amplitude such that the average strain rate was constant at 0.01 s^{-1}. A tested specimen was considered to have failed when the tensile load dropped to 50% of its peak value or the specimen fractured. For tests exceeding 10^4 cycles, the test was paused when the peak tensile and compressive forces stabilized and the test was changed to load control mode operating at a frequency of 30 Hz until failure or a cycle count of 10^7 cycles (considered as runout) was achieved. Fractured specimens were retained for future fractographic analysis.

4.2. Results

4.2.1. Cyclic stress-strain properties

The plot of cyclic stress-strain (σ_c-$\Delta\varepsilon_t/2$) of AZ31B alloy where σ_c is the peak stress at mid-life in tension/compression and $\Delta\varepsilon_t$ is the total strain range, is shown in Fig 28. The corresponding quasi-static stress-strain plots are also included up to a total strain of 1.0% for reference. It is obvious that the alloy in both as-cast and forged conditions displayed remarkably higher hardening behavior during cyclic loading compared to quasi-static loading. The cyclic tests indicated that the as-cast alloy

achieved a 0.2% offset cyclic YS of 109 MPa and 97 MPa in tension (Fig 28a) and compression (Fig 28b), which is significantly higher than the values in quasi-static tension (56 MPa) and compression YS (74 MPa). Similarly, the forged alloy also exhibits a significant improvement in cyclic YS of 200 MPa and 112 MPa in tension and compression, respectively. The forged AZ31B demonstrated an 84 % increase in cyclic tensile YS and a 16 % increase in cyclic compression YS compared to the as-cast alloy (Table 3). The mechanisms responsible for the substantial increase in the cyclic tension curve of the forged material are discussed later.

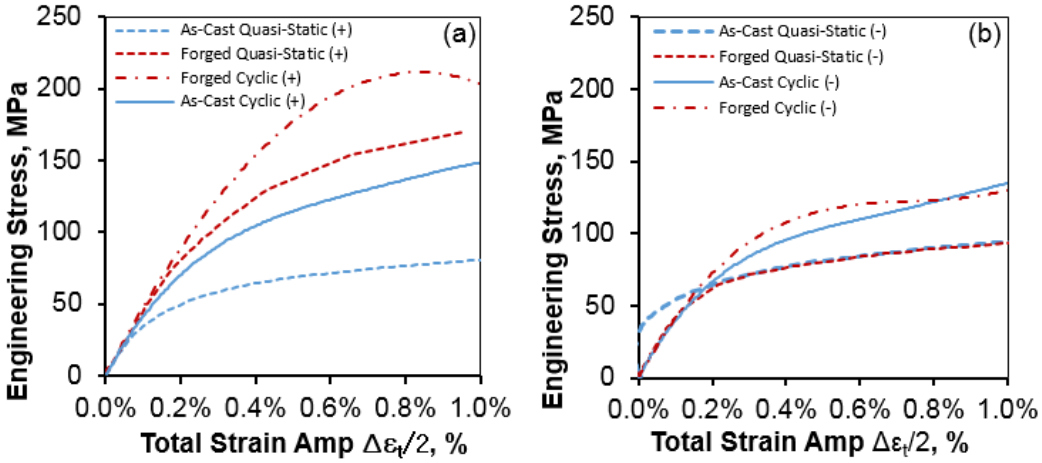

Fig 28: *Cyclic stress-strain curves for cast and forged AZ31B showing (a) cyclic tension curves and (b) cyclic compression curves. For reference, quasi-static tension and compression curves have also been included.*

Table 3: *Summary of cyclic tension and compressive yield stress for the as-cast and forged AZ31B.*

	Cyclic TYS, MPa	Cyclic CYS, MPa
Cast	109	97
Forged	200	112

4.2.2. Hysteresis loops and fatigue life

Fig 29 depicts typical engineering stress–strain hysteresis loops of the first and half-life cycles for a total strain amplitude of 0.2% and 1.0% for the as-cast and forged AZ31B. It is seen in Fig 29a that the slope during the first reversal (tension) is the same in both conditions and for both low and high strain amplitudes which indicates that forging did not alter the elastic modulus of the alloy. Also in Fig 29a, the as-cast alloy exhibits a symmetric hysteresis loop at the lower strain amplitude (0.2%) whereas when the strain amplitude is increased to 1.0%, a slightly concave shape appears in the hysteresis loop, which is an indication of mild activity of a twinning-detwinning mechanism (Fig 29b). In contrast, the forged material exhibits asymmetric stabilized hysteresis loops (Fig 29c) for strain amplitudes higher than 0.4%, which are similar to those observed for rolled or extruded AZ31B

Mg alloys [48], [81]. It is worth noting the serrations (stress drop and reloading to the plateau stress) observed in the hysteresis loops during the compressive reversal for the forged material (Fig 29a), and a possible explanation for these serrations is discussed in section 4.3.1.

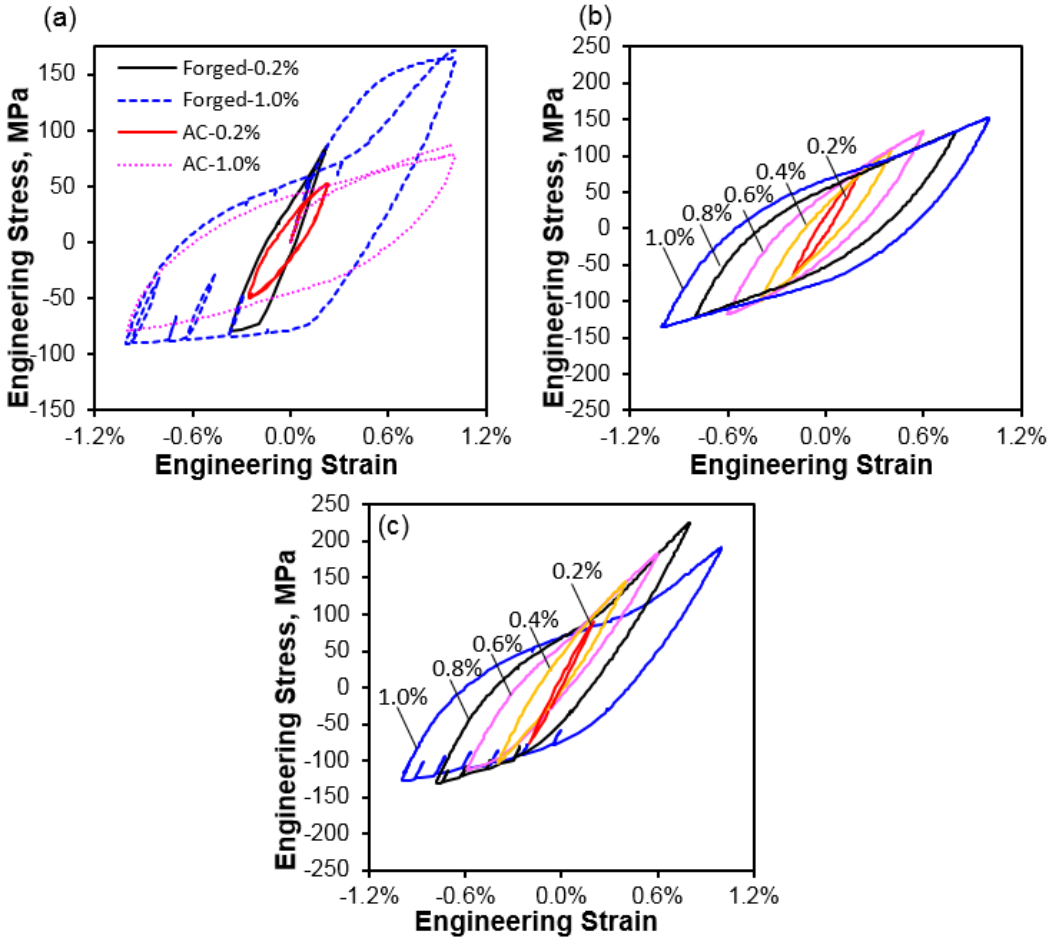

Fig 29: *Stress–strain hysteresis loops for (a) first cycle of the cast and forged materials and (b, c) half-life cycle for (b) as-cast and (c) forged AZ31B Mg alloy obtained from strain-controlled testing.*

The evolution of hysteresis loops for the forged material at strain amplitudes of 0.4% and 1.0% is included in Fig 30. At the lower strain amplitude (Fig 30a), the second cycle hysteresis loop has an obvious asymmetric shape. By cycle 100, the loop evolves to be virtually symmetric and this symmetry is maintained up to the half-life (cycle 2400) of the test. A similar evolution of low amplitude hysteresis loops was observed by Roostaei et al. for extruded AM30 alloy [60]. In comparison to the low strain amplitude test, at the high amplitude (Fig 30b), pronounced asymmetry is observed at the second cycle and this asymmetry is maintained throughout the test.

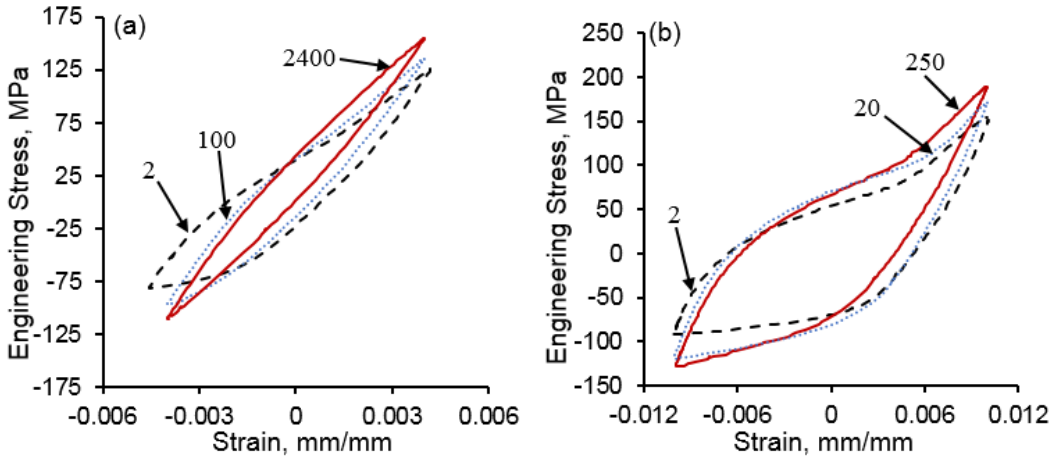

Fig 30: *Intermediate hysteresis loops for forged AZ31B tested at total strain amplitude of (a) 0.4% and (b) 1.0%. The 0.4% test failed after 4741 cycles whereas the 1.0% test failed after 497 cycles.*

Optical microscopy was performed on post-failure specimens of the as-cast and forged alloys tested at both low and high strain amplitudes and the results are included in Fig 31. Residual twins are observed in both the as-cast and forged AZ31B at higher strain amplitudes, but are absent at lower strain amplitudes. Twinning in the cast material is restricted to a few favorably oriented grains whereas it is far more prolific in the textured forged material. Additionally, at high strain amplitude (Fig 31d) the forged material demonstrated several instances of cracks nucleating at twin boundaries (yellow arrows). A high magnification SEM image of such cracks is shown in Fig 32 (red arrows). A discussion on the mechanism responsible for the formation of these cracks is included in the Discussion section of this chapter.

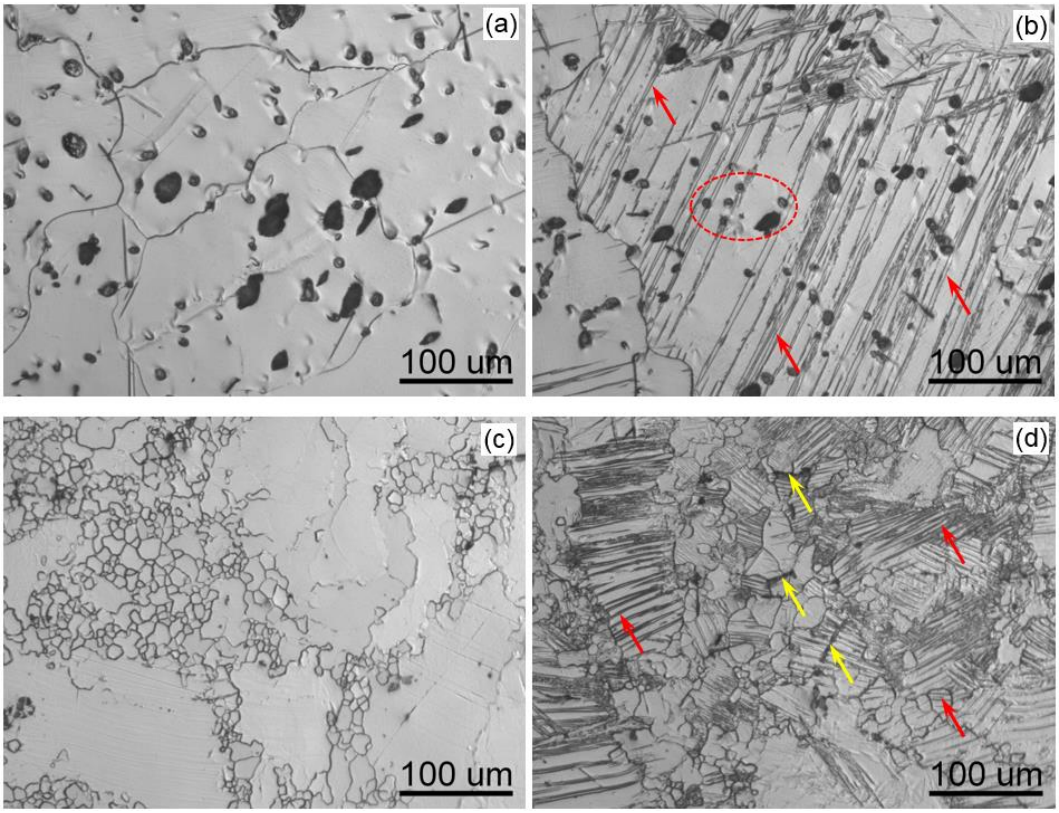

Fig 31: *Optical micrographs near the fracture surface at the gauge section of the (a, b) as-cast and (c, d) forged AZ31B Mg alloy observed post failure after testing at a total strain amplitude of (a, c) 0.3% and (b, d) 1.0%. The red and yellow arrows denote residual twins and cracks observed along twin boundaries respectively. The red ellipse denotes extension twins being blocked by intermetallics.*

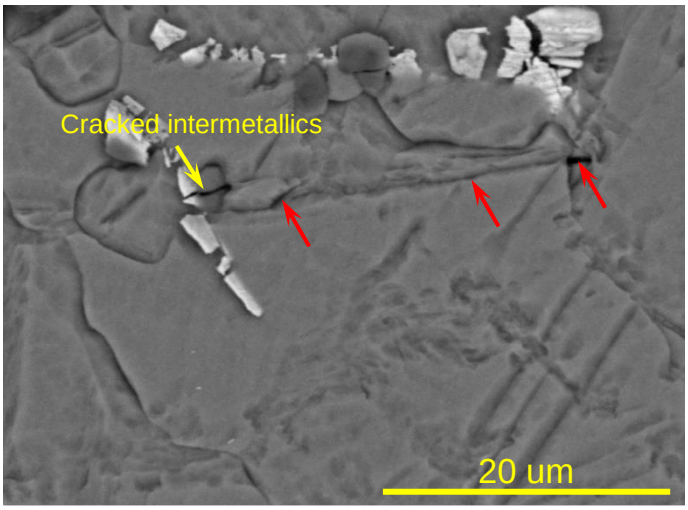

Fig 32: *SEM image of the polished gauge-section of forged material perpendicular to the fracture surface tested at a strain amplitude of 1.0%. Note the cracked intermetallics and secondary cracks (SC) along the twin boundary indicated by red arrows.*

The number of cycles to failure, N_f, against the imposed total strain amplitudes ($\Delta\varepsilon_t/2$) for the AZ31B alloy in as-cast and forged conditions is plotted in Fig 33, along with some data available in literature for wrought AZ31 processed via extrusion [82] and rolling [83]. The as-cast alloy displayed lower fatigue life to that of the forged Mg alloy at high strain amplitudes and significantly shorter life compared to the forged alloy at low strain amplitudes. The other conditions (from literature) generally exhibited lower fatigue life for the same total strain amplitude. It should be noted that the fatigue life is always higher in forged material compared to the rolled and extruded materials above a total strain amplitude of 0.6%. The Coffin-Manson fatigue life parameters were evaluated and are listed in Table 4. It is also observed that the obtained Manson-Coffin parameters for the forged material in this study were considerably higher compared to the as-cast alloy and those obtained for wrought AZ31 obtained in other studies [82], [83].

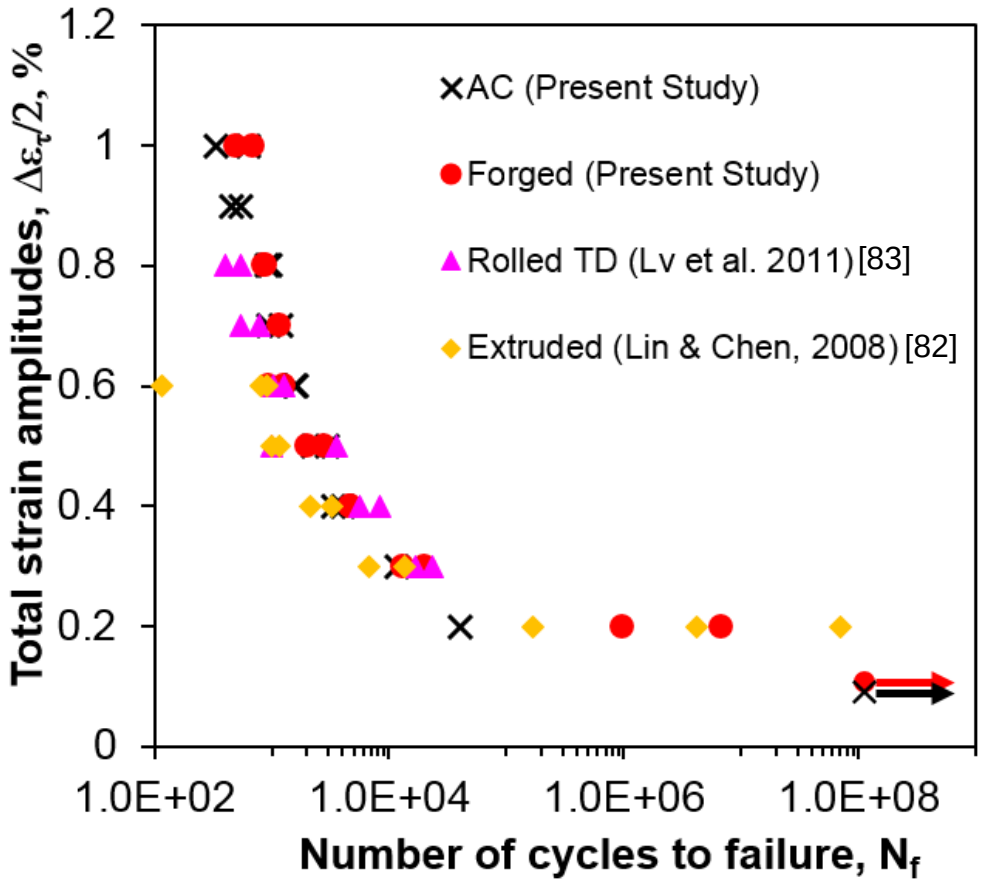

Fig 33: *Total strain amplitude vs. number of cycles to failure for cast and forged AZ31B Mg-alloy. Similar strain-controlled results for rolled and extrusion AZ31B Mg-alloy are presented for comparison.*

Table 4: *Summary of Manson-Coffin parameters for the tested as-cast and forged AZ31B alloy along with values found in literature for thermo-mechanically processed AZ31B.*

	This Study		Lv et al., 2011[83]	Lin & Chen, 2008 [82]
Condition	Cast	Forged	Rolled	Extrusion
σ_f', MPa	396	482	434	467
b	-0.16	-0.14	-0.097	-0.13
ε_f', %	39	53	7.11	1.89
c	-0.59	-0.66	-0.49	-0.39

4.2.3. Cyclic deformation response

Fig 34 depicts the obtained stress amplitudes with respect to the number of cycles at several different total strain amplitudes on a semi-log scale. It is seen that the forged alloy always exhibited higher peak stress amplitude compared to the as-cast material for a particular strain amplitude (Fig 34c). In order to characterize the cyclic hardening exhibited by the two material conditions, a power function of the form shown in Eq. (4) was fitted to the curves in Fig 34a, b for cycles up to just prior to failure.

$$\boldsymbol{\sigma_a = AN^b} \qquad (4)$$

Where σ_a is the stress amplitude, N is the number of cycles, and A and b are the fitting parameters. The values of these fitting parameters along with their respective correlation coefficients are included in Table 5. The cyclic hardening rate $d\sigma_a/dN$ derived from Eq. (4) was then plotted for the as-cast and forged alloys for the first 10 cycles and is included in Fig 34d. It is seen from this plot that at each cycle, the forged material demonstrates a higher cyclic hardening rate compared to the as-cast material for the same strain amplitude. Note that a more complex stress amplitude behavior was observed for the forged material at a low strain amplitude (0.2%). Specifically at this strain amplitude a certain extent of cyclic softening occurred up to ~80 cycles following which the material started to harden slightly until it reached the stabilization stage. Due to this behavior, a good fit to Eq. (4) was not obtained and this amplitude was therefore not included in Fig 34d.

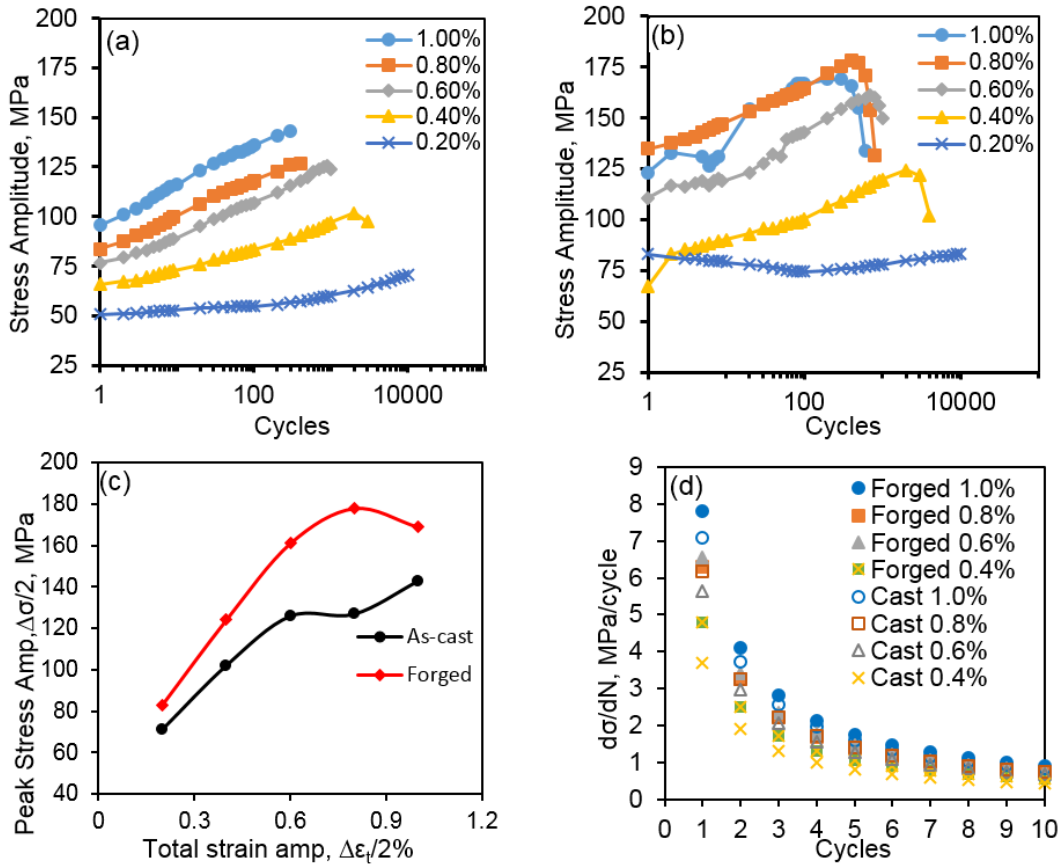

Fig 34: *Stress amplitude vs. number of cycles for AZ31B Mg alloy derived from LCF test data in (a) as-cast and (b) forged conditions, (c) a comparison of peak stress amplitude versus total strain amplitude for the two material conditions and (d) plot of change in stress amplitude vs. cycles for cast and forged conditions.*

Table 5: *Summary of curve fitting parameters and associated coefficient of determination for cyclic hardening behavior of as-cast and forged AZ31B.*

	As-Cast			Forged		
Strain Amp.	A	b	R^2	A	b	R^2
1.0%	97.5	0.0726	0.987	121.2	0.064	0.865
0.8%	84.2	0.0732	0.991	132.6	0.048	0.996
0.6%	75.6	0.0747	0.997	107.1	0.061	0.969
0.4%	64.4	0.0572	0.991	76.6	0.062	0.952
0.2%	48.2	0.0354	0.912	-	-	-

Additionally, during LCF testing, plastic strain amplitude is considered as a physical quantity that affects the microstructure and is strictly related to the resistance of strain. Thus plastic strain amplitude ultimately influences fatigue life. The obtained plastic strain amplitude ($\Delta\varepsilon_p/2$) during the current LCF tests is presented in Fig 35, and the results correspond well with the change of the stress amplitude during cyclic loading as illustrated in Fig 34 at different applied strain amplitudes. Note the considerable decrease in plastic strain amplitude in forged samples as the strain amplitude decreases.

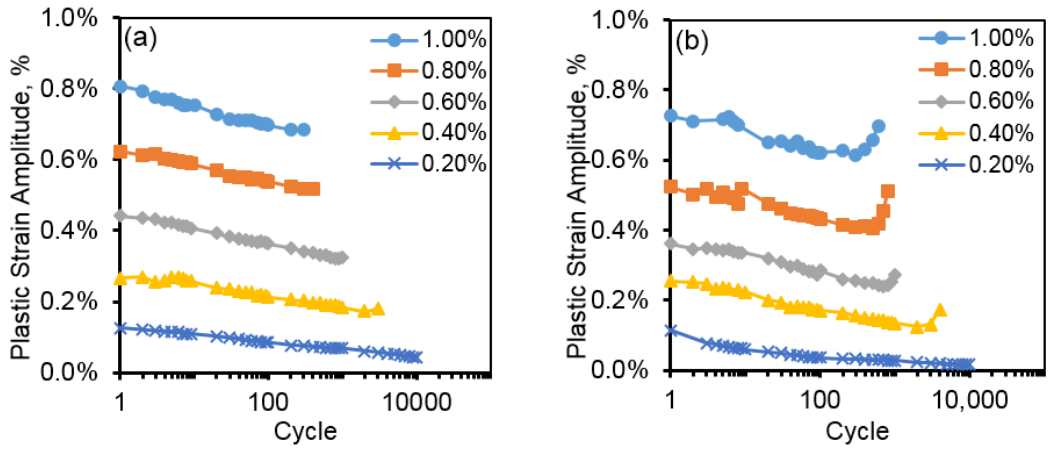

Fig 35: *Plastic strain amplitude vs. number of cycles for (a) as-cast and (b) forged AZ31B derived from LCF test data.*

4.2.4. Fatigue fracture surfaces

Fig 36 shows SEM images of the as-cast and forged AZ31B alloy tested at two different total strain amplitudes of 0.3% and 1.0%. For the tested samples, three distinct features were observed on the fracture surface: (i) fatigue crack initiation (FCI), (ii) fatigue crack growth/propagation (FCG) zone and (iii) final fracture (FF) zone adjacent to the FCG zone. River like patterns with twin lamellae which are irregular or broken and grow along the crack propagation direction, were seen in all samples. However, profuse twin lamellae were observed in forged samples, especially at the higher strain amplitude of 1.0%. It is also noticed that multiple FCI sites (marked by red arrows) are visible in the samples tested at the higher strain amplitude (1.0%). At the same time, at the higher strain amplitudes the fracture surfaces exhibit almost tensile-like fracture features for both as-cast (Fig 36b) and forged specimens (Fig 36d). Higher magnification images of the FCI areas are presented in Fig 37 and show that most of the cracks initiated at the surface due to intrusion-extrusion (Fig 37a) or casting defects such as large surface porosity (Fig 37b) for the as-cast sample, and the presence of twin lamellae, secondary particles and oxide layers (Fig 37c, d) for the forged sample. These features

act as stress concentrators which nucleate the fatigue cracks [84], [85]. The locations enclosed in green, white and yellow boxes in Fig 36, are magnified and included in Fig 38, Fig 39 and Fig 40, respectively to show more detailed features of the fatigue fracture surfaces corresponding to the as-cast and forged samples tested at total strain amplitude of 0.3% and 1.0%. As mentioned previously, the FCG zone is quite different depending on the alloy condition (i.e. cast versus forged). For example, the samples tested at a lower total strain amplitude (0.3%) exhibit fatigue striations (FS) within the FCG zone with each striation representing the growth of the crack during a load cycle. For this strain amplitude, the as-cast sample (Fig 38a) revealed comparatively coarse FS with an average distance of 1.9 μm between striations, whereas, the forged sample (Fig 38b) exhibited much finer FS (~ 0.5 μm between striations) surrounded by tear ridges. The finer FS observed in the forged specimens at lower strain amplitudes corresponds well with the considerably longer fatigue life observed in the forged material compared to the cast AZ31B (Fig 33). Finally, the FF zone of the samples tested at a strain amplitude of 0.3% show ductile type fracture with dimples surrounded by tear ridges, with porosity in as-cast sample (Fig 39a), and secondary cracks (marked by green arrows) in the forged sample (Fig 39c). For tests at the high strain amplitude of 1.0% (Fig 39b, d) typical ductile features (similar to those observed during quasi-static loading) were observed all over the fracture surfaces. An interesting feature observed in the samples tested at all strain amplitudes is the presence of micro-cracks passing along or through intermetallics, which results in the generation of voids in the matrix (Fig 40). With continued cycling, these voids coalescence leading to final fracture. Since the as-cast material contained a higher concentration of intermetallics compared to the forged sample (chapter 3, Fig 16), more voids and cracks could be expected in the as-cast material contributing to the lower fatigue life.

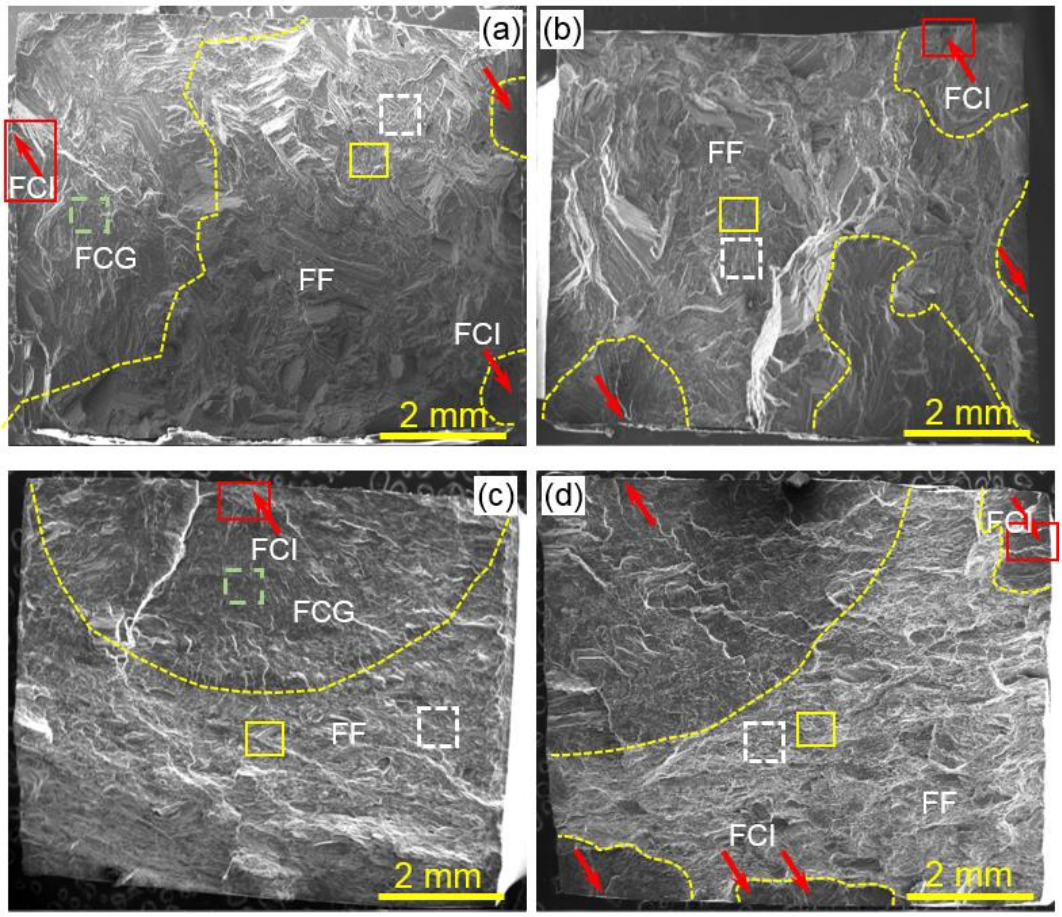

Fig 36: *SEM images of fatigue fracture surfaces of the samples tested at a total strain amplitude of 0.3% (a, c) and 1.0% (b, d) showing an overall view for as-cast (a, b) and forged (c, d) material. The yellow lines separate the fatigue crack growth (FCG) zone from the fast fracture (FF) zone. The red arrows indicate fatigue crack initiation (FCI). The enclosed boxes are magnified and presented in Fig 37 (red boxes), Fig 38 (green boxes), Fig 39 (yellow boxes) and Fig 40 (white boxes) showing the FCI, FCG, FF regions, and the presence of intermetallics, respectively, for the studied AZ31B Mg alloys.*

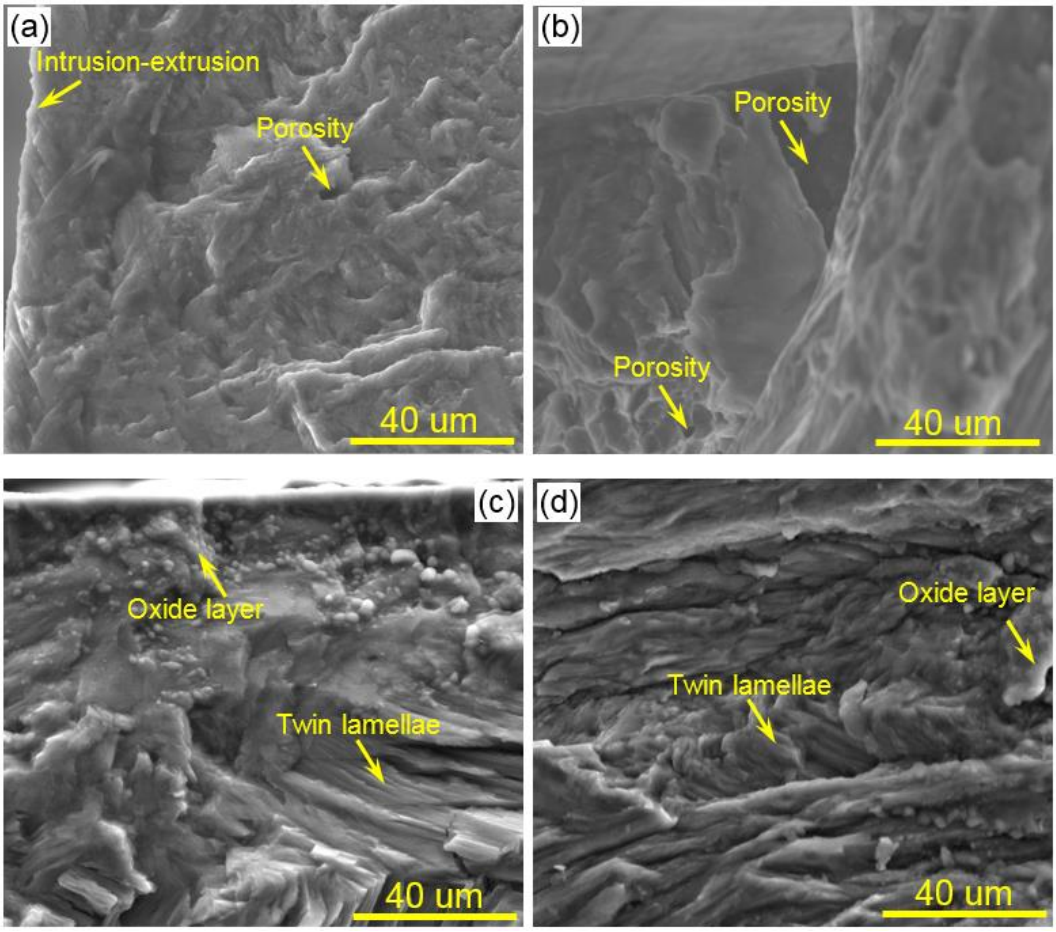

Fig 37: *SEM images of fatigue fracture surfaces of the samples tested at a total strain amplitude of 0.3% (a, c) and 1.0% (b, d) showing the crack initiation sites for as-cast (a, b) and forged (c, d). Note: fatigue cracks initiate due to (a) intrusion-extrusion, (b) the presence of a large surface pores, and (c, d) extension twin activity and oxide layers.*

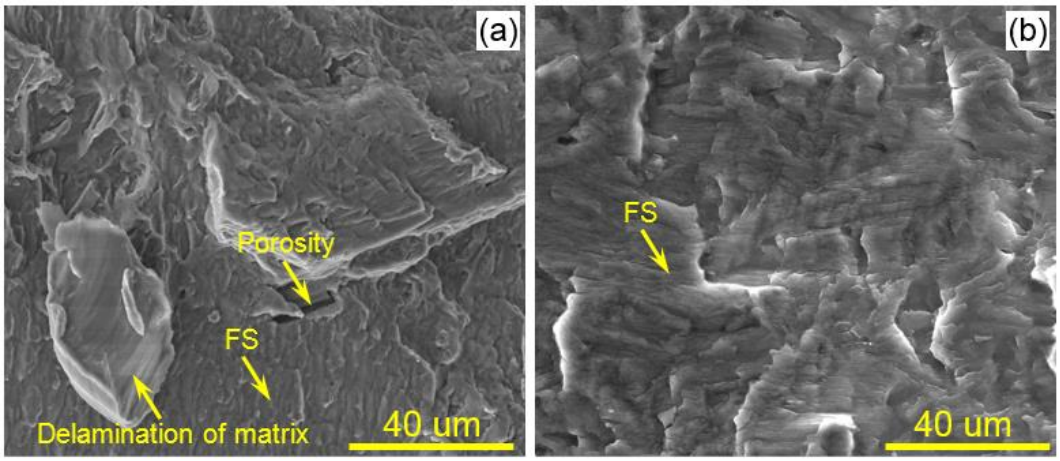

Fig 38: *SEM images of fatigue fracture surface in the FCG regions showing fatigue striation (FS) in the matrix of the samples tested at a total strain amplitude of 0.3% for (a) as-cast and (b) forged AZ31B.*

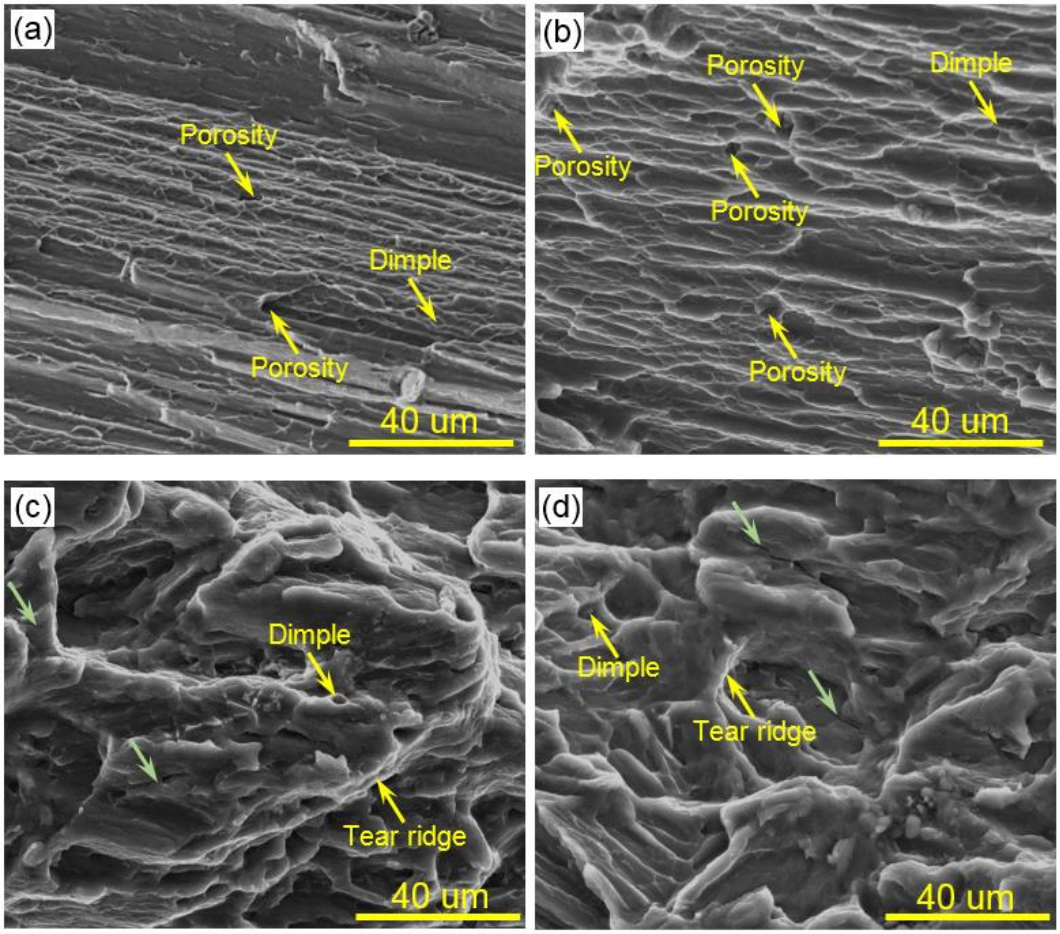

Fig 39: *SEM images of fatigue fracture surfaces of the samples tested at a total strain amplitude of 0.3% (a, c) and 1.0% (b, d) showing the morphology in the FF zone for the as-cast (a, b) and forged (c, d) AZ31B Mg alloy. Note: green arrows indicate the secondary cracks in the matrix.*

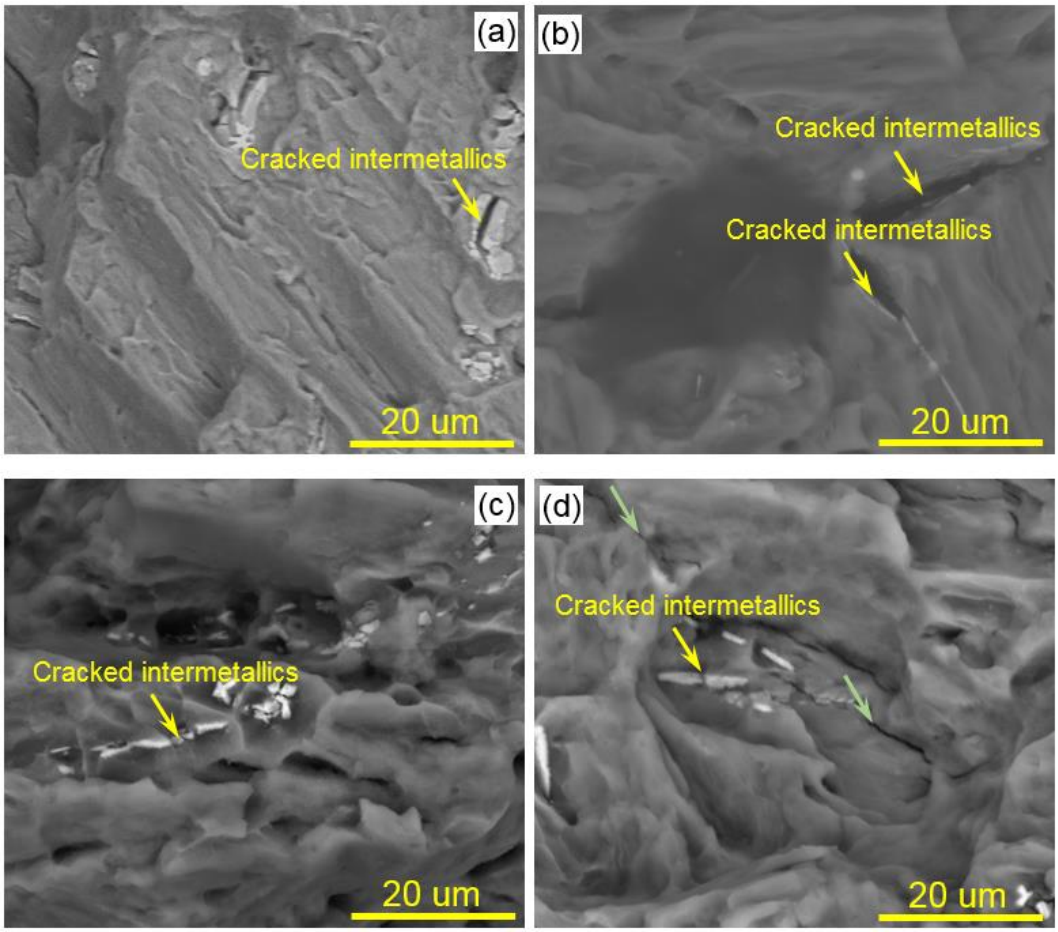

Fig 40: *SEM images of fatigue fracture surfaces of the samples tested at a total strain amplitude of 0.3% (a, c) and 1.0% (b, d) illustrating the role of intermetallics during cyclic loading of as-cast (a, b) and forged (c, d) material. Note: green arrows indicate the secondary cracks in the matrix.*

4.3. Discussion

4.3.1. Deformation behavior

The mechanical properties of Mg alloys are strongly related to the crystallographic texture, which controls the slip and/or twinning system(s) activated during loading and thereby influences the tension-compression yield asymmetry [27], [86]. It is well established that $\{10\bar{1}2\}\langle 10\bar{1}1\rangle$ extension twinning and basal slip are the main room temperature deformation mechanisms in Mg alloys [12], [84]. As described in section 3.2.1, the forged AZ31B developed a strong basal texture (Fig 17) compared to the starting as-cast alloy. Additionally, the as-cast material contained precipitates of β-$Mg_{17}Al_{12}$ and $MgZn_2$ distributed along the inter-dendritic regions. The evolution of microstructure from the as-cast to the forged material includes the dissolution of precipitates and the recrystallization of grains (Fig 16). Thus, forging at elevated temperature plays an important role in the formation of

a strong basal texture which exhibits yield asymmetry of the forged AZ31B alloy (chapter 3, Fig 18 and Fig 20). As seen in Fig 28 and Table 3, the ratio of the compression-to-tension cyclic yield stress was ~0.56 for forged material, compared to the as-cast material where the ratio was ~1. Additionally, the peak stress amplitudes of the forged alloy at all tested strain amplitudes were higher than the as-cast samples. This is an indication of improved fatigue strength in the forged material. The higher cyclic tensile curve of the forged alloy compared to the cast alloy is thought to be due to the contributions of: i) the overall strengthening of the forged alloy via grain refinement (Fig 16) and hindrance of basal slip during tension due to the developed texture (Fig 17), and ii) a pronounced twinning-detwinning mechanism resulting in extensive cyclic hardening. Twinning impacts the cyclic response of the current alloy which is generally governed by i) the cyclic stability of the microstructure, ii) gliding and multiplication of dislocations, iii) twinning-detwinning behavior, and iv) interactions between twins and dislocations. Particularly, strain hardening in the as-cast and forged materials was due to dislocation-dislocation interactions which impede their motion by interlocking. Profuse twinning in the forged material including higher residual twin density provides additional barriers to the movement of dislocations on the original slip plane leading to a pile-up of dislocations at the twin or grain boundary, which generates a back stress and thus contributes to additional strain hardening observed in Fig 34 [87], [88].

It is also observed that compared to the as-cast material, the hysteresis loops of the forged AZ31B alloy (Fig 29) were asymmetric. This asymmetry in the higher strain amplitude hysteresis loops of the forged material is a result of twinning and subsequent detwinning during cyclic loading. At lower strain amplitudes (up to ~0.4%) in the forged material, extension twinning is activated during the initial compressive reversals due to the developed basal texture [89] and is evident by the shape of the second cycle hysteresis loop in Fig 30a. During the following tensile reversal, detwinning occurs which is characterized by the early reverse yielding and a subsequent inflection due to the exhaustion of detwinning and activation of slip [90]–[92]. As the loading is repeated, cyclic hardening occurs in both tension and compression which appears to inhibit twin activation with continued loading. By the hundredth cycle (Fig 30a), further extension twinning and corresponding detwinning appeared to be completely inhibited resulting in the development of a symmetric hysteresis loop. The symmetry of the hysteresis loop is retained up to the point of crack initiation. As the applied strain amplitude is increased, stresses during the compressive reversal are sufficient to activate more extensive extension twinning in favorably oriented grains. Detwinning occurs during

the subsequent strain reversal however due to increasing dislocation density restricting dislocation motion, detwinning becomes difficult resulting in residual twins [93]. This phenomena is demonstrated in Fig 30b where asymmetry is observed all the way up to the half-life (cycle 250) of the material. Similar twinning–detwinning behavior in wrought Mg alloys under cyclic loading were reported in [48], [90]. As pointed out in section 4.2.2, serrations were observed in the hysteresis loops during the compressive reversal for the forged material (Fig 29a). These serrations are more pronounced during the initial reversals and normally disappear with continued cycling (Fig 29c). This phenomenon was not observed under quasi-static compression, and is believed to be due to the different control modes (i.e., displacement control versus strain control), and accommodation of twin bands of localized deformation [94], [95].

An additional feature observed in the post-failure microstructure is the effect of intermetallics on twin growth. When the as-cast material is sufficiently loaded, twin bands originate and traverse the width of favorably oriented grains. However, intermetallics present within grains (Fig 31b) act as barriers to these twins, inhibiting their growth, and limiting their influence on the overall deformation behavior of the alloy. Note that such intergranular intermetallics were only observed in the as-cast material (Fig 16a). Instead, the post-failure forged microstructure displayed cracks along twin and grain boundaries (marked by arrows in Fig 31 and Fig 32). These cracks are thought to be a result of dislocation buildup at twin boundaries. The underlying mechanism was reported by Hazeli et al. [96] during fatigue fracture of AZ31 Mg plate: i) At room temperature, extension twins may occur in a grain that have undergone profuse slip. These twins are formed as a result of a mechanism activated to accommodate the stain induced by slip. ii) Increasing the applied stress generates more dislocations, leading to the disassociation of the twin boundary which is related to magnitude of the imposed strain. iii) When the loading direction changes (i.e. after a reversal) twin boundary migration is reversed (i.e. detwinning occurs). However, as detwinning is a harder process requiring additional strain for completion, some residual twins remain in the fully reversed strain controlled fatigue test. iv) This twinning-detwinning mechanism is repeated during cycling leading to accumulation of dislocations at these residual twin boundaries. v) This dislocation accumulation at twin boundaries may then result in the nucleation of a fatigue crack along the twin boundary.

Fig 33 demonstrated that the forged material exhibited longer fatigue life compared to the as-cast material particularly at lower strain amplitudes. This can be attributed to the difference in microstructural features present in the as-cast and forged conditions. Firstly, in both cast and forged materials, the crack originated at the specimen surface. This is due to higher propensity for unconstrained plastic flow to develop at a free surfaces resulting in surface roughening and eventually crack nucleation. In the case of the cast material, the crack initiation zone was found to contain intrusion-extrusion features and/or near surface voids (Fig 37a, b) which served as stress concentrators, thereby facilitating early crack formation [97]. In contrast, crack nucleation in the forged material may be a result of plastic strain accumulation at twin boundaries due to the buildup of non-reversible twins during cycling as was reported in [84], [96]. This is supported by the presence of numerous twin lamellae in the fatigue crack initiation region of the forged material (Fig 37c, d). Besides the mechanisms responsible for crack initiation, it is also well known that grain size plays an important role in controlling the crack growth rate with grain boundaries acting as barriers to the advancing crack front [9], [98]. Consequently, the relatively low grain boundary density in the as-cast alloy is thought to provide less impedance to crack propagation compared to the considerably higher grain boundary density observed in the recrystallized forged material. Further, other researchers have suggested additional roles for $\{10\bar{1}2\}$ extension twins (that were observed abundantly in the forged material) in lowering the crack growth rate, for example, by extension twins serving as roughness induced crack closures [99], [100].

4.3.2. Fatigue modelling

Fatigue is the primary failure mechanism in most engineering components and therefore, accurate prediction of the fatigue life of an in-service component is of critical importance. In order to predict the fatigue damage per cycle and consequently the fatigue life of a material, several fatigue models that incorporate experimental fatigue life data have been proposed [52], [89], [101], [102]. The proposed models may be either stress-, strain- or energy-based however, as is visible in Fig 29 and Fig 33, lower stress does not necessarily imply longer fatigue life for the current alloy. Accordingly, a stress based approached may not be ideal for modelling the current alloy subjected to strain-controlled testing, although such an approach has been used for prediction of fatigue life under stress-control testing of AZ31B [103]. Additionally, the well-developed fatigue models currently available in literature were either established for isotropic materials, or developed for other forms of wrought Mg alloys (such as rolling or extrusions) with different characteristics than the current forged

alloy. Consequently, the robustness of some available models to predict the fatigue life of the current forged AZ31B is investigated below.

During cyclic loading, total strain amplitude may be decomposed into elastic and plastic strain components [104], [105]:

$$\frac{\Delta \boldsymbol{\varepsilon_t}}{\mathbf{2}} = \frac{\Delta \boldsymbol{\varepsilon_e}}{\mathbf{2}} + \frac{\Delta \boldsymbol{\varepsilon_p}}{\mathbf{2}} \qquad (5)$$

Where, $\frac{\Delta \varepsilon_t}{2}$ is the total strain amplitude, $\frac{\Delta \varepsilon_e}{2}$ is the elastic portion of the strain amplitude and $\frac{\Delta \varepsilon_p}{2}$ is the plastic portion of strain amplitude.

The relation between elastic strain amplitude and number of reversals fatigue life ($2N_f$) may be represented by the well-known Basquin equation [104], [106]:

$$\frac{\Delta \boldsymbol{\varepsilon_e}}{\mathbf{2}} = \frac{\boldsymbol{\sigma_f'}}{\boldsymbol{E}} \left(\mathbf{2}\boldsymbol{N_f}\right)^{\boldsymbol{b}} \qquad (6)$$

where E is Young's modulus, N_f is the number of cycles to failure, σ'_f is the fatigue strength coefficient and b is the fatigue strength exponent.

Similarly, the relation between plastic strain amplitude and the number of reversals to failure can be represented by the Coffin-Manson equation [104], [106]:

$$\frac{\Delta \varepsilon_p}{2} = \varepsilon_f' \left(2N_f\right)^c \qquad (7)$$

where ε'_f is the fatigue ductility coefficient and c is the fatigue ductility exponent.

Combining Eq. (4), (5) and (6), fatigue life can be estimated using the following relationship known as the Coffin-Manson relation [104]:

$$\frac{\Delta \boldsymbol{\varepsilon}}{\mathbf{2}} = \frac{\boldsymbol{\sigma_f'}}{\boldsymbol{E}} \left(\mathbf{2}\boldsymbol{N_f}\right)^{\boldsymbol{b}} + \boldsymbol{\varepsilon_f'} \left(\mathbf{2}\boldsymbol{N_f}\right)^{\boldsymbol{c}} \qquad (8)$$

Elastic strain amplitudes and plastic strain amplitudes plotted versus reversals to failure ($2N_f$) for as-cast AZ31B are included in Fig 41 as an example and the calculated Coffin-Manson parameters are summarized in Table 4 along with values obtained from literature for other thermo-mechanically processed AZ31B [82], [83].

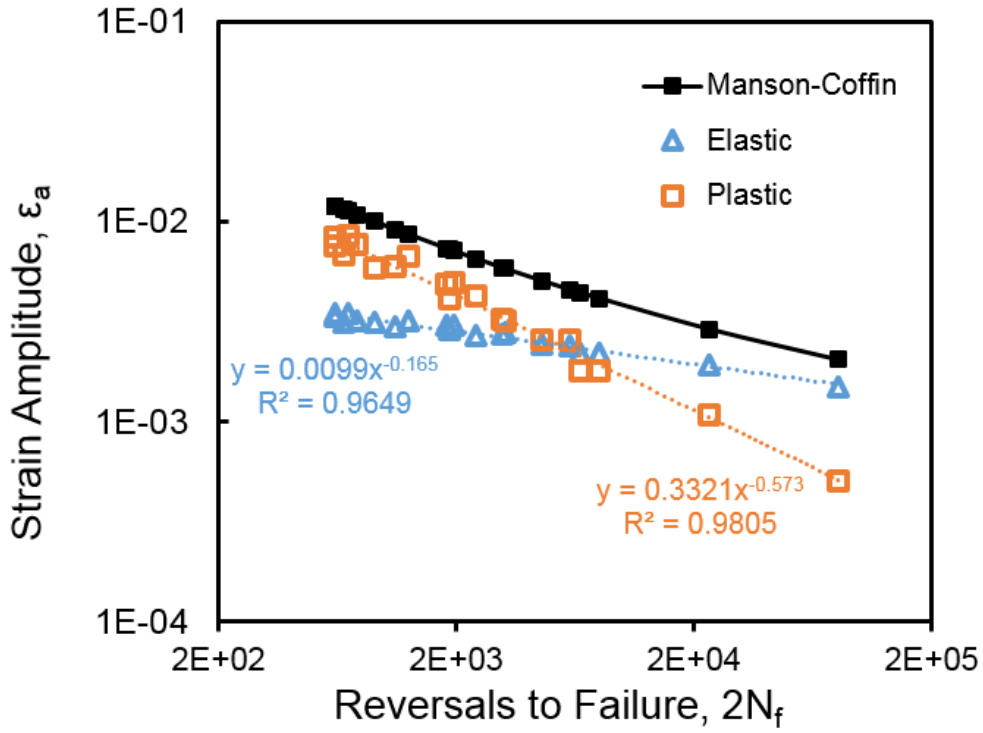

Fig 41: *Manson-Coffin plots for as-cast AZ31B LCF data on a logarithmic scale.*

A drawback of the Coffin-Manson relation discussed above is its inability to account for mean stress effects, resulting in inaccurate prediction for asymmetric materials such as Mg [99]. Consequently other models were developed to account of the effect of mean stress on fatigue life.

4.3.2.1 Smith-Watson-Topper (SWT) model

SWT was developed as a modification to the Manson-Coffin relation to account for mean stress affect by considering an energy-like parameter evaluated at the plane of maximum axial strain. The SWT parameter is related to fatigue life as:

$$\sigma_{n,max}\frac{\Delta\varepsilon}{2} = \frac{\sigma_f'^{\,2}}{E}\left(2N_f\right)^{2b} + \sigma_f'\varepsilon_f'\left(2N_f\right)^{b+c} \qquad (9)$$

Where $\Delta\varepsilon/2$ is the normal strain amplitude, $\sigma_{n,max}$ is the maximum normal stress on the maximum normal strain plane and E is the modulus of elasticity. The fatigue life predicted using the SWT model (Eq. 9) is plotted against the experimentally obtained fatigue life in Fig 42. The solid diagonal line represents a perfect prediction whereas the diagonal orange and black dashed lines represent factor of 1.5 and factor of 2 bounds respectively between the predicted and experimental life. From Fig 42 it is seen that all the experimental data lies within the factor of 2 bounds for both as-cast and forged condition within the tested strain amplitudes indicating that the SWT model is suitable for modelling the current test data including the subject forged AZ31B.

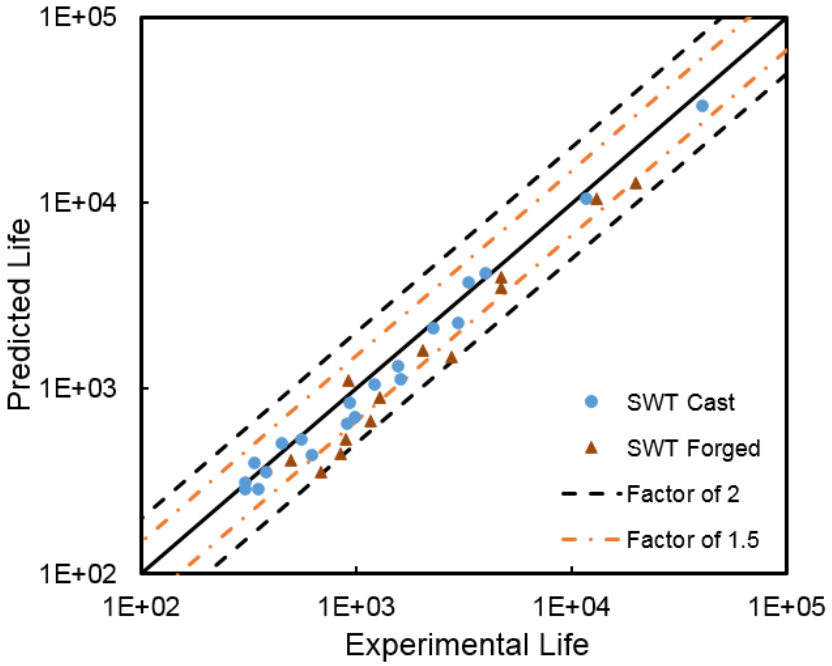

Fig 42: *Predicted fatigue life versus experimental fatigue life for as-cast and forged AZ31B using SWT fatigue model.*

4.3.2.2 Jahed-Varvani (JV) model

In addition to the SWT model discussed above, an energy based fatigue model was also considered in this study. Energy based models are commonly used particularly for asymmetric/anisotropic materials due to the invariant nature of strain energy density. The current chapter considers an energy model proposed by Jahed and Varvani that predicts fatigue life using elastic and plastic energy relations [107], [108]. The significance of this energy model is in the evaluation of material's fatigue parameters. The fatigue parameters in the JV model are calculated

from experimentally obtained total energy density vs. life curves. The total strain energy density, E, is related to number of reversals, $2N_f$, as:

$$\boldsymbol{E = E'_e(2N_f)^B + E'_f(2N_f)^C} \quad \textit{(10)}$$

E'_e, B, E'_f, C are energy-based fatigue properties obtained analogous to those in the Manson-Coffin relation and are determined in the same way. The values of these fatigue parameters calculated for the current alloy have been summarized in Table 6. E is the total strain energy density which is composed of the plastic energy density and the positive elastic energy density [109], where the plastic portion of the energy density is the area enclosed by the half-life hysteresis loop and the positive elastic portion is calculated by:

$$\boldsymbol{E_e^+ = \frac{\sigma_{max}^2}{2E}} \quad \textit{(11)}$$

Where σ_{max} is the tensile peak stress of the hysteresis loop.

Table 6: *Summary of Jahed-Varvani energy parameters for the tested as-cast and forged AZ31B alloy.*

	E'_e, MJ/m^3	B	E'_f, MJ/m^3	C
Cast	2.17	-0.319	387.5	-0.782
Forged	5.48	-0.332	344.6	-0.776

The plot of predicted life versus experimentally observed fatigue life obtained from this model is included in Fig 43 along with dashed diagonal lines that represent factor of 1.5 and factor of 2 bounds as was shown for the SWT model. The majority of data was found to be clustered quite tightly about the ideal prediction (solid line) within a factor of 1.5. The tight clustering of data points about the ideal model demonstrates the good predictive power of the JV model in the current study and it has also been reported to provide good multiaxial fatigue life prediction in the case of extruded AZ31B [52], [86].

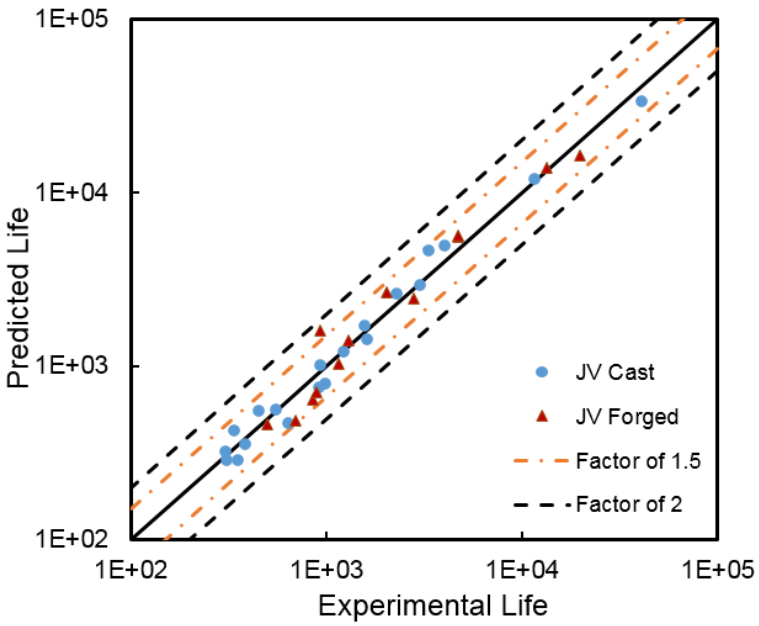

Fig 43: *Predicted fatigue life versus experimental fatigue life for as-cast and forged AZ31B using Jahed-Varvani fatigue model.*

4.4. Chapter Conclusions

Strain-controlled fatigue tests were performed on as-cast and cast followed by forged AZ31B Mg alloy in order to evaluate the effect of forging on the low cycle fatigue life of the alloy. From the above presented results, the following conclusions can be made.

- Dynamic recrystallization resulted in the occurrence of grain refinement in the forged alloy along with a development of a basal texture such that the basal planes were perpendicular to the forging direction.
- The as-cast condition displayed symmetric cyclic tension-compression deformation due to the random texture of the cast alloy whereas, the forged condition displayed substantial asymmetry due to the activation of $\{10\bar{1}2\}\langle 10\bar{1}1\rangle$ extension twinning in compression and subsequent detwinning followed by slip during tension.
- In general, the forged material displayed in overall improvement in low cycle fatigue life compared to the as-cast material attributed to the refined grain morphology, absence of casting defects, dissolution of intermetallics and texture modification.
- The strain-based SWT model and energy-based JV model both yielded good fatigue life prediction for both as-cast and forging conditions within the tested strain amplitudes.

Chapter 5: Determination of optimal forging parameters for AZ31B Mg alloy

The effect of processing temperature and pre-form condition on the final microstructure, quasi-static response, and stress-controlled fatigue behavior of closed-die forged AZ31B Mg alloy is investigated. The forging process was conducted on billets of cast as well as extruded AZ31B at temperatures of 250°C and 375°C and a forging rate of 20mm/s. Quasi-static tension tests as well as fully-reversed stress-controlled cyclic tests under total stress amplitudes of 120 to 160 MPa were performed on both the initial and final material conditions. The cast and forged material exhibited a neckless-type strong bimodal grain structure indicating incomplete dynamic recrystallization in addition to the development of a sharp basal texture at both forging temperatures. The extruded and forged material also exhibited recrystallization during forging, however the resulting degree of bimodality in the final grain morphology was far less pronounced. The obtained mechanical test results showed a strong influence of processing temperature and initial material condition on the mechanical response of the forged product. For a given starting condition (either cast or extruded) a lower forging temperature resulted in superior quasi-static and cyclic properties whereas for a given processing temperature, the extruded starting billet displayed better mechanical properties compared to its cast counterpart post-forging. An optimization function developed within the research group was employed to determine that extruded AZ31B forged at 250°C was considered to yield the best overall mechanical properties.

5.1. Experimental Details

5.1.1. Forging process and sample preparation

This study employed both as-cast and as-extruded AZ31B alloy. The as-received AZ31B material was machined into smaller cylindrical billets, 65 mm in length and 63.5 mm in diameter which were identical to those used in the open-die forging studies. As in the case of the open-die forging, the extracted billets were heated for 3 hours in a furnace to the selected forging temperature of either 250°C or 375°C prior to being placed in the hydraulic press. The forging press was installed with isothermally heated dies containing the cavity profile illustrated in Fig 44a. The cavity profile constrained material flow along all three directions (LD, RD and FD) during the forging process. The heated billet was forged in a single step with the overall forging direction aligned parallel to the radial direction of the billet (Fig 44a). The forging process was performed at an initial ram speed of 20

mm/s (the highest controllable speed of the press) with graphite used as a lubricant. The forging operation resulted in an "*I-beam*" shaped geometry with approximate dimensions as shown in Fig 44b, c. The finished forgings (Fig 45) were air-cooled back down to room temperature.

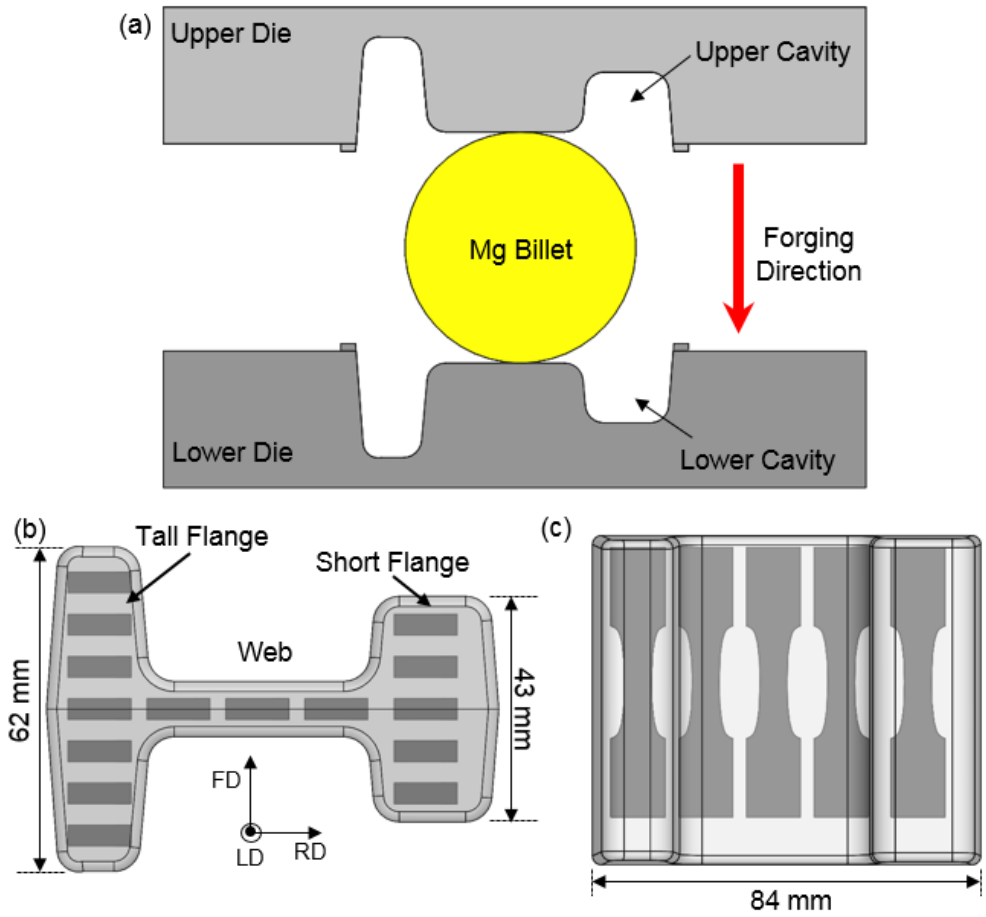

Fig 44: *Schematic of (a) die design and forging orientation, (b) view along the LD of the forging showing basic forging dimensions and specimen locations and (c) view along the FD showing more forging dimensions and specimen locations. Note, LD: Longitudinal Direction, RD: Radial Direction and FD: Forging Direction.*

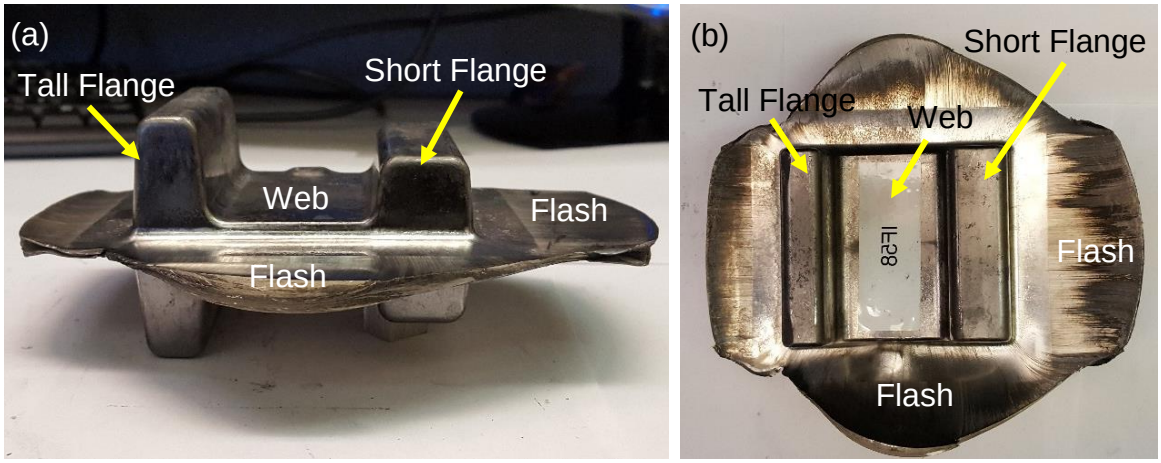

Fig 45: *Photographs of a finished forging processed at 375°C and starting with extruded AZ31B.*

5.1.2. Microstructure and texture analysis

In order to better characterize any in-homogeneity in the forging, the obtained I-beams were divided into three regions: *Tall Flange*, *Web*, and *Short Flange*. Specimens for microstructural analysis were extracted from each of these locations and from a depth of approximately 10 mm from the edge (Fig 46). These specimens were mounted using a two-part cold mount epoxy and were prepared as described in section 3.1.2.

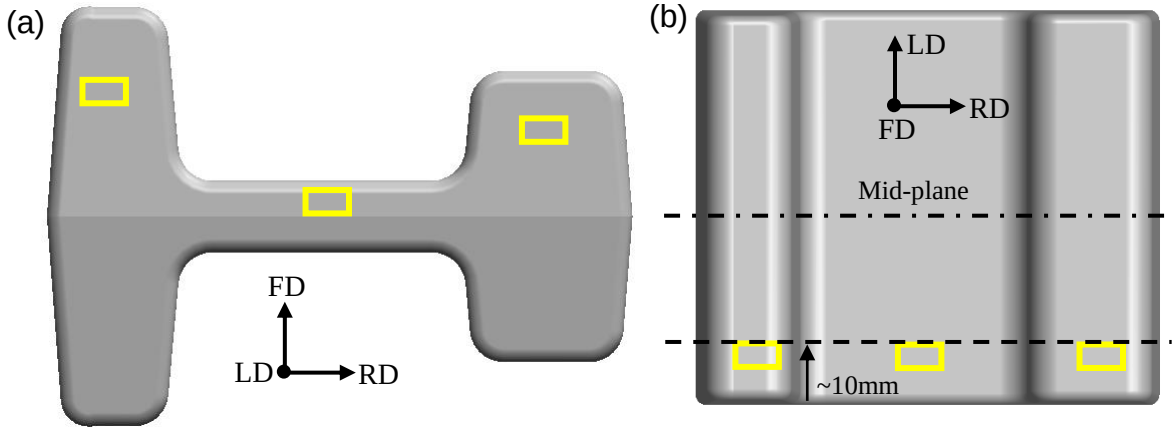

Fig 46: *Illustration of the sample locations (yellow rectangles) used for microstructure and texture analysis. Note that the surface closer to the mid-plane of the forging was prepared for observations.*

5.1.3. Mechanical testing

Superficial hardness measurements were performed using a United Tru-Blue II digital hardness tester equipped with a 1/16 inch steel ball indenter on a Rockwell 15T scale. Hardness measurements were made on a plane located approximately 10mm from the edge of the forging as illustrated in Fig 46b. As described in chapter 3, quasi-static tests were performed on an MTS 810

uniaxial load frame and strain was measured using the ARAMIS-3D DIC system. The quasi-static testing was performed in displacement control at a rate of 1mm/min. Fully-reversed stress-controlled cyclic testing (R_σ = -1) was performed using the same MTS 810 frame at stress amplitudes of 120MPa, 140MPa and 160MPa and at frequencies ranging from 1 to 20 Hz.

5.2. Results

5.2.1. Microstructure and texture evolution

The microstructure and texture measurements of the starting cast material have been presented in section 3.2.1. As stated therein, as-cast AZ31B demonstrated relatively large equiaxed grains with an average size of ~278 µm ±30 and was un-textured as was expected. In contrast, the microstructure and (0002) pole figure for the 63.5mm extrusion billet is shown in Fig 47. Microstructural observations indicated a non-homogeneous grain distribution with the center of the billet showing relatively fine grains with an average size of 12.2 µm ±1.9 (Fig 47a). The average grain size grew towards the surface of the billet where it increased almost fourfold to 46.8 µm ±7.2 (Fig 47c). Texture measurements indicated a typical extrusion texture with the basal planes parallel to the extrusion axis as illustrated schematically in (Fig 47d).

Optical micrographs obtained from the tall flange, web and short flange for the different forged conditions are included in Fig 48 through Fig 51. In comparison to the as-received microstructures (i.e. cast/extrusion), the forged material displayed a higher degree of inhomogeneity in grain size distribution. This inhomogeneity was more pronounced for the cast and forged conditions (Fig 48 and Fig 49) compared to the extruded and forged conditions (Fig 50 and Fig 51). Optical micrographs for cast AZ31B forged at 250°C are shown in Fig 48. The microstructure exhibits a strongly bimodal morphology with large deformed grains surrounded by finer neckless DRX grains. The average grain size of these DRX grains is approximately 3.9 µm ±2.1. The large deformed grains resemble the original cast microstructure (Fig 16) and suggests the occurrence of partial recrystallization during the forging process. Cast material forged at the higher temperature of 375°C (Fig 49) displayed a similar grain morphology compared to the lower temperature forging however, the average grain size of the DRX grains was larger at 4.4 µm ±1 and the intermetallics observed at the lower temperature were absent.

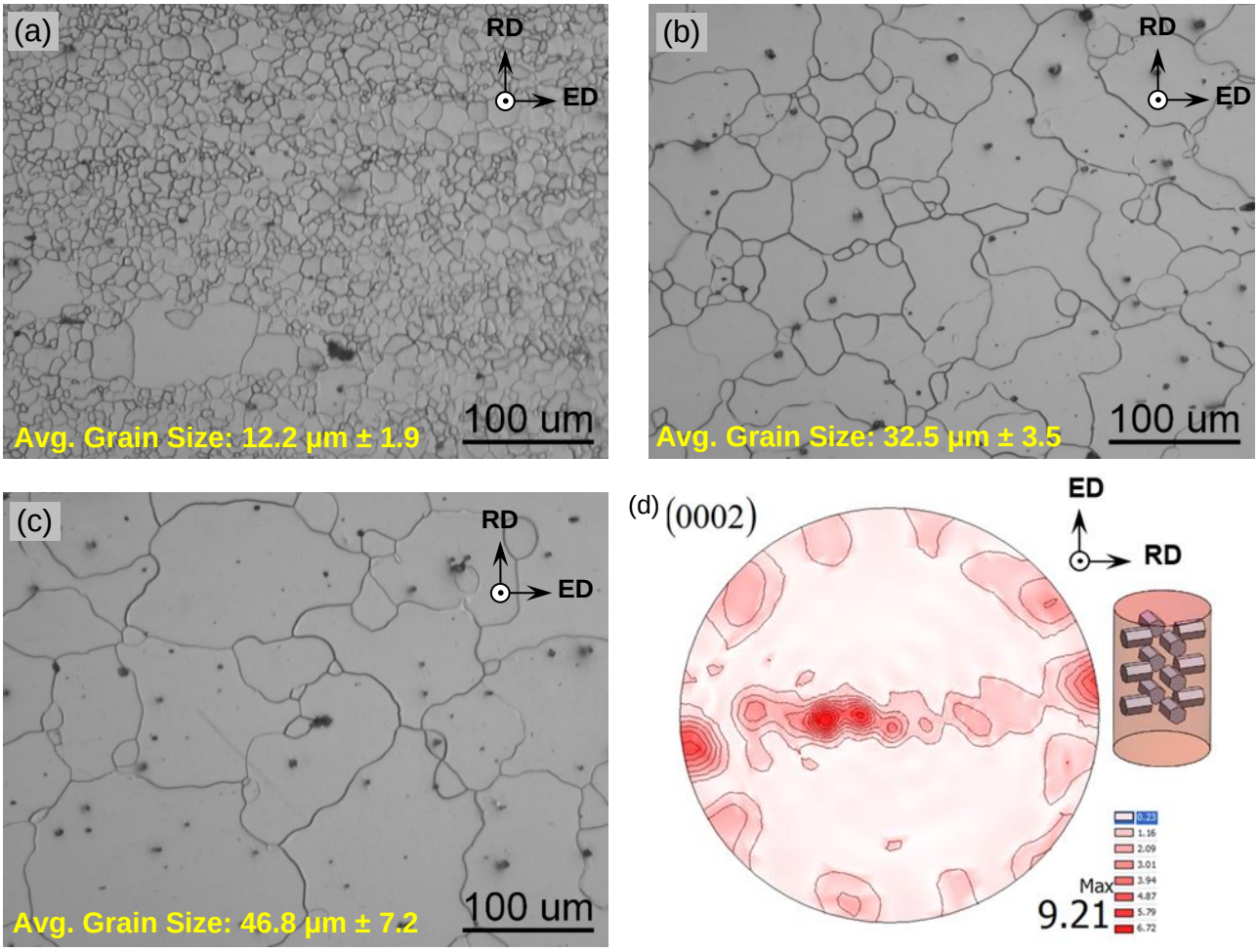

Fig 47: *Optical micrographs of the as-received extruded billet at (a) the billet center, (b) one half of the billet radius (~15.9mm), (c) outer edge of the billet (~31.8mm) and (d) (0002) pole figure for the extruded alloy with inset schematic of crystallographic orientation.*

The grain morphology for the extruded and forged material at both 250°C and 375°C was quite similar with average sizes of 9.9 µm ± 5.0 and 15.8 µm ± 7.5 respectively. As with the cast material, forging of the extruded material at both temperatures resulted in grain recrystallization, however due to the existing wrought nature of the starting extrusion, the grain size distribution was far less bimodal than in the cast and forged conditions. As such the grain size reported for the extruded and forged conditions represents the average overall grain size and not just that of the recrystallized grains.

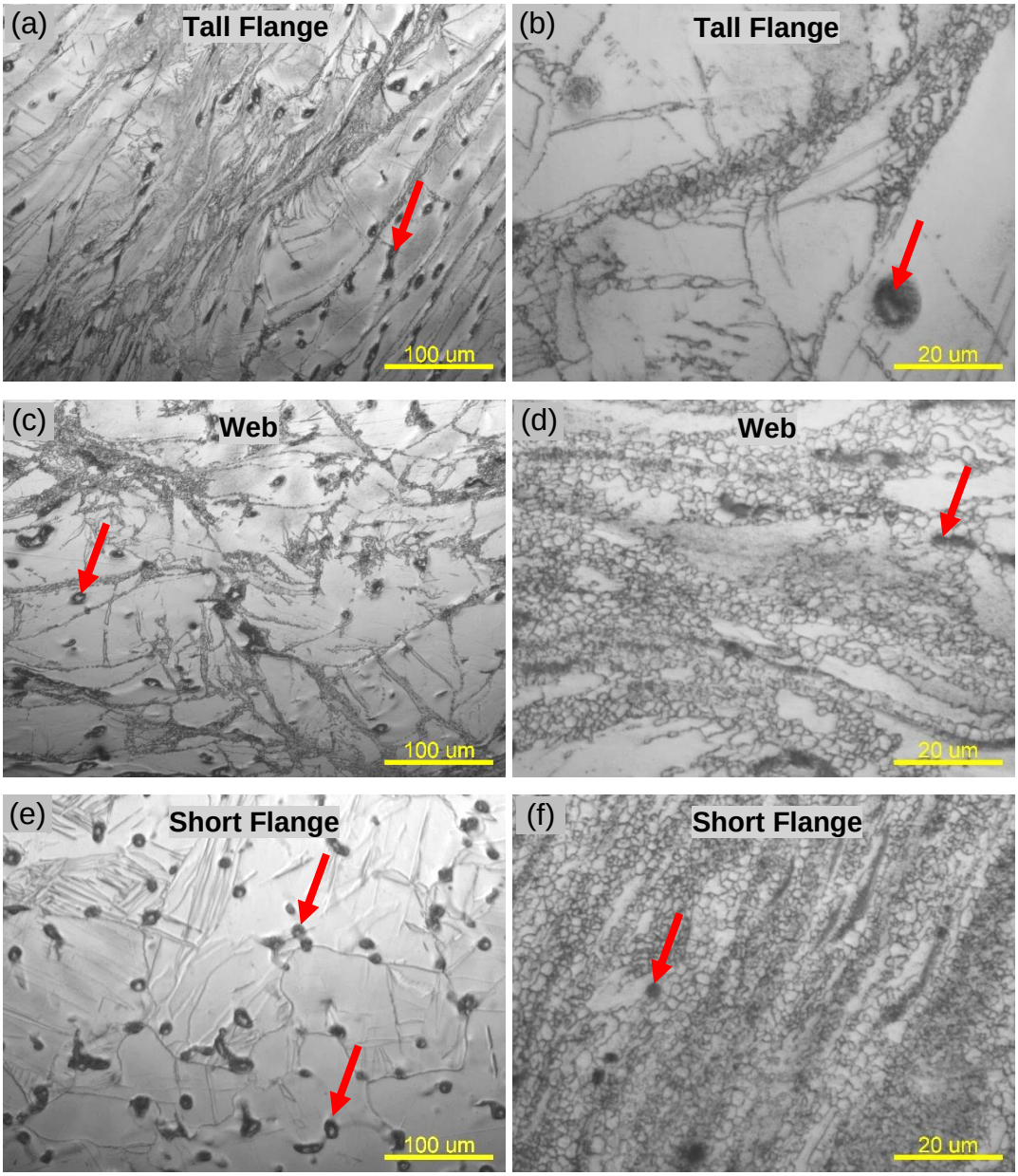

Fig 48: *Optical micrographs of cast AZ31B after forging at 250°C showing (a, b) the tall flange, (c, d) the web, and (e, f) the short flange. The red arrows indicate several examples of the presence of intermetallic particles.*

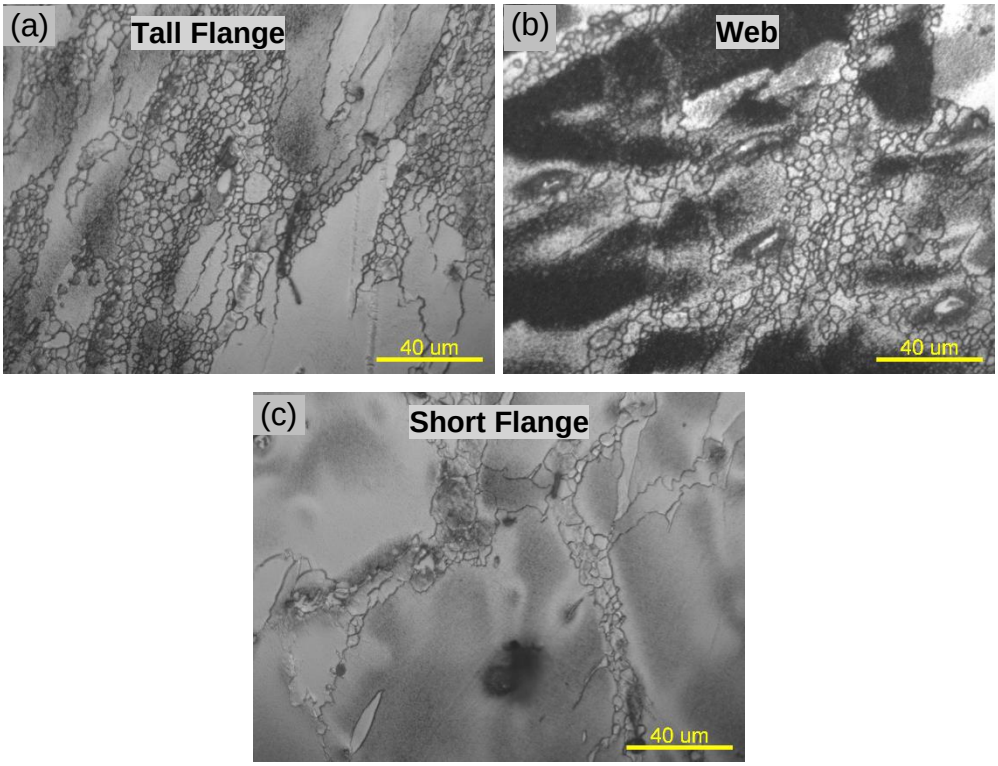

Fig 49: *Optical micrographs of cast AZ31B after forging at 375°C showing (a) the tall flange, (b) the web, and (c) the short flange.*

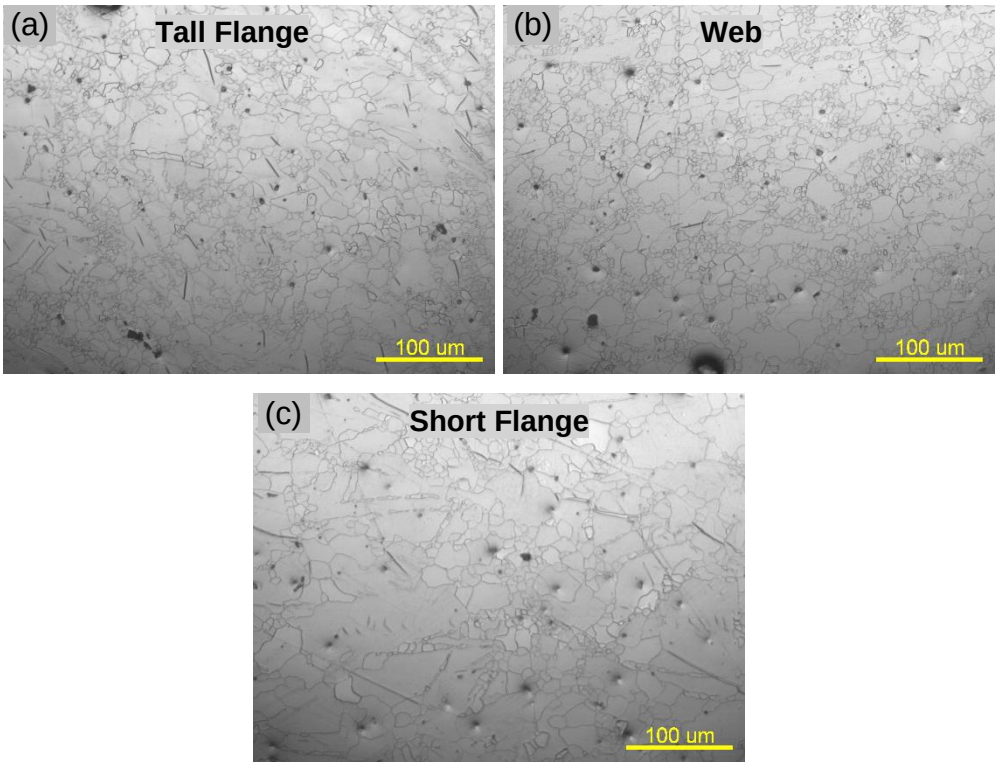

Fig 50: *Optical micrographs of extruded AZ31B after forging at 250°C showing (a) the tall flange, (b) the web, and (c) the short flange. Note that the dark spots are surface oxides developed after the etching process.*

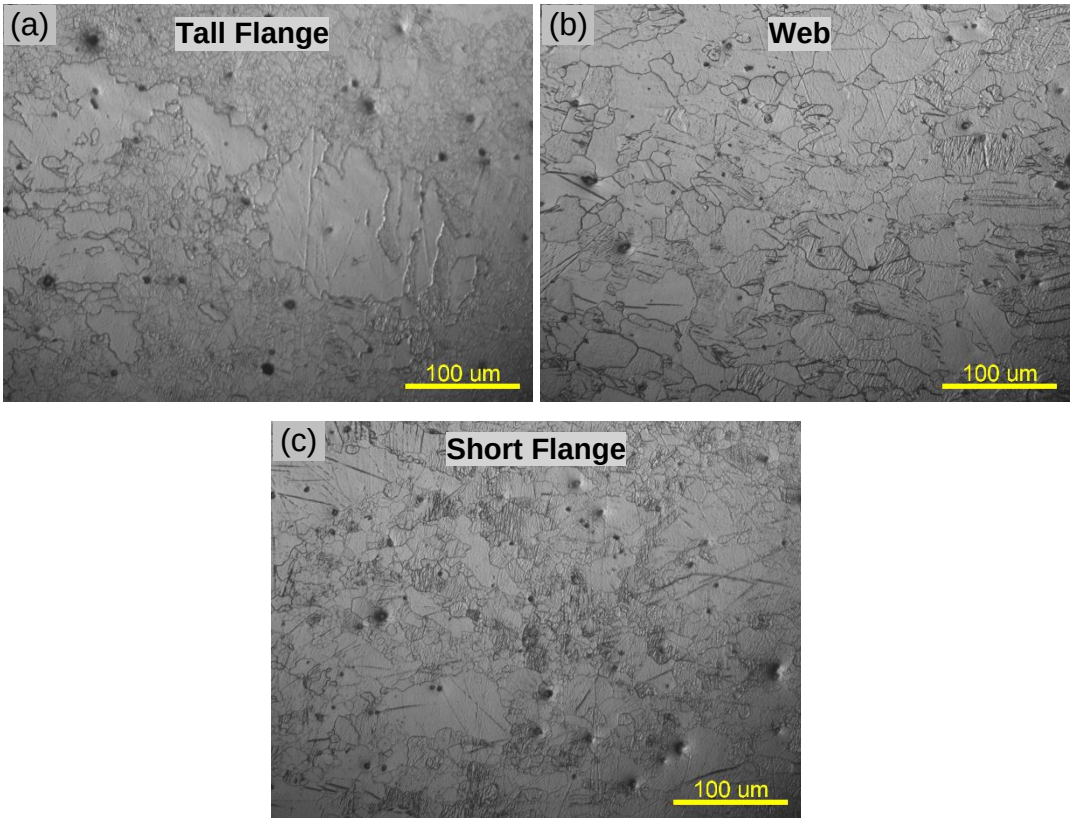

Fig 51: *Optical micrographs of extruded AZ31B after forging at 375°C showing (a) the tall flange, (b) the web, and (c) the short flange. Note that the dark spots are surface oxides developed after the etching process.*

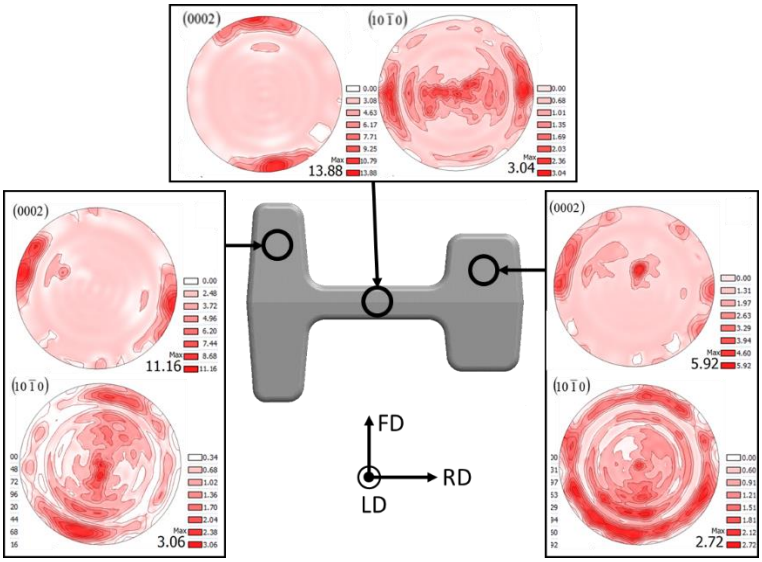

Fig 52: *Pole figures for cast and forged AZ31B at 250°C measured at the tall flange, the web, and the short flange.*

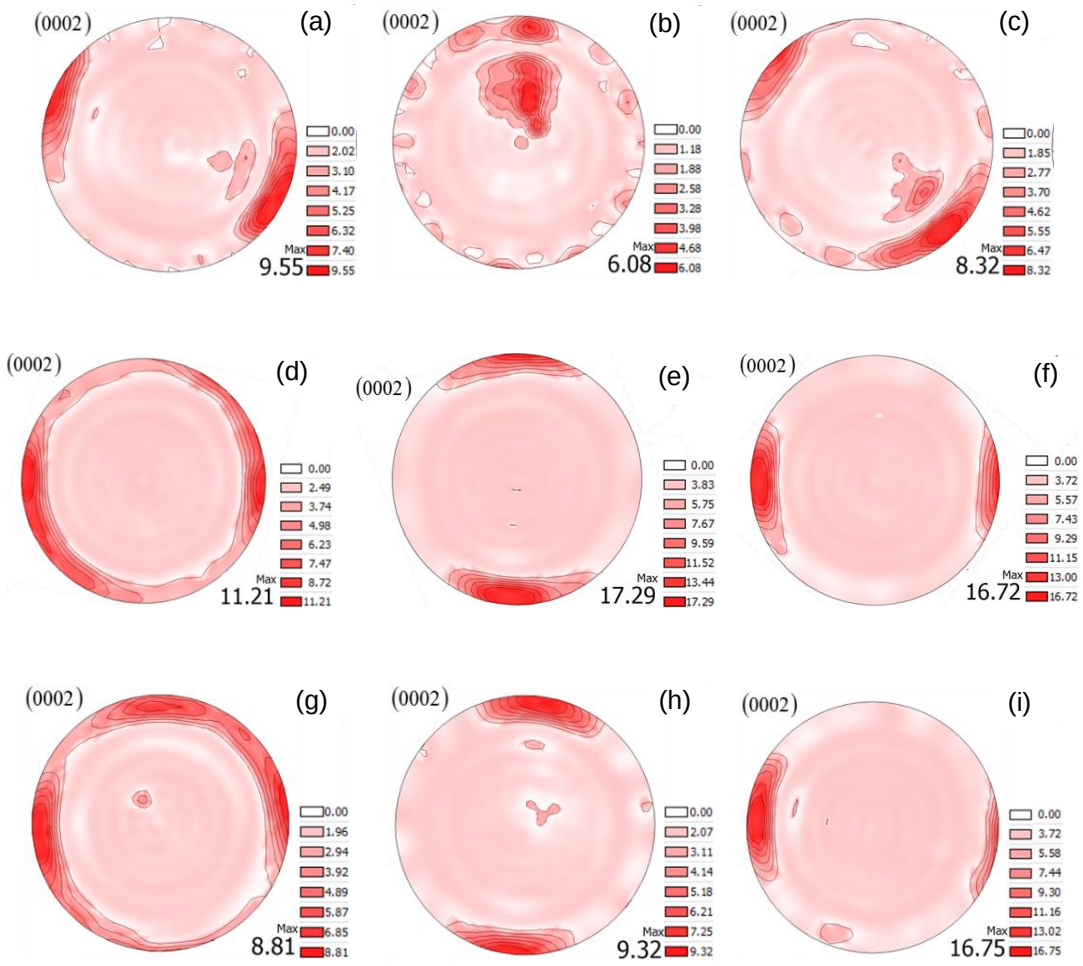

Fig 53: *(0002) pole figures for the closed-die forged AZ31B starting with (a, b, c) cast material forged at 375°C, (d, e, f) extruded material at 250°C, and (g, h, i) extruded material at 375°C measured at (a, d, g) the tall flange, (b, e, h) the web, and (c, f, i) the short flange.*

Pole figures measured at the three locations of interest using X-Ray diffraction are shown in Fig 52. For each of these locations (tall flange, web and short flange), it is observed that the c-axes have been reoriented to align roughly along the localized deformation direction. For example, the (0002) pole figures show c-axis orientation along the RD with an intensity of 11.16 MRD for the tall flange and along the FD with an intensity of 13.88 MRD for measurements made at the web. Very similar results were observed for the other forging conditions and are included in Fig 53. The mechanism responsible for this texture reorientation is thought to be the same as that described in chapter 3 viz. RDRX and will be discussed later. It should be noted that the short flange pole figure in Fig 52 and the web pole figure in Fig 53b suggests some degree of out-of-plane c-axis rotation (i.e. towards LD). This is thought to be due to texture measurements being made approximately 10 mm into the depth of the forging where a LD loading component arising from die constraints may

influence the final texture of the forging. Another point to note is the decrease in texture intensity with increasing forging temperature. For example, the intensity in the web of the extruded and forged material decreases from 17.29 MRD to 9.32 MRD when the forging temperature was increased from 250°C to 375°C. An explanation for this behavior will also be addressed later.

5.2.2. Hardness mapping

Superficial hardness intensity maps for the various forging conditions are included in Fig 54 on the same scale (Rockwell 15T).

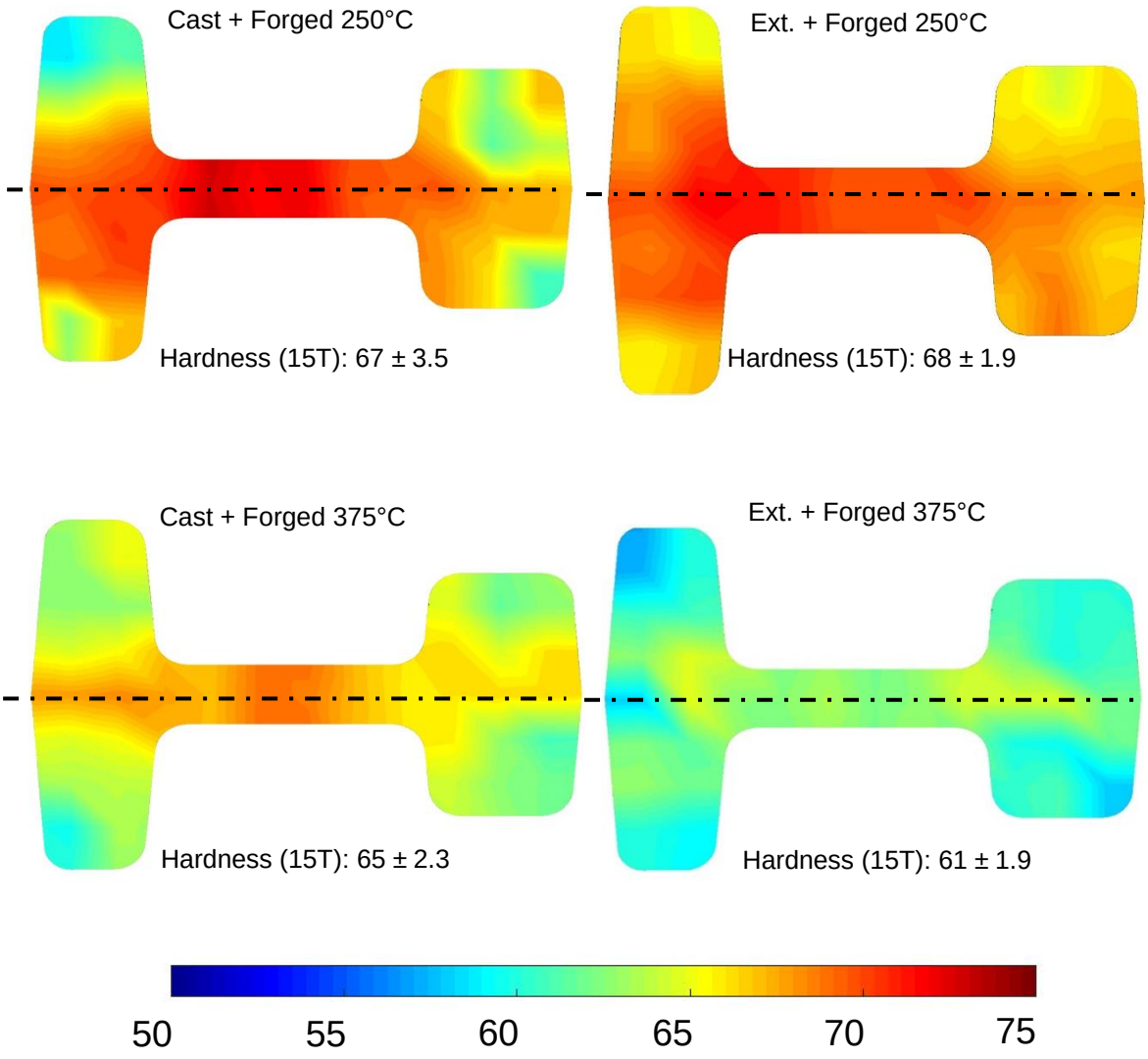

Fig 54: *Superficial hardness maps for the different forging conditions measured on a Rockwell 15T scale.*

As hardness is a measure of a materials resistance to plastic deformation, these hardness maps reveal several qualitative features about the different forging conditions. First, the hardness distribution is virtually symmetric about the parting line of the dies (dashed lines). Second, for the cast and forged material, the variance in measured hardness is higher than in the extruded and forged material. Lastly, the variation in the hardness values for the cast and forged material decreases, with increasing temperature. The differences in hardness variation with starting condition (i.e. cast or forged) as well as the decrease in hardness variation at the higher temperatures of the cast and forged material will be discussed in section 5.3.2.

5.2.3 Quasi-static behavior

Engineering stress-strain tension curves for the different forging conditions are shown in Fig 55 along with curves for as-cast and as-extruded AZ31B for reference. Note that the curves in Fig 55 were obtained from specimens extracted from the tall flange of the forgings. It is observed that the tensile curves for the forged material lie between those of the as-received cast and extruded materials; this was also observed for specimens extracted from the web and short flange of the forgings. Specifically, the cast material demonstrates the lowest strength, followed by the two cast and forged conditions, the extruded and forged conditions and finally the as-extruded condition.

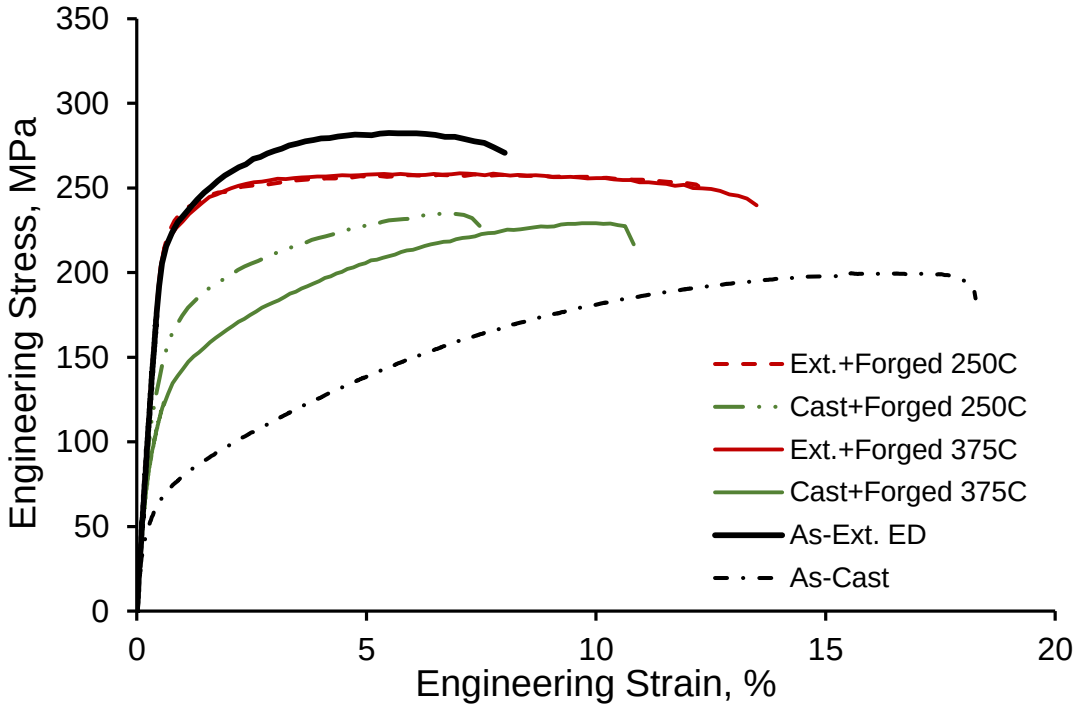

Fig 55: *Quasi-static tension curves for the different forged conditions. Tension curves for the as-cast and as-extruded conditions (loading along the extrusion direction) have also been included for reference.*

A comparison of the tensile curves for cast and forged, and extruded and forged AZ31B at 250°C are shown in Fig 56. It is obvious that the behavior of the material is location-dependent with the two flanges showing similar properties which are poorer than that of the web region. The discrepancy between the web and flanges is far more pronounced for the cast and forged condition and such a discrepancy was even observed in the higher temperature forgings (curves not shown).

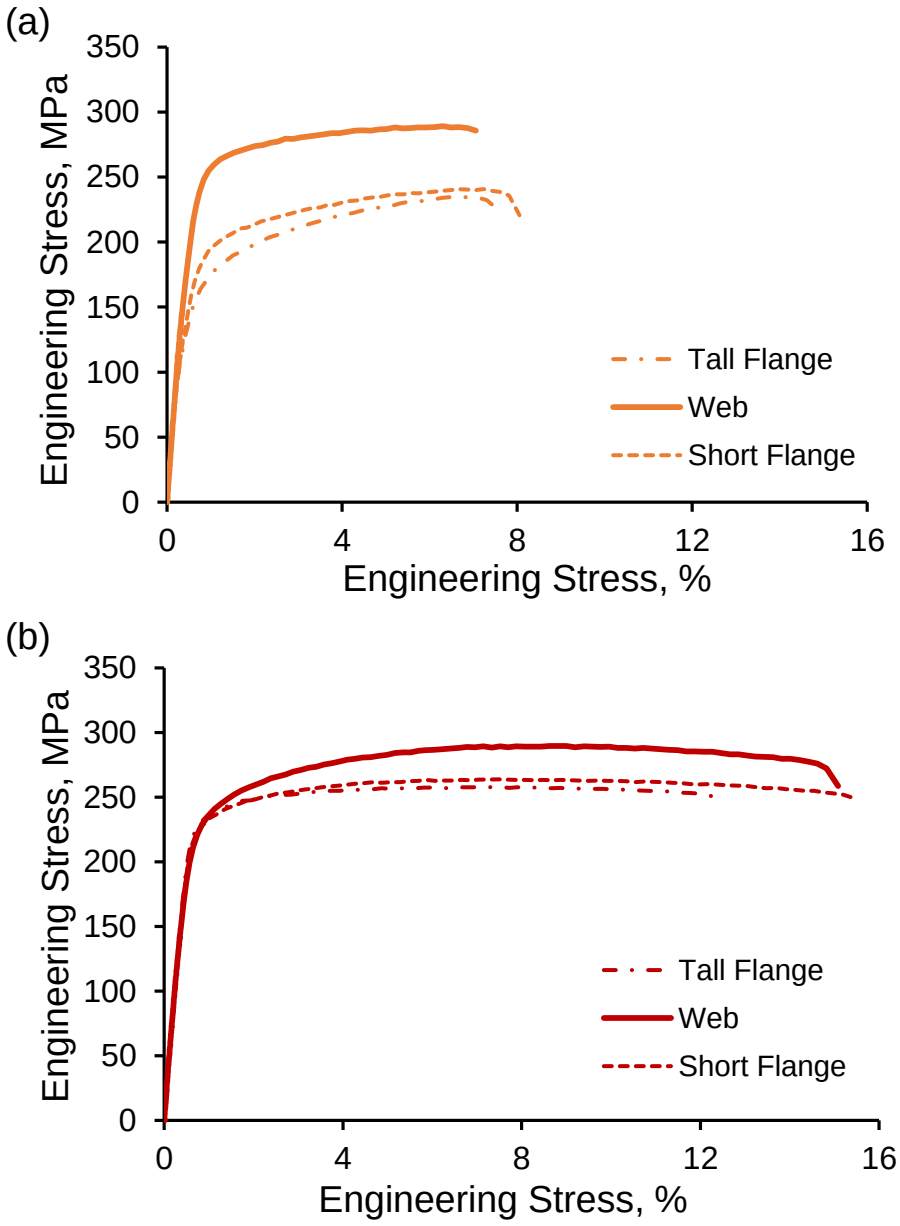

Fig 56: *Engineering stress versus strain tension curves for (a) cast and forged AZ31B at 250°C and (b) extruded and forged AZ31B at 250°C.*

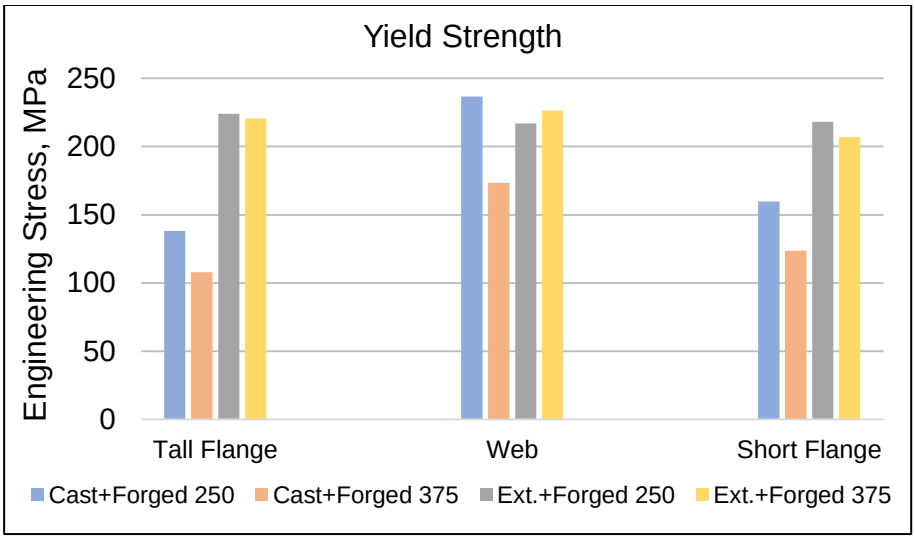

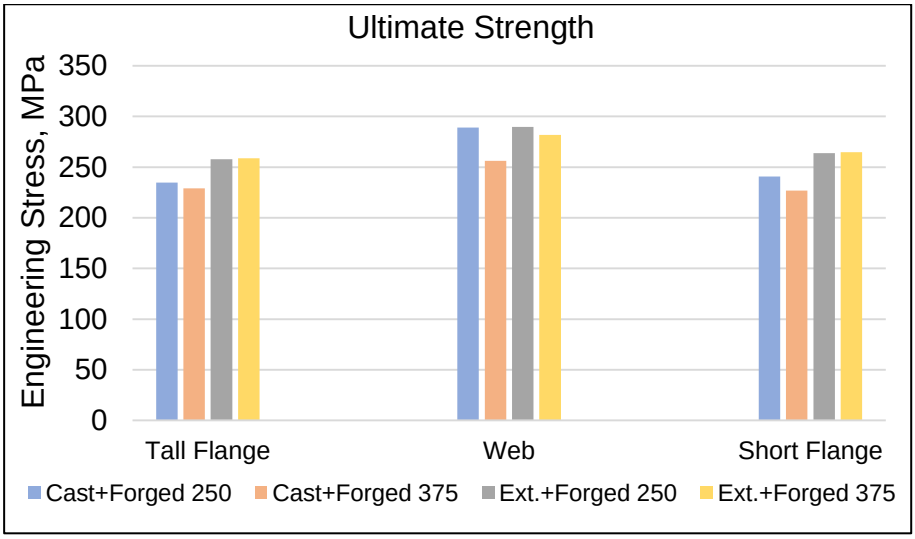

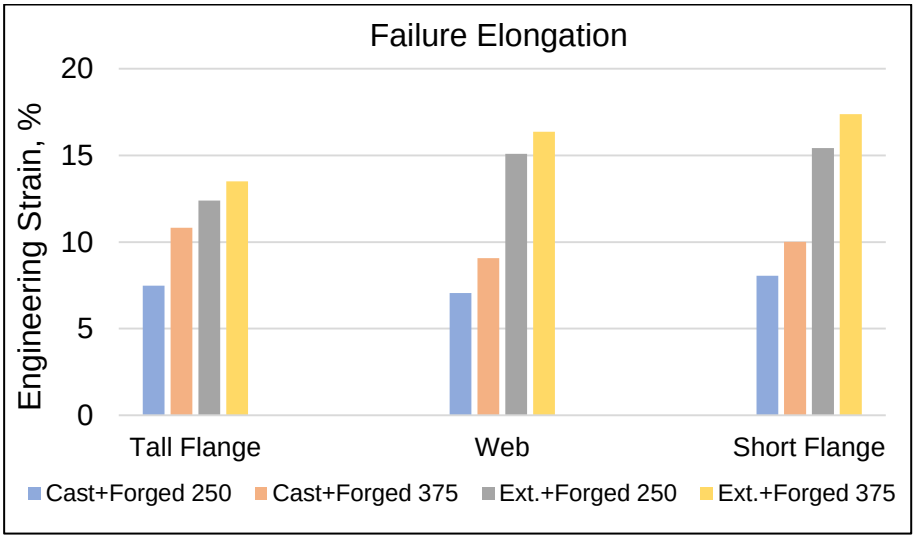

Fig 57: *Summary of the primary tensile properties obtained for the different closed die forged conditions.*

A summary of the primary tension properties (yield strength, ultimate tensile strength and failure elongation) for the different forging conditions included in Fig 57. From this figure, several observations may be made. Firstly, as alluded to by Fig 56, the web region of the forging exhibits higher yield and ultimate strengths compared to the two flanges. This spatial variation in the yield and ultimate strengths was much more pronounced for the two cast and forged conditions. Second, with a few exceptions, the cast and forged material exhibited poorer tensile properties (yield, ultimate strength, failure elongation) compared to their extruded and forged counterparts. Finally, the effect of forging temperature on the observed tension properties was far more pronounced for the cast and forged conditions compared to the extruded and forged conditions with a lower forging temperature generally resulting in higher strengths and lower failure elongations. A similar effect of processing temperature on the tensile behavior of wrought AZ31B alloy was noted in [41], [42].

5.2.4 Cyclic response

The plot of stress amplitude versus cycles to failure obtained during cyclic testing for the different forging conditions is illustrated in Fig 58 along with the results of the as-received alloy conditions for reference.

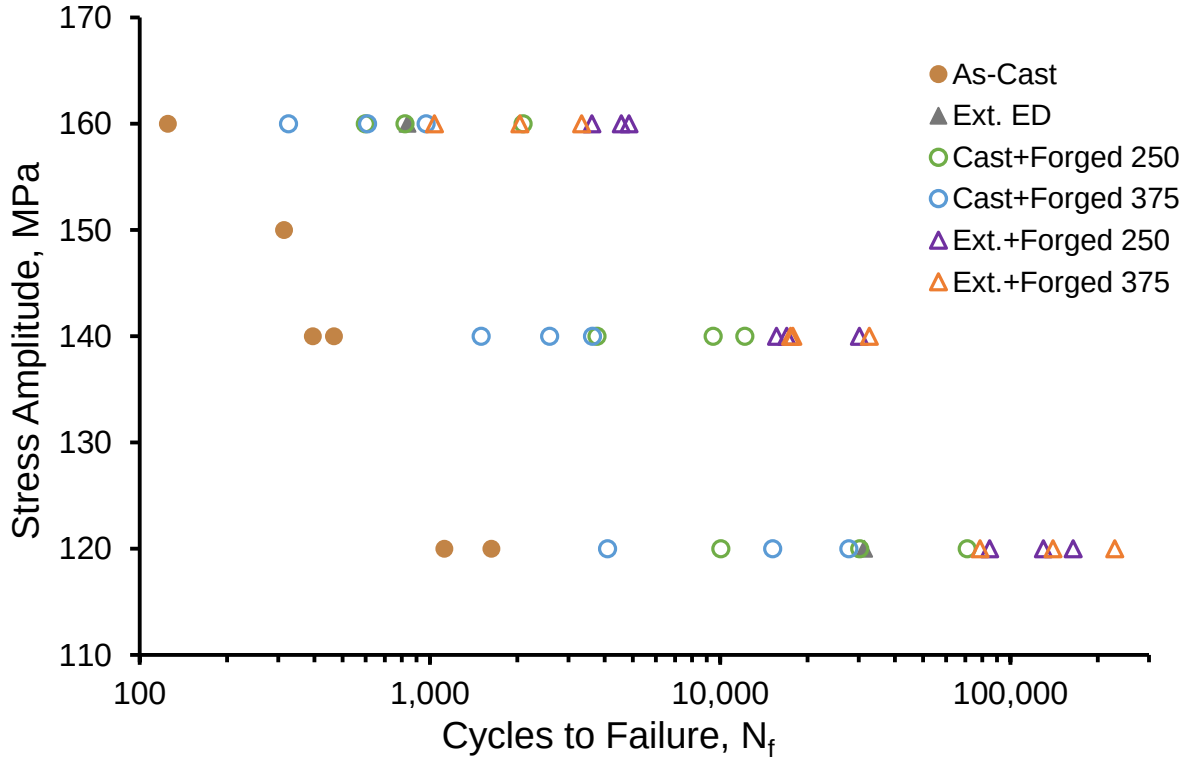

Fig 58: *Plot of stress amplitudes vs. cycles to failure for the different AZ31B conditions under consideration.*

The cyclic results generally reflected the trends observed in quasi-static testing with the as-cast condition displaying the poorest lives for the tested stress amplitudes. The cast and forged conditions showed a significant improvement compared to the as-cast alloy and were comparable to the as-extruded condition. It should be noted that the cast material forged at the lower temperature showed slightly improved life compared to the higher temperature forging. The extruded and forged conditions exhibited the best fatigue lives of all the tested conditions with the lower temperature forging exhibited slightly superior behavior especially at higher stress amplitudes. It is worth noting the large scatter in fatigue life at a given stress amplitude especially for the cast and forged conditions. Such a scatter is attributed to the inhomogeneity of microstructure in the flanges and the web, all three locations of which were tested at each stress amplitude.

The cyclic results for the forgings performed at 250°C have been redrawn in Fig 59 along with S-N curves obtained from literature for other thermo-mechanically processed AZ31 for further reference.

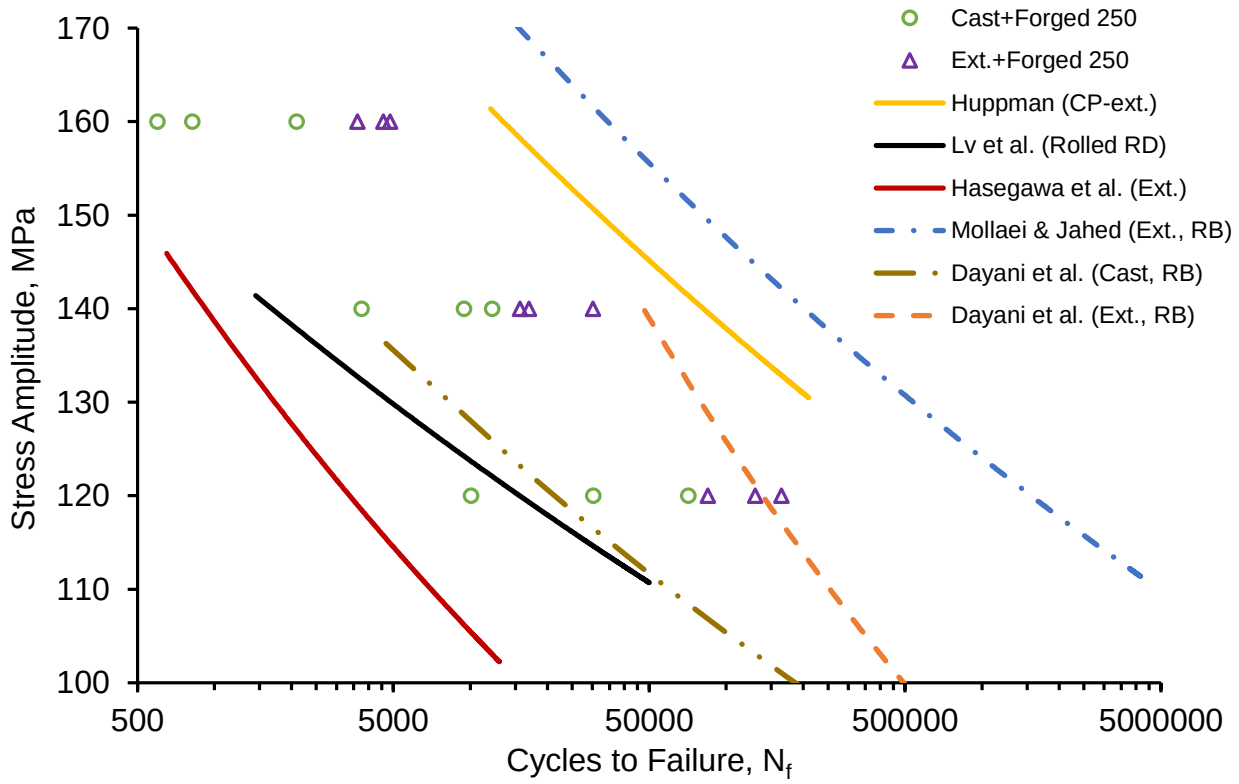

Fig 59: *Plot of stress amplitudes vs. cycles to failure for cast and forged and extruded and forged AZ31B at 250℃ S-N curves from literature have also been plotted for reference.*

Both forging conditions in this study display superior fatigue response compared to the rolled and extruded conditions investigated by Lv et al. [83] and Hasegawa et al. [90] respectively. However, extrusions against counter-pressure (CP) performed by Huppmann et al. [46] displayed higher fatigue lives than the current forgings. Note that while not directly comparable, results of rotating bending (RB) fatigue for cast [110] and extruded [110], [111] AZ31B are also included in Fig 59.

5.3. Discussion

5.3.1. Microstructure and Texture

For all the considered conditions, the forging process resulted in varying degrees of grain refinement and texture modification depending upon the processing temperature. For the starting cast alloy at the lower forging temperature (250°C), the post forging microstructure shows a considerable amount of neckless type DRX along the boundaries of un-recrystallized grains. These un-recrystallized grains also contained substantial β-phase $Mg_{17}Al_{12}$ as was observed in the starting cast material (section 3.2.1). Increasing the forging temperature to 375°C did appear to appreciably affect the average size of recrystallized gains (3.9 µm versus 4.4 µm) and the higher forging temperature was sufficient to send β-phase particles back into solution. For the starting extrusion billet, differences in the post-forging microstructure was far less pronounced with overall average grain sizes being statistically indistinguishable at a 5% significance level. However, considering just the tall and short flanges, the lower temperature forging (average grain size of 13.4 µm) shows a statistically greater degree of grain refinement compared to the forging at 375°C (average grain size of 28.9 µm).

As shown in Fig 52 and Fig 53, the texture evolution for all forging conditions was similar with a reorientation of the c-axis towards the localized deformation directions. However as mentioned in the results section, the intensity of the observed texture showed a dependency on the forging temperature with lower temperature forging generally resulting in a higher texture intensity. As stated previously, rotational dynamic recrystallization (RDRX) was considered to be responsible for overall texture modification during the forging process. However, based on the deformation temperature, the underlying mechanism of RDRX was reported to change [112]. For deformation at temperatures of 250°C – 350°C, RDRX is dominated by twin-formation. Specifically, for deformation within this temperature range, Sitdikov and Kaibyshev [112] reported that deformation twins are nucleated at grain boundaries. With continued deformation, secondary twins nucleate within primary twin

lamellae, resulting in subdivisions of the coarse primary twin lamellas. As deformation continues, recrystallization occurs in the regions of these twins. Such a recrystallization mechanism is thought to occur concurrently with more conventional continuous dynamic recrystallization (rotation from hard slip to stable slip directions) and was also reported by Chino and Mabuchi [35]. As forging temperature is increased above 350°C, deformation twinning gives way to slip due to easier activation of non-basal slip systems [14], [41]. It is thought that the more pronounced lattice rotations associated with deformation twins compared to non-basal slip is responsible the higher texture intensity observed for both the 250°C forging conditions. It is noteworthy however that the difference in intensity between the two forging temperatures while statistically significant is not vastly different as the upper forging temperatures is only 25°C above the reported cutoff for major deformation twin activation (350°C) [112].

5.3.2. Deformation Behaviour

As presented in Fig 54, the hardness maps for all the forging conditions were virtually symmetric about the parting line of the forging dies (dashed lines) which was expected given the axisymmetric nature of the starting billet and the geometry of the die cavities. The increased variation in the hardness values for the cast and forged material may be explained by the greater degree microstructural in-homogeneity for that material condition. When the indenter penetrates the material surface, the induced deformation results in the localized movement of dislocations in the material. Microstructural features such as grain boundaries and intermetallics, server as barriers to these dislocations, impeding their movement and resisting further deformation. Consequently, finer grained material may be expected to exhibit higher macro-hardness compared to their coarser grained counterparts according to a Hall-Petch type relationship [113], [114]. Since the cast and forged materials were characterized by large grains surrounded by much finer DRX grains, the locations where the indenter penetrates the coarser grains would yield lower hardness values than locations with the finer DRX grains. This is supported by the cold-spots observed in the tall- and short flanges of the cast and forged conditions where microstructural observations suggested larger proportion of coarse grains compared to the web (Fig 48 and Fig 49). Additionally, in regards to hardness of the cast and forged conditions, it is noticed that the variation in hardness values is lower for the higher temperature forging compared to that performed at the lower temperature (Fig 54) even though there was little statistical difference between average hardness values. As the texture between the two conditions remains largely unchanged (Fig 52 and Fig 53), it is thought that the increased

homogeneity of the higher temperature forging is a result of a higher degree of recrystallization resulting in a narrower overall grain size distribution and consequently hardness distribution [113], [115]. Such an increase in the overall fraction of recrystallized grains may be explained by a tendency for DRX to shift to lower activation strains as deformation temperature increases [116]–[118]. Lastly, it should be mentioned that both cast and extruded material displayed a decrease in average hardness when forged at 375°C. Such a result was also reported by Cai et al. [119] and Maksoud et al. [120] who attributed this decrease to DRX behavior at the different temperatures. However it is currently unclear why the extruded and forged material shows a higher sensitivity to temperature compared to the cast and forged condition.

A comparison of the tension stress-strain curves for the various forging conditions along with those of the starting pre-form material was presented in Fig 55. As discussed in previous chapters, the as-cast material displayed isotropic tensile behavior with a very low yield strength of approximately 56 MPa due to the presence of casting defects like porosity and activation of basal slip followed primarily by monotonic hardening behavior suggesting largely slip dominated plasticity throughout the test, albeit with several grains being favorably oriented for tensile twinning (chapter 3). The starting extruded material, exhibited the highest yield and ultimate strengths, but poorest ductility due to the unfavorable texture inhibiting basal slip and extension twinning, instead requiring the activation of the more brittle prismatic and pyramidal slip modes or compression twinning to accommodate plastic strains [31], [42], [80], [115]. The tensile curves for the various forged conditions lay between those of the as-cast and as-extruded conditions. It is seen that all forging conditions showed a remarkable increase in strength compared to the cast material with the two extruded and forged conditions displaying almost identical curves. Specifically, the two cast and forged conditions exhibited yield strengths increased by a factor of 3.2 times and 2.4 times that of the as-cast condition for forging at low and high temperatures respectively. However this increase in strength came at the expense of ductility with both cast and forged conditions exhibiting considerably lower failure elongations compared to the starting cast alloy. The reason for this decrease in ductility is thought to be twofold: (i) the considerably finer DRX grains in the cast and forged alloys would provide increased barriers to dislocation motion compared to the very coarse as-cast condition. The increased impedance to dislocation motion would contribute to increased strength and reduced ductility of the forging [121] and (ii) The forging process resulted in the development of a relatively strong texture which increased inhibition of basal slip and extension twinning and therefore decreased

ductility compared to the starting cast material. Texture evolution is also thought to be responsible for the virtually unchanged yield strength (-0.9%) but significant increase in ductility (by ~ 72% to 89%) of the extruded and forged conditions compared to the as-extruded material. To be more specific, forging weakened the intense extrusion texture increasing the propensity for basal slip while additional grain refinement maintained the majority of the strength of this forging condition.

It is noteworthy from Fig 56 and Fig 57 that the tensile behaviors for the tall and short flanges are quite similar whereas that for the web show higher strengths with this difference being far more pronounced in the case of the cast and forged conditions. This variation in tensile properties may be explained by the more severe strain accumulation in the web region as a consequence of the starting billet shape and die design resulting in a more refined microstructure and stronger texture in the web section. The increased spatial inhomogeneity between the cast- and extruded-and forged conditions is attributed to the more significant microstructural refinement that was observed in the cast and forged condition.

The cyclic results (Fig 58) for the various forging conditions were similar to those obtained during quasi-static tension with the cast material displaying the poorest fatigue lives, followed by the cast and forged conditions and finally the extruded and forged conditions which exhibited fatigue lives that were at least an order of magnitude improved over the cast condition. It is worth noting that the closed-die forgings exhibit a fair degree of scatter in the fatigue life for the same stress amplitude and this scatter is ascribed to microstructural variations in the different sections of the forgings (tall flange, short flange and web). The reason for the increase in the fatigue life of the forged alloys is thought to be two-fold: i) due to the general strengthening of the material which delays crack initiation and ii) effect of grain refinement and texture modification on the crack growth rate. In regards to the strengthening effect, a stronger forged material can be expected to exhibit substantially reduced gross plastic deformation during cyclic loading compared a weaker material condition. As the process of fatigue crack initiation is related to the accumulation of damage, i.e., irreversible plastic deformation, the lower overall plastic strain induced in a stronger forged material for a given stress amplitude increases the cycles required to initiate a fatigue crack [84]. Once a fatigue crack nucleates, it propagates through the material with every additional cycle. The large uniform grains with low grain boundary density in the cast alloy provide relatively little resistance to this crack propagation. In contrast, the very fine grains observed in the DRX regions of the forging would serve to lower crack

growth rate and increase overall life [9], [47], [98]. Consequently, the considerably finer overall grain morphology of the extruded and forged conditions should increase the propagation life of these alloy conditions compared to the far more bimodal morphology of the cast and forged conditions. It is worth reiterating that some studies have suggested that surface roughness due to extension twinning along the crack path also delay crack growth due to roughness induced crack closure mechanism [99]. Such a mechanism may also aid in the overall improvement of the fatigue life observed in the textured closed-die forged material.

5.3.3. Selection of optimal forging conditions

The fatigue critical component considered in this project (a front lower control arm) was subject to a set of proprietary mechanical requirements that specified limits on total defections, static strengths and minimum fatigue performance. Note that for confidentiality purposes, specific details regarding the mechanical requirements have been omitted from this document. In order to select an optimal forging condition for AZ31B to meet these mechanical requirements, an optimization function was developed within the research group [122]. The general form of the optimization function is illustrated by Eq. (12).

$$\boldsymbol{\Phi = 0.5\varphi_1 + 0.4\varphi_2 + 0.1\varphi_3} \qquad (12)$$

Where φ_1, φ_2 and φ_3 are parameters that account for the quasi-static properties, cyclic response and spatial homogeneity of the forgings, respectively. The coefficients attached to each of these parameters represent their perceived importance given the provided design requirements.

The quasi-static parameter of Eq. 12 (φ_1) is defined as,

$$\boldsymbol{\varphi_1 = 0.5\frac{S_y^T}{S_{y_{MAX}}^T} + 0.5\frac{E^T}{E_{MAX}^T}} \qquad (13)$$

Where S_y^T and E^T are the tensile yield strength and total strain energy dissipated under 4.5% plastic strain respectively. The 4.5% plastic strain metric was selected based on a provided mechanical requirement. Note that each term is normalized by their maximum value obtained from among all the forging conditions and each term is weighted equally. An illustration of the quantities comprising Eq. 13 is shown in Fig 60a.

The cyclic parameter φ_2 is defined as,

$$\boldsymbol{\varphi_2 = 0.65\frac{\sigma_f'}{\sigma_{f_{MAX}}'} + 0.35\frac{b_{max}-b}{b_{max}-b_{min}}} \qquad (14)$$

Where σ_f' and b are the Basquin parameters representing the intercept and slope of the stress-life curves. Once again, each term is normalized against its maximum and or minimum values with more importance being placed on the intercept term (i.e. on low-cycle response). As before, an illustration of the Basquin parameters is included in Fig 60b.

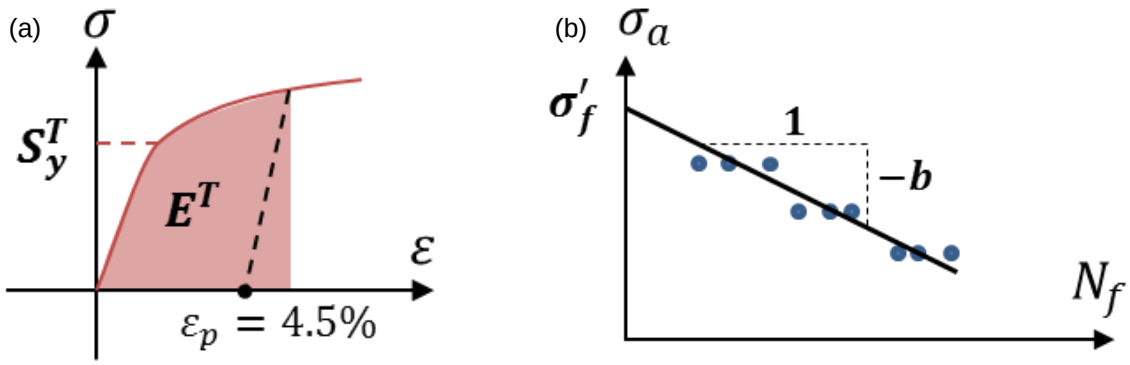

Fig 60: *Illustration of the input parameters used to determine optimal forging parameters.*

The spatial homogeneity parameter φ_3 is based on the variation in superficial hardness values illustrated in Fig 54 and is defined as,

$$\varphi_3 = \frac{H_{max}-H}{H_{max}-H_{min}} \qquad (15)$$

In the above equation, H is the standard deviation of the hardness in the forging cross-section with H_{max} and H_{min} being the extreme values of the standard deviation across all forging conditions.

A summary plot each of the optimization parameters versus the starting billet condition and forging temperature is illustrated in Fig 61 and the values of the various inputs of the optimization function are summarized in Table 7.

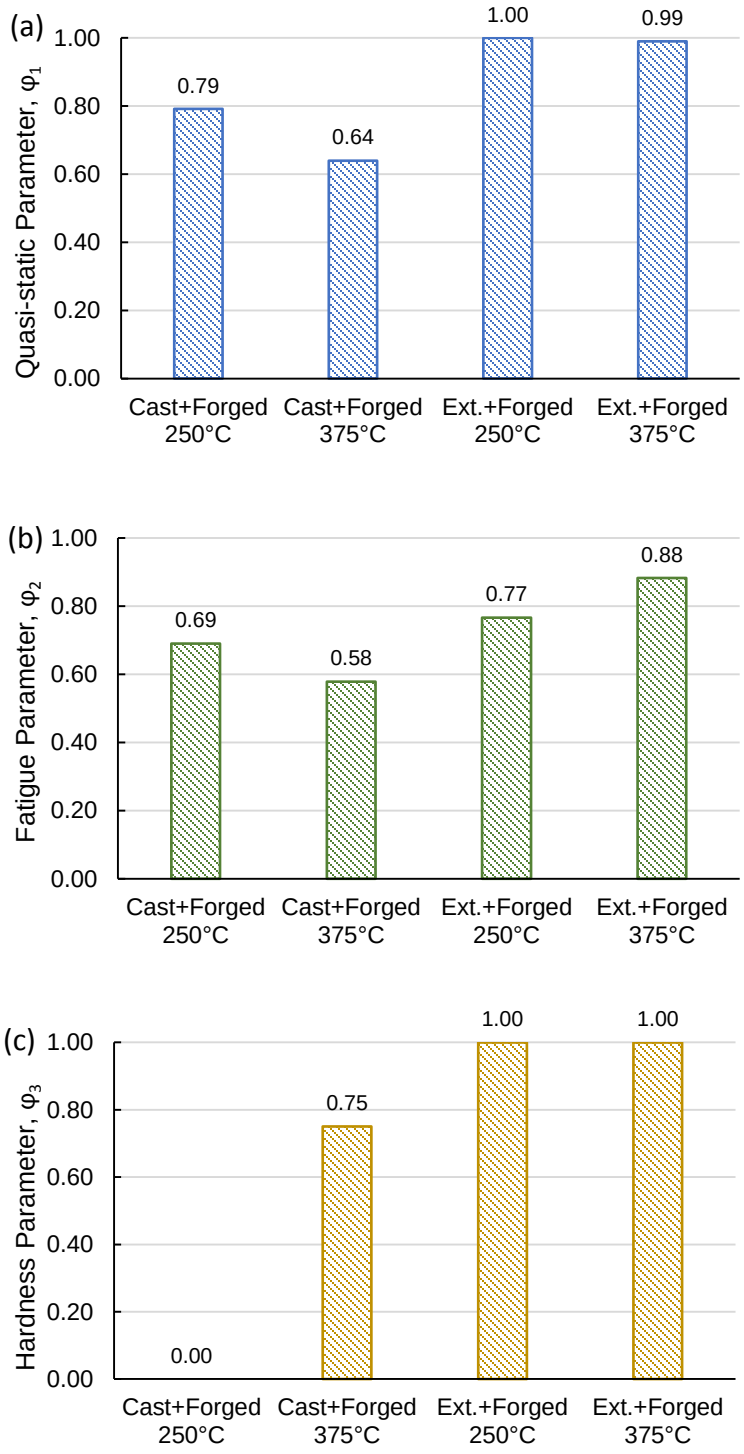

Fig 61: *Plots for the components of the proposed optimization function showing the values obtained for (a) the quasi-static component, (b) fatigue component and (c) the hardness component.*

Table 7: *Summary of inputs used in the proposed optimization function.*

	S_y^T (MPa)	E^T (MJ/m^3)	σ_f' (MPa)	b	H
Cast & Forged 250°C	178	11.02	297	0.087	3.5
Cast & Forged 375°C	135	9.15	293	0.095	2.3
Ext. & Forged 250°C	220	12.17	329	0.086	1.9
Ext. & Forged 375°C	218	12.04	270	0.068	1.9

The summary of the final optimization parameter (Φ) is included in Fig 62 form where it can be seen that a starting extrusion billet forged at 375°C appears to result in the most desirable mechanical properties.

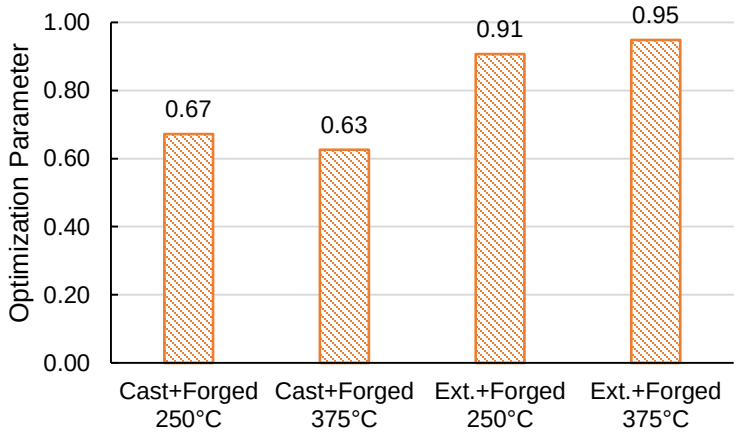

Fig 62: *Bar plot of the final objective function for closed-die forged AZ31B.*

However, a careful review of the optimization function indicates that the material with the highest values of yield strength (S_y^T), strain energy (E^T) and fatigue strength coefficient (σ_f') and the lowest values of Basquin slope (b) and standard deviations (H) should be optimal. Amongst all the forging conditions, the extruded material forged at 250°C satisfies all these requirements with the exception of the Basquin slope which was at a minimum for the extruded material forged at the higher temperature. Examining the raw stress amplitude versus life data for the two extruded and forged conditions (Fig 63) indicates two data points (black arrows) that are responsible for this shallower slope. These two data points for the extruded and forged condition at 375°C were obtained for specimens in slightly different locations than those of the other forging conditions due to experimental errors that resulted in the loss of some specimens. Consequently, it is believed that these two tests were performed on samples with slightly different thermo-mechanical histories compared to the other conditions resulting in improved lower amplitude fatigue lives and therefore an artificially reduced Basquin slope.

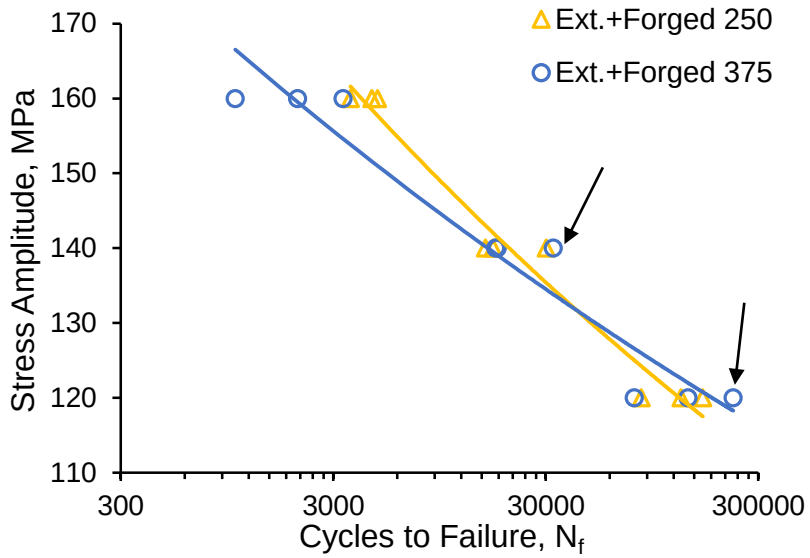

Fig 63: *Plot of stress amplitudes vs. cycles to failure for extruded and forged AZ31B.*

Accounting for this potential source of experimental error and considering the higher importance placed on the low-cycle fatigue performance as well on static strength, the output of the objective function was over-ridden and extruded AZ31B forged at 250°C was considered to possess optimal mechanical properties for the desired application. Note that the difference in the final optimization parameter (Φ) for the two conditions deviated by only ~4% considering all the original data.

5.4. Chapter conclusions

AZ31B under extrusion and cast conditions was isothermally forged at two different temperatures. Surface hardness, quasi-static tension and stress-controlled fatigue tests were performed on specimens extracted from each forging condition. The results of the testing lead to the following conclusions:

- Closed-die forging at both temperatures and for both cast and extruded conditions resulted in a partly recrystallized microstructure and a change in texture such that c-axes were reoriented to lie parallel to the localized deformation direction.
- Superficial hardness mapping suggested inhomogeneous strain distribution during forging with higher hardness values being observed in the web compared to the flanges.
    - The variance in hardness values was higher for the cast and forged conditions with the variation decreasing with higher forging temperature.

- Quasi-static tension tests confirmed the inhomogeneity suggested by the superficial hardness measurements with the web region exhibiting higher strengths compared to the two flange regions.
    - The difference between the tensile curves for the flanges and the web was much more pronounced for the cast and forged conditions, and for both starting conditions (cast/extruded), the discrepancy decreased with increasing forging temperature.
- Similar to the quasi-static results, cyclic tests indicated that the cast and forged conditions exhibited a remarkable improvement in fatigue performance compared to the starting cast material.
    - Both the extruded and forged conditions displayed superior fatigue response compared to the cast and forged conditions.
    - Between the two extruded and forged conditions, the lower temperature forging exhibited superior fatigue behavior.
- An optimization function was employed to identify the optimal forging condition based on a set of provided mechanical requirements.
    - Considering this optimization function and accounting for experimental error, extruded AZ31B forging at 250°C was found to yield the best static and cyclic mechanical properties.

Chapter 6: Characterization of cyclic axial, shear and multi-axial behavior of low temperature closed-die forged AZ31B

Extruded AZ31B was close-die forged at 250°C which was previously determined to result in the most desirable room temperature mechanical properties. Quasi-static tension and shear tests in addition to cyclic axial and cyclic shear tests were also performed to characterize the uniaxial cyclic response of the finished forgings. The cyclic axial behavior of the forging was superior to the starting extruded material while the cyclic shear behavior was comparable to low cycle behavior of extruded AZ31B in literature although it exhibited superior high cycle shear response compared to the conditions in literature. Multi-axial fatigue tests revealed an increase in cyclic hardening as a result of non-proportionality however, overall fatigue life showed only a weak sensitivity of phase difference. A modified SWT model and Jahed-Varvani (JV) model were developed using the uniaxial cyclic test results. The modified SWT model was found to provide good life prediction for all the tested multi-axial load cases. The multi-axial formulation of the JV model yields good life predictions for in-phase and 45° out-of-phase multi-axial scenarios but slightly over-predicts fatigue life for certain 90° out-of-phase loading cases.

6.1. Experimental Details

6.1.1. Forging Process and Sample Extraction

Based on the results of the optimal forging selection presented in chapter 5, extruded AZ31B was close-die forged at 250°C for further mechanical characterization. In total, nine such "*optimal*" forgings were produced for evaluation. The details of the forging process were identical to those outlined in section 5.1.1 and a photograph of the finished forgings is included in Fig 64.

Smooth dog-bone specimens were extracted from the two flanges of the forgings (Fig 65a) and used for quasi-static and cyclic axial tests. The geometry of these specimens was identical to that presented in Fig 27a. Due to the geometric limitation of the forging width, standard tubular shear specimens could not be extracted. Therefore a new thin-walled tubular specimen geometry was developed for quasi-static and cyclic shear testing under the guidance of the ASTM E2207 specification. To account of the reduced specimen length, steel inserts were used to prevent excessive deformation of the grip section as well as to prevent jaw "*chatter*" during cyclic testing. The sample

extraction locations and geometry for the tubular specimens are illustrated in Fig 65 b, c, and a photograph of the steel inserts is included in Fig 66.

Fig 64: *Photographs of extruded AZ31B closed-die forged at 250°C.*

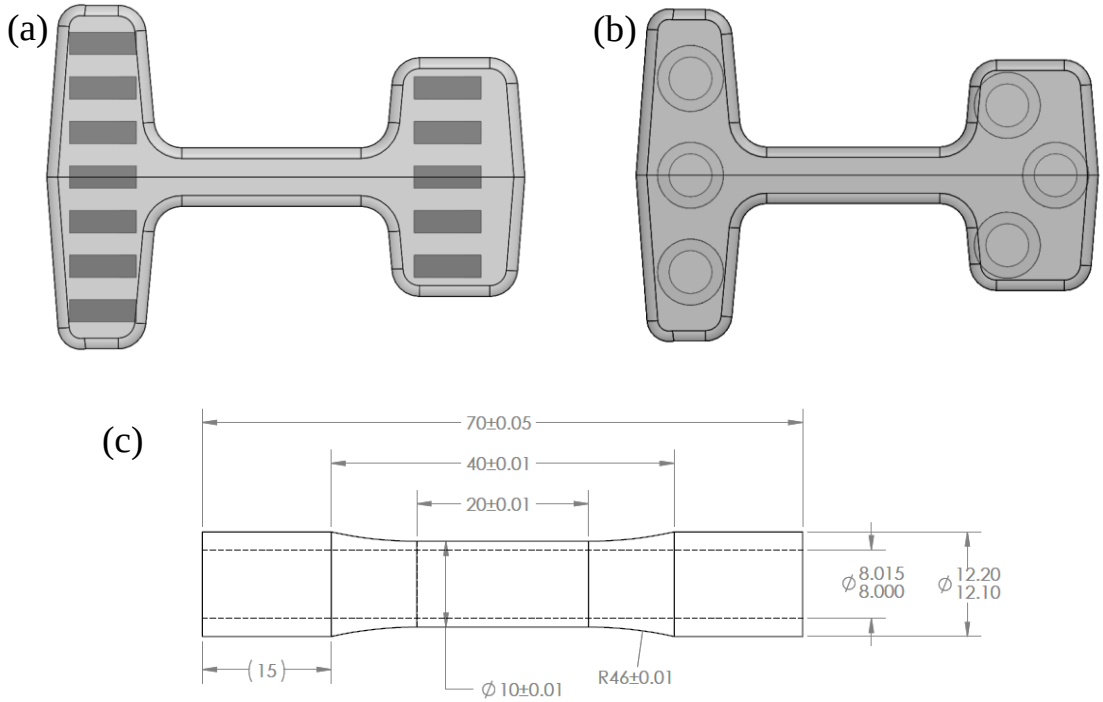

Fig 65: *Illustration of sample extraction locations for (a) axial tests and (b) shear tests as well as (c) geometry of the tubular shear specimens.*

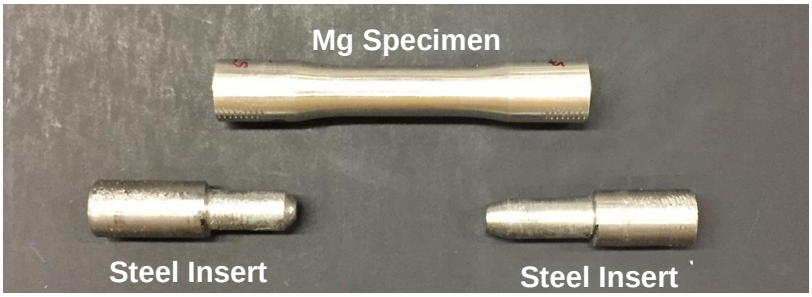

Fig 66: *Photograph of the steel inserts used along with the newly developed thin walled tubular specimens.*

6.1.2. Mechanical Testing

All mechanical tests were performed on an Instron 8874 bi-axial load frame. For uniaxial tests, the second axis of the load frame was set to maintain zero load/torque. Quasi-static tension and shear tests were performed at a displacement rates of 1 mm/min and 12 deg/min respectively with axial and shear strains being measured using DIC. For cyclic axial tests, five total strain amplitudes ($\Delta\varepsilon/2$) ranging from 0.35% to 0.9% were tested with four tests being performed at each amplitude. Strain was monitored and controlled using an Instron uniaxial extensometer with a gauge length of 10 mm. This extensometer was secured to the specimen using elastic bands and well as the same adhesive described in section 4.1.2. Cyclic shear tests were performed at total shear strain amplitudes ($\Delta\gamma/2$) ranging from 0.3% to 1.0% with three tests being performed at each amplitude. Shear strain was monitored and controlled using an Epsilon bi-axial extensometer with a gauge length of 20 mm. The surface of the specimen was prepared with an acrylic based coating to ensure the extensometer was securely affixed to the specimen surface. For tests extending into the high cycle regime (>10^4 cycles), the tests were paused after any cyclic hardening stabilized and the test was continued under torque control up to failure or until runout (>10^7 cycles).

Multi-axial tests were performed for three phase differences between the axial and shear strain waveforms: 0°/in-phase, 45° and 90°. Under the in-phase strain path (Fig 67b), both axial and shear peak strains have the same sign and are achieved simultaneously. In Fig 67c the shear strain leads the axial strain by 45° resulting in a strain path resembling a rotated ellipse in $\Delta\varepsilon/2 - \Delta\gamma/2$ strain space. Fig 67d illustrates the 90° out-of-phase path where the peak axial/shear strain is achieved while the strain along the other axis is zero. For each phase difference, two levels of axial strain amplitude (0.4% and 0.7%) were selected along with a constant shear strain amplitude of 0.5%. The two axial strain amplitudes were selected to investigate differences associated with no twin activation (0.4%) and twin activation (0.7%) respectively.

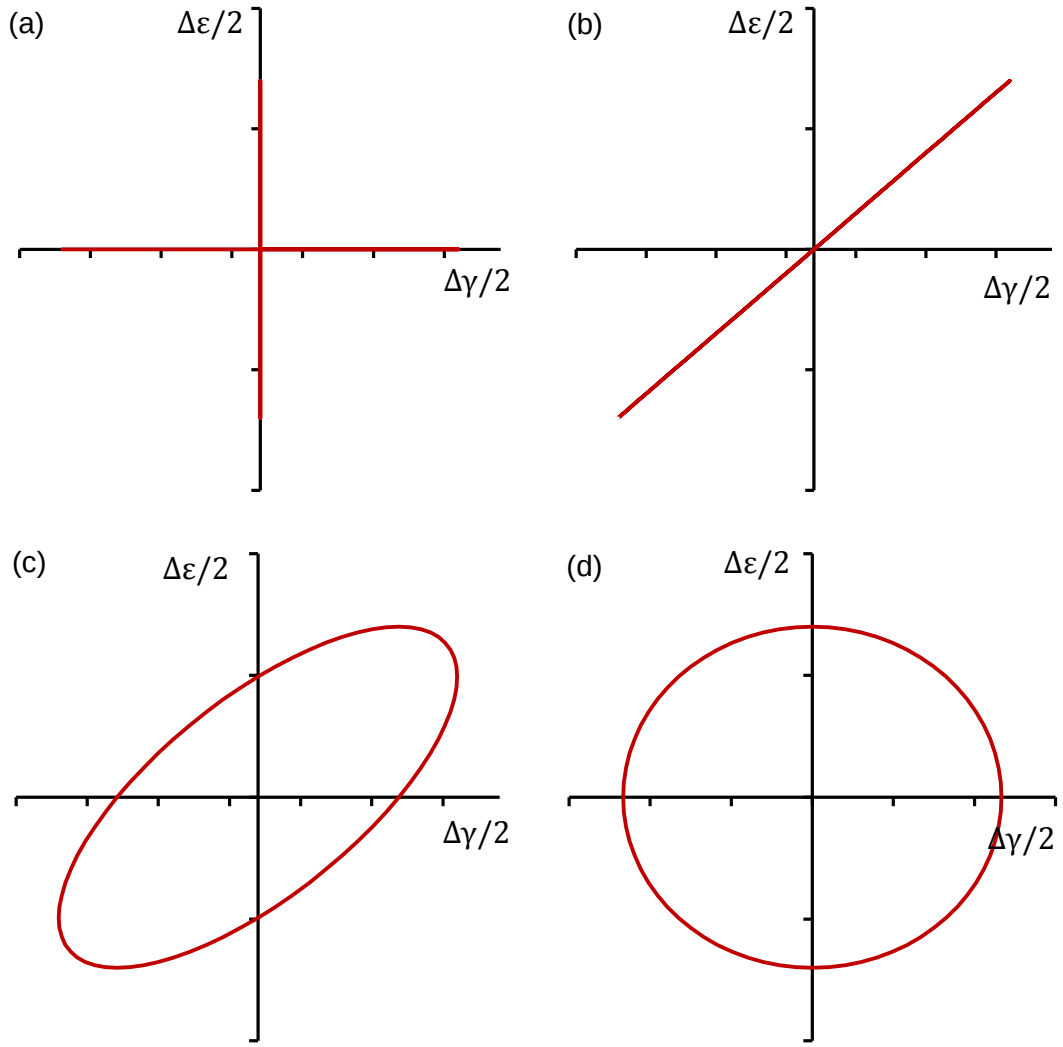

Fig 67: *Illustration of the different strain paths employed in this study including (a) pure axial and pure shear, (b) in-phase, (c) 45° out-of-phase, and (d) 90° out-of-phase.*

Additional in-phase tests were also performed at two shear strain amplitudes (0.5% and 0.75%) for the purpose of examining the effect of shear strain amplitude on axial hysteresis response and vice versa. For all multiaxial tests, both axial and shear strain waveforms had the same frequency which ranged from 0.2Hz to 0.4Hz. A summary of the employed multi-axial test matrix is included in Table 8.

Table 8: *Summary of axial and shear strain amplitudes used for multi-axial tests.*

In-Phase		**45° Out-of-Phase**		**90° Out-of-Phase**	
$\Delta\varepsilon/2$	$\Delta\gamma/2$	$\Delta\varepsilon/2$	$\Delta\gamma/2$	$\Delta\varepsilon/2$	$\Delta\gamma/2$
0.4%	0.5%	0.4%	0.5%	0.4%	0.5%
0.7%	0.5%	0.7%	0.5%	0.7%	0.5%
0.4%	0.75%	-	-	-	-
0.7%	0.75%	-	-	-	-

6.2. Results and Discussion

6.2.1. Quasi-Static Axial and Shear

The quasi-static tension and shear stress-strain plot for samples extracted from the two flanges of the forgings are included in Fig 68. The axial plots were very consistent with virtually identical yield and ultimate strengths. Additionally, the axial curves demonstrated a relatively high yield strength followed by a continually decreasing strain hardening rate after the initiation of plasticity (Fig 68c). In comparison, the shear stress-strain curves demonstrated a much lower yield strength followed by an almost constant hardening rate as is apparent from Fig 68c.

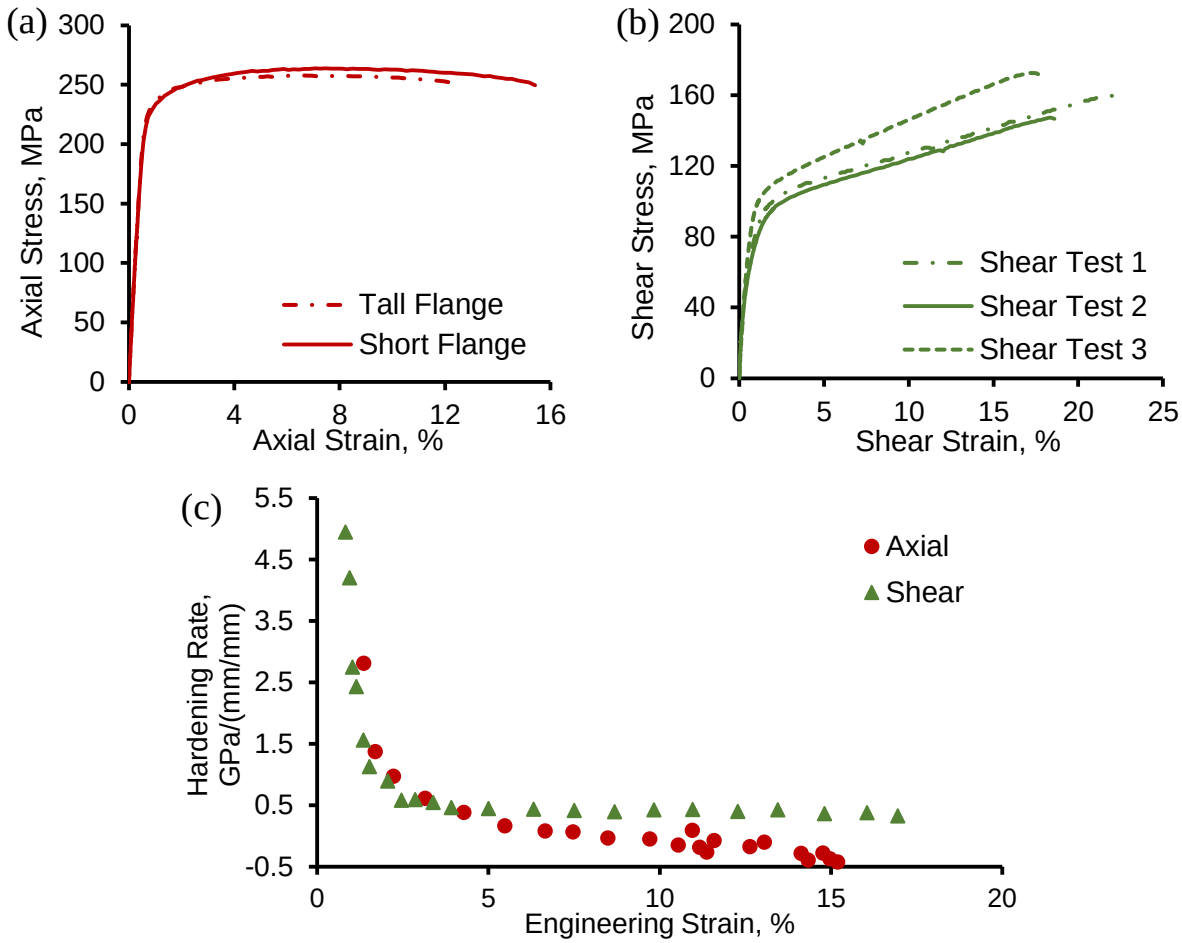

Fig 68: *Quasi-static engineering stress vs. strain curves for optimally forged AZ31B tested in (a) tension and (b) shear, and (c) hardening rate vs. total strain for quasi-static axial and shear tests post yield.*

A summary of the yield and ultimate strengths as well as the failure elongation obtained during quasi-static testing along the axial and shear axes is included in Fig 69, along with the standard deviations observed in the measurements. Note that Fig 69a also includes the results obtained for the starting as-extruded material as a reference.

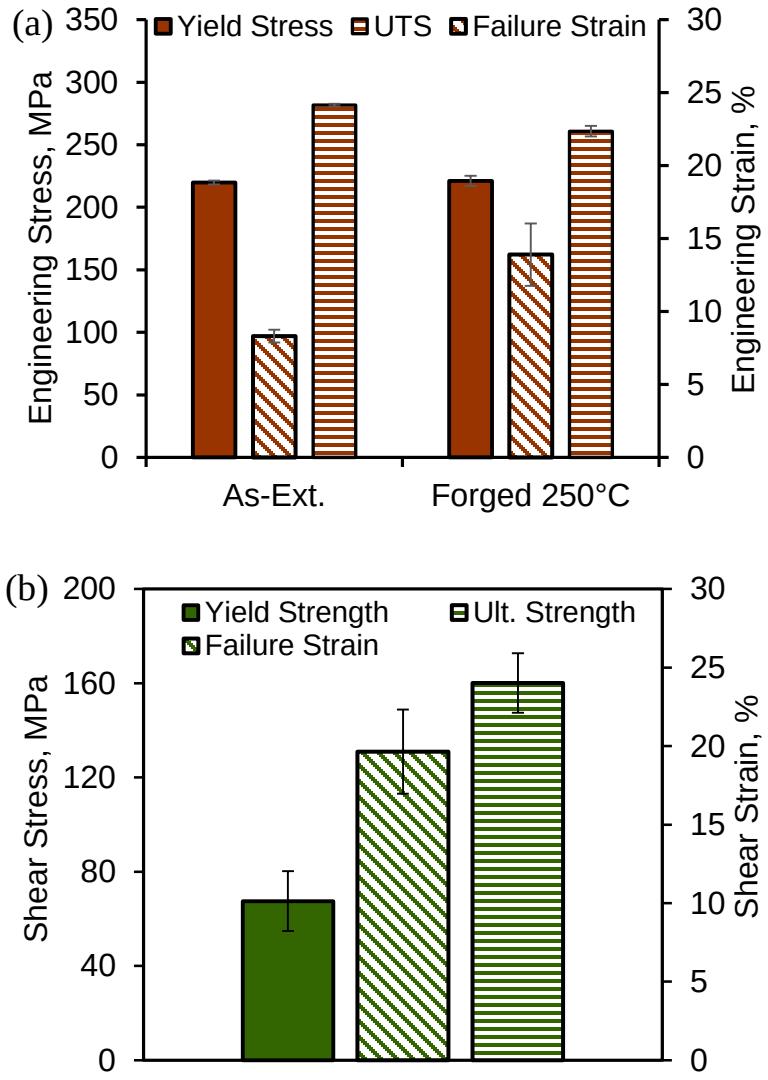

Fig 69: *Summary of yield strength, ultimate strength and failure strain obtained during quasi-static testing along the (a) axial direction and (b) shear direction.*

6.2.2. Strain-Controlled Low Cycle Tension-Compression

Fig 70a shows the plot of strain amplitude versus cycles to failure for the current optimally forged AZ31B for strain amplitudes between 0.35% and 0.9%. By separating the total strain amplitudes into their elastic and plastic components and plotting these components against the corresponding reversals to failure, the Manson-Coffin parameters for the axial cyclic tests were obtained as was described in detail in section 4.3.2.

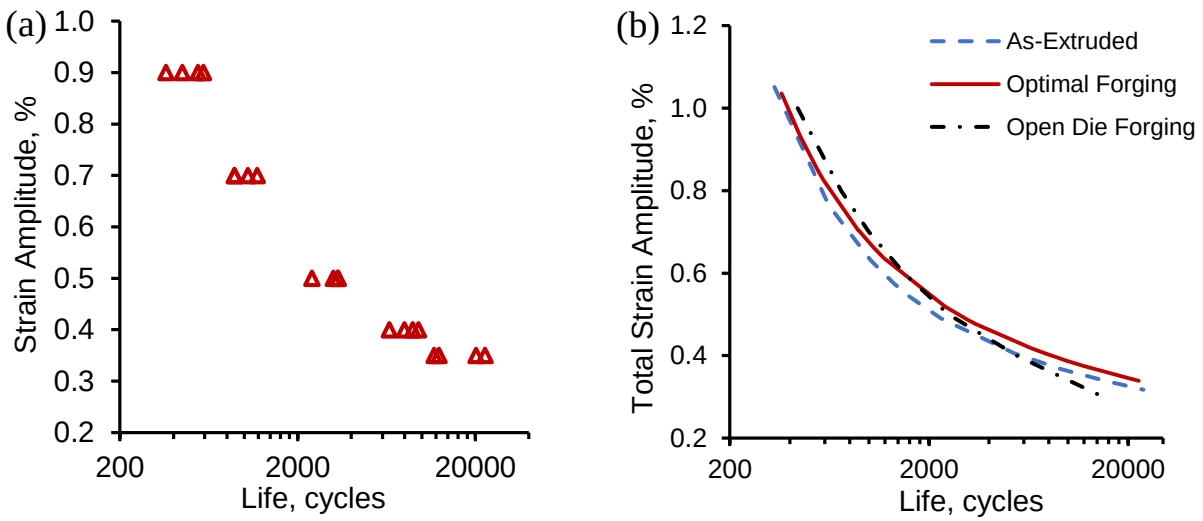

Fig 70: *Plots of strain amplitude vs. cycles to failure including (a) raw cyclic data and (b) Manson-Coffin curve for the current forged alloy as well as other thermo-mechanical conditions.*

The resulting Manson-Coffin curve for the optimally forged AZ31B along with those for the starting as-extruded AZ31B and the open-die forged AZ31B presented in chapter 4 is illustrated in Fig 70b and the Manson-Coffin parameters are summarized in Table 9. From these curves it is evident that the current forging resulted in a modest improvement in fatigue life compared to the starting extruded material. This improvement was more pronounced at the lower strain amplitudes. In contrast, the results obtained for open-die forged AZ31B was quite surprising. At amplitudes above approximately 0.6%, the open-die forged material displayed slightly superior fatigue life compared to the current forging condition, however as the total strain amplitude decreased below 0.6%, the current forging shows substantially increased fatigue life.

The superior high amplitude fatigue life demonstrated by the open-die forged material is thought to be due to the development of a more significant tensile mean stress in the current forging compared to in the case of the previous flatbread forging. For example, at a total strain amplitude of 0.7%, the current forging exhibits a tensile mean stress of ~ 55 MPa which is almost 38% higher than that of the flatbread condition (~ 40 MPa). The detrimental effect of tensile mean stress on fatigue life has been well documented [90], [123], [124], and it is the development of such differing mean stress values that is thought to be responsible for the poorer high amplitude behavior of the current forging condition.

Table 9: *Summary of Manson-Coffin parameters for thermo-mechanically processed AZ31B.*

	σ_f' [MPa]	b	ε_f' [mm/mm]	c
Optimally Forged AZ31B	599	-0.13	2.58	-0.96
Extruded AZ31B	535	-0.12	4.85	-1.03
Open Die Forged AZ31B	482	-0.14	0.53	-0.66

The substantial increase in the fatigue life of the current forging at lower strain amplitudes is thought to be due to the significantly increased yield strength of the closed-die forged alloy compared to the previous open-die forged condition. Specifically, for total strain amplitudes below ~ 0.6%, the amount of plastic energy dissipated per cycle tends to be considerably less for the optimally forged alloy compared to the open-die forged alloy. For example, at 0.4% total strain amplitude (Fig 71), the plastic energy dissipated during a stabilized cycle for the optimal forging (~ 0.08 MJ/m^3) is more than 3 times less than that dissipated by the open-die forged material (~ 0.25 MJ/m^3) even though the total energy dissipated (elastic and plastic) was similar (0.47 MJ/m^3 vs. 0.49 MJ/m^3). As irreversible plastic damage is the primary fatigue damage mechanism, the substantially higher plastic energy dissipated by the open-die forged material at lower strain amplitudes does correspond to the poorer observed fatigue life.

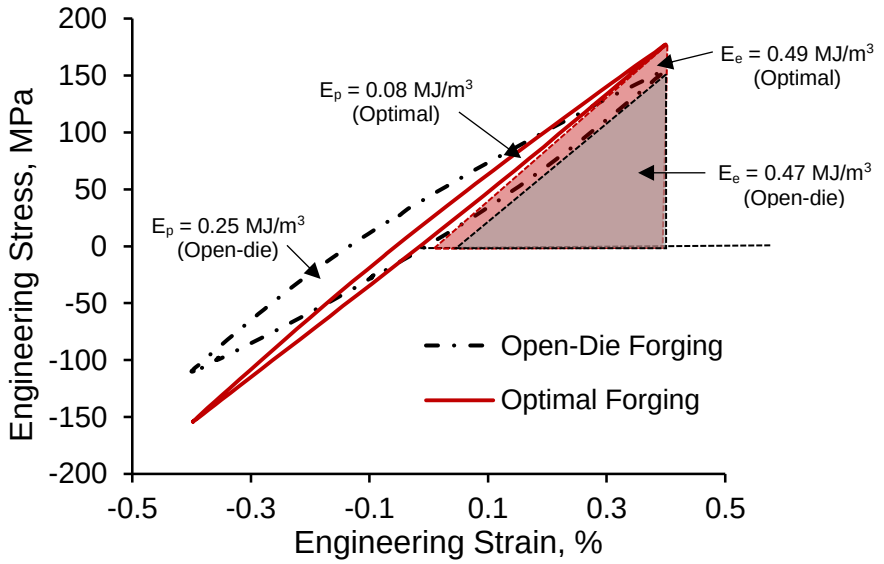

Fig 71: *Stabilized axial hysteresis loops for a total strain amplitude of 0.4% for open-die forged and optimal closed-die forged AZ31B.*

The stabilized (half-life) hysteresis loops for the various axial tests are shown in Fig 72. It is noted that at the lower strain amplitudes the stabilized loops are symmetric (Fig 72a) however these loops develop a pronounced asymmetry at higher strain amplitudes (Fig 72b). The highly asymmetric

hysteresis loops were similar to those obtained during cyclic testing of open-die forged AZ31B and is due to the activation of extension twinning during the compression reversals and de-twinning during the subsequent tension reversals. Such extension twinning is also active during the initial cycles at lower amplitudes (0.4% - 0.5%) and is responsible for the progressively higher mean stresses observed at these amplitudes (Fig 72a). A detailed discussion on the hysteresis loops obtained during strain-controlled axial fatigue testing may be found in chapter 4.

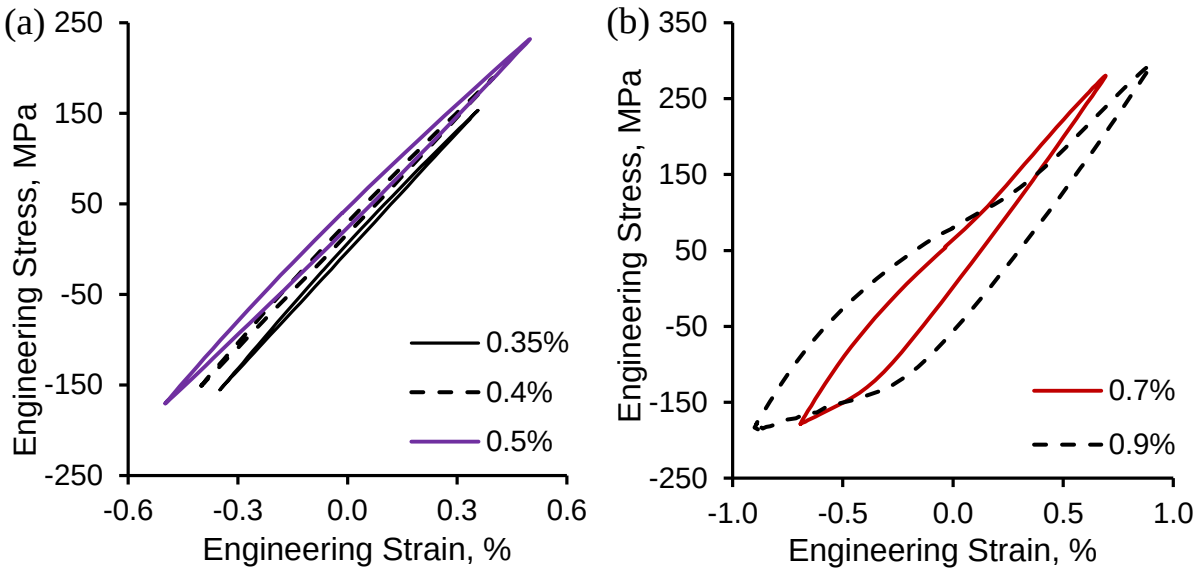

Fig 72: *Stabilized axial hysteresis loops for total strain amplitudes of (a) 0.35% to 0.5% and (b) 0.7% to 0.9%.*

The tension and compression axial cyclic stress-strain curves for the current closed-die forged AZ31B is included Fig 73. These curves were obtained by considering the peak tensile and compression stresses obtained from the stabilized hysteresis loops. The standard deviation of the tension and compression peak loads have also been included for each tested data point. It is clear from these cyclic curves that the forged AZ31B is substantially stronger in tension compared to compression. Specifically the cyclic 0.2% yield strength in tension (287 MPa) is 70 percent higher than the cyclic compression yield (169 MPa). As in the case of the open-die forged material, this asymmetry in the cyclic yield is due to relatively early yield during compression due to large scale activation of $\{10\bar{1}2\}\langle 10\bar{1}1\rangle$ extension twinning on account of the developed basal texture. Note that data points below 0.35% strain amplitude in Fig 73 represent theoretical values and have been included to facilitate visualization of the cyclic curves.

Fig 74 illustrates a comparison between the cyclic curves for the current forged alloy, the starting as-extruded condition and the previously investigated open-die forged AZ31B. It is seen that the cyclic tensile behavior of the current forged alloy is considerably superior to the open-die forging condition however it is lower than that of the starting extruded condition. On the other hand, the cyclic compression curves exhibit a different trend with the current forging showing superior cyclic strengths than both other conditions.

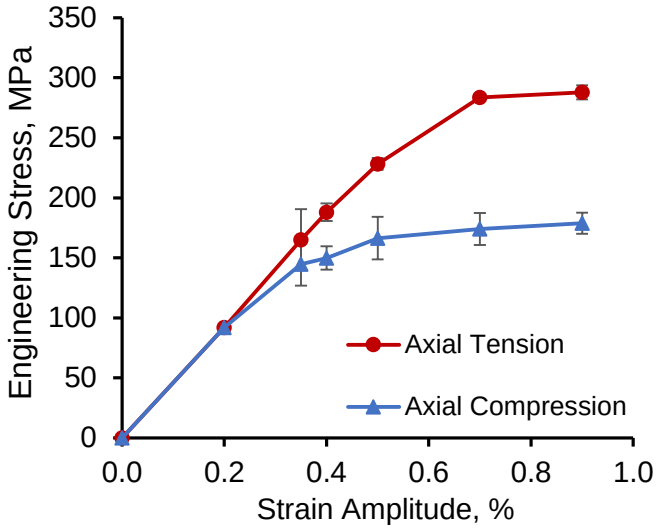

Fig 73: *Cyclic tension and compression stress-strain curves for the current optimally forged AZ31B.*

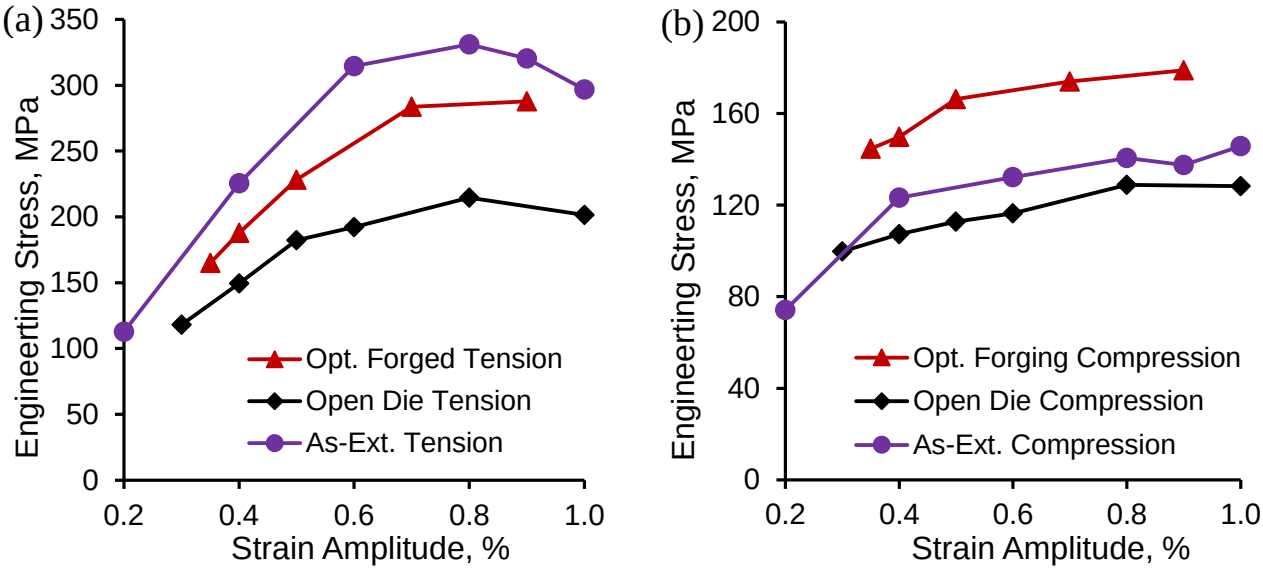

Fig 74: *Comparison of cyclic stress strain curves for several thermo-mechanically processed AZ31B showing (a) tension curves and (b) compression curves.*

The improvement of the cyclic tensile response of the current forging compared to the open-die forging is thought to be due to the combined effect of a more homogenous and refined grain morphology as well as a sharper basal texture in the closed-die forging compared to that of the open-die forged material. Specifically, the current forging exhibited a fully recrystallized grain structure with an average grain of 9.9 µm ± 5.0 (Fig 50) whereas the open die forged alloy exhibited a strongly bimodal grain distribution (Fig 16). The higher fraction of recrystallized grains and consequently higher grain boundary density of the current forging would then increase dislocation pileup during cyclic loading increasing the overall extent of cyclic hardening in the material during cyclic loading. Additionally, the sharper basal texture of the current forging (Fig 53) compared to the open-die forged alloy (Fig 17) may result in increased basal slip inhibition for the closed-die forged alloy further increasing the peak tensile stress during cyclic loading. Such an effect of texture would also explain the higher cyclic tensile curve of the as-extruded material which due to its strong extrusion texture results in the applied tensile loading being virtually perpendicular to the c-axis. According to the Schmid law [125] this would cause a negligible shear stress component along the basal planes effectively inhibiting basal slip and instead accommodating plasticity by the activation of harder non-basal slip systems [38], [42].

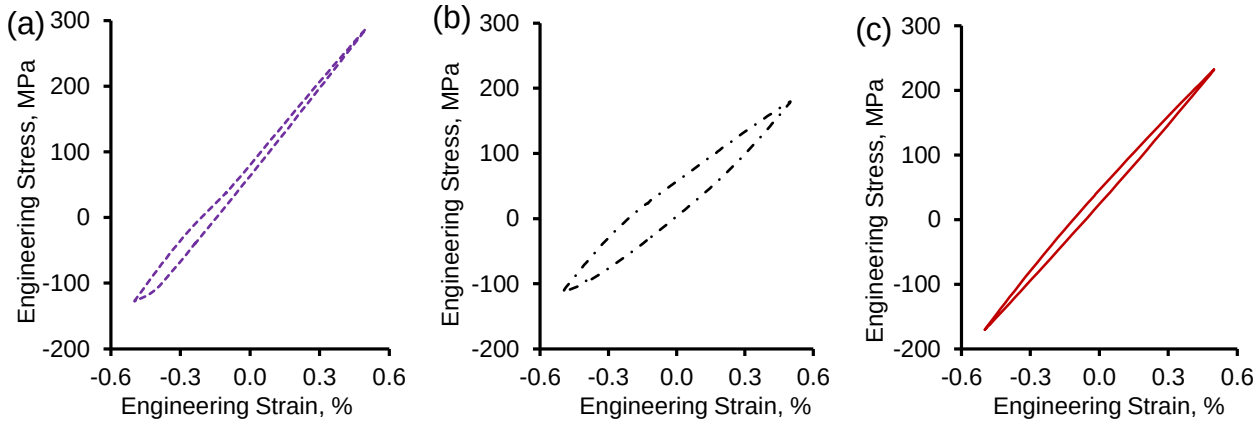

Fig 75: *Comparison of the stabilized hysteresis loops for (a) as-extruded, (b) open-die forged and, (c) closed-die forged AZ31B tested at a strain amplitude of 0.5%.*

In comparison to the cyclic tensile behavior, the closed-die forged alloy exhibited the highest cyclic compression response of the three illustrated conditions. Such a behavior observed for the current forged condition is believed to be due to finer grain size of the forging compared to the other two conditions which can inhibit extension twin activation and therefore require high compressive stresses to activate [126]–[128]. Such an effect of grain size on extension twin activation may be

further confirmed by comparing the threshold strain amplitude required for the formation of an asymmetric hysteresis loop. Note that for both the as-extruded and open-die forged alloy, this threshold amplitude was found to be approximately 0.4% whereas for the closed-die forged alloy, the stabilized loop was more or less symmetric up to about 0.5% strain amplitude (Fig 75).

The cyclic hardening behavior of the current alloy is presented in Fig 76 which shows the stress amplitude evolution for the various tested strain amplitudes. For the low strain amplitudes (0.35% and 0.4%) it can be observed that very little cyclic hardening occurs. As the strain amplitude is increased to 0.5%, the macroscopic plasticity increases along with the activation of extension twins during the early cycles. This twin activation eventually ceases resulting in symmetric half-life hysteresis loops however the increased dislocation motion and pileup associated with the larger plastic deformation at this strain amplitude leads to higher degree of cyclic hardening compared to the lower strain amplitudes. At even higher strain amplitudes (>0.7%), extensive extension twinning is activated in compression and these twins are not entirely annihilated through detwinning during the subsequent tensile reversal. This results in the buildup of residual twins which provide additional barriers to dislocation motion [87], [88] and explains the significant amount of cyclic hardening observed for the 0.7% and 0.9% strain amplitudes. The presence of such residual twins was observed previously for the open-die alloy Fig 31.

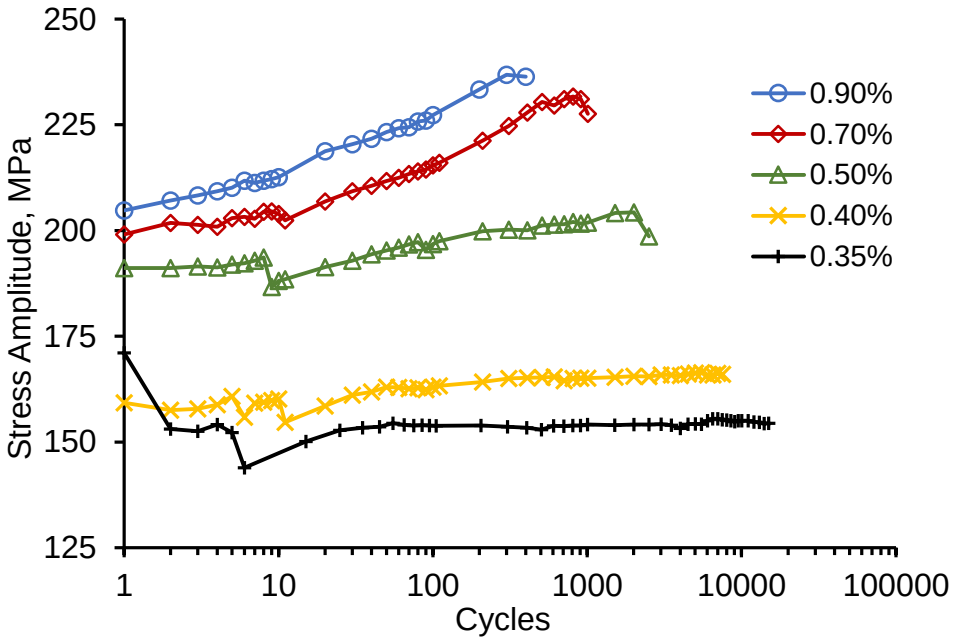

Fig 76: *Cyclic hardening evolution for the current forged alloy at the various tested axial strain amplitudes.*

SEM examination of the fatigue fracture surface was performed for samples tested at 0.4% (Fig 77) and 0.9% (Fig 78) axial strain amplitudes. As in the case of the previously examined open-die forging, three zones were observed on the fracture surface: (i) *Crack Initiation* (CI), (ii) *Fatigue Crack Growth* (FCG), and *Final Fracture* (FF). These regions have been highlighted in Fig 77a and Fig 78a. At both tested axial strain amplitudes, multiple crack initiation sites were identified, originating from the sample surface. In the case of the high amplitude test, the primary fatigue crack was found to original from an Al-Mn rich intermetallic Fig 78b. The identified localized crack path around this particle is illustrated by the dashed arrows (Fig 78b).

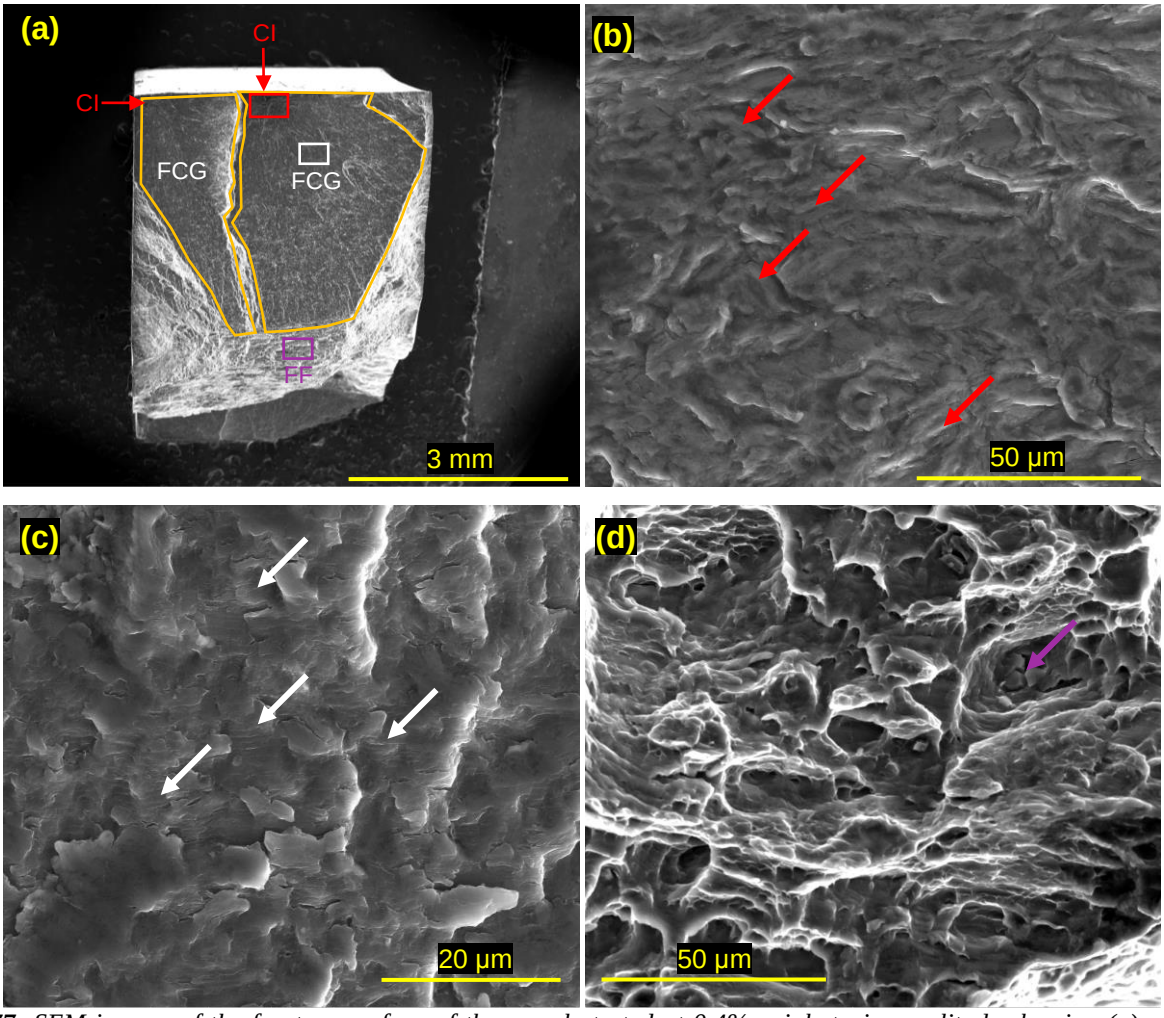

Fig 77: *SEM images of the fracture surface of the sample tested at 0.4% axial strain amplitude showing (a) overall fracture surface, (b) evidence of extension twins (red arrows) near crack initiation, (c) fatigue striations (white arrows) and (d) final fracture with cracked intermetallics (purple arrow). CI: crack initiation, FCG: fatigue crack growth, FF: Final fracture.*

Following the initiation, the fatigue crack grew during subsequent cycles which was characterized by clear fatigue striations in the FCG zone (Fig 77c and Fig 78c). Eventually, crack growth destabilizes resulting in final fracture of the specimen. At both strain amplitudes this final fracture zone was characterized by a dimpled fracture surface containing cracked intermetallics as well as numerous secondary cracks – an indication of the enhanced strength and ductility of the forged alloy.

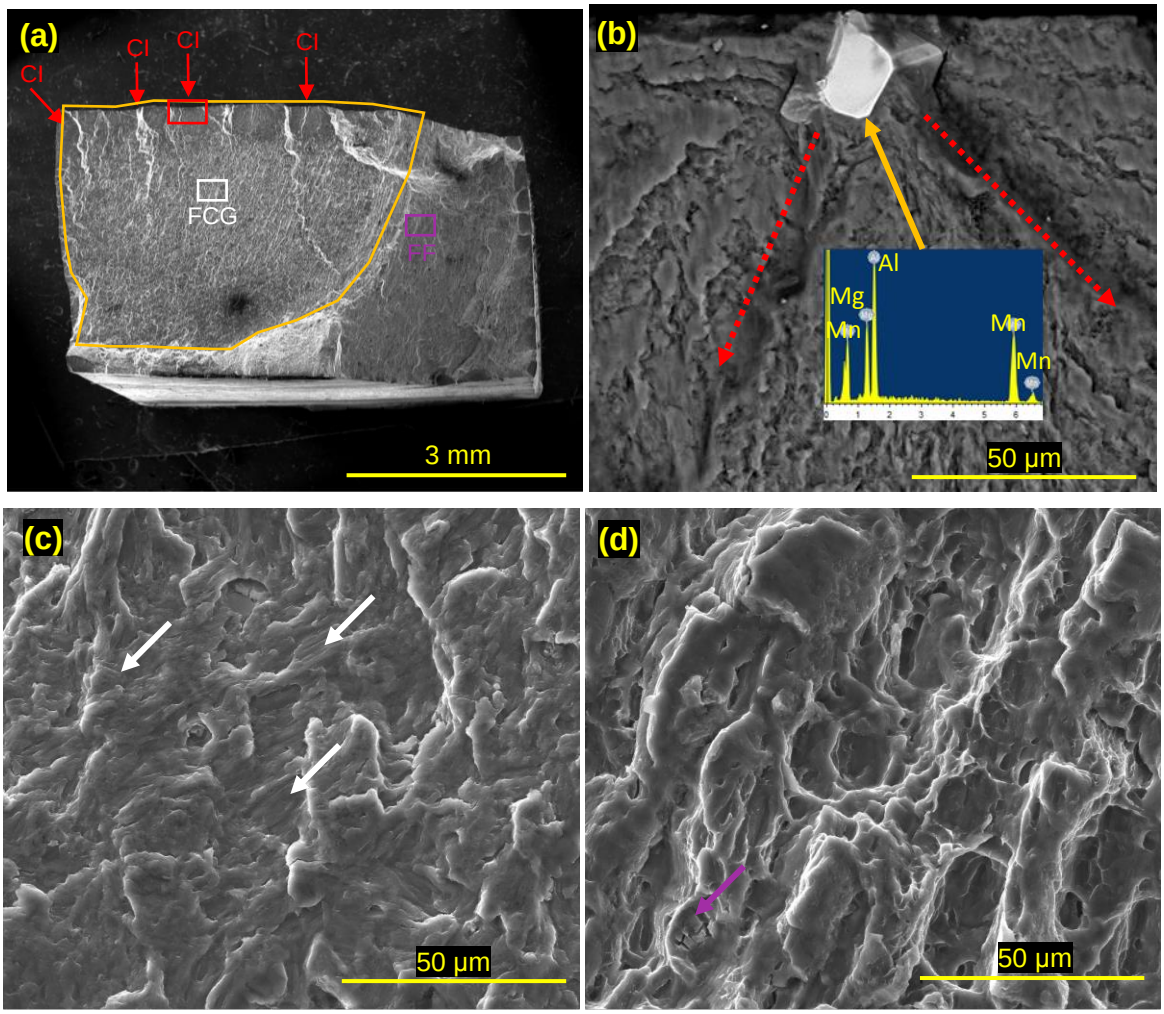

Fig 78: *SEM images of the fracture surface of the sample tested at 0.9% axial strain amplitude showing (a) overall fracture surface, (b) evidence of crack initiation from an intermetallic, (c) fatigue striations (white arrows) and (d) final fracture with cracked intermetallics (purple arrow). CI: crack initiation, FCG: fatigue crack growth, FF: Final fracture.*

6.2.3. Strain-Controlled Cyclic Shear

The stabilized hysteresis loops for the various tested shear strain amplitudes are illustrated in Fig 79. Unlike the hysteresis loops obtained for the axial direction, the shear loops were symmetric at all the tested strain amplitudes which can be ascribed to primarily slip dominated plasticity during fully reversed shear loading. It is noteworthy that at a shear strain amplitude of 1.0%, a slight sigmoidal shape (suggestive of twin activity) was observed near the loading and unloading peaks of the loop (black arrows in Fig 79b). Such twin activation at shear strain amplitudes above 1.0% were also reported in [56], [57], [59], [87] during fully reversed cyclic shear testing.

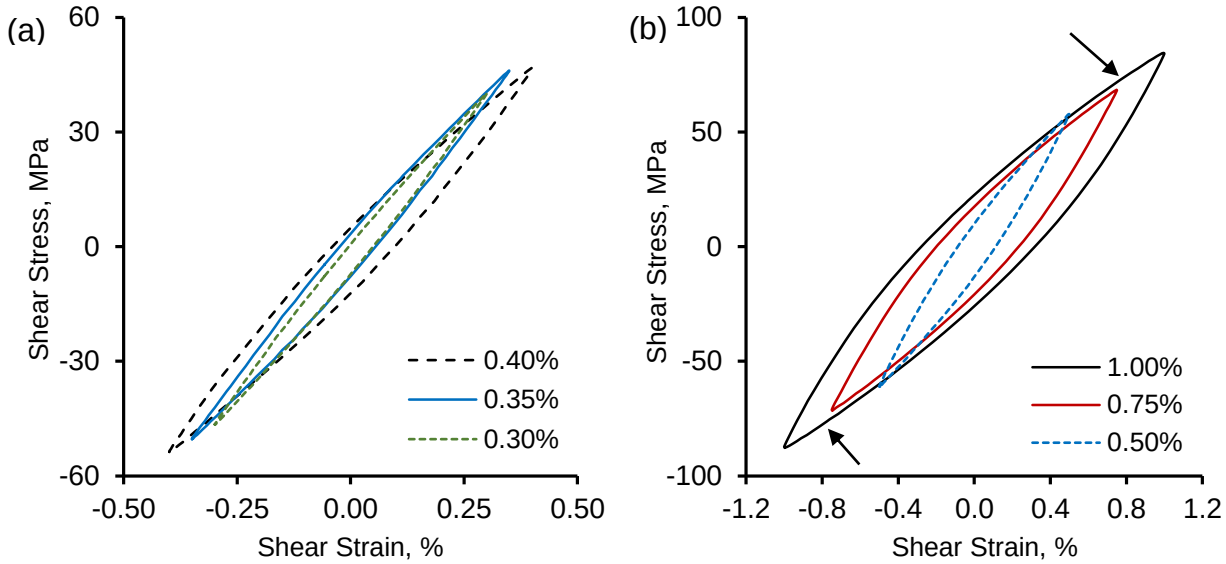

Fig 79: *Stabilized shear hysteresis loops for total shear strain amplitudes of (a) 0.3% to 0.4% and (b) 0.5% to 1.0%.*

Another difference between the cyclic axial and cyclic shear response of the current alloy is the significantly lower degree of cyclic hardening exhibited along the shear axis. The evolution of shear stress amplitude with continued cycling is shown in Fig 80a which illustrates only a minor degree of cyclic hardening even at the higher tested shear strain amplitudes. This was in contrast to the much more significant degree of hardening observed along the axial direction (Fig 76) especially at axial strain amplitudes above 0.5%. Similar low cyclic hardening along the shear direction was reported by Albinmousa et al. [86] for extruded AZ31B, however more significant cyclic shear hardening was reported for other Mg alloys such as extruded AM30 [56]. The low degree of cyclic shear hardening may also be observed in the cyclic shear stress-strain plot in Fig 80b. In this figure, the stabilized positive and negative (absolute value) peak shear stresses are plotted against their corresponding shear strain amplitude. For reference, the quasi-static shear curve up to a shear strain

of 1.2% has been superimposed on the plot. It is clear from Fig 80b that for shear strain amplitudes below 0.75% the extent of cyclic hardening is negligible compared to the quasi-static curve. At a shear strain amplitude of 1.0%, there appears to be some degree of cyclic hardening resulting in peak shear stress values that are slightly higher than the quasi-static curve. This slight increases in the extent of cyclic hardening at a shear strain amplitude of 1.0% is supported by the observations made in [56], [57] and is believed to be due to the onset of extension twin activation which provide additional hindrance to dislocations. It is worth noting that the values of positive and negative shear stresses at their corresponding shear strain amplitudes are very similar which further emphasizes the symmetry of the cyclic shear response compared to the axial direction.

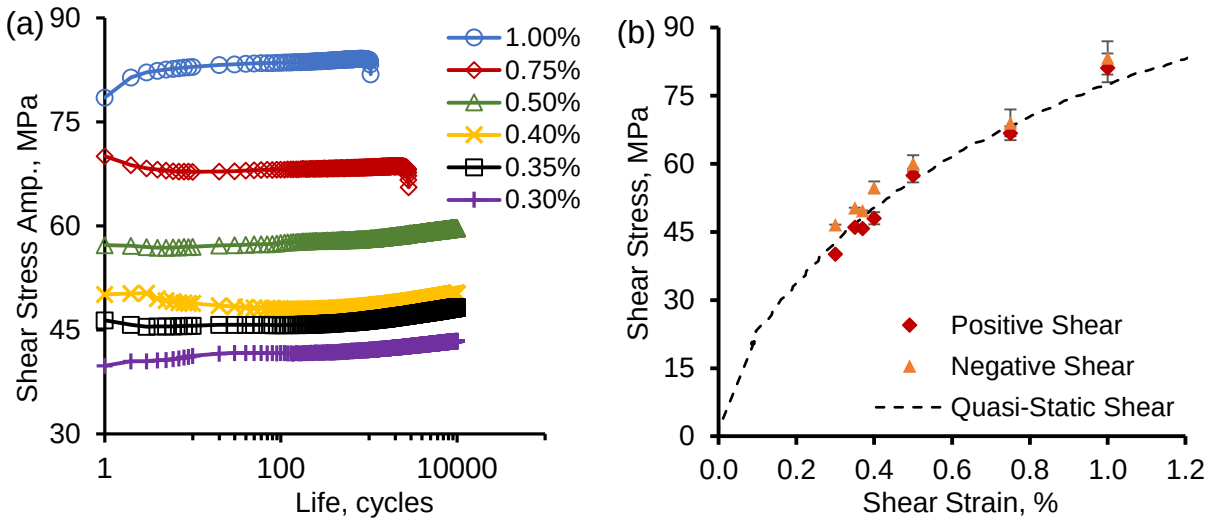

Fig 80: *Cyclic shear behavior of the current closed-die forged AZ31B showing (a) evolution of the shear stress amplitude vs. number of cycles and (b) comparison of the cyclic shear stress-strain plot and the quasi-static shear curve. Note that for negative shear stresses the absolute values are shown.*

Fig 81 shows the plot of shear strain amplitude versus cycles to failure for the current forged alloy along with the results of similar tests on AZ31B obtained from literature [57], [86]. From this figure it can be seen that the current forged alloy shows superior cyclic shear response compared to the extruded AZ31B studied by Albinmousa et al. [86] within the tested range. This may be understood by comparing the quasi-static shear curves for the two alloy conditions which is included in Fig 82 up to shear strain of 10%. It is obvious from this plot that the extruded AZ31B considered by Albinmousa et al. is substantially weaker than the current forged alloy, especially within the range of cyclic shear strain amplitudes considered in this chapter and this translates to superior cyclic response for the forged AZ31B.

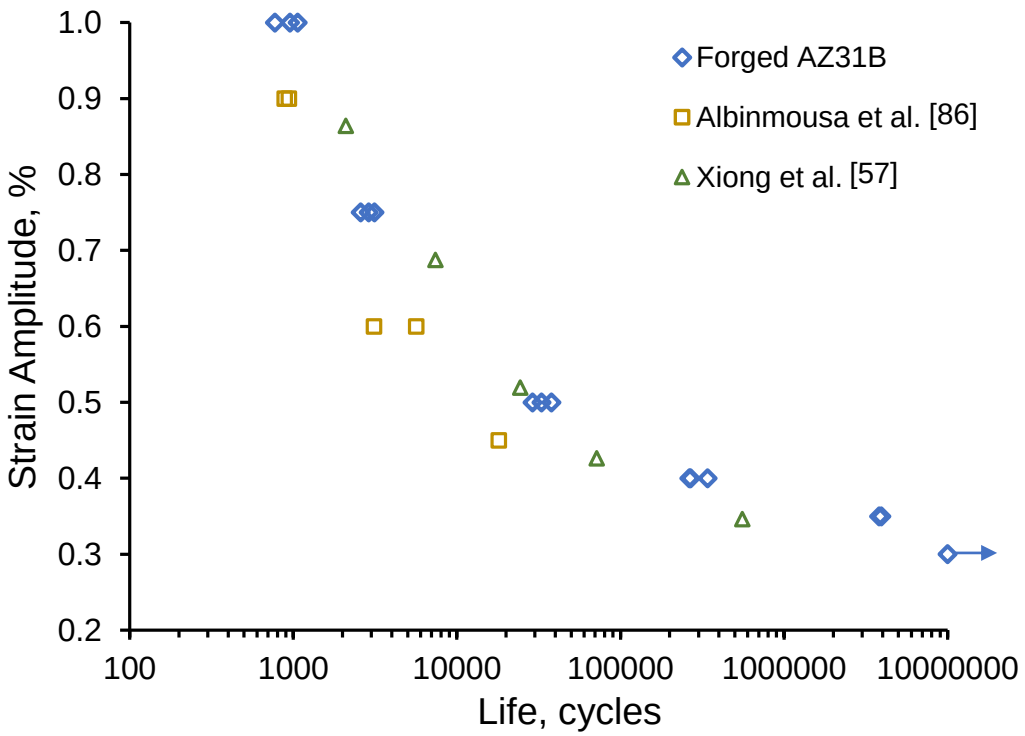

Fig 81: *Plot of shear strain amplitude vs. cycles to failure for the current forged AZ31B. Cyclic shear data from literature for extruded AZ31B has also been included for comparison. Note that the horizontal axis is shown on a logarithmic scale.*

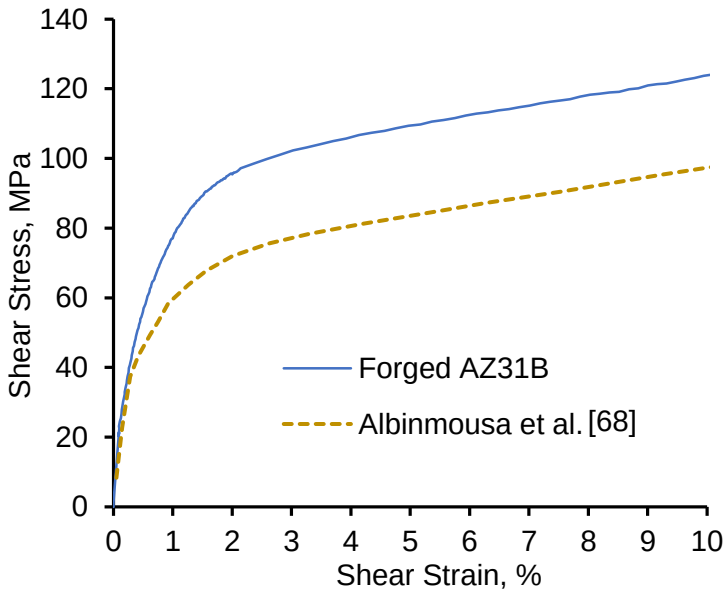

Fig 82: *Comparison of the quasi-static shear curve for forged AZ31B considered in this study and that for extruded AZ31B considered by Albinmousa et al.*[86]. *Note: the two curves have been illustrated to a total shear strain of 10%.*

Xiong et al. [57] investigated a different extruded AZ31B and presented cyclic shear behavior that corresponds well with the forged alloy at shear strain amplitudes between 0.5% – 1.0%. Below a shear strain amplitude of 0.5%, the current forged condition exhibits superior fatigue life with this

improvement being more pronounced in the high cycle range (10^5 – 10^7 cycles). The superior high cycle shear response of the current alloy might be explained by considering the microstructures of the different alloy conditions. For example, the extruded AZ31B considered by Xiong et al. was reported to have a strong bimodal grain distribution with average grain sizes ranging between 8μm – 50μm. In comparison, the current forged alloy was found to have an overall average grain size of 9.9 μm ± 5.0. At lower shear strain amplitudes, the increased microstructural homogeneity of the forged alloy may result in reduced local plastic deformation (due to the strengthening effect of finer grains [121], [129]) compared to considerable bimodal extrusion condition considered by Xiong et al. and this may explain the superior high cycle fatigue response of the forged alloy.

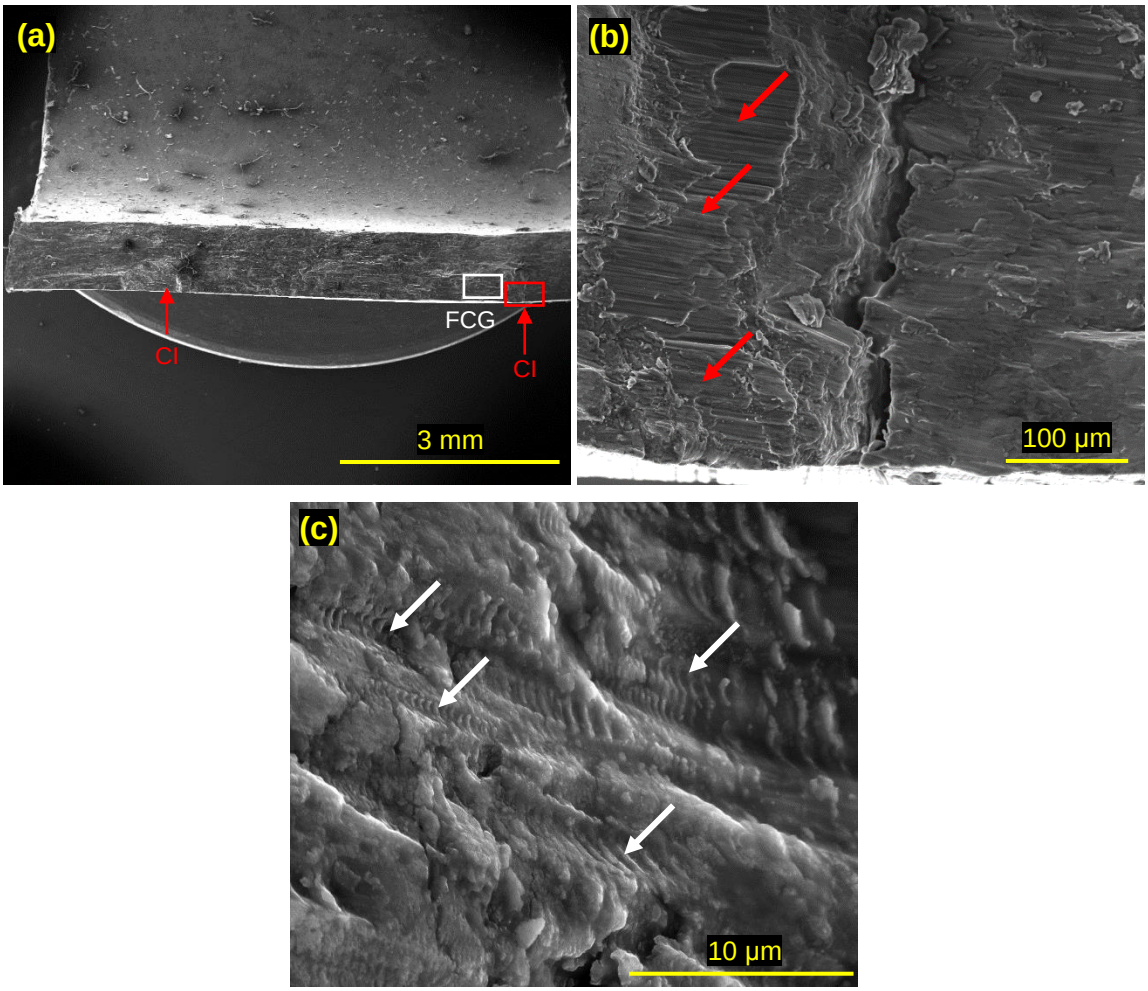

Fig 83: *SEM images of the fracture surface of a cyclic shear sample tested at 0.4% strain amplitude showing (a) overall fracture surface, (b) crack initiation (CI) location surrounded by shear bands (red arrows), and (c) fatigue striations (white arrows) found in the fatigue crack growth (FCG) region.*

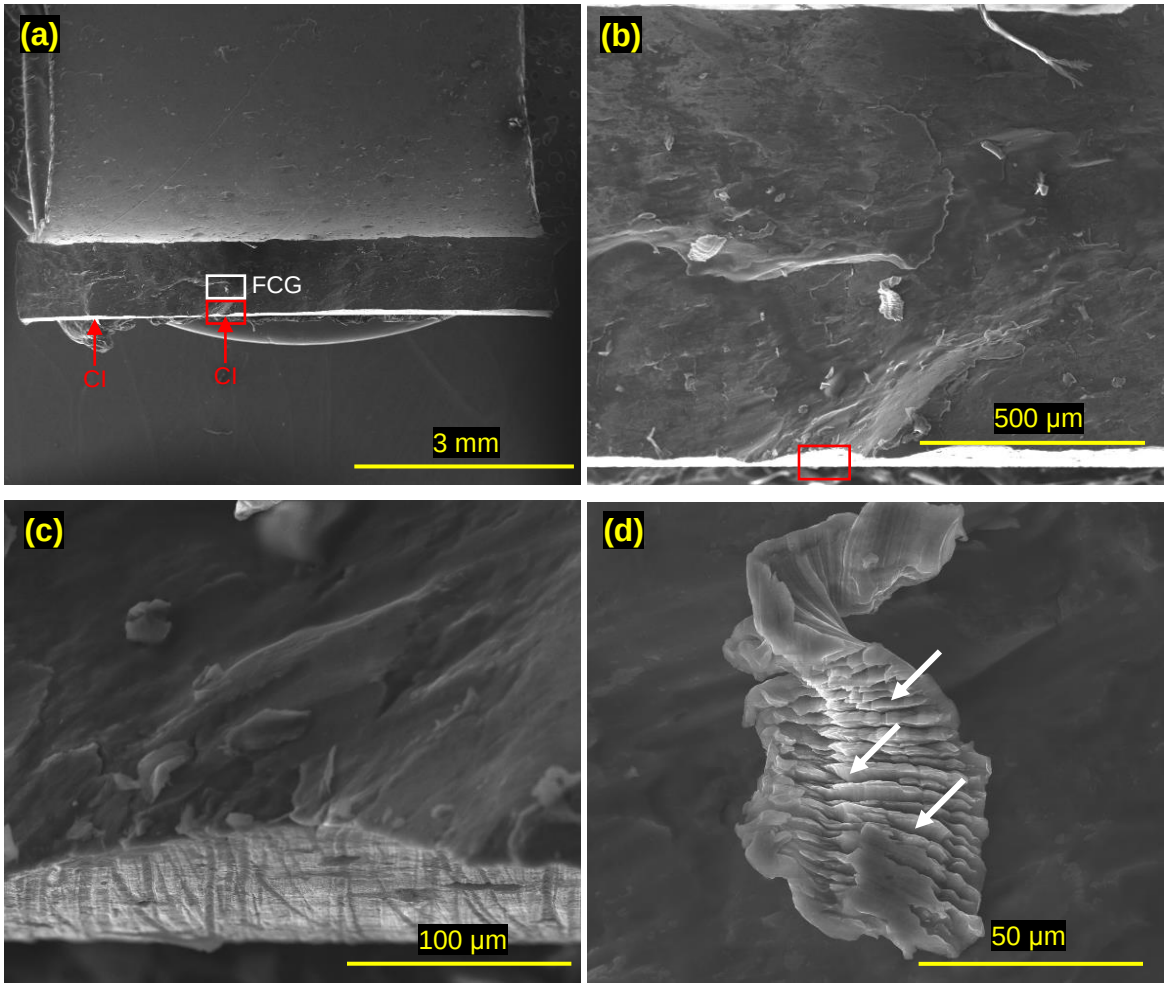

Fig 84: *SEM images of the fracture surface of a cyclic shear sample tested at 1.0% strain amplitude showing (a) overall fracture surface, (b, c) crack initiation (CI) location and (d) matrix delamination containing fatigue striations (white arrows).*

SEM images of the fracture surface for a shear sample tested at 0.4% shear strain amplitude is included in Fig 83 (a photograph of a macroscopic cyclic shear crack is shown in Fig 91a). Due to the large crack size developed during cyclic shear, only a portion of the fracture surface (~ 8 mm in length) was examined. An overall image of the fracture surface is shown in Fig 83a and the locations enclosed by the red and white boxes are magnified and presented in Fig 83 b – c respectively. Fig 83b shows a location thought to be initiation location for the primary shear crack. This location was characterized by extensive slip bands (red arrows) surrounding significant secondary cracks. Further away from this location, clear "tire marks" indicative of fatigue crack growth were observed seemingly directed away from the identified initiation location Fig 83c. Note that no final rupture was identified for the specimen due to the shear crack growth continuing until the torque amplitude dropped by 50% ending the test prior to complete failure of the specimen.

Similar fracture surface features were observed at a shear strain amplitude of 1.0% (Fig 84). At this higher strain amplitude, several crack initiation locations were identified (Fig 84 a – c) however, it is thought that the primary crack initiation responsible for eventual failure was not contained within the examined section of the specimen. As was identified for the lower shear strain amplitude, sharp fatigue striations were observed near the crack initiation locations (Fig 84d), however unlike the lower amplitude, these striations were observed to be constrained to delaminated sections of the material. Readers should note that the author is not aware of any existing studies that examine the fracture surface of a magnesium alloy subjected to cyclic shear loading. Consequently, the images included above represent a preliminary investigation of the shear fracture surface morphology and a more thorough investigation would be prudent.

6.2.4. Strain-Controlled Multi-axial Testing

As discussed in the experimental details of this chapter, multi-axial cyclic tests were conducted by imposing fully-reversed axial and shear strains simultaneously at various strain amplitudes and/or phase angles. The axial strain amplitudes in particular were selected so as to observe any effects associated with the activation of extensive extension twinning. The results of these multi-axial tests were examined from two perspectives: (i) the effect of axial and shear loading on each other's cyclic behaviour, and (ii) the effect of a phase difference between two strain waveforms. Note that in the subsequent discussion all applied axial and shear strains are cyclic in nature and fully-reversed unless otherwise stated.

6.2.4.1. Effect of Axial and Shear loading

The effect of an imposed shear strain of the axial fatigue response was considered by examining any changes in the stabilized axial hysteresis loops resulting from the applied shear strain. These axial hysteresis loops are shown in Fig 85 along with the stabilized loops for pure cyclic axial loading. It can be seen that for an axial strain amplitude of 0.4% (Fig 85a), a simultaneous application of a 0.5% shear strain amplitude results in an axial loop with a lower tensile peak suggesting earlier onset of plasticity compared to pure axial loading. A near identical reduction in the tensile peak is observed for a shear strain amplitude of 0.75%, however at this shear amplitude, a decrease in the peak compressive stress is also observed along with a widening of the compressive half of the loop suggesting some extent of extension twinning is activated. At higher axial strain amplitude (Fig 85b),

both shear strain amplitudes result in an identical reduction of the peak tensile stress however no additional effects were observed for the two shear strain amplitudes.

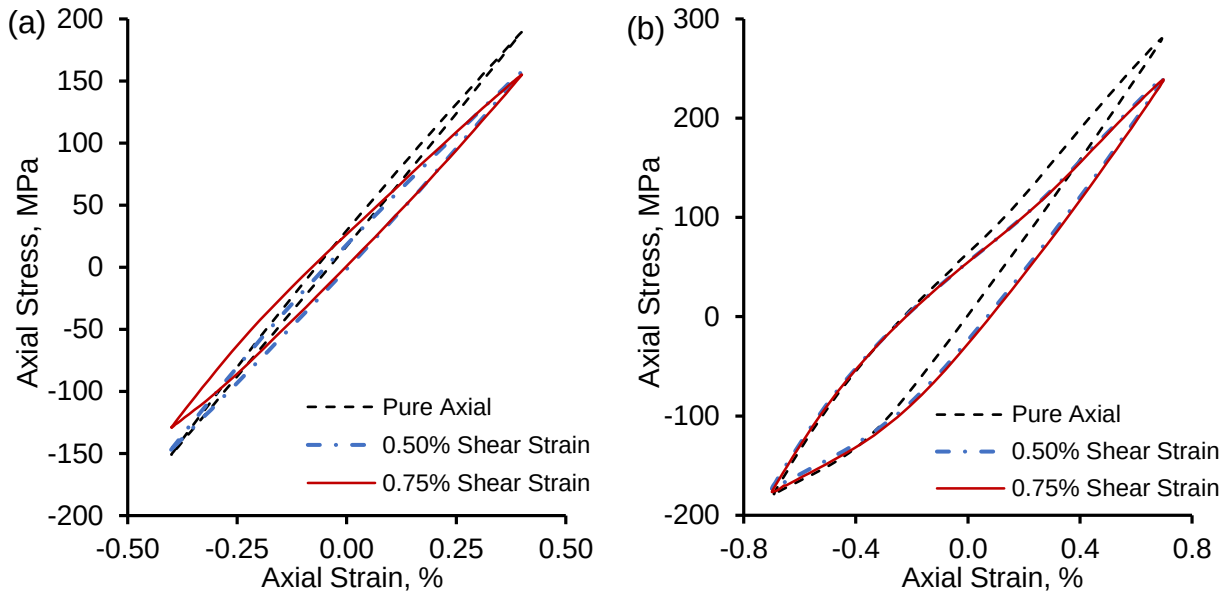

Fig 85: *Illustration of the effect of shear strain on the axial hysteresis loop for (a) 0.4% and (b) 0.7% axial strain amplitude.*

The effect of shear loading on the cyclic axial response observed in Fig 85 can be quantified by examining changes in axial strain energy arising from various applied shear strains. These average axial energies are summarized in Fig 86. From this summary it can be seen that for a 0.4% axial strain amplitude, the superposition of a 0.5% shear amplitude results in a ~28% reduction in positive elastic energy which is clearly visible by the lower tensile peak in Fig 85. Simultaneously, the plastic energy dissipated increases by ~25% as a result of the applied shear strain. These effects are amplified when the shear strain amplitude is increased to 0.75%, resulting in a 33% decrease in positive elastic energy and an exceptional ~88% increase in plastic energy. Such a substantial increase in plastic energy (i.e. loop area) is believed to be due to the initiation of some degree of extension twinning in the axial direction due to the high shear loading. A similar effect of shear loading on the axial elastic energy was observed at the higher axial strain amplitude (0.7%) with a ~24% and ~30% decrease for an imposed shear strain amplitude of 0.5% and 0.75% respectively. However, the effect on the plastic energy density was far less pronounced with increases of ~15% and ~18% respectively of the low and high shear strain amplitudes. This relative insensitivity of axial plastic energy to the applied shear strains at high axial amplitudes is ascribed to the CRSS required for twin activation. At low axial

strain amplitudes the addition of a sufficiently high shear component would contribute to the resolved shear stress acting on the twin planes and allow for activation of extension twinning at lower axial strain amplitudes; consequently resulting in a substantial increase in plastic loop energy [56]. However, at suitably high amplitudes of axial strain (such as the tested 0.7%), the axial amplitude is more than sufficient to activate extensive extension twins and the addition of an in-phase shear strain would not be expected to contribute as substantially to the overall twin volume fraction. With that being said, the contribution of the shear loading to the CRSS on the twin plane is visible as a decrease in compressive axial strain required for twin activation in Fig 85b.

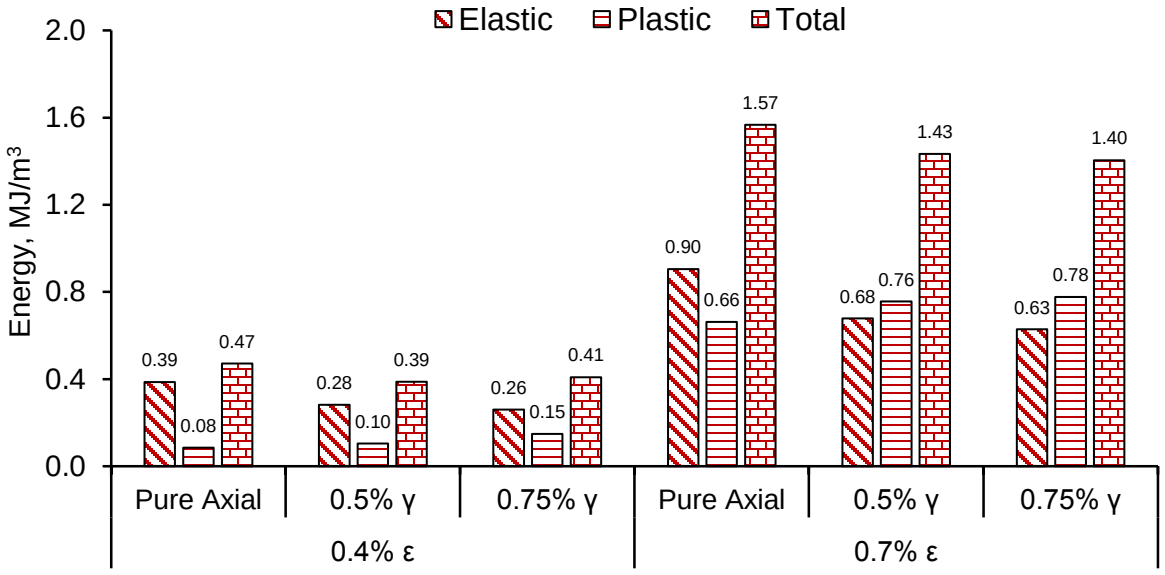

Fig 86: *Summary of axial hysteresis loop energy for different shear strain amplitudes.*

The effect of shear strain amplitude on the axial cyclic hardening behavior (at both 0.4% and 0.7% axial strain amplitude) is presented in Fig 87. Note that the horizontal axis is presented on a linear scale in this plot. From Fig 87a, it is clear that for pure axial loading at a strain amplitude of 0.4%, the extent of cyclic hardening is negligible beyond the first 500 cycles. The addition of an in-phase shear strain appears to result in a decrease in overall hardening within the same 500 cycles that is proportional to the applied shear strain amplitude. Beyond 500 cycles all three cases with 0.4% axial strain amplitude show minimal cyclic hardening up to failure. This behavior is more pronounced at an axial amplitude of 0.7% (Fig 87b) where substantial hardening is observed for the pure axial condition with a substantially lower degree of hardening when shear loading is included. The lower axial cyclic hardening associated with the application of a cyclic shear strain was also reported by

Roostaei et al. [56] for AM30 alloy and was suggested to be due to the additional shear loading providing an additional driving force to dislocations travel. As cyclic hardening is a result of restrictions to dislocation motions either through pileup at grain/twin boundaries or intermetallics, or due to dislocation-dislocation interactions, the added shear loading may overcome such restrictions resulting to lower overall cyclic hardening. Such a mechanism would support the observed decrease in overall axial hardening with increasing shear strain amplitude.

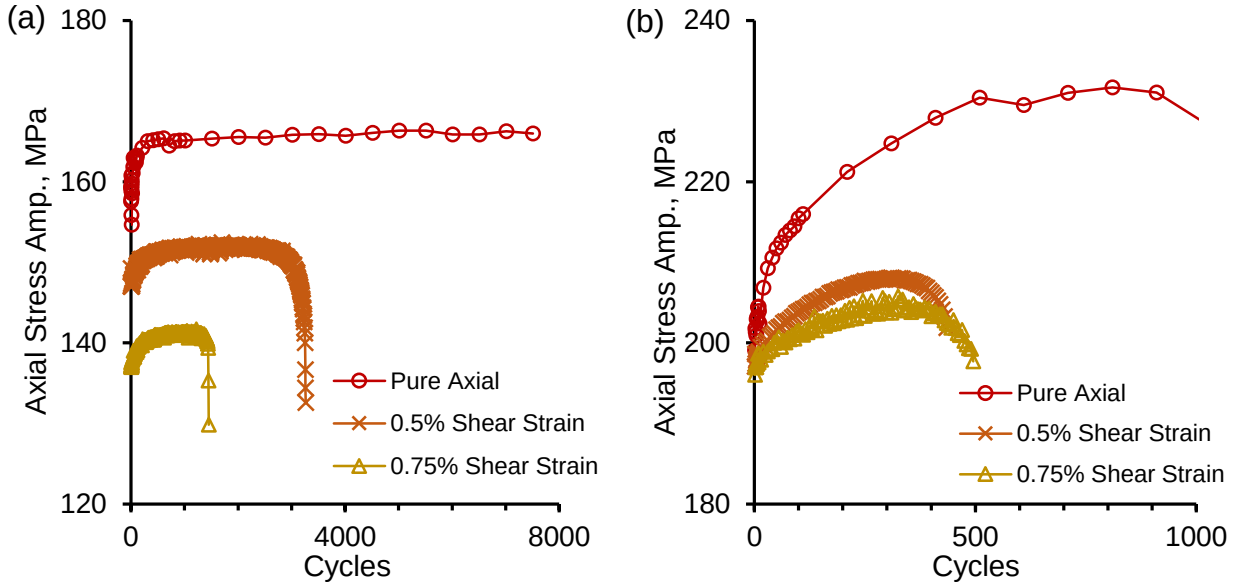

Fig 87: *Cyclic evolution of axial stress amplitude for different shear strain amplitudes observed for (a) 0.4% and (b) 0.7% axial strain amplitudes.*

In a manner analogous to that presented in Fig 85, the effect of applied axial strain on the stabilized shear hysteresis loops is shown in Fig 88. In general the effect of axial loading was similar at both tested shear strain amplitudes with the lower axial strain (0.4%) resulting in a lowering of the peak loop stresses while the loop remained more or less symmetric. However, when the axial strain amplitude was increased to 0.7%, the corresponding shear loops exhibited significant asymmetry. Accompanied with the substantial degree of asymmetry, the inclusion of a high axial strain amplitude also resulted in a reduction of both the tension and compression peak stresses for both shear strain amplitudes (0.5% and 0.75%). The substantial asymmetry in the shear loops at high axial strain amplitude was also observed by Xiong et al. [57] and Roostaei et al. [56] for AZ31B and AM30 respectively and was attributed to the effect of twin development due to the axial loading. Specifically, the occurrence of twinning during the compressive portion of axial loading results in a 86.3° reorientation of texture within the twinned portion of the material. This reorientation allows for

easier motivation of basal slip within twins compared to the matrix resulting in a lower negative shear peak in the hysteresis loops. During the tensile reversal, detwinning saturation occurs, substantially decreasing the volume fraction of twins and increasing basal slip inhibition compared to during the compressive reversal producing the comparatively higher positive shear peak. The contribution of extension twins resulting from the axial strain component on the shape of the shear hysteresis loop is further supported by noting the symmetry of the shear loop at 0.4% axial strain where twinning is not activated.

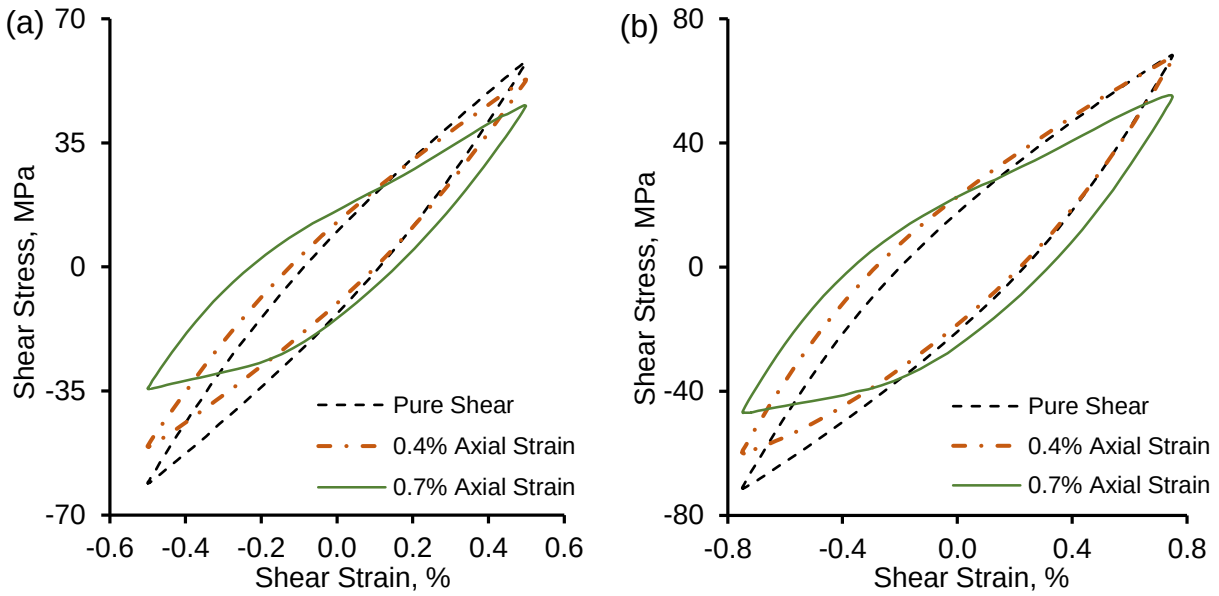

Fig 88: *Illustration of the effect of axial strain on the shear hysteresis loop for (a) 0.5% and (b) 0.75% shear strain amplitude.*

An evaluation of the shear loop energy associated with the in-phase multi-axial tests is presented in Fig 89 along with those obtained for pure cyclic shear. It is clear from this figure that the effect of axial loading on the positive elastic energy is similar to that for the reverse condition (i.e. the effect of shear loading on the axial behavior). Specifically, the addition of an axial strain amplitude lowers the elastic energy of the shear loop due to the contribution of the axial loading to the CRSS along the slip/twin planes associated with the shear deformation. Additionally, the added axial strain also increases the plastic energy dissipated during a cycle due earlier onset of plasticity resulting in loop widening. For example, and addition of 0.4% axial strain amplitude increases the plastic energy dissipation by ~13% and ~8% respectively for shear strain amplitudes of 0.5% and 0.75%, whereas an axial strain amplitude of 0.7% results in ~40% and ~23% increase in plastic energy for the low and high shear strain amplitudes respectively.

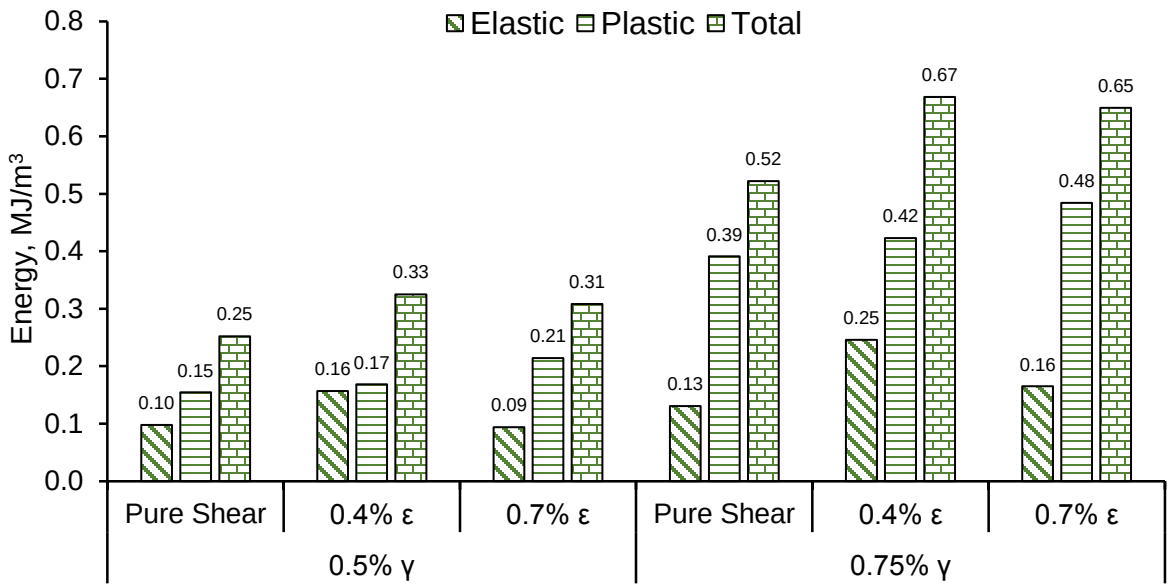

Fig 89: *Summary of shear hysteresis loop energy for different axial strain amplitudes.*

Fig 90 illustrates the cyclic shear hardening behavior for two shear amplitudes (0.5% and 0.75%) under pure shear, 0.4% axial strain amplitude and 0.7% axial strain amplitude respectively. It is clear that the pure shear conditions show little cyclic hardening as was previously presented in Fig 80a. The addition of an axial loading component increases the extent of cyclic hardening with higher axial amplitude corresponding to a greater degree of hardening. The higher hardening observed for combined axial and shear loading may be due to the effect of the twinning/detwinning mechanism active along the axial direction. As was previously presented in chapter 4 and also reported in [87], [130] the cyclic twinning/detwinning process results in a buildup of residual twins in the material. The continual accumulation of such residual twins would result in cyclically increasing twin boundary density which has been noted to impede dislocation movement along activated slip planes [131]. This effect of residual twin buildup is thought to be responsible for the higher cyclic shear hardening observed during combined shear and axial loading. It is interesting that a 0.4% axial strain shows a higher impact on cyclic shear hardening at 0.75% shear strain amplitude compared to 0.5% shear strain amplitude. This may be the result of the higher shear amplitude (0.75%) resulting in greater twin activation along the axial direction (Fig 85a) thereby increasing the fraction of residual twins compared to the 0.5% shear strain and 0.4% axial strain condition. Microstructural observations are recommended to confirm the presence of such residual twins.

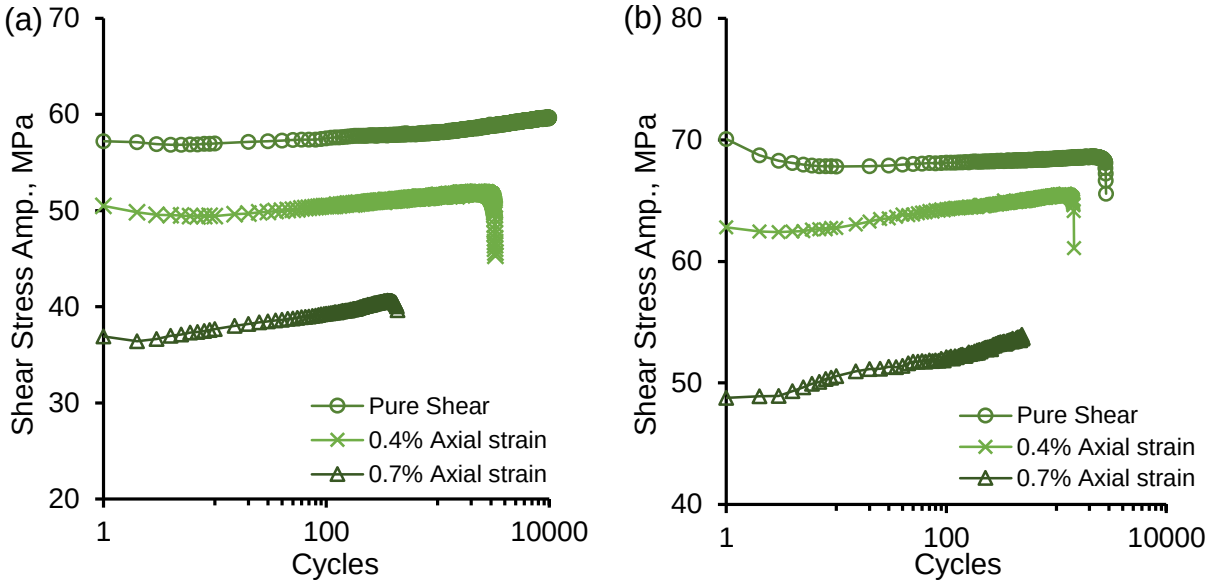

Fig 90: *Cyclic evolution of shear stress amplitude for different axial strain amplitudes observed for (a) 0.5% and (b) 0.75% shear strain amplitudes.*

Finally, it is interesting to note the effect of cyclic axial loading on the crack growth behavior of the current alloy. The primary fatigue crack at the end of life for 0.5% pure shear strain, 0.5% shear and 0.4% axial strains, and 0.5% shear and 0.7% axial strains are shown in Fig 91 a, b and c respectively. For the pure shear condition, the fatigue crack growth was aligned with the longitudinal axis of the sample. This was similar to that reported by Albinmousa et al. [86] as being a result of the longitudinal direction being the weakest material direction (considering material texture) for shear crack propagation. The addition of an axial strain component then changes the crack development from a shear mode to tensile cracking mode and this was observed at both shear strain amplitudes (0.5% and 0.75%). The change in cracking mode from shear to tensile cracking is expected to be a result of the different mechanisms being activated to accommodate plasticity along the two axes (e.g. basal slip during shear and non-basal slip/extension twinning during axial) however additional study is needed to identify the underlying cause for this transition. It should be noted however that the addition of a relatively small axial strain amplitude (viz. 0.4%) is sufficient to change crack behavior regardless of the two tested shear strain amplitudes.

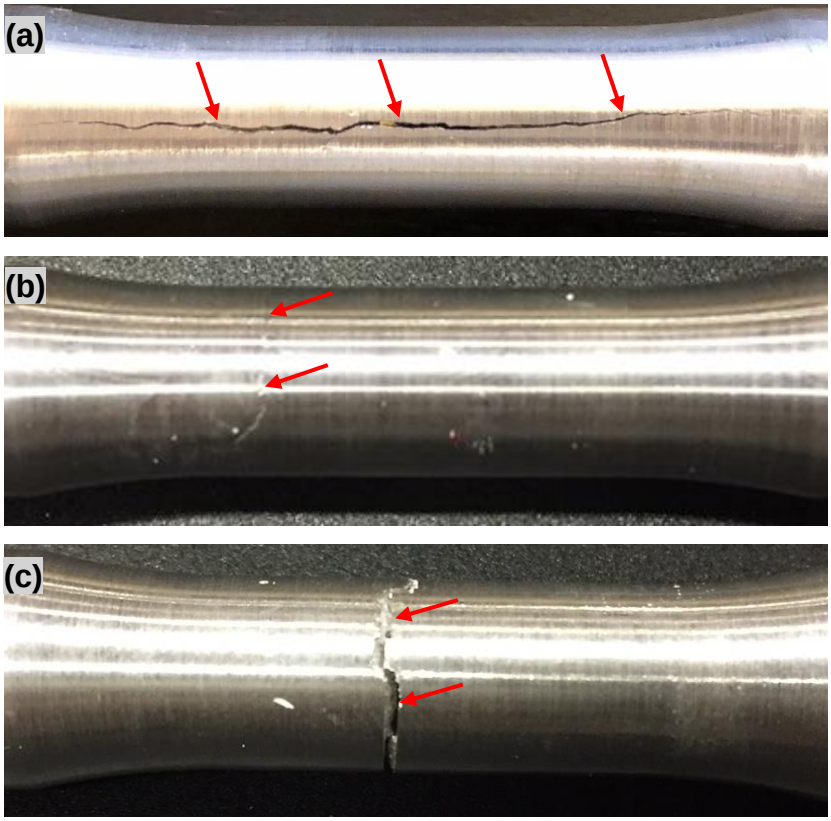

Fig 91: *Fatigue crack orientation following cyclic testing in (a) 0.5% shear strain, (b) 0.5% shear and 0.4% axial strains and (c) 0.5% shear and 0.7% axial strains. Note that the primary fatigue crack is indicated by the red arrows.*

6.2.4.2. Effect of Phase Angle

Multi-axial fatigue tests were performed at axial strain amplitudes of 0.4% and 0.7% and with a constant shear strain amplitude of 0.5%. The applied shear strain waveform was fixed to be either in-phase, 45° out-of-phase or 90° out-of-phase with the applied axial strain. The qualitative and quantitative effects on non-proportionality on the axial hysteresis loops are presented in Fig 92 and Fig 93 respectively. It is obvious from Fig 92 that changing the phase angle between the axial and shear strain amplitudes does not result in a significant change in shape of the axial hysteresis loops both for 0.4% and 0.7% axial strain amplitudes. Examination of the stabilized loop energies (Fig 93) yields further insight into the effect of non-proportionality. First is that non-proportionality does not appear to affect the positive elastic energy with elastic energy for the non-proportional cases being within 10% or less of the value for proportional loading. The degree of non-proportionality however does appear to have a greater effect on the plastic strain energy of the 45° out-of-phase condition but not with the 90° out-of-phase loading when compared to the in-phase condition. To be more specific, for axial strain amplitudes of 0.4% and 0.7% respectively, the plastic energy for the 45° out-of-phase

condition was found to be on average ~60% and ~20% lower than that for the in-phase condition, whereas for 90° out-of-phase, the plastic energy dissipation was within about 7% of the in-phase values. A similar insensitivity of the axial hysteresis loops to differences in loading phases was reported in previously discussed multi-axial literature [52], [56].

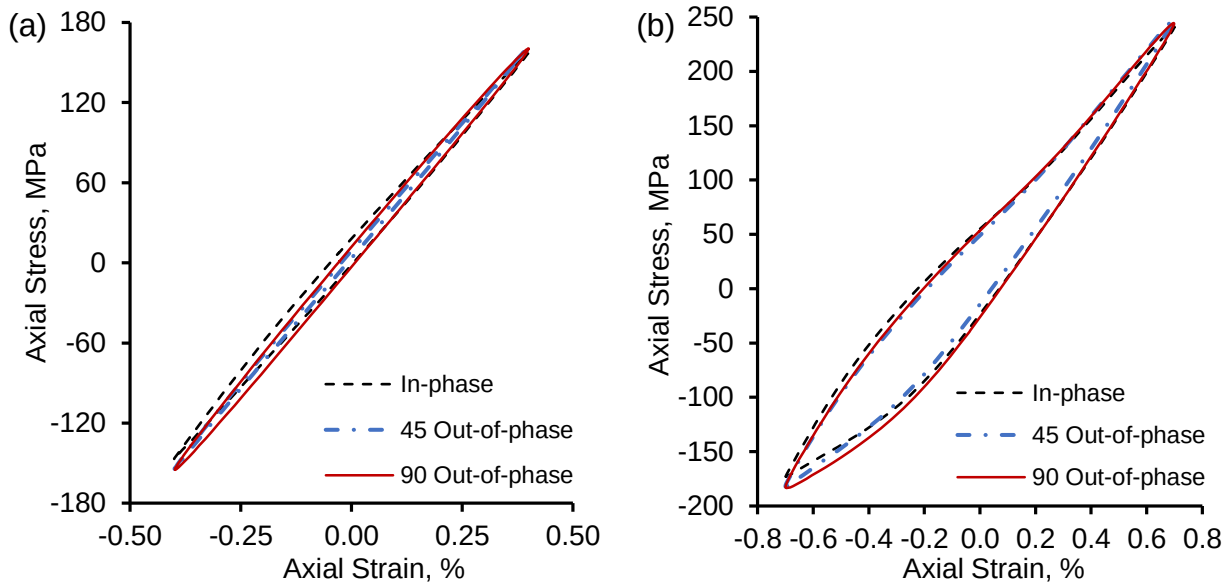

Fig 92: *Axial hysteresis loops for (a) 0.4% and (b) 0.7% axial strain amplitudes and for different phase angles. Note that shear strain amplitude is 0.5%.*

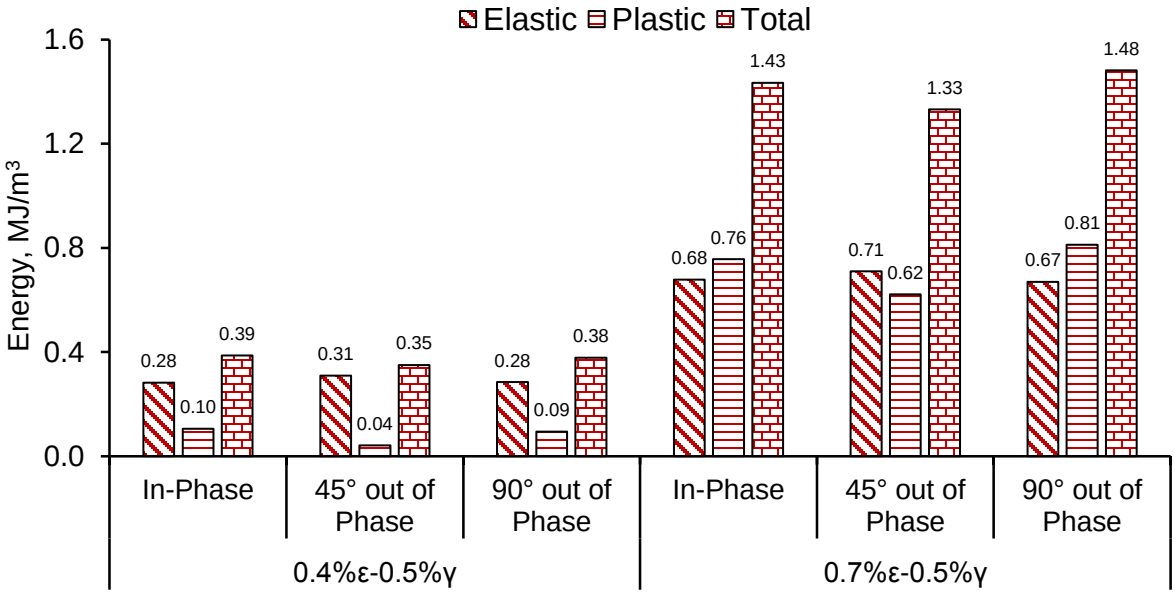

Fig 93: *Summary of axial hysteresis loop energy for different phase angles.*

The cyclic evolution of axial stress amplitude at the tested axial strain amplitudes and various phase angles is illustrated in Fig 94 for a constant shear strain amplitude of 0.5%. It is observed that

at 0.4% axial strain amplitude, non-proportionality has no noticeable impact on the degree of cyclic hardening. However, when the axial strain amplitude is increased to 0.7% a contribution of non-proportionality is visible with the degree of hardening increasing with the degree of non-proportionality. This may be understood by considering that the direction of the principal stress axes change in non-proportional loading [132]. Such a change in the principal axes would result in additional slip along planes with normally insufficient CRSS under proportional loading [133], thereby increasing overall dislocation movement and subsequent pile at microstructural barriers (such as twin boundaries) resulting in increased hardening. The lack of a significant degree of additional hardening due to non-proportionality at 0.4% axial strain amplitude is thought to be due to the low degree of plasticity achieved at this strain amplitude diminishing the effect of non-proportionality on slip activation.

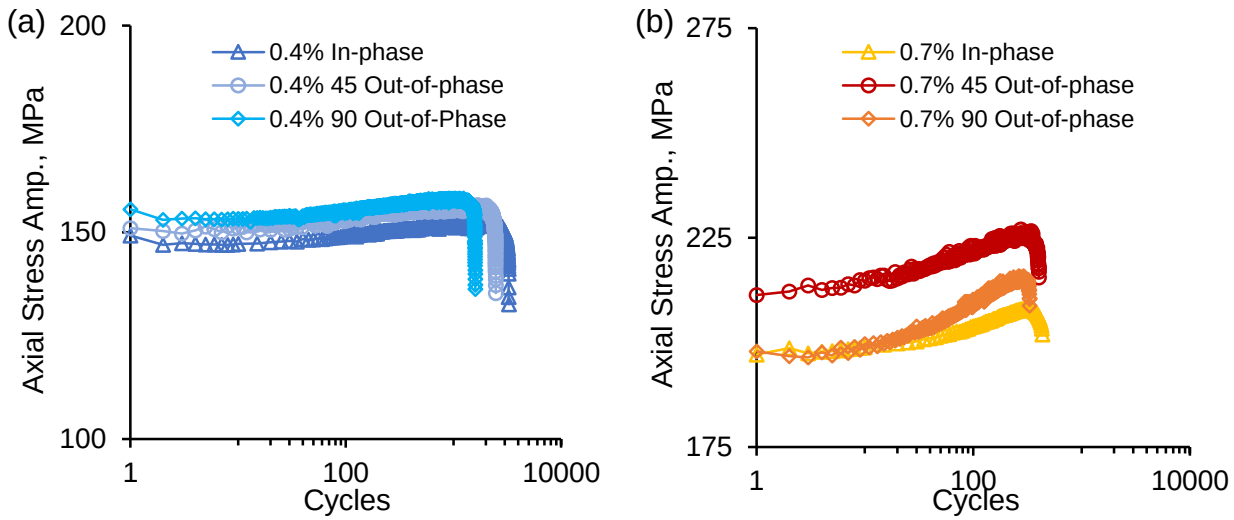

Fig 94: *Cyclic evolution of (a) 0.4%, and (b) 0.7% axial strain amplitude and different phase angles.*

As opposed to what was presented in Fig 92, non-proportionality has a far more pronounced effect on the cyclic shear behavior as is obvious from Fig 95. At low axial strain amplitude (0.4%), non-proportionality increases the loop area while maintaining the overall shape of the hysteresis loop. Increasing the axial strain amplitude to 0.7% reveals a substantial change in the shape of the shear hysteresis loop with changes in phase angle. At both axial strain amplitudes, the 45° out-of-phase condition produces larger hysteresis loops than the in-phase and 90° out-of-phase conditions. Quantitatively, for both axial strain amplitudes, the positive elastic is largely invariant with phase difference (Fig 96). However plastic energy dissipation varies substantially with phase angle as can be observed for the 0.7% strain amplitude condition where non-proportionality increases plastic loop

energy by ~67% and ~14% respectively for 45° out-of-phase and 90° out-of-phase loading. The significant change in the shear hysteresis loop as a result of non-proportionality was recognized by Albinmousa et al. [53] for extruded AZ31B and was attributed to a change in the activation of extension twinning along the axial direction relative to the current loading condition of the shear loop; an illustration of this concept is shown in Fig 97 and Fig 98.

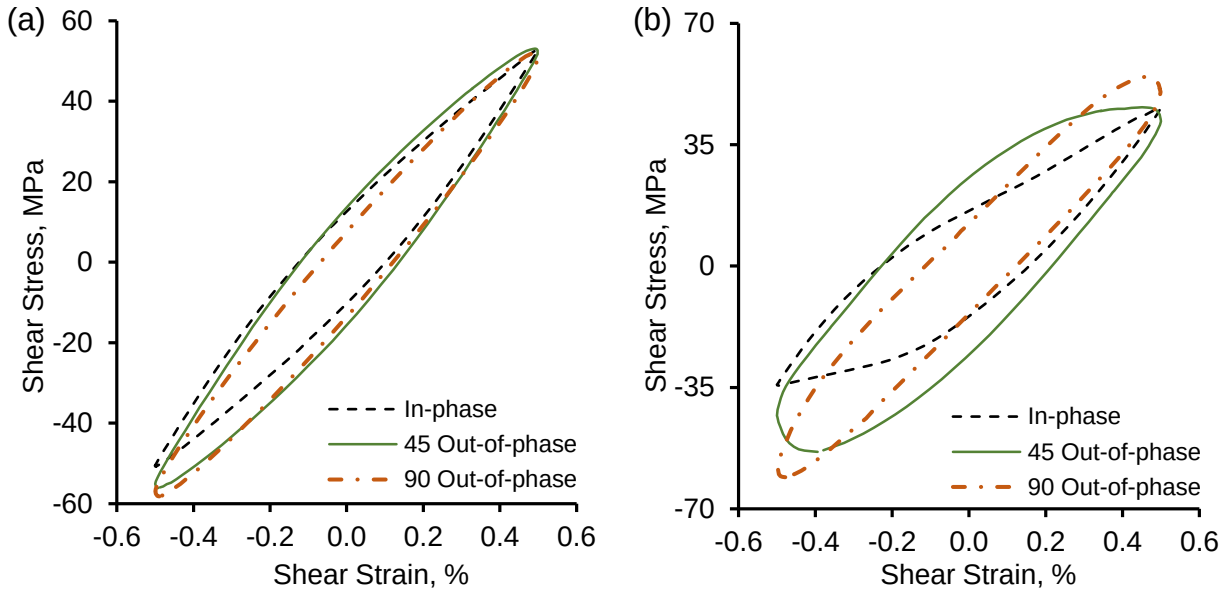

Fig 95: *Shear hysteresis loops for (a) 0.4% and (b) 0.7% axial strain amplitudes and for different phase angles. Note that shear strain amplitude is 0.5%.*

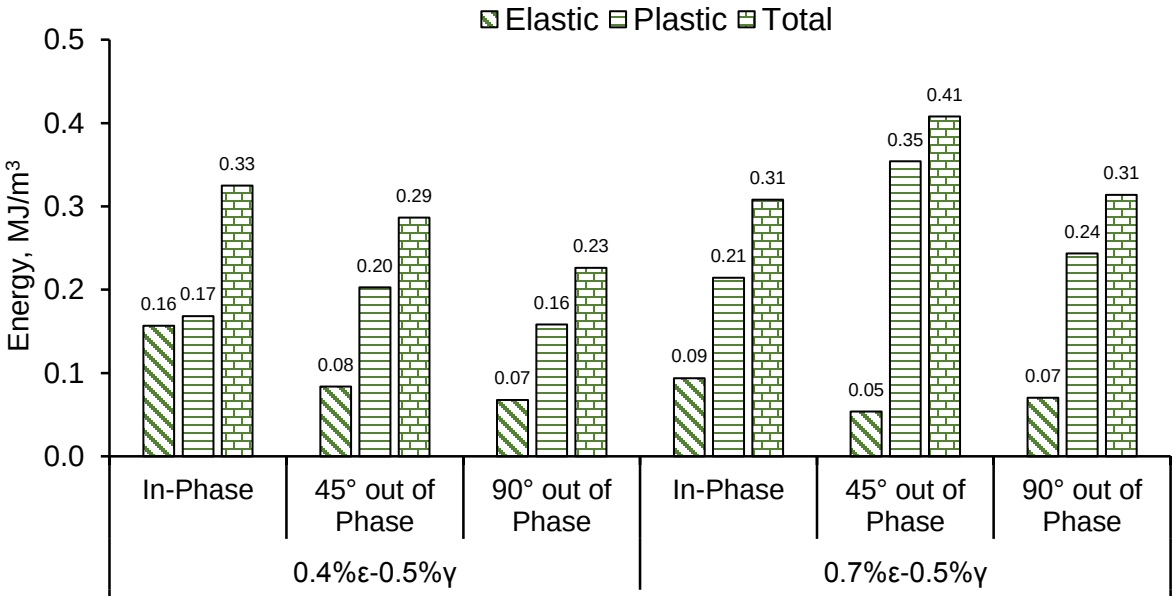

Fig 96: *Summary of shear hysteresis loop energy for different phase angles.*

During in-phase loading, both axial and shear strain peaks are achieved simultaneous as illustrated in Fig 97a. Due to the texture of the forged material, extension twinning gets activated between points 3 and 4 of the axial loop Fig 97b. As discussed previously (section 6.2.4.1), the re-orientation of the twinned sections increases the propensity for basal slip in the twin resulting in earlier yielding between points 3 and 4 of the shear loop (Fig 97c). Between points 4 and 5 of the axial loop de-twinning occurs and saturates between points 5 and 2. As detwinning occurs and saturates, twin volume fraction decreases, and makes basal slip in the material more difficult, producing the mild inflection observed between points 5 and 2 of the shear loop. Therefore, the activation of extension twinning along the axial direction is responsible for the asymmetry of the shear loop during in-phase multi-axial loading.

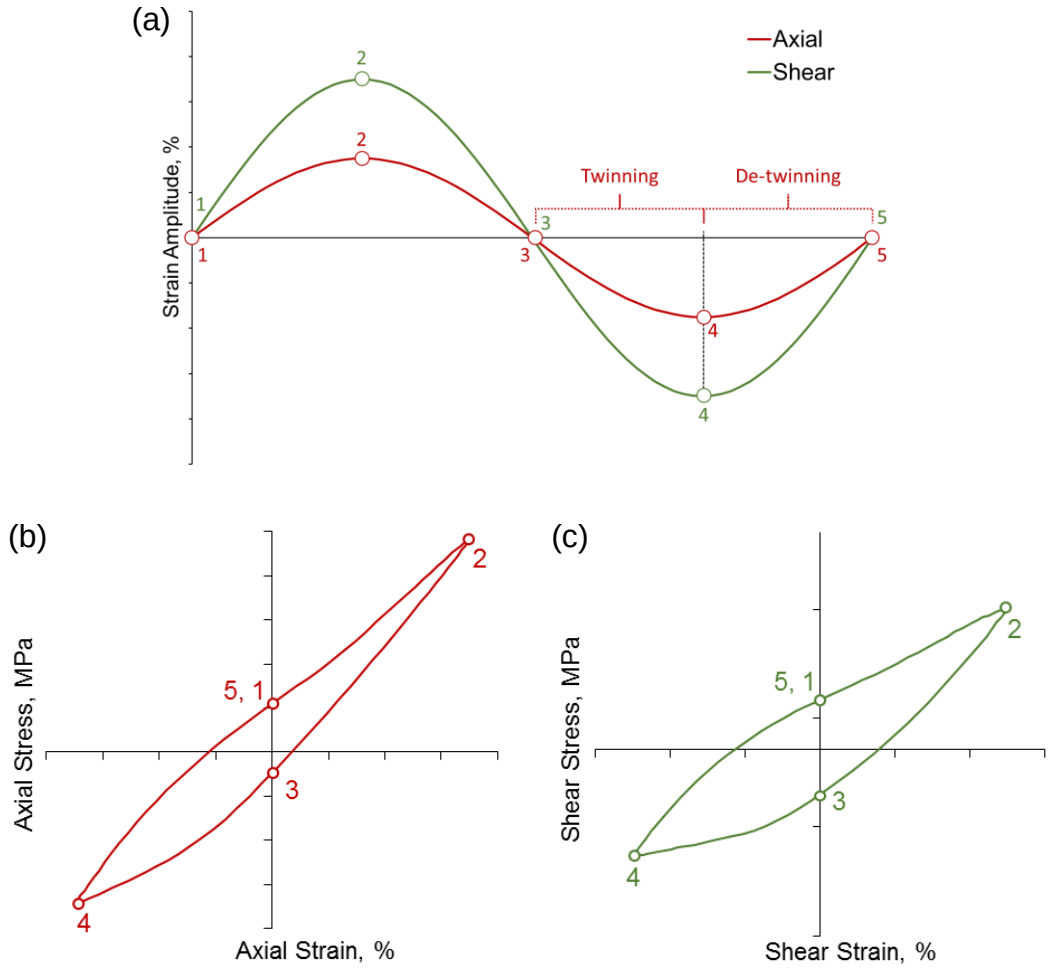

Fig 97: *Illustration of (a) in-phase axial and shear strain waveforms, (b) stabilized axial hysteresis loop and (c) stabilized shear hysteresis loop.*

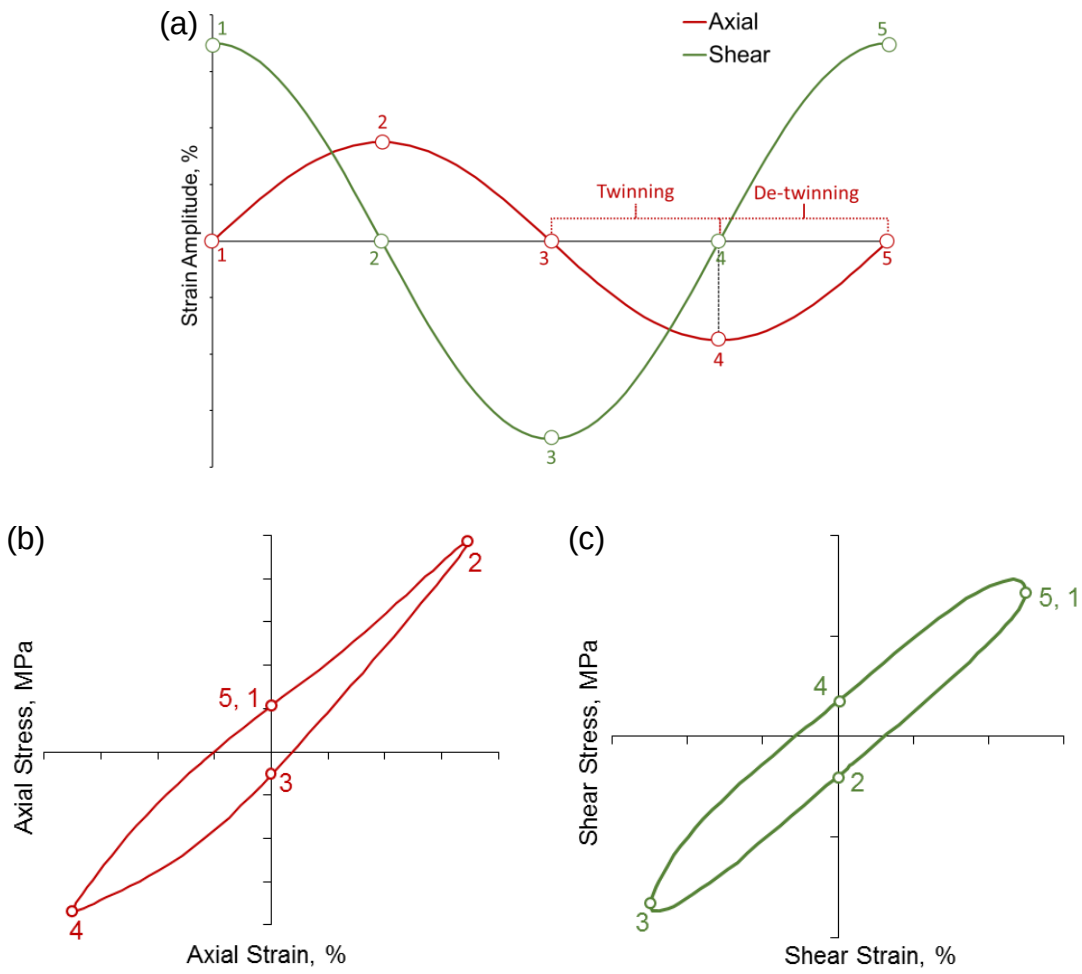

Fig 98: *Illustration of (a) 90° out-of-phase axial and shear strain waveforms, (b) stabilized axial hysteresis loop and (c) stabilized shear hysteresis loop.*

However, when the phase angle between the two waveforms is changed, for example to be 90° out-of-phase, the peak axial strain amplitudes are achieved when the shear strain amplitude is zero and vice-versa (Fig 98a). As a result, during twin activation along the axial direction (between points 3 and 4 in Fig 98b), the peak negative shear strain already been achieved and elastic shear unloading is already in progress. As shear reloading occurs (points 4 – 5), de-twinning initiates in the axial direction with the majority of detwinning occurring while the shear loop is still in the elastic regime. In other words, the easier motivation of basal slip afforded by twinning is not exploitable by the shear direction as the material is virtually elastic during this phase. Finally, as both waveforms approach point 5, the shear stress in the material is sufficient to initiated plasticity however, due to the changing orientation of the principal axes, various slip systems are activated to accommodate this plasticity resulting in a drop in stress with increasing shear strain (point 5) until the selected shear

strain amplitude is achieved. Note that when the axial strain lags the shear strain by 45°, some overlap occurs between shear loading and extension twin activation, resulting in a shear loop with characteristics of both in-phase and 90° out-of-phase as is evident from Fig 95b.

The effect of non-proportionality on cyclic shear hardening is shown in Fig 99. It's clear that some degree of softening occurs during the initial cycles followed by cyclic hardening for most of the tested conditions. At low axial strain amplitudes (Fig 99a), there is little variation in the extent of cyclic hardening due to changes in phase angle with the 90° out-of-phase tests showing only slightly higher hardening that the other two conditions. As in the case with the axial direction, increasing the axial strain amplitude results in a corresponding increase in the cyclic shear hardening along with a noticeable phase angle effect. Specifically, for an axial strain amplitude of 0.7%, both in-phase and 45° out-of-phase tests exhibited a similar degree of cyclic shear hardening, however, the 90° out-of-phase tests yielded substantially high cyclic hardening. This increased non-proportional hardening was also observed for extruded AZ31B [53] and AM30 [56] and was attributed to a rotation of the principal axes occurring as a result of the phase difference between the axial- and shear- strain waveforms as was discussed previously for axial hardening.

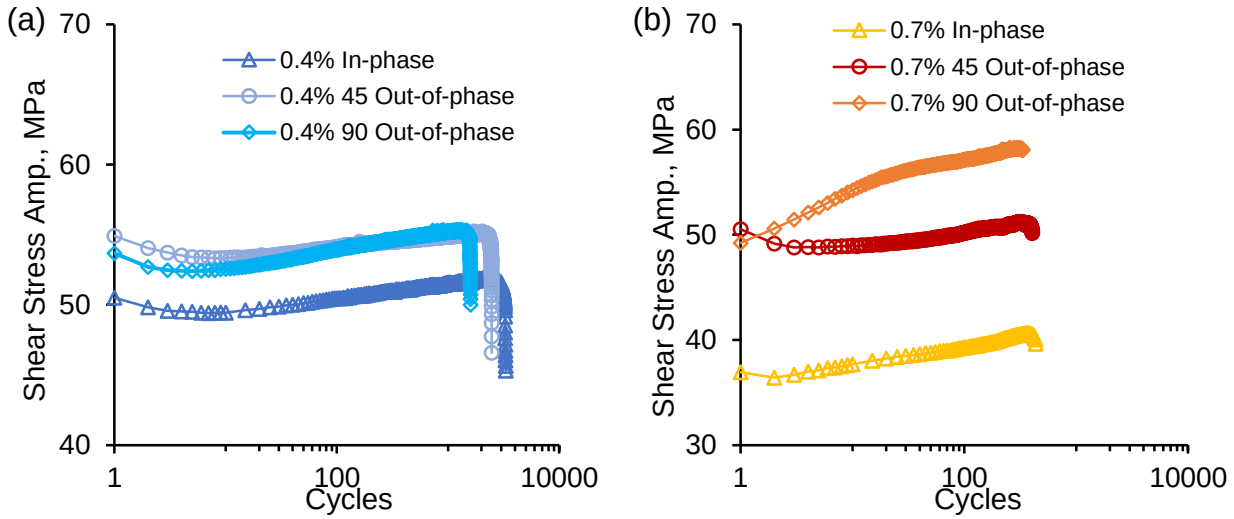

Fig 99: *Cyclic evolution of shear stress amplitude for (a) 0.4%, and (b) 0.7% axial strain amplitude and different phase angles.*

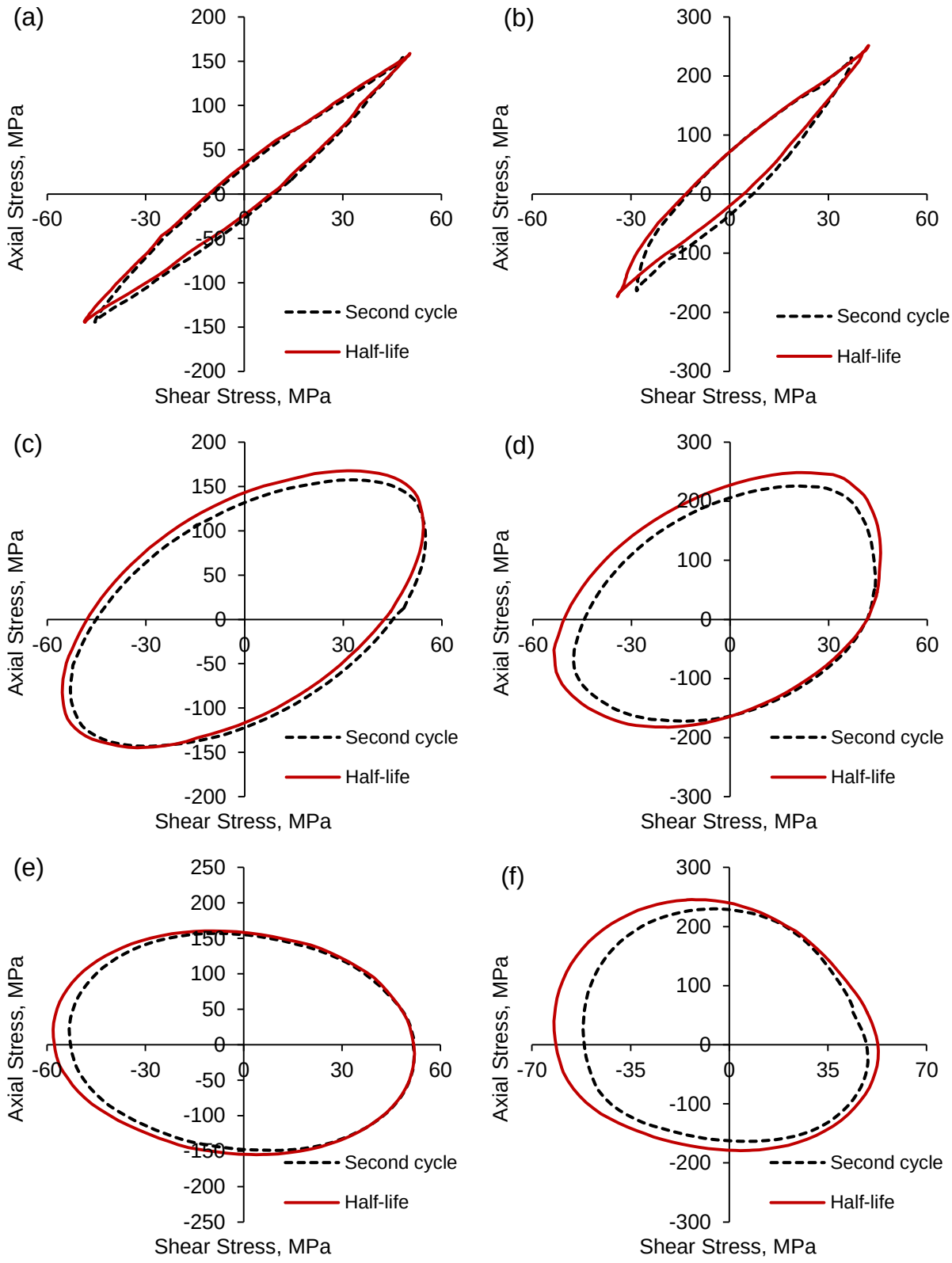

Fig 100: *Plots of axial stress vs. shear stress for (a, b) in-phase, (c, d) 45° out-of-phase and (e, f) 90° out-of-phase multi-axial tests with axial strain amplitudes of (a, c, e) 0.4% and (b, d, f) 0.7% respectively. Note: The shear strain amplitude was constant at 0.5%.*

Another way to visualize the effects of non-proportionality on cyclic hardening is to examine the plots of axial versus shear stress for the various multi-axial test conditions (Fig 100). Fig 100 confirms the results presented above by illustrating the general increase in overall cyclic hardening as the phase difference between the axial and shear waveforms increases (suggested by increase in the size of the area bounded by the plot between the second and half-life cycles). At low axial strain amplitudes (Fig 100 a, c, e) the extent of cyclic hardening is low for all conditions due to the generally low amount of plasticity incurred at this strain amplitude. However, a clear increase in hardening is observed between the in-phase (Fig 100a) and 90 out-of-phase (Fig 100e) conditions, particularly along the shear axis. This is consistent with the observations made in Fig 99a. When the axial strain amplitude was increased to 0.7% (Fig 100 b, d, f), overall cyclic hardening for all three phase angles was increased due to the increased activation of slip/twin systems associated with the higher strain amplitude. The plot of axial vs. shear stress confirms the results presented in Fig 94b and Fig 99b which showed increased extent of cyclic hardening as non-proportionality increased. Note also that the effect of non-proportionality on cyclic hardening was more pronounced for the shear axis. As stated previously, the increased hardening occurring due to non-proportionality is thought to be due the rotation of the principal axis, activating additional deformation mechanisms, and affording more dislocation motion and pileup.

Finally, the obtained fatigue lives for the various multi-axial tests are presented in Fig 101 which shows that both the in-phase and 45° out-of-phase tests yield similar life values, whereas the fatigue life for the 90° out-of-phase tests were slightly poorer. This result was slightly different from those observed for extruded AZ31B where no considerable effect of phase angle was reported [52], [53] however it similar to the results of Roostaei et al. [56] in which in-phase loading yielded slightly superior fatigue life compared to out-of-phase loading. The lower fatigue lives observed for the 90° out-of-phase tests line up well with the additional cyclic hardening observed for this loading scenario which has been reported to be deleterious to fatigue life [132], [134], [135].

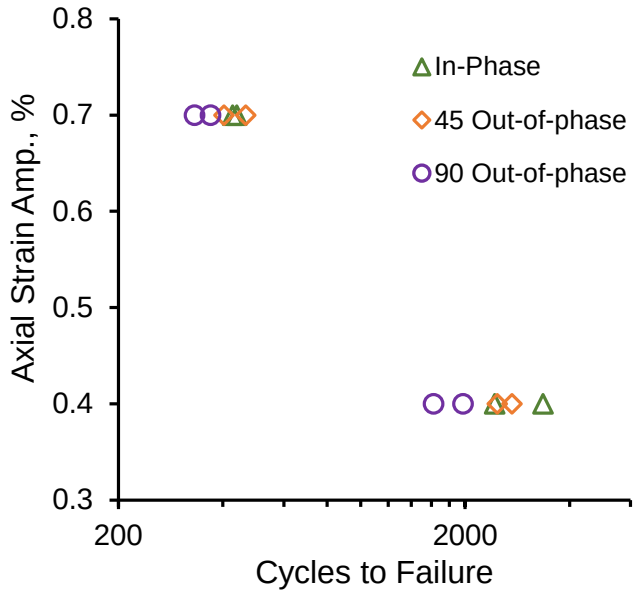

Fig 101: *Axial strain amplitude vs. cycles to failure for bi-axial tests performed at different phase angles. Note that the shear strain amplitude was kept constant at 0.5%.*

It should be noted that Xiong et al. [57] and Yu et al. [58] noted a significant discrepancy between fatigue lives of Mg alloys for proportional (in-phase) and non-proportional (out-of-phase) loading however, these authors employed an equivalent plastic strain method which required the application of different axial and shear strain amplitudes depending on the employed strain path. Consequently, the fatigue life results of these studies may not be directly comparable to those investigated in this chapter.

6.3. Fatigue Modelling

6.3.1. Modified Smith-Watson-Topper model

The original SWT fatigue model was introduced in section 4.3.2.1 and was developed for predicting fatigue life under uniaxial loading conditions. The SWT damage parameter was employed by Socie and Marquis [136] for multiaxial fatigue analysis when the failure mode was dominated by tensile cracking. In their work, Socie and Marquis replaced the normal strain range listed in Eq. 9 with the principal strain range. Other studies however have reported an inability of this model to accurately account for shear cracking behavior [53], [57]. To remedy this shortcoming, Jiang and Sehitoglu [137] proposed a modification to the SWT criterion (MSWT) by accounting for a generalized cracking mode. Their modification took to form of:

$$\boldsymbol{MSWT\ parameter} = \boldsymbol{2b\Delta\varepsilon\sigma_{max}} + \boldsymbol{\frac{1-b}{2}\Delta\tau\Delta\gamma} \qquad (16)$$

Where $\Delta\varepsilon$, $\Delta\tau$ and $\Delta\gamma$ are the ranges for axial strain, shear stress and shear strain respectively. Note that *b* is a material constant that represents the cracking mode and varies from 0 to 1. For $b = 1$, Eq. 16 reduces to the original SWT parameter. It has been suggested that $b \leq 0.37$ represents shear cracking whereas $b \geq 0.5$ represents tensile cracking, and values between 0.37 and 0.5 suggest a mixed cracking mode [57], [58].

For the current forged alloy, the value of *b* was set by considering pure cyclic axial and pure cyclic shear experimental data and plotting the corresponding MSWT parameter versus reversals to failure ($2N_f$) on a log-log plot Fig 102a. The value of *b* was varied until the best fit regression curve was obtained for the amalgamation of both data sets. Based on this method, the value of *b* for the current alloy was found to be 0.2 and the resulting regression curve was found to be:

$$\boldsymbol{MSWT\ parameter = 24.148\left(2N_f\right)^{-0.373}} \qquad (17)$$

Eq. 16 and Eq. 17 can then be combined (Eq. 18) and used along with experimental data to predict the fatigue live of the current forged alloy under both uniaxial and bi-axial loading scenarios.

$$\boldsymbol{2b\Delta\varepsilon\sigma_{max} + \frac{1-b}{2}\Delta\tau\Delta\gamma = 24.148\left(2N_f\right)^{-0.373}} \qquad (18)$$

A plot of the MSWT parameter for all the current cyclic loading conditions calculated using Eq. 18 and $b = 0.2$ and included in Fig 102b. It is clear that the calculated MSWT parameter versus number or reversals for all loading scenarios follow a strong linear trend on a log-log scale supporting the suitability of this model for the current set of experiments. Indeed a plot of experimental life against predicted life (Fig 102c) clearly shows that the obtained model yields good life predictions for both uniaxial and multi-axial cyclic loading with the majority of predictions falling within a factor of ±1.5 (dashed black lines) and no prediction exceeding a factor of ±2 (solid black lines).

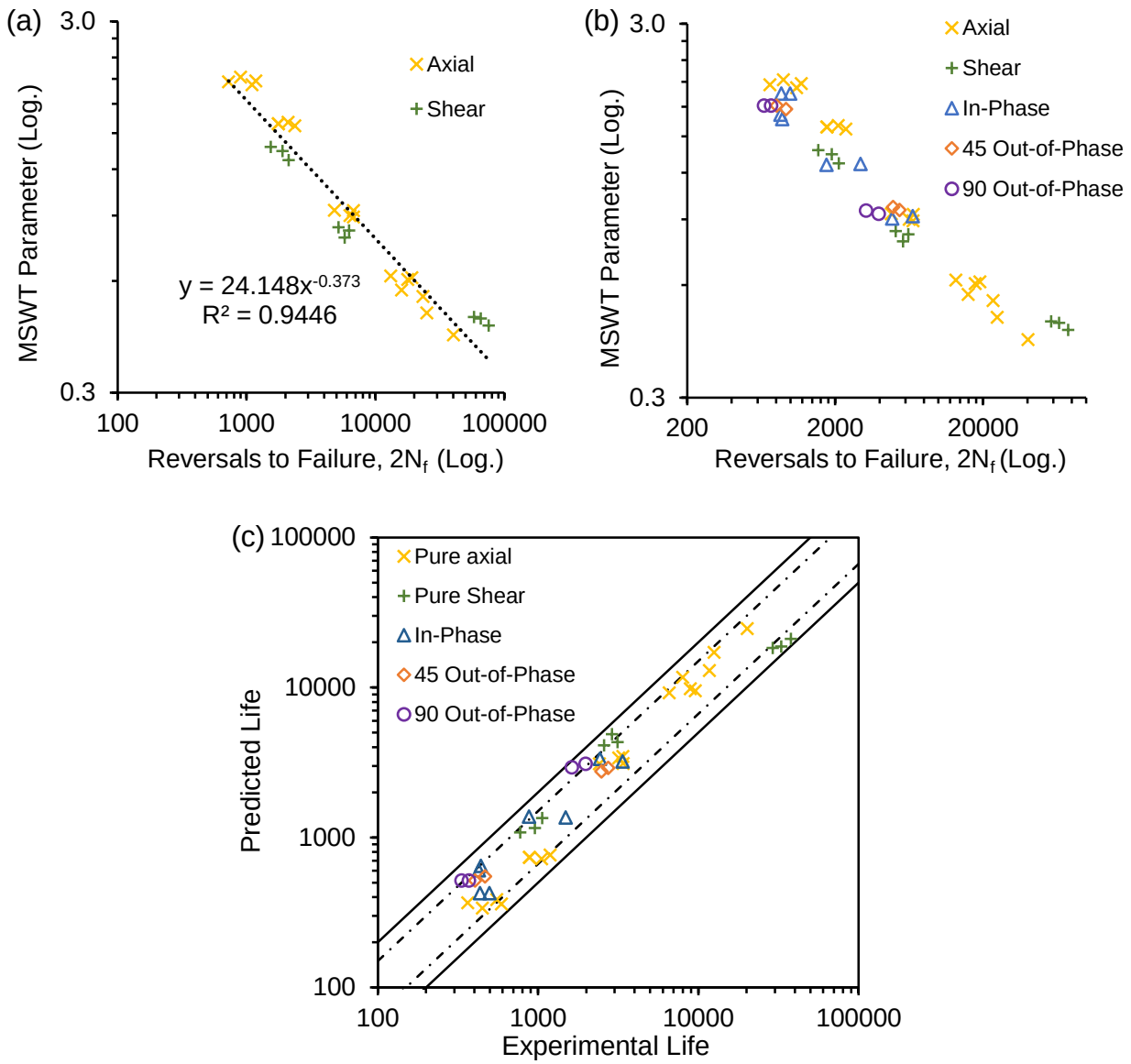

Fig 102: *Log-log plots of (a) MSWT parameter vs. reversals used to calibrate the model, (b) MSWT parameter vs. reversals for all closed-die forged cyclic tests and (c) predicted life vs. experimental life for the calibrated MSWT model. Note: Dashed black lines represent factor of 1.5 bands and solid black lines represent factor of 2 bands on life prediction.*

It should be noted that only shear strain amplitudes up to 0.5% were considered for model calibration as the axial- and shear- strain amplitudes employed during multiaxial loading were limited to low cycle fatigue range where non-proportionality may have a meaningful influence on fatigue life.

6.3.2. Jahed-Varvani Energy model

The Jahed-Varvani (JV) energy model was introduced in chapter 4 and is expected to provide good fatigue life predictions for asymmetric Mg alloys due to the invariant nature of strain energy density. Albinmousa et al. [138] successfully adopted this energy model for the first time to predict fatigue life of AZ31B extrusion under multi-axial loads. A detailed description of the JV model is included in section 4.3.2.2. For the current study, the JV energy parameters were evaluated for both pure cyclic axial and shear data. The two independent models are then combined to provide life predictions for multi-axial loading conditions.

6.3.2.1. JV Axial Model

The total energy dissipated during the stabilized cyclic can be separated into positive elastic (E_e^+) and plastic (E_p) components. The elastic energy per cycle is calculated according to Eq. 11 and the plastic energy per cycle is represented by the area of the stabilized hysteresis loop. Plotting the elastic and plastic energies respectively versus the cycles to failure (Fig 103a) provides the axial JV model parameters (Eq. 19) which are summarized in Table 10.

$$\boldsymbol{E_a = E'_e(N_a)^B + E'_f(N_a)^C} \qquad (19)$$

Table 10: *Summary of axial JV parameters for closed-die forged AZ31B.*

	E'_e [MJ/m^3]	B	E'_f [MJ/m^3]	C
Closed-die Forged AZ31B	10.97	-0.37	935.44	-1.05

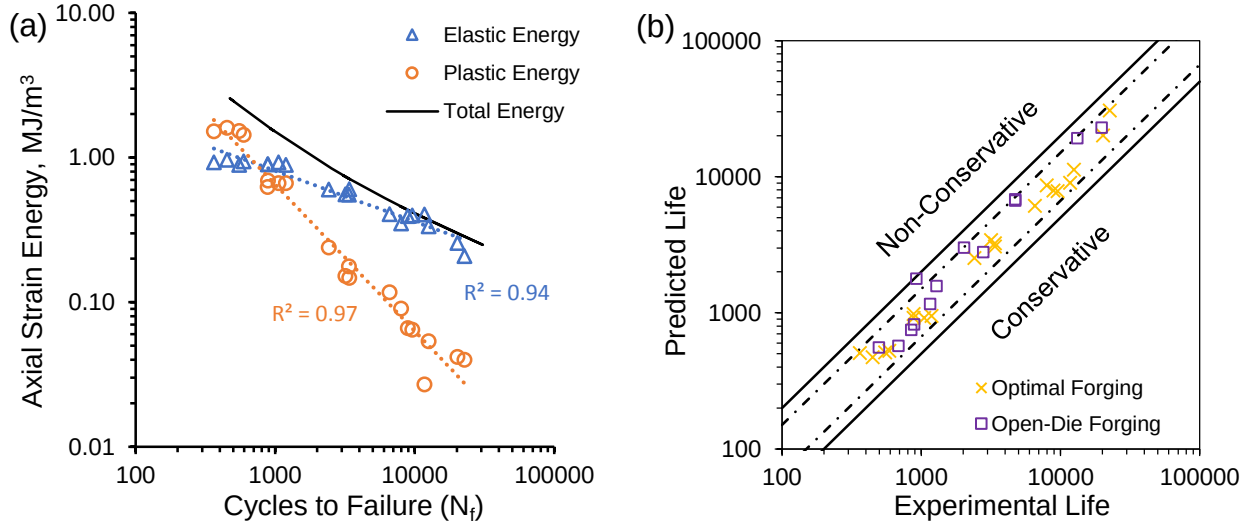

Fig 103: *Plots showing (a) log of elastic and plastic energy vs. cycles for pure cyclic axial tests, and (b) predicted vs. experimental life for open-die and closed-die forged AZ31B. Note: Dashed black lines represent factor of 1.5 bands and solid black lines represent factor of 2 bands on life prediction.*

The predictive capability of the obtained axial JV model is illustrated in Fig 103b where the model is capable of predicting all the cyclic axial data for closed-die forged AZ31B within a factor of ±1.5. As a comparison, the model was also used to predict life for the open-die forged alloy discussed in chapter 4, and was found to yield good predictions within a factor of ±2.

6.3.2.2. JV Shear Model

The formulation of the JV model for cyclic shear is analogous to that of the axial model:

$$W_s = W'_e(N_s)^F + W'_f(N_s)^G \qquad (20)$$

And the elastic loop energy is defined as:

$$W_e = \left(\frac{\tau^2_{max} + \tau^2_{min}}{2G}\right) \qquad (21)$$

W'_e, F, W'_f, G are energy-based cyclic shear properties determined in an identical manner as in the axial direction (Fig 104b) and the elastic energy is the sum of positive and negative elastic energy (Fig 104a) as specified in [108]. The values of these parameters calculated for the current alloy have been summarized in Table 11.

Table 11: *Summary of shear JV parameters for closed-die forged AZ31B.*

	W'_e [MJ/m^3]	F	W'_f [MJ/m^3]	G
Closed-die Forged AZ31B	1.00	-0.15	5.65	-0.33

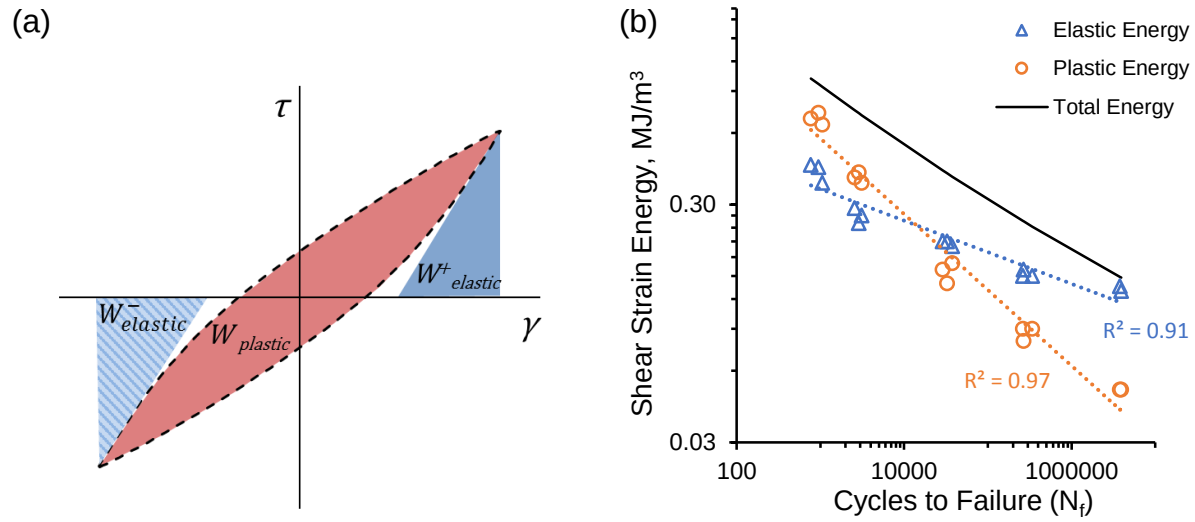

Fig 104: *Illustration of (a) elastic and plastic energy components of cyclic shear hysteresis loops, and (b) elastic and plastic energy vs. cycles to failure for pure cyclic shear tests.*

The predicted life for the pure cyclic shear tests versus their experimentally obtained values using the developed JV model is shown in Fig 105. It is clear that the prediction provided by this model is not as good as that obtained for the axial model. The comparatively poorer prediction offered by the shear model is a result of the much larger range of data for which the model is constructed. Specifically, the axial model was generated specifically for low cycle fatigue tests (up to ~ 10^4 cycles) whereas, the shear model was calibrated for tests extending into the 10^6 range of life. At these very high fatigue lives, the assumption of elastic and plastic energy being linearly related to cycles (on a log scale) breaks down resulting in inaccuracies of prediction.

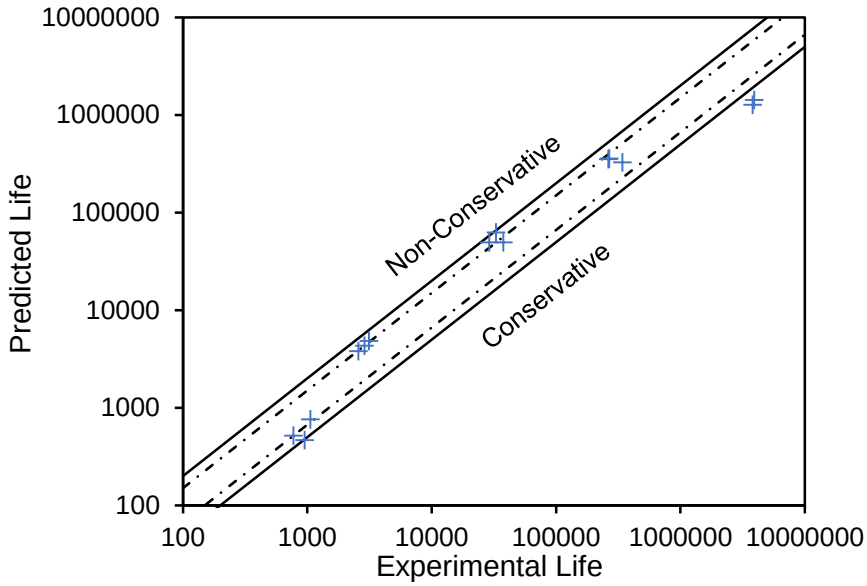

Fig 105: *Plot showing predicted vs. experimental life for closed-die forged AZ31B under cyclic shear. Note: Dashed black lines represent factor of 1.5 bands and solid black lines represent factor of 2 bands on life prediction.*

6.3.2.3. JV Multi-axial Model

Fatigue life predictions for multi-axial tests were obtained by considering an independent equivalent fatigue life prediction for both the axial (N_a) and shear (N_s) models assuming the total multi-axial energy dissipation (E_{total}) to be equal to the total energy dissipation for a uniaxial test (i.e. $E_a = E_{total}$ in Eq. 19 and $W_s = E_{total}$ in Eq. 20). These independent axial/shear life predictions were then weighted by considering the ratio of axial/shear energy to total multi-axial energy according to Eq. 22 [107].

$$\boldsymbol{N_f = \left(\frac{E_a}{E_{total}} N_a + \frac{W_s}{E_{total}} N_s\right)} \qquad (22)$$

A plot of the total experimental energy dissipation (as a damage parameter) versus cycles to failure for both pure cyclic axial and pure cyclic shear tests is shown in Fig 106a from where it can be seen that for a give total value of energy, shear loading appears to be slightly more damaging compared to axial loading, and similar to the various multiaxial loading conditions. A similar observation was reported in [53]. Fig 106b shows the predicted versus experimental life for the various multi-axial tests using the presented multi-axial JV model. This model is capable of good life prediction for in-phase and 45° out-of-phase loading within a factor of ±1.5. Note that 90° out-of-phase conditions tend to be slightly over predicted although still within the generally accepted error bands of ±2.

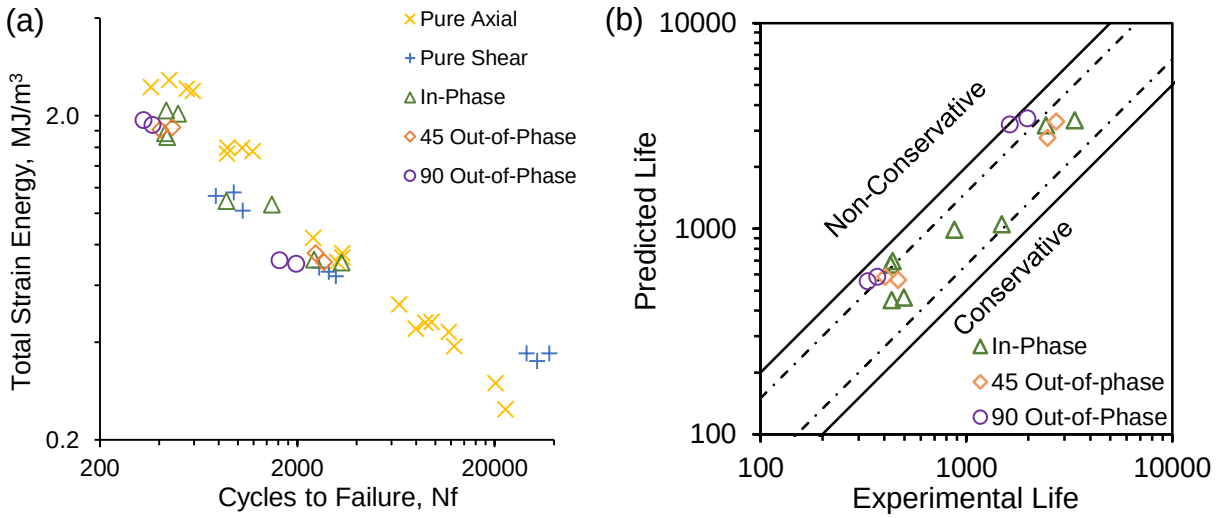

Fig 106: *Plot of (a) total energy vs. cycles to failure for all cyclic tests on a logarithmic scale, and (b) predicted vs. experimental life for closed-die forged AZ31B under multi-axial loading and different phase angles using the JV model. Note: Dashed black lines represent factor of 1.5 bands and solid black lines represent factor of 2 bands on life prediction.*

6.4. Chapter Conclusions

Pure axial, shear, and multi-axial cyclic tests were performed on extruded AZ31B alloy that was closed-die forged at a temperature of 250°C and the following observation were made:

- The current forged alloy exhibited an overall improvement in axial fatigue response and cyclic strengths compared to the starting as extruded condition.
- The texture developed in the forged AZ31B resulted in asymmetric axial hysteresis loops for axial strain amplitudes above 0.5%.
    - Significant cyclic hardening was also noted for these higher axial strain amplitudes.
- Cyclic shear tests resulted in stabilized hysteresis loops that were virtually symmetric at all tested shear strain amplitudes.
    - All tested shear strain amplitudes demonstrated only minor cyclic hardening.
- In-phase multi-axial tests combining various axial and shear strain amplitudes indicated that the each strain component affected the hysteresis loop of the other generally resulting in a decrease in positive elastic energy and an increase in plastic energy.
- Changing the phase angle between the applied axial and shear strain amplitudes exhibited a minor effect on fatigue life.
    - The effect of non-proportionality was far more pronounced on the shear hysteresis behavior than on the axial hysteresis behavior.
    - Non-proportional loading did result in additional cyclic hardening compared to the proportional condition.
- A modified SWT model provided good prediction for both uni-axial and multi-axial fatigue scenarios.
- The Jahed-Varvani (JV) energy model was also found to provide good prediction for most of the tested loading scenarios.

Chapter 7: Conclusions and Future work

7.1. Thesis Conclusions

This thesis investigated the effect of a forging process on the microstructural and mechanical response of AZ31B magnesium alloy. In chapters 3 and 4, the effect of simple open-die forging was investigated to identify the potential benefits of the process. Chapter 5 investigated a more complex closed-die forging process along with the effects of temperature and starting material condition and ended with the selection of an optimal setting for these parameters. Lastly a full quasi-static and fatigue characterization of AZ31B forged at the optimal condition was performed along with the evaluation of several fatigue models. The conclusions of each of these stages of testing were included at the end of their relevant chapters and have been reiterated below for convenience.

Chapter 3

- Forging as-cast AZ31B at 450 °C at a speed of 39 mm/min resulted in a partially recrystallized grain structure with a bimodal grain size distribution.
- Forging resulted in an increase in the tensile-compression asymmetry of the alloy. However, a substantial increase in tensile yield strength of 143 percent and ultimate strength of 23 percent was measured while the maximum yield strength and ultimate strength in compression increased by 75 percent (in the FD) and 22 percent respectively.
- Microstructure and texture analysis of the forged specimens compressed at room temperature showed that $\{10\bar{1}2\}\langle 10\bar{1}1\rangle$ extension twins controlled the deformation along the LD/TD accompanied by a c-axis rotation of about 86.3° to be aligned with the compression direction. Extension twinning also occurred in the as-cast samples although to a lesser degree.
- The occurrence of extension twinning in the as-cast material during tension loading appeared to increase the overall elongation of the specimens prior to failure resulting in the as-cast material displaying higher failure elongation compared to the forged material.

Chapter 4

- Dynamic recrystallization resulted in the occurrence of grain refinement in the forged alloy along with a development of a basal texture such that the basal planes were perpendicular to the forging direction.

- The as-cast condition displayed symmetric cyclic tension-compression deformation due to the random texture of the cast alloy whereas, the forged condition displayed substantial asymmetry due to the activation of $\{10\bar{1}2\}\langle 10\bar{1}1\rangle$ extension twinning in compression and subsequent detwinning followed by slip during tension.
- In general, the forged material displayed in overall improvement in low cycle fatigue life compared to the as-cast material attributed to the refined grain morphology, absence of casting defects, dissolution of intermetallics and texture modification.
- The strain-based SWT model and energy-based JV model both yielded good fatigue life prediction for both as-cast and forging conditions within the range of tested strain amplitudes.

Chapter 5

- Closed-die forging at both temperatures and for both cast and extruded conditions resulted in a partly recrystallized microstructure and a change in texture such that c-axes were reoriented to lie parallel to the localized deformation direction.
- Superficial hardness mapping suggested inhomogeneous strain distribution during forging with higher hardness values being observed in the web compared to the flanges.
    - The variance in hardness values was higher for the cast and forged conditions with the variation decreasing with higher forging temperature.
- Quasi-static tension tests confirmed the inhomogeneity suggested by the superficial hardness measurements with the web region exhibiting higher strengths compared to the two flange regions.
    - The difference between the tensile curves for the flanges and the web was much more pronounced for the cast and forged conditions, and for both starting conditions (cast/extruded), the discrepancy decreased with increasing forging temperature.
- Similar to the quasi-static results, cyclic tests indicated that the cast and forged conditions exhibited a remarkable improvement in fatigue performance compared to the starting cast material.
    - Both the extruded and forged conditions displayed superior fatigue response compared to the cast and forged conditions.
    - Between the two extruded and forged conditions, the lower temperature forging exhibited superior fatigue behavior.

- An optimization function was developed within the research group to identify the optimal forging condition based on a set of provided mechanical requirements.
    - Considering this optimization function and accounting for experimental error, extruded AZ31B forging at 250°C was found to yield the best static and cyclic mechanical properties.

Chapter 6

- The current forged alloy exhibited an overall improvement in axial fatigue response and cyclic strengths compared to the starting as extruded condition.
- The texture developed in the forged AZ31B resulted in asymmetric axial hysteresis loops for axial strain amplitudes above 0.5%.
    - Significant cyclic hardening was also noted for these higher axial strain amplitudes.
- Cyclic shear tests resulted in stabilized hysteresis loops that were virtually symmetric at all tested shear strain amplitudes.
    - All tested shear strain amplitudes demonstrated only minor cyclic hardening.
- In-phase multi-axial tests combining various axial and shear strain amplitudes indicated that the each strain component affected the hysteresis loop of the other generally resulting in a decrease in positive elastic energy and an increase in plastic energy.
- Changing the phase angle between the applied axial and shear strain amplitudes exhibited a minor effect on fatigue life.
    - The effect of non-proportionality was far more pronounced on the shear hysteresis behavior than on the axial hysteresis behavior.
    - Non-proportional loading did result in additional cyclic hardening compared to the proportional condition.
- A modified SWT model provided good prediction for both uni-axial and multi-axial fatigue scenarios.
- The Jahed-Varvani (JV) energy model was also found to provide good prediction for most of the tested loading scenarios.

7.2. Recommended Future Work

Considering the work done to date, the suggested next steps for this work include:

- In-depth investigation of the microstructure and texture of the material pre- and post- cyclic tests to identify whether localized deformation mechanisms affect the location of crack initiation and growth.
    - Identification of microstructural evolution between the second and stabilized cycle.
    - EBSD/TEM analysis may be employed for this investigation.
- Thorough SEM examination of the fracture surfaces of cyclic shear and multi-axial specimens.

Bibliography

[1] S. Callery, H. Shaftel, and R. Jackson, "Global Climate Change: Vital Signs of the Planet," *NASA Jet Propulsion Laboratory, Caltech*, 2017. [Online]. Available: https://climate.nasa.gov/. [Accessed: 04-Dec-2017].

[2] "Greenhouse Gas Inventory Data Explorer," *United States Environmental Protection Agency*. [Online]. Available: https://www3.epa.gov/climatechange/ghgemissions/inventoryexplorer/. [Accessed: 04-Dec-2017].

[3] "Learn the facts: Weight affects fuel consumption," *Natural Resources Canada*, 2017. [Online]. Available: http://www.nrcan.gc.ca/energy/efficiency/transportation/cars-light-trucks/buying/16755. [Accessed: 04-Dec-2017].

[4] J. D. K. Bishop, N. P. D. Martin, and A. M. Boies, "Cost-effectiveness of alternative powertrains for reduced energy use and CO2 emissions in passenger vehicles," *Appl. Energy*, vol. 124, no. April 2013, pp. 44–61, 2014.

[5] G. Fontaras, N. G. Zacharof, and B. Ciuffo, "Fuel consumption and CO2 emissions from passenger cars in Europe – Laboratory versus real-world emissions," *Prog. Energy Combust. Sci.*, vol. 60, pp. 97–131, 2017.

[6] G. Fontaras and Z. Samaras, "On the way to 130 g CO2/km-Estimating the future characteristics of the average European passenger car," *Energy Policy*, vol. 38, no. 4, pp. 1826–1833, 2010.

[7] S. Kobayashi, S. Plotkin, and S. K. Ribeiro, "Energy efficiency technologies for road vehicles," *Energy Effic.*, vol. 2, no. 2, pp. 125–137, 2009.

[8] G. Huang, J. Li, T. Han, H. Zhang, and F. Pan, "Improving low-cycle fatigue properties of rolled AZ31 magnesium alloy by pre-compression deformation," *Mater. Des.*, vol. 58, pp. 439–444, 2014.

[9] S. Zheng, Q. Yu, and Y. Jiang, "An experimental study of fatigue crack propagation in extruded AZ31B magnesium alloy," *Int. J. Fatigue*, vol. 47, pp. 174–183, 2013.

[10] S. Li, A. C. Bacco, N. Birbilis, and H. Cong, “Passivation and potential fluctuation of Mg alloy AZ31B in alkaline environments,” *Corros. Sci.*, vol. 112, pp. 596–610, 2016.

[11] S. B. Yi, C. H. J. Davies, H. G. Brokmeier, R. E. Bolmaro, K. U. Kainer, and J. Homeyer, “Deformation and texture evolution in AZ31 magnesium alloy during uniaxial loading,” *Acta Mater.*, vol. 54, no. 2, pp. 549–562, 2006.

[12] A. Jäger, P. Lukáč, V. Gärtnerová, J. Haloda, and M. Dopita, “Influence of annealing on the microstructure of commercial Mg alloy AZ31 after mechanical forming,” *Mater. Sci. Eng. A*, vol. 432, no. 1–2, pp. 20–25, 2006.

[13] E. Dogan, I. Karaman, G. Ayoub, and G. Kridli, “Reduction in tension-compression asymmetry via grain refinement and texture design in Mg-3Al-1Zn sheets,” *Mater. Sci. Eng. A*, vol. 610, pp. 220–227, 2014.

[14] Y. Chino, K. Kimura, and M. Mabuchi, “Deformation characteristics at room temperature under biaxial tensile stress in textured AZ31 Mg alloy sheets,” *Acta Mater.*, vol. 57, no. 5, pp. 1476–1485, 2009.

[15] A. Chapuis and J. H. Driver, “Temperature dependency of slip and twinning in plane strain compressed magnesium single crystals,” *Acta Mater.*, vol. 59, no. 5, pp. 1986–1994, 2011.

[16] J. Zhang and S. P. Joshi, “Phenomenological crystal plasticity modeling and detailed micromechanical investigations of pure magnesium,” *J. Mech. Phys. Solids*, vol. 60, no. 5, pp. 945–972, 2012.

[17] J.-H. Cho and S.-B. Kang, “Magnesium Alloys Deformation and Recrystallization Behaviors in Magnesium Alloys,” in *Recent Developments in the Study of Recrystallization*, P. P. Wilson, Ed. 2013.

[18] H. Fan and J. A. El-Awady, “Molecular Dynamics Simulations of Orientation Effects During Tension, Compression, and Bending Deformations of Magnesium Nanocrystals,” *J. Appl. Mech.*, vol. 82, no. 10, p. 101006, 2015.

[19] A. Jain, O. Duygulu, D. W. Brown, C. N. Tomé, and S. R. Agnew, “Grain size effects on the tensile properties and deformation mechanisms of a magnesium alloy, AZ31B, sheet,” *Mater. Sci. Eng. A*, vol. 486, no. 1–2, pp. 545–555, 2008.

[20] J. Lin, X. Wang, W. Ren, X. Yang, and Q. Wang, “Enhanced Strength and Ductility Due to Microstructure Refinement and Texture Weakening of the GW102K Alloy by Cyclic Extrusion Compression,” *J. Mater. Sci. Technol.*, vol. 32, no. 8, pp. 783–789, 2016.

[21] É. Martin and J. J. Jonas, “Evolution of microstructure and microtexture during the hot deformation of Mg-3% Al,” *Acta Mater.*, vol. 58, no. 12, pp. 4253–4266, 2010.

[22] J. Tan and M. Tan, “Dynamic continuous recrystallization characteristics in two stage deformation of Mg Á 3Al Á 1Zn alloy sheet,” *Mater. Sci. Eng. A*, vol. 339, pp. 124–132, 2003.

[23] H. J. McQueen, “Initiating nucleation of dynamic recrystallization, primarily in polycrystals,” *Mater. Sci. Eng. A*, vol. 101, no. C, pp. 149–160, 1988.

[24] “Constitutive Modeling & Computational Materials Science Recrystallization and grain growth,” 2014. [Online]. Available: http://www.hhallberg.com/?p=556.

[25] S. Kleiner and P. J. Uggowitzer, “Mechanical anisotropy of extruded Mg-6% Al-1% Zn alloy,” *Mater. Sci. Eng. A*, vol. 379, no. 1–2, pp. 258–263, 2004.

[26] H. T. Jeong and T. K. Ha, “Texture development in a warm rolled AZ31 magnesium alloy,” *J. Mater. Process. Technol.*, vol. 187–188, pp. 559–561, 2007.

[27] C. H. J. Davies, S. B. Yi, J. Bohlen, K. U. Kainer, and H. G. Brokmeier, “Synchrotron Radiation Investigation of Twinning in Extruded Magnesium Alloy AZ31,” *Mater. Sci. Forum*, vol. 495–497, pp. 1633–1638, 2005.

[28] S. R. Agnew, C. N. Tomé, D. W. Brown, T. M. Holden, and S. C. Vogel, “Study of slip mechanisms in a magnesium alloy by neutron diffraction and modeling,” *Scr. Mater.*, vol. 48, no. 8, pp. 1003–1008, 2003.

[29] J. Casey and H. Jahedmotlagh, “The strength-differential effect in plasticity,” *Int. J. Solids Struct.*, vol. 20, no. 4, pp. 377–393, 1984.

[30] R. Abbaschian, L. Abbaschian, and R. E. Reed-Hill, *Physical Metallurgy Principles*, 4th ed. Boston: KWS-Kent Publishing Company, 1994.

[31] M. R. Barnett, “Twinning and the ductility of magnesium alloys. Part II. ‘Contraction’

twins," *Mater. Sci. Eng. A*, vol. 464, no. 1–2, pp. 8–16, 2007.

[32] S. Godet, L. Jiang, A. A. Luo, and J. J. Jonas, "Use of Schmid factors to select extension twin variants in extruded magnesium alloy tubes," *Scr. Mater.*, vol. 55, no. 11, pp. 1055–1058, 2006.

[33] A. Jain and S. R. Agnew, "Modeling the temperature dependent effect of twinning on the behavior of magnesium alloy AZ31B sheet," *Mater. Sci. Eng. A*, vol. 462, no. 1–2, pp. 29–36, 2007.

[34] S. H. Choi, E. J. Shin, and B. S. Seong, "Simulation of deformation twins and deformation texture in an AZ31 Mg alloy under uniaxial compression," *Acta Mater.*, vol. 55, no. 12, pp. 4181–4192, 2007.

[35] Y. Chino and M. Mabuchi, "Enhanced stretch formability of Mg-Al-Zn alloy sheets rolled at high temperature (723 K)," *Scr. Mater.*, vol. 60, no. 6, pp. 447–450, 2009.

[36] M. Graf, M. Ullmann, and R. Kawalla, "Property-oriented Production of Forged Magnesium Components," *Mater. Today Proc.*, vol. 2, pp. S76–S84, 2015.

[37] M. Graf, M. Ullmann, and R. Kawalla, "Influence of initial state on forgeability and microstructure development of magnesium alloys," *Procedia Eng.*, vol. 81, no. October, pp. 546–551, 2014.

[38] G. Garcés, A. Müller, E. Oñorbe, P. Pérez, and P. Adeva, "Effect of hot forging on the microstructure and mechanical properties of Mg-Zn-Y alloy," *J. Mater. Process. Technol.*, vol. 206, no. 1–3, pp. 99–105, 2008.

[39] A. Gryguc, S. K. Shaha, S. B. Behravesh, H. Jahed, M. Wells, and B. Williams, "Compression Behaviour of Semi-closed Die Forged AZ80 Extrusion," *Charact. Miner. Met. Mater. 2017*, pp. 361–369, 2017.

[40] S. M. H. Karparvarfard *et al.*, "Characterization of Semi-Closed Die-Forged ZK60 Mg Alloy Extrusion," *Magnes. Technol. 2017. Springer Int. Publ.*, pp. 329–334, 2017.

[41] J. Ma, X. Yang, H. Sun, Q. Huo, J. Wang, and J. Qin, "Anisotropy in the mechanical properties of AZ31 magnesium alloy after being compressed at high temperatures (up to

823K),” *Mater. Sci. Eng. A*, vol. 584, pp. 156–162, 2013.

[42] W. Guo, Q. Wang, B. Ye, and H. Zhou, “Microstructure and mechanical properties of AZ31 magnesium alloy processed by cyclic closed-die forging,” *J. Alloys Compd.*, vol. 558, pp. 164–171, 2013.

[43] H. T. Kang and T. Ostrom, “Mechanical behavior of cast and forged magnesium alloys and their microstructures,” *Mater. Sci. Eng. A*, vol. 490, no. 1–2, pp. 52–56, 2008.

[44] A. Gryguc, S. K. Shaha, H. Jahed, M. Wells, B. Williams, and J. McKinley, “Tensile and fatigue behaviour of as-forged AZ31B extrusion,” *Frat. ed Integrita Strutt.*, vol. 10, no. 38, pp. 251–258, 2016.

[45] A. Gryguc *et al.*, “Monotonic and cyclic behaviour of cast and cast-forged AZ80 Mg,” *Int. J. Fatigue*, vol. 104, pp. 136–149, 2017.

[46] M. Huppmann, M. Lentz, K. Brömmelhoff, and W. Reimers, “Fatigue properties of the hot extruded magnesium alloy AZ31,” *Mater. Sci. Eng. A*, vol. 527, no. 21–22, pp. 5514–5521, 2010.

[47] M. Kamakura, K. Tokaji, H. Shibata, and N. Bekku, “Grain Refinement and Improvement of Fatigue Strength due to Controlled Extrusion in Magnesium Alloys,” *J. Soc. Mater. Sci. Japan*, vol. 54, no. 3, pp. 245–250, 2005.

[48] S. Hyuk Park, S. G. Hong, B. Ho Lee, W. Bang, and C. Soo Lee, “Low-cycle fatigue characteristics of rolled Mg-3Al-1Zn alloy,” *Int. J. Fatigue*, vol. 32, no. 11, pp. 1835–1842, 2010.

[49] L. Wu *et al.*, “The effects of texture and extension twinning on the low-cycle fatigue behavior of a rolled magnesium alloy, AZ31B,” *Mater. Sci. Eng. A*, vol. 527, no. 26, pp. 7057–7067, 2010.

[50] S. B. Behravesh, H. Jahed, and S. Lambert, “Characterization of magnesium spot welds under tensile and cyclic loadings,” *Mater. Des.*, vol. 32, no. 10, pp. 4890–4900, 2011.

[51] S. B. Behravesh, H. Jahed, and S. Lambert, “Fatigue characterization and modeling of AZ31B magnesium alloy spot-welds,” *Int. J. Fatigue*, vol. 64, pp. 1–13, 2014.

[52] J. Albinmousa and H. Jahed, “Multiaxial effects on LCF behaviour and fatigue failure of AZ31B magnesium extrusion,” *Int. J. Fatigue*, vol. 67, pp. 103–116, 2014.

[53] J. Albinmousa, H. Jahed, and S. Lambert, “Cyclic behaviour of wrought magnesium alloy under multiaxial load,” *Int. J. Fatigue*, vol. 33, no. 8, pp. 1127–1139, 2011.

[54] M. Noban, H. Jahed, S. Winkler, and A. Ince, “Fatigue characterization and modeling of 30CrNiMo8HH under multiaxial loading,” *Mater. Sci. Eng. A*, vol. 528, no. 6, pp. 2484–2494, 2011.

[55] M. Noban, H. Jahed, E. Ibrahim, and A. Ince, “Load path sensitivity and fatigue life estimation of 30CrNiMo8HH,” *Int. J. Fatigue*, vol. 37, pp. 123–133, 2012.

[56] A. A. Roostaei and H. Jahed, “Multiaxial cyclic behaviour and fatigue modelling of AM30 Mg alloy extrusion,” *Int. J. Fatigue*, vol. 97, pp. 150–161, 2017.

[57] Y. Xiong, Q. Yu, and Y. Jiang, “Multiaxial fatigue of extruded AZ31B magnesium alloy,” *Mater. Sci. Eng. A*, vol. 546, pp. 119–128, 2012.

[58] Q. Yu, J. Zhang, Y. Jiang, and Q. Li, “Multiaxial fatigue of extruded AZ61A magnesium alloy,” *Int. J. Fatigue*, vol. 33, no. 3, pp. 437–447, 2011.

[59] J. Zhang, Q. Yu, Y. Jiang, and Q. Li, “An experimental study of cyclic deformation of extruded AZ61A magnesium alloy,” *Int. J. Plast.*, vol. 27, no. 5, pp. 768–787, 2011.

[60] A. A. Roostaei and H. Jahed, “Role of loading direction on cyclic behaviour characteristics of AM30 extrusion and its fatigue damage modelling,” *Mater. Sci. Eng. A*, vol. 670, pp. 26–40, 2016.

[61] M. Lalpoor, J. S. Dzwonczyk, N. Hort, and S. E. Offerman, “Nucleation mechanism of Mg17Al12-precipitates in binary Mg-7 wt.% Al alloy,” *J. Alloys Compd.*, vol. 557, pp. 73–76, 2013.

[62] I. Ulacia *et al.*, “Texture Evolution of AZ31 Magnesium Alloy Sheet at High Strain Rates,” *4th Int. Conf. High Speed Form.*, pp. 189–197, 2010.

[63] J. Luo, Z. Mei, W. Tian, and Z. Wang, “Diminishing of work hardening in electroformed polycrystalline copper with nano-sized and uf-sized twins,” *Mater. Sci. Eng. A*, vol. 441, no.

1–2, pp. 282–290, 2006.

[64] J. A. del Valle, F. Carreño, and O. A. Ruano, “Influence of texture and grain size on work hardening and ductility in magnesium-based alloys processed by ECAP and rolling,” *Acta Mater.*, vol. 54, no. 16, pp. 4247–4259, 2006.

[65] M. R. Barnett, Z. Keshavarz, A. G. Beer, and D. Atwell, “Influence of grain size on the compressive deformation of wrought Mg-3Al-1Zn,” *Acta Mater.*, vol. 52, no. 17, pp. 5093–5103, 2004.

[66] M. A. Gharghouri, G. C. Weatherly, and J. D. Embury, “The interaction of twins and precipitates in a Mg-7.7 at.% Al alloy,” *Philos. Mag. a-Physics Condens. Matter Struct. Defects Mech. Prop.*, vol. 78, no. 5, pp. 1137–1149, 1998.

[67] D. Sarker, J. Friedman, and D. L. Chen, “De-twinning and Texture Change in an Extruded AM30 Magnesium Alloy during Compression along Normal Direction,” *J. Mater. Sci. Technol.*, vol. 31, no. 3, pp. 264–268, 2015.

[68] D. Sarker, J. Friedman, and D. L. Chen, “Twin growth and texture evolution in an extruded AM30 magnesium alloy during compression,” *J. Mater. Sci. Technol.*, vol. 30, no. 9, pp. 884–887, 2014.

[69] S. Spigarelli *et al.*, “Analysis of high-temperature deformation and microstructure of an AZ31 magnesium alloy,” *Mater. Sci. Eng. A*, vol. 462, no. 1–2, pp. 197–201, 2007.

[70] M. Kavyani, G. R. Ebrahimi, M. Sanjari, and M. Haghshenas, “Texture evaluation in warm deformation of an extruded Mg-6Al-3Zn alloy,” *J. Magnes. Alloy.*, vol. 4, no. 2, pp. 89–98, 2016.

[71] X. yue Yang, Z. sheng Ji, H. Miura, and T. Sakai, “Dynamic recrystallization and texture development during hot deformation of magnesium alloy AZ31,” *Trans. Nonferrous Met. Soc. China (English Ed.*, vol. 19, no. 1, pp. 55–60, 2009.

[72] H. Zhang, G. Huang, J. Fan, H. Jørgen Roven, F. Pan, and B. Xu, “Deep drawability and deformation behavior of AZ31 magnesium alloy sheets at 473K,” *Mater. Sci. Eng. A*, vol. 608, pp. 234–241, 2014.

[73] S. M. Razavi *et al.*, "Effect of grain size on prismatic slip in Mg-3Al-1Zn alloy," *Scr. Mater.*, vol. 67, no. 5, pp. 439–442, 2012.

[74] S. Seipp, M. F. X. Wagner, K. Hockauf, I. Schneider, L. W. Meyer, and M. Hockauf, "Microstructure, crystallographic texture and mechanical properties of the magnesium alloy AZ31B after different routes of thermo-mechanical processing," *Int. J. Plast.*, vol. 35, pp. 155–166, 2012.

[75] N. Hansen, "Hall-petch relation and boundary strengthening," *Scr. Mater.*, vol. 51, no. 8 SPEC. ISS., pp. 801–806, 2004.

[76] S. H. Park, J. H. Lee, B. G. Moon, and B. S. You, "Tension-compression yield asymmetry in as-cast magnesium alloy," *J. Alloys Compd.*, vol. 617, pp. 277–280, 2014.

[77] K. Máthis, P. Beran, J. Čapek, and P. Lukáš, "In-situ neutron diffraction and acoustic emission investigation of twinning activity in magnesium," *J. Phys. Conf. Ser.*, vol. 340, p. 12096, 2012.

[78] M. R. Barnett, "Twinning and the ductility of magnesium alloys. Part I: 'Tension' twins," *Mater. Sci. Eng. A*, vol. 464, no. 1–2, pp. 1–7, 2007.

[79] B.-C. Suh, J. H. Kim, J. H. Hwang, M.-S. Shim, and N. J. Kim, "Twinning-mediated formability in Mg alloys," *Sci. Rep.*, vol. 6, no. 1, p. 22364, 2016.

[80] B. Q. Shi, R. S. Chen, and W. Ke, "Influence of grain size on the tensile ductility and deformation modes of rolled Mg-1.02 wt.% Zn alloy," *J. Magnes. Alloy.*, vol. 1, no. 3, pp. 210–216, 2013.

[81] R. Zhu, X. Cai, Y. Wu, L. Liu, W. Ji, and B. Hua, "Low-cycle fatigue behavior of extruded Mg-10Gd-2Y-0.5Zr alloys," *Mater. Des.*, vol. 53, pp. 992–997, 2014.

[82] X. Z. Lin and D. L. Chen, "Strain controlled cyclic deformation behavior of an extruded magnesium alloy," *Mater. Sci. Eng. A*, vol. 496, no. 1–2, pp. 106–113, 2008.

[83] F. Lv *et al.*, "Fatigue properties of rolled magnesium alloy (AZ31) sheet: Influence of specimen orientation," *Int. J. Fatigue*, vol. 33, no. 5, pp. 672–682, 2011.

[84] F. Yang, S. M. Yin, S. X. Li, and Z. F. Zhang, "Crack initiation mechanism of extruded

AZ31 magnesium alloy in the very high cycle fatigue regime," *Mater. Sci. Eng. A*, vol. 491, no. 1–2, pp. 131–136, 2008.

[85] H. Mayer, M. Papakyriacou, B. Zettl, and S. E. Stanzl-Tschegg, "Influence of porosity on the fatigue limit of die cast magnesium and aluminium alloys," *Int. J. Fatigue*, vol. 25, no. 3, pp. 245–256, 2003.

[86] J. Albinmousa, H. Jahed, and S. Lambert, "Cyclic axial and cyclic torsional behaviour of extruded AZ31B magnesium alloy," *Int. J. Fatigue*, vol. 33, no. 11, pp. 1403–1416, 2011.

[87] X. Y. Lou, M. Li, R. K. Boger, S. R. Agnew, and R. H. Wagoner, "Hardening evolution of AZ31B Mg sheet," *Int. J. Plast.*, vol. 23, no. 1, pp. 44–86, 2007.

[88] H. Yu, Y. Xin, A. Chapuis, X. Huang, R. Xin, and Q. Liu, "The different effects of twin boundary and grain boundary on reducing tension-compression yield asymmetry of Mg alloys," *Sci. Rep.*, vol. 6, no. 1, p. 29283, 2016.

[89] J. Dallmeier, O. Huber, H. Saage, and K. Eigenfeld, "Uniaxial cyclic deformation and fatigue behavior of AM50 magnesium alloy sheet metals under symmetric and asymmetric loadings," *Mater. Des.*, vol. 70, pp. 10–30, 2015.

[90] S. Hasegawa, Y. Tsuchida, H. Yano, and M. Matsui, "Evaluation of low cycle fatigue life in AZ31 magnesium alloy," *Int. J. Fatigue*, vol. 29, no. 9–11, pp. 1839–1845, 2007.

[91] S. M. Yin, H. J. Yang, S. X. Li, S. D. Wu, and F. Yang, "Cyclic deformation behavior of as-extruded Mg-3%Al-1%Zn," *Scr. Mater.*, vol. 58, no. 9, pp. 751–754, 2008.

[92] L. Wu *et al.*, "Twinning-detwinning behavior during the strain-controlled low-cycle fatigue testing of a wrought magnesium alloy, ZK60A," *Acta Mater.*, vol. 56, no. 4, pp. 688–695, 2008.

[93] G. Huang, J. Li, T. Han, H. Zhang, and F. Pan, "Improving low-cycle fatigue properties of rolled AZ31 magnesium alloy by pre-compression deformation," *Mater. Des.*, vol. 58, pp. 439–444, 2014.

[94] D. W. Brown, A. Jain, S. R. Agnew, and B. Clausen, "Twinning and detwinning during cyclic deformation of Mg alloy AZ31B," *Thermec 2006, Pts 1-5*, vol. 539–543, pp. 3407–

3413, 2007.

[95] Q. Yu, J. Zhang, Y. Jiang, and Q. Li, “An experimental study on cyclic deformation and fatigue of extruded ZK60 magnesium alloy,” *Int. J. Fatigue*, vol. 36, no. 1, pp. 47–58, 2012.

[96] K. Hazeli *et al.*, “Microstructure-sensitive investigation of magnesium alloy fatigue,” *Int. J. Plast.*, vol. 68, pp. 55–76, 2015.

[97] Derek Hull, *Fractography: Observing, Measuring and Interpreting Fracture Surface Topography*. Cambridge University Press, 1999.

[98] M. Tsushida, K. Shikada, H. Kitahara, S. Ando, and H. Tonda, “Relationship between Fatigue Strength and Grain Size in AZ31 Magnesium Alloys,” *Mater. Trans.*, vol. 49, no. 5, pp. 1157–1161, 2008.

[99] Y. J. Wu, R. Zhu, J. T. Wang, and W. Q. Ji, “Role of twinning and slip in cyclic deformation of extruded Mg-3%Al-1%Zn alloys,” *Scr. Mater.*, vol. 63, no. 11, pp. 1077–1080, 2010.

[100] S. Ando, Y. Ikejiri, N. Iida, M. Tsushida, and H. Tonda, “Orientation Dependence of Fatigue Crack Propagation in Magnesium Single Crystal,” *J. Japan Institude Met. Mater.*, vol. 70, no. 8, pp. 634–637, 2006.

[101] Kn. Smith, T. H. Topper, and P. Watson, “A stress-strain function for the fatigue of metals(Stress-strain function for metal fatigue including mean stress effect),” *J. Mater.*, vol. 5, no. April, pp. 767–778, 1970.

[102] H. Jahed and J. Albinmousa, “Multiaxial behaviour of wrought magnesium alloys - A review and suitability of energy-based fatigue life model,” *Theor. Appl. Fract. Mech.*, vol. 73, pp. 97–108, 2014.

[103] Y. C. Lin, Z. H. Liu, X. M. Chen, and J. Chen, “Stress-based fatigue life prediction models for AZ31B magnesium alloy under single-step and multi-step asymmetric stress-controlled cyclic loadings,” *Comput. Mater. Sci.*, vol. 73, pp. 128–138, 2013.

[104] P. A. Rometsch and G. B. Schaffer, “An age hardening model for Al-7Si-Mg casting alloys,” *Mater. Sci. Eng. A*, vol. 325, no. 1–2, pp. 424–434, 2002.

[105] K. L. Fan *et al.*, “Tensile and fatigue properties of gravity casting aluminum alloys for

engine cylinder heads," *Mater. Sci. Eng. A*, vol. 586, pp. 78–85, 2013.

[106] S. K. Shaha, F. Czerwinski, W. Kasprzak, J. Friedman, and D. L. Chen, "Monotonic and cyclic deformation behavior of the Al-Si-Cu-Mg cast alloy with micro-additions of Ti, V and Zr," *Int. J. Fatigue*, vol. 70, pp. 383–394, 2015.

[107] H. Jahed and A. Varvani-Farahani, "Upper and lower fatigue life limits model using energy-based fatigue properties," *Int. J. Fatigue*, vol. 28, no. 5–6, pp. 467–473, 2006.

[108] H. Jahed, A. Varvani-Farahani, M. Noban, and I. Khalaji, "An energy-based fatigue life assessment model for various metallic materials under proportional and non-proportional loading conditions," *Int. J. Fatigue*, vol. 29, no. 4, pp. 647–655, 2007.

[109] K. Golos and F. Ellyin, "Generalization of cumulative damage criterion to multilevel cyclic loading," *Theor. Appl. Fract. Mech.*, vol. 7, no. 3, pp. 169–176, 1987.

[110] S. B. Dayani, S. K. Shaha, R. Ghelichi, J. F. Wang, and H. Jahed, "The impact of AA7075 cold spray coating on the fatigue life of AZ31B cast alloy," *Surf. Coatings Technol.*, vol. 337, no. June 2017, pp. 150–158, 2018.

[111] E. Kalateh Mollaei and H. Jahed, "Load Controlled Fatigue of AZ31B," *J. Mech. Res. Appl.*, vol. 4, no. 2, pp. 41–47, 2013.

[112] O. Sitdikov and R. Kaibyshev, "Dynamic Recrystallization in Pure Magnesium," *Mater. Trans.*, vol. 42, no. 9, pp. 1928–1937, 2001.

[113] W. Yuan, S. K. Panigrahi, J. Q. Su, and R. S. Mishra, "Influence of grain size and texture on Hall-Petch relationship for a magnesium alloy," *Scr. Mater.*, vol. 65, no. 11, pp. 994–997, 2011.

[114] L. L. Chang, Y. N. Wang, X. Zhao, and M. Qi, "Grain size and texture effect on compression behavior of hot-extruded Mg-3Al-1Zn alloys at room temperature," *Mater. Charact.*, vol. 60, no. 9, pp. 991–994, 2009.

[115] Y. Wang and H. Choo, "Influence of texture on Hall-Petch relationships in an Mg alloy," *Acta Mater.*, vol. 81, pp. 83–97, 2014.

[116] G. Z. Quan, Y. Shi, Y. X. Wang, B. S. Kang, T. W. Ku, and W. J. Song, "Constitutive

modeling for the dynamic recrystallization evolution of AZ80 magnesium alloy based on stress-strain data," *Mater. Sci. Eng. A*, vol. 528, no. 28, pp. 8051–8059, 2011.

[117] S. Aliakbari Sani, G. R. Ebrahimi, and A. R. Kiani Rashid, "Hot deformation behavior and dynamic recrystallization kinetics of AZ61 and AZ61 + Sr magnesium alloys," *J. Magnes. Alloy.*, vol. 4, no. 2, pp. 104–114, 2016.

[118] Y. Xu, L. Hua, and Y. Sun, "Deformation behaviour and dynamic recrystallization of AZ61 magnesium alloy," *J. Alloys Compd.*, vol. 580, pp. 262–269, 2013.

[119] G. Cai, X. Huang, and S. Qu, "Effect of hot compression process on recrystallization microstructure and mechanical properties of AZ31 magnesium alloy," *Phys. Procedia*, vol. 50, no. October 2012, pp. 61–67, 2013.

[120] I. A. Maksoud, H. Ahmed, and J. R??del, "Investigation of the effect of strain rate and temperature on the deformability and microstructure evolution of AZ31 magnesium alloy," *Mater. Sci. Eng. A*, vol. 504, no. 1–2, pp. 40–48, 2009.

[121] C. M. Cepeda-Jimenez, J. M. Molina-Aldareguia, and M. T. Perez-Prado, "Effect of grain size on slip activity in pure magnesium polycrystals," *Acta Mater.*, vol. 84, pp. 443–456, 2015.

[122] H. Jahed, S. B. Behravesh, A. Gryguc, S. M. H. Karparvarfard, and D. Toscano, "Internal Discussions." Waterloo, ON, 2017.

[123] S. Begum, D. L. Chen, S. Xu, and A. A. Luo, "Effect of strain ratio and strain rate on low cycle fatigue behavior of AZ31 wrought magnesium alloy," *Mater. Sci. Eng. A*, vol. 517, no. 1–2, pp. 334–343, 2009.

[124] S. H. Park, S. G. Hong, W. Bang, and C. S. Lee, "Effect of anisotropy on the low-cycle fatigue behavior of rolled AZ31 magnesium alloy," *Mater. Sci. Eng. A*, vol. 527, no. 3, pp. 417–423, 2010.

[125] E. Schmid and W. Boas, *Kristallplastizität*. 1935.

[126] H. Fan, S. Aubry, A. Arsenlis, and J. A. El-Awady, "Grain size effects on dislocation and twinning mediated plasticity in magnesium," *Scr. Mater.*, vol. 112, pp. 50–53, 2016.

[127] H. J. Choi, Y. Kim, J. H. Shin, and D. H. Bae, “Deformation behavior of magnesium in the grain size spectrum from nano- to micrometer,” *Mater. Sci. Eng. A*, vol. 527, no. 6, pp. 1565–1570, 2010.

[128] J. Li, W. Xu, X. Wu, H. Ding, and K. Xia, “Effects of grain size on compressive behaviour in ultrafine grained pure Mg processed by equal channel angular pressing at room temperature,” *Mater. Sci. Eng. A*, vol. 528, no. 18, pp. 5993–5998, 2011.

[129] J. Lin, W. Ren, Q. Wang, L. Ma, and Y. Chen, “Influence of grain size and texture on the yield strength of Mg alloys processed by severe plastic deformation,” *Adv. Mater. Sci. Eng.*, vol. 2014, pp. 24–32, 2014.

[130] S. Begum, D. L. Chen, S. Xu, and A. A. Luo, “Erratum: Strain-controlled low-cycle fatigue properties of a newly developed extruded magnesium alloy (Metallurgical and Materials Transactions A (2008) vol. 39 (12) (3014-3026) 10.1007/s11661-008-9677-0)),” *Metall. Mater. Trans. A Phys. Metall. Mater. Sci.*, vol. 40, no. 1, p. 255, 2009.

[131] W. Wu, P. K. Liaw, and K. An, “Unraveling cyclic deformation mechanisms of a rolled magnesium alloy using in situ neutron diffraction,” *Acta Mater.*, vol. 85, pp. 343–353, 2015.

[132] A. Fatemi and D. F. Socie, “A Critical Plane Approach To Multiaxial Fatigue Damage Including Out-of-Phase Loading,” *Fatigue Fract. Eng. Mater. Struct.*, vol. 11, no. 3, pp. 149–165, 1988.

[133] F. Ellyin, K. Golos, and Z. Xia, “In-Phase and Out-of-Phase Multiaxial Fatigue,” *J. Eng. Mater. Technol.*, vol. 113, no. 1, pp. 112–118, 1991.

[134] X. Chen, S. Xu, and D. Huang, “Critical plane-strain energy density criterion for multiaxial low-cycle fatigue life under non-proportional loading,” *Fatigue Fract. Eng. Mater. Struct.*, vol. 22, no. 8, pp. 679–686, 1999.

[135] T. Itoh, M. Sakane, D. F. Socie, and M. Ohnami, “Non-proportional low cycle fatigue criterion for type 304 stainless steel,” *J. Eng. Mater. Technol.*, vol. 117, no. July 1995, pp. 285–292, 1995.

[136] S. D.F. and M. G.B., “Multiaxial Fatigue,” in *SAE International*, Warrendale (PA), 2000.

[137] Y. Jiang and H. Sehitoglu, “Fatigue and stress analyses of rolling contact,” no. 161. Urbana-champaign, pp. 1-1-38, 1992.

[138] J. Albinmousa, H. Jahed, and S. Lambert, “An Energy-Based Fatigue Model for Wrought Magnesium Alloy under Multiaxial Load,” *Ninth Int. Conf. Multiaxial Fatigue Fract.*, pp. 471–478, 2010.